SAPIENZA
Università di Roma

Advancements in Photogrammetric and LiDAR Techniques: Innovations, Applications, and Implications for Precision Mapping and 3D Modeling

Dottorato di Ricerca in Ingegneria Idraulica ed Ambientale – Curriculum ambientale

XXXVI Cicle

	Thesis Tutor	Co-Tutor
Candidate: **Ing. Felicia Monti**	Prof. Valerio Baiocchi	Prof.ssa Francesca Giannone

Author's address Felicia Monti

Department of Civil, Building and Environmental Engineering

Sapienza University of Rome, Italy

Via Eudossiana, 18, 00184, Rome, Italy

Felicia.monti@uniroma1.it

Supervisor Prof. Paolo Monti

Department of Civil, Building and Environmental Engineering

Sapienza University of Rome, Italy

Tutor Prof. Valerio Baiocchi

Department of Civil, Building and Environmental Engineering

Sapienza University of Rome, Italy

Co-tutor Prof. Francesca Giannone

Department of Engineering

Niccolò Cusano University, Rome, Italy

Reviewers

Dott. ssa Grazia Pietrantonio, National Institute for Geophysics and Vulcanology (INGV)

Prof. Gino Dardanelli, University of Palermo, Italy

"If we knew what we were doing, it would not be called research, would it?

ABSTRACT

My doctoral project involved the study, deepening, and improvement of the most recent geomatic techniques, with particular reference to the geometric processing of optical images and new sensors based on laser technologies. Photogrammetry has actually been developed since the inception of photographic techniques and, according to some authors, even from the mid-19th century. However, digital techniques have radically changed the approach methodologies, both at the level of software tools and software for processing and handling them. It is noteworthy that until the 20th century, photogrammetric techniques had achieved a certain stabilization, and acquisition and processing tools remained valid for decades. Currently, according to some of the most recognized authors in the field, certain photogrammetric survey instruments become obsolete in about two years.

Regarding laser scanning survey techniques, recent years have been characterized by a succession of new sensors with, in some cases, surprisingly high performance, such as new miniaturized laser scanners that can be airborne by drones or installed in SLAM devices.

In this climate of technological ferment, this thesis aimed to understand the potential and possible optimization methods of sensors that became available and evolved during the course of the thesis. For a broader overview, the focus was on photogrammetric sensors installed on drones, those within semi-professional cameras, as well as those mounted on simple smartphones and, finally, the more "traditional" panchromatic and hyperspectral sensors installed on satellite platforms.

The processing of optical images is an issue that began and was developed during my undergraduate thesis (the results of which are reported in the appendix for completeness); the foundations of this initial research were deepened in the first chapter, where the experimental hyperspectral satellite PRISMA (then recently released) was evaluated and tested, revealing itself to be one of the complex satellite sensors to be geometrically processed.

However, "classic" photogrammetric processing must now be integrated with more modern techniques borrowed from computer vision, primarily Structure From Motion (SFM). For this reason, in the second chapter, we will see how SFM techniques, applied to acquisitions with semi-professional cameras, drones, and smartphones, enabled a complete survey (previously impossible) of an area characterized by the presence of cavities of historical and environmental importance, also allowing the development of new theories on the tectonic evolution of the area by an international and multidisciplinary research team.

Still by another international research team, the third chapter will illustrate the study of the combined potential of photogrammetric survey and high-precision GNSS positioning enabled by some smartphones, particularly in very remote areas where sensor miniaturization is of primary importance, making otherwise impossible surveys feasible.

The fourth chapter will compare various recent survey techniques in a complex site of cultural and environmental significance, highlighting both the potential and the unexpected limitations of some of the latest generation sensors.

The thesis concludes with the bibliography consulted for its development and the aforementioned appendix containing a study related to my undergraduate thesis on the development of satellite image orientation procedures, which formed the basis for some of the in-depth studies during my doctorate. Also in the appendix are very preliminary results of an ongoing research on the use of Cosmoskymed images on the island of Ischia and a comparison with permanent GNSS stations for the study of geodynamic movements.

CONTENTS

INTRODUCTION

The development of geomatic techniques has experienced unprecedented growth in recent years, leading some authors to claim that certain equipment has become obsolete within just a few years. Indeed, the landscape of devices and software strategies available in both open-source and commercial software requires constant experimentation and validation of the most current techniques.

For example, in recent years, there have been significant technological and methodological advancements in the field of photogrammetry, greatly improving the precision and efficiency of its applications.

Among the most recent geomatic developments, we can highlight:

- Integration of Drones and UAVs (Unmanned Aerial Vehicles)

Drones are revolutionizing photogrammetry due to their ability to cover vast areas in a short amount of time and to collect high-resolution data from angles that are difficult to access using traditional methods. It is important to note that aerial photogrammetry over large areas remains faster and, therefore, irreplaceable for many acquisitions; however, drones can prove to be much more versatile for limited areas. These devices are equipped with high-definition cameras (see Chapter 2) and LiDAR sensors (see Chapter 4), enabling the production of detailed 3D models of the terrain and structures.

- Multi-Sensor Systems

The integration of various sensors, such as RGB cameras, multispectral cameras, thermal sensors, and LiDAR (see Chapter 4), allows for the collection of complementary data that enhances the quality and accuracy of photogrammetric models. This combination of data can be used for

applications in precision agriculture, archaeology, natural resource management, environmental monitoring, and the preservation of cultural heritage (see Chapter 4).

- Advanced Processing Software

Recent advancements in photogrammetry software, such as Agisoft Metashape, Pix4D, and RealityCapture, have enabled the efficient and accurate processing of large volumes of data. These software packages primarily rely on Structure From Motion (SFM) algorithms to optimize image alignment, 3D model generation, and residual error analysis (see Chapters 2, 3, & 4).

- Mobile Photogrammetry

The use of mobile devices, such as smartphones and tablets, for collecting photogrammetric data is becoming increasingly common (see Chapter 3). These devices are equipped with high-resolution cameras and real-time processing software, making photogrammetry accessible to a wider audience for applications such as architectural documentation, interior modeling, and scanning of small objects.

- Augmented and Virtual Reality

The combination of photogrammetry with augmented reality (AR) and virtual reality (VR) technologies is opening new possibilities for the visualization and analysis of data. These tools allow users to interact with 3D models in immersive environments, enhancing spatial understanding (see Chapter 2) and communication of results.

These developments are making photogrammetry, and geomatic techniques in general, increasingly powerful and versatile tools, with applications ranging from cartography (see Chapter 3) to cultural heritage preservation (see

Chapter 2), from civil engineering (see Chapter 1) to environmental management (see Chapter 4). The continuous evolution of photogrammetric technologies and methodologies promises further improvements in terms of precision, efficiency, and accessibility.

1.1 PANCROMATIC AND HYPERSPECTRAL SATELLITE IMAGERY ORIENTATION STRATEGIES WITHOUT STANDARD METADATA

High and very high-resolution satellite images are currently processed through a "classic" photogrammetric approach, which involves defining the camera's internal orientation parameters and the external orientation parameters. This approach, despite updates, is not significantly different from the one applied to aerial images for decades. Generally, this approach is based on the prior knowledge of certain parameters such as the camera's characteristics and the orbital parameters of the platform itself. Some satellite operators, mainly for technological and industrial confidentiality reasons, do not release these data openly and prefer to release Rational Polynomial Coefficient (RPC) parameters of the Rational Polynomial Functions (RPF) transformations.

For simplicity, the metadata files containing the RPC parameters have been standardized according to specific guidelines from the National Imagery and Mapping Agency (NIMA) of the United States, and many satellite operators adhere to these standards. This adherence allows Dynamic Link Libraries (DLL) such as GDAL to handle various types of images in a metrically correct manner.

In summary, satellite images can be correctly oriented using photogrammetrically rigorous models if the internal orientation parameters and orbital information are known, or through RPC parameters if available in standard format. In some cases, even very recent satellite platforms (such as the PRISMA satellite from the Italian Space Agency) do not release either the

parameters for the rigorous model or the RPCs in a standard format, but only non-standard metadata. In such cases, it is necessary to verify if there is a possibility to convert the information contained in the metadata to construct standard metadata and proceed with the correct geometric processing of the images necessary for any subsequent metrically correct use.

The feasibility of this approach was tested for the recently released PRISMA satellite, and despite encountering several challenges, a procedure was defined that allows for the exploitation of the interesting hyperspectral characteristics of these otherwise difficult-to-use images.

1.2 STRUCTURE FROM MOTION IN VERY NARROW AREAS

Surveying in outdoor environments has been significantly facilitated for many years by the capabilities offered by satellite positioning and optical and/or laser sensors. Conversely, surveying indoor and very narrow areas remains highly complex. This complexity arises not only because automatic positioning is not possible but also, and especially, because in some very narrow passages it is not feasible to use and/or transport the most common geomatic instruments. This is the case for hypogeal structures of technical infrastructures such as aqueducts, mining areas, and similar environments. It is even more frequently the case for areas containing completely underground cultural heritage sites, such as the catacombs beneath the cities of Rome and Naples in Italy, or the underground city of Derinkuyu in Turkey, to name a few examples. Similar challenges arise when surveying historic buildings, which often feature very narrow service areas or connections between levels via tight openings such as spiral staircases.

In all these scenarios, connecting multiple surveys or continuing the survey through certain passages is technically challenging but necessary to

understand the relative positions between the various surveyed environments and their spatial relationships to the outside.

A particularly complex case was the survey of the La Sassa cave (Italy), characterized by multiple hypogeal environments connected by very narrow passages. The cave is of particular interest as it has been inhabited by humans since the Bronze Age and even earlier by various animal species. Surveying all these environments required a multidisciplinary study within a research team and allowed for the localization and reopening of the original entrance. Additionally, it enabled the hypothesis that the current morphology, characterized by very narrow passages connecting larger rooms, is actually the result of geodynamic action on the enclosing rocks.

1.3 POST PROCESSING GNSS AND HIGH-RESOLUTION CAMERA INTEGRATION IN A SMARTPHONE DEVICE

As illustrated in the previous paragraph, the reduction in the size of sensors used for geomatic surveys is revolutionizing survey methods. Additionally, it is worth noting that, in some cases, devices not initially designed for geomatic purposes, such as smartphones, are beginning to possess features and functionalities suitable for metrically accurate surveys. Indeed, while the photographic capabilities of smartphones have reached those of professional cameras, at least in terms of resolution, the positioning sensors in these devices have also shown remarkable advancements over the past few years. These improvements enable the creation of post-processing files for both code and phase data. The latest releases of mobile devices from one of the most renowned manufacturers even include the capability to perform LIDAR surveys at short distances, up to approximately 5 meters. The availability of such surveying capabilities in commonly used devices makes it possible to conduct surveys that would otherwise be unfeasible or require the organization of complex measurement campaigns.

During an experimental project at Machu Picchu (Peru), conducted as part of an international collaboration, the feasibility of surveying the Intihuatana stone was tested using only a smartphone equipped with a 5-megapixel camera and a dual-frequency GNSS receiver. This setup allowed for the acquisition of photogrammetric images and the survey of reference points using only a common device that can be easily transported to a logistically challenging area like Machu Picchu. Additionally, it does not require special permits either at the time of the survey or for importing and exporting the equipment from a foreign country. These latter aspects are particularly significant in many countries, where such surveys can be complicated or, in some cases, impossible due to stringent regulations.

For the sake of completeness, it should be noted that the post-processing file writing capabilities, enabled in 2017, appear to have been subsequently restricted by the Android operating system in its latest versions and updates. This restriction poses a potential limitation to the full utilization of smartphones for advanced geomatic surveys, highlighting the ongoing need for specialized equipment in certain contexts. However, the progress made so far demonstrates a promising trend towards more accessible and versatile surveying technologies, enabling a broader range of applications and fostering innovation in the field of geomatics.

1.4 LIDAR BY DRONE AND SLAM SENSORS CAPABILITIES AND THEIR LIMITATIONS

LIDAR sensors have undergone significant advancements. A few years ago, they were composed solely of heavy hardware requiring substantial electrical power, necessitating large and cumbersome batteries. Today, however, LIDAR sensors have become much more compact and lightweight, to the point that they can be carried on portable devices by operators or even mounted on drones. Although their metric accuracy is still somewhat lower compared to

static terrestrial laser scanners, their portability—whether by operators or drones—opens up new surveying possibilities.

A recent experiment was conducted on a Roman nymphaeum in Gaeta, Italy, which is partially above ground and partially subterranean. The survey utilized four different techniques for comparison: traditional optical survey from a drone, RTK drone-based LIDAR survey, terrestrial laser scanning, and manual survey using a SLAM sensor. The LIDAR sensors, both UAV-mounted and SLAM-based, demonstrated remarkable precision and detail, comparable to terrestrial laser scanners. However, when evaluating the accuracy of the RTK drone LIDAR survey, it was found that although it could create a very dense point cloud, there was a systematic vertical discrepancy of a few centimeters compared to the more traditional point cloud from the optical drone survey without RTK. This discrepancy is hypothesized to be due to imperfect modeling of the GNSS RTK antenna height mounted on the LIDAR drone. Additionally, it was observed that the penetration capability of the drone-mounted sensor could be insufficient in cases of dense vegetation cover.

In the case of the SLAM sensor survey, it showed good agreement with traditional laser scanning in exterior areas but exhibited drift as it progressed into the subterranean sections. It is worth noting that traditional laser scanning for such surveys would also require connecting points to maintain accuracy.

These developments highlight the rapid evolution of LIDAR technology and its increasing versatility in geomatic applications. The ability to mount LIDAR sensors on drones or carry them manually has significant implications for surveying difficult-to-reach areas, such as those with complex topographies or limited accessibility. This was particularly evident in the Gaeta nymphaeum experiment, where each technique provided valuable data, but the portability of the LIDAR sensors offered unique advantages. Despite some limitations, such as the need for precise antenna modeling and challenges with dense

vegetation, the use of LIDAR sensors on UAVs and SLAM devices represents a major step forward in the field of geomatics. The continuous improvement and miniaturization of these sensors promise to further enhance their application range, making high-precision surveys more feasible and efficient across diverse and challenging environments.

1.5 THESIS AIM

In the current landscape of rapid evolution and miniaturization of various geomatic sensors, this thesis aims to study some of the newly available sensors and evaluate their capabilities, precision, accuracy, and consistency of the data they provide. To achieve this, the approach begins with a theoretical study of the operating principles of these sensors. This foundational knowledge will then be applied in practical experiments conducted in real-world survey situations. These practical experiments are designed to test the sensors against actual application problems, thereby assessing their true capabilities and applicability.

The focus of the research will be on several cutting-edge technologies, including hyperspectral satellite platforms, optical and LIDAR drones, sensors integrated into smartphones, and SLAM-based instruments. Each of these technologies represents a significant advancement in the field of geomatics, offering new methods and tools for data collection and analysis.

Hyperspectral satellite platforms provide detailed spectral information that can be used for a variety of applications, such as environmental monitoring, agriculture, and geology. The ability to capture data across a wide range of wavelengths allows for the identification and analysis of materials and conditions that would be difficult or impossible to discern with traditional imaging techniques.

Optical and LIDAR drones offer unparalleled flexibility and accessibility for aerial surveys. These drones can capture high-resolution images and generate precise 3D models of the surveyed areas. The integration of LIDAR technology enhances their capability to penetrate vegetation and other obstacles, providing accurate topographical data even in challenging environments.

Smartphone sensors have become increasingly sophisticated, with many modern smartphones equipped with high-resolution cameras and advanced positioning sensors. These devices can now be used for basic geomatic surveys, offering a convenient and readily available tool for data collection. The use of smartphones for surveying can significantly reduce the cost and complexity of survey operations, making it more accessible for a wide range of users.

SLAM (Simultaneous Localization and Mapping) instruments are particularly valuable for indoor and underground surveys where GNSS signals are not available. SLAM technology allows for real-time mapping and navigation, providing accurate spatial data even in complex and constrained environments. This makes SLAM-based instruments ideal for applications such as mining, underground construction, and archaeological surveys.

By thoroughly examining these technologies, this thesis aims to provide a comprehensive evaluation of the current state of geomatic sensors and their potential for future applications. The research will not only highlight the strengths and limitations of each sensor type but also explore their synergistic use in integrated survey solutions. This approach hope to contribute to advancing the field of geomatics, offering new insights and methodologies for effective and efficient data collection and analysis in various applications.

REFERENCES

This brief paragraph contains the general bibliography for the thesis; more specific bibliographic references are available in the individual chapters and are not repeated here.

C.S. Fraser, T. Yamakawa, Insights into the affine model for high-resolution satellite sensor orientation, 2003

Clive S. Fraser and Harry B. Hanley, Bias-compensated RPCs for Sensor Orientation of High-resolution Satellite Imagery, 2005

Clive S. Fraser and Harry B. Hanley, Bias Compensation in Rational Functions for Ikonos Satellite Imagery, 2003

Zhen Xiong and Yun Zhang, A Generic Method for RPC Refinement Using Ground Control Information

C.S. Fraser, G. Dial b, J. Grodecki, Sensor orientation via RPCs, 2006

Loizzo R., Ananasso C., Guarini R., Lopinto E., Candela L., Pisani A.R., THE PRISMA HYPERSPECTRAL MISSION, 2016

ASI-AGI partners, Analisi Sistemi Iperspettrali per le Applicazioni Geofisiche Integrate, 2015

Progetto OPTIMA, 2014

Perissin D., Geometric Processing: Active Sensor Modeling and Calibration (SAR)

Perissin D., Interferometric SAR MultiTemporal processing (techniques and applications)

M. Manzo, G.P. Ricciardi, F. Casu, G. Ventura, G. Zeni, S. Borgstro, P. Berardino, C. Del Gaudio, R. Lanari, Surface deformation analysis in the Ischia Island (Italy) based on spaceborne radar interferometry, 2005

Kraus K., Fotogrammetria, Volume 1: Teoria e applicazioni

Mayer C., Gomes Pereira L. M., Kersten T. P., A Comprehensive Workflow to Process UAV Images for the Efficient Production of Accurate Geo-information, 2018

La Rocca A., Lingua A. M., Grigillio D., Un'applicazione della fotogrammetria al monitoraggio di una frana in roccia; il caso

studio di Belca, Slovenia

USGS, Unmanned Aircraft Systems Data Post-Processing, Structure-from-Motion Photogrammetry

1 CHAPTER I HOW TO ORIENT AND ORTHORECTIFY PRISMA IMAGES AND RELATED ISSUES

(published in *Remote sensing*)

Article

How to Orient and Orthorectify PRISMA Images and Related Issues

Valerio Baiocchi, Francesca Giannone and Felicia Monti

Article

How to Orient and Orthorectify PRISMA Images and Related Issues

Valerio Baiocchi [1,*], Francesca Giannone [2] and Felicia Monti [1]

1   Department of Civil Construction and Environmental Engineering, Sapienza University of Rome, 00184 Rome, Italy; felicia.monti@uniroma1.it
2   Engineering Faculty, Niccolò Cusano University, Via Don Carlo Gnocchi 3, 00166 Rome, Italy; francesca.giannone@unicusano.it
*   Correspondence: valerio.baiocchi@uniroma1.it

Abstract: The orientation of satellite images is a necessary operation for the correct geometric use of satellite images whether they are used individually to obtain an orthophoto or as stereocouples to extract three-dimensional information. The orientation allows us to reconstruct the correct position on the ground of the single pixels that form the image, which normally can be performed using certain functions of commercial software customised for each specific satellite. These functions read the metadata parameters provided by the satellite operator and use them to correctly orient the images. Unfortunately, these parameters have not been standardised and various satellites report them according to variable conventions, so new satellites or those that are not widely used cannot be oriented automatically. The PRISMA satellite launched by the Italian Space Agency (ASI) releases free hyperspectral and panchromatic images with metric resolution, but there is not yet a standardised procedure for orienting its images and this limits its usability. This paper reports on the first experimentation of orientation and orthorectification of PRISMA (PRecursore IperSpettrale della Missione Applicativa) images carried out using the three most widely used models, namely the rigorous, the Rational Polynomial Coefficients (RPC) and the Rational Polynomial Functions (RPF) tools. The results obtained by interpreting the parameters and making them suitable for use in standard procedures have made it possible to obtain results with an accuracy equal to the maximum resolution of panchromatic images (5 m), thus making it possible to achieve the highest level of geometric accuracy that can be extracted from the images themselves.

Keywords: PRISMA; orthorectification; RPC; RPF; Rome; Fucino; Ischia

1. Introduction

In the last twenty years, many satellite missions dedicated to earth observation have become operational. As a result, on-board technologically advanced sensors have allowed for the acquisition of panchromatic and multispectral images with, respectively, sub-metric and metric resolutions. The applications of such images cover a very wide and continuously evolving field of application from automatic feature extraction [1] to landslide monitoring [2,3] and image classification [4]. In all applications, geometric accuracy is of particular importance, especially in cases where positional comparability determines the final accuracy, as in the case of cartography updates or change detection analyses [5]. Nowadays, the available products have a wide range of spatial resolutions, while, with regard to the spectral resolution, hyperspectral satellites are still poorly represented in spaceborne missions compared to multispectral ones [6].

In March 2019, the Italian Space Agency (ASI) launched a new satellite named "PRISMA" (PRecursore IperSpettrale della Missione Applicativa) equipped with hyperspectral and medium resolution panchromatic sensors [7–9]. Specifically, the spatial resolution of panchromatic product is 5 m, while the hyperspectral sensor acquires scenes with

a Ground Sampling Distance (GSD) of 30 m in the spectral range between 400 and 2500 nm with 10 nm spectral sampling.

It is important to note that PRISMA satellite is, in the current panorama, a unique platform of its kind as it combines the possibilities of hyperspectral sensors with those of panchromatic sensors, thereby promoting a more detailed analysis and a more precise detection of the ground features. The only commonly known satellite platform with similar characteristics is the EO-1 Hyperion/ALI, which had a lower resolution for panchromatic data (10 metres) and is currently (as of 2017) no longer operational. The open and free availability of the images for the scientific community, both for archival and new acquisitions images, makes the study of the PRISMA sensor even more interesting for the world of research.

This mission offers a new opportunity for environmental monitoring in cases such as forest analysis and water application [10,11]. Considering the newness of the mission, the studies conducted so far have focused on possible hyperspectral applications, using already georeferenced data; however, it is necessary to verify the accuracy of geolocation [12]. In fact, the hyperspectral and panchromatic PRISMA products are currently available with a declared geolocation accuracy of 200 m, which ASI plans to increase to half a pixel in the near future by introducing geometric correction of the images with Ground Control Points (GCPs).

Apart from the application used, satellite images are affected by deformation mainly due to camera distortions and acquisition geometry, after which they must undergo a geometric rectification process in order to define the precision and accuracy level, this process is known as orthorectification.

Geometric rectification is performed by describing the relationship between image and ground coordinates with the following approaches: with the empirical or photogrammetric-based model [13,14]. Usually, the orthorectification includes the following two processes: first, the orientation parameters are estimated by using GCP with the aim to reconstruct the acquisition characteristic (sensor's attitude, position and internal parameters), then the oriented images are projected after considering a DEM or DSM.

At present, orientation methods can be classified into the following three categories: empirical methodologies, such as Rational Polynomial Functions—RPFs, that are independent of specific platform or sensor characteristics and acquisition geometry; physically based models that follow a photogrammetric approach (rigorous model), which takes into account several aspects influencing the acquisition procedure; a third type of model that represents a compromise between the first two, RPC—Rational Polynomial Coefficients models, in which the RPF approach is used with known coefficients supplied in the imagery metadata and "blind" produced by companies managing sensors with their own rigorous models. The RPC approach results may be enhanced by users estimating some additional parameters (e.g., an affine transform) on the basis of eventually available GCPs [15–18].

The different orthorectification approaches have been extensively tested on the most popular satellite platforms outlining the advantages and disadvantages of the various approaches in a consolidated way, therefore the results obtained with PRISMA must be considered in relation to the state of the art that is well documented in the literature for most other platforms.

The rigorous model reconstructs the reality of the acquisition geometry starting from the satellite platform information, such as satellite ephemeris and attitude and sensor and image characteristics; therefore, such models prove to be specific for each satellite system and produce results that are more robust with respect to the RPF empirical model. Furthermore, with RPF the geometric correction is applied locally and conditioned by the GCP distribution and number.

Nowadays, the third type of model, the RPC, represents an interesting and attractive solution to orienting satellite images, as it can apply geometric correction with a good level of accuracy, which in some cases is comparable with the rigorous model, using fewer GCPs

than the RPF model. Finally, this type of model is supported by almost all commercial and free software and it is independent of the sensor characteristics [10,19–21].

Geometric correction is a fundamental step that affects all subsequent forms of processing of the image itself and the accuracy of the final product strictly depends on the original image characteristics, on the quality of the known coordinates of ground control points and on the model chosen to perform the orientation. Satellite image processing methods and the analysis of precision and accuracy of derived products are widely investigated [22–27].

However, the PRISMA satellite has specific characteristics and problems that make simple orientation and orthorectification complex, if not impossible for non-expert users, significantly limiting the application possibilities of an otherwise very interesting platform. In the present work, a specific procedure has been developed on the basis of the experience and state of the art of other platforms to solve specific problems of PRISMA never previously observed on other satellites. As a result of experimentation we were able to define and verify certain procedures that provide a correct orientation of PRISMA images even for users who are not experts in the photogrammetric aspect. Presently, there are no other scientific contributions on the specific problem of the orthorectification of PRISMA images.

Nowadays, the main commercial software implements all three models, but it does not yet provide processing with rigorous approaches or RPCs for PRISMA images, probably due to the recent availability of these products.

When a new sensor is not supported by commercial software, such as PCI-Geomatica OrthoEngine, the function Read Generic Image File can be used, which provides the image orientation using a photogrammetric approach only if the user manually enters information about the orbit and acquisition characteristics.

This approach was also applied to PRISMA but the results are limited due to the scarce official data available for the specific platform.

2. Materials and Methods

Geometric correction of the PRISMA panchromatic products was performed by considering three images (Figure 1) representing morphologically different areas, since the altimetric aspect characterizes the orthorectification process. The panchromatic images processed are 30 km × 30 km in size and include both catalogue products and new acquisitions. Table 1 shows the main characteristics of the images analysed.
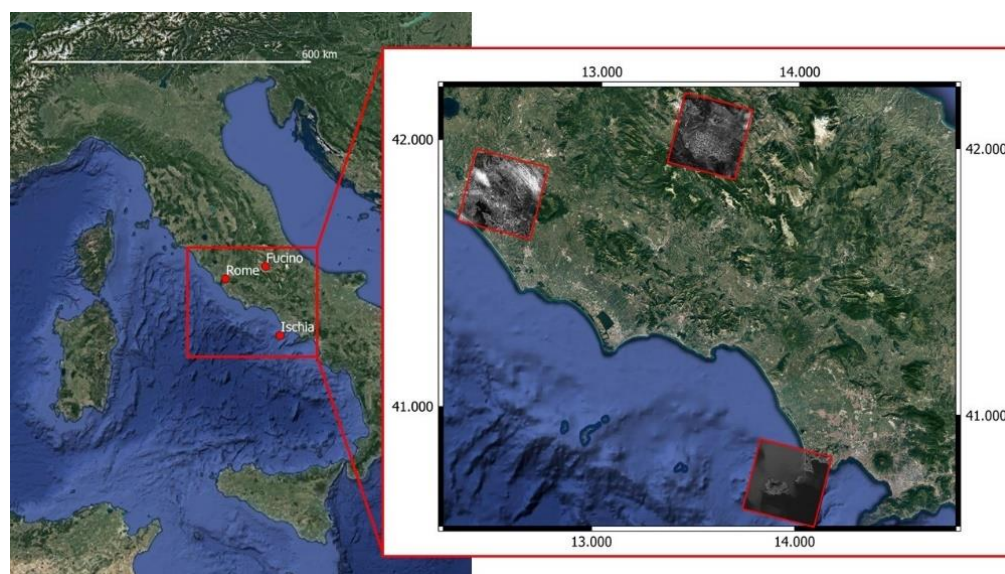
Figure 1. Location of the three test fields.

Table 1. Main features of PRISMA images.

Test Field	Approximate Range of Orthometric Heights	View Zenith Angle	Geomorphology and Notable Features
Rome	0 to 596 m	0.420°	Low relief and mountainous area
Fucino	500 m to 2475 m	1.459°	Mountainous terrain
Ischia	0 to 777 m	12.435°	Mountainous terrain appears only in the central part of the whole image

The first test field covers a central area of the city of Rome, which is rich in urban elements facilitating the identification of GCPs. In particular, large, historical buildings are essential elements because they are clearly recognizable even on panchromatic products with a medium spatial resolution such as PRSIMA images. The GCPs were collimated homogeneously on the image as accurately as possible given the presence of a modest partial cloud cover. The coordinates of GCPs were obtained from vector cartography at a scale of 1:5000 provided by the Lazio Region portal (http://dati.lazio.it, accessed on 22 February 2022), while the altimetric information was obtained from the digital terrain model (DEM) in orthometric elevations with TINITALY/01 provided by INGV [28] and a resolution of 10 m per pixel. This DEM was selected because its resolution is adequate for the orthorectification of an image with a resolution of 5 m; other DEMs with a higher resolution are available (e.g., from maps at a scale of 1:5000), but, in our opinion, they would have unnecessarily burdened the processing.

The second test field covers the Fucino plain (Abruzzo region, Italy), a morphologically depressed structure surrounded by major mountain reliefs. This area represents an interesting test field due to the particular altimetric-geomorphological condition, characterised by rapid altimetric variations in the correspondence of reliefs which cover the entire perimeter of the image. In this case, GCP identification is more complex because the plain is mainly agricultural and therefore lacks easily recognisable urban elements. For this reason, the crossroads of the plain and the small buildings distributed among the cultivated fields were used. The GCP coordinates for the Fucino image were obtained using vector cartography with a scale of 1:5000 and the digital terrain model, both provided by the web page of the Abruzzo Region administration (http://opendata.regione.abruzzo.it/, accessed on 22 February 2022).

The last test field is the isle of Ischia (Campania Region, Italy), which covers only a partial area (approximately 10 km E-W × 8 km N-S) of the acquired image. This choice is justified by the particular morphological condition of the island, surmounted by Mount Epomeo at 789 m above sea level. GCP identification was complex due to the presence of irregular settlements and a road network that conforms to the complexity of the territory. Despite these difficulties and the spatial resolution at 5 m, enough GCPs were identified, whose coordinates and elevations were obtained from the vector cartography at a scale of 1:2000, provided by the Metropolitan City of Naples; furthermore, the digital terrain model, with 1 m resolution, was obtained from regional cartography.

2.1. Export Procedure for Specific Bands and Related Issues

PRISMA products are provided at different processing levels and are widely described in the literature [7]. Their differences mainly concern the hyperspectral data. In the present experimentation, panchromatic products of L2C level, i.e., "geolocated and geocoded atmospherically corrected HYP and PAN images", were used. Specifically, the geolocation process of the PRISMA products consists of the estimation of the orientation model based on the Line of Sight, without the use of DEM and GCPs. In order to improve the geometric accuracy, the model parameters could be refined using an automatic method of GCPs searching; currently, this phase has not yet been performed, so the geolocation information was released with approximate accuracy (200 m) in the form of Rational Function Model (RFM). The RFM model is applied to L2D products, providing orthorectified ground reflectance images, while in L2C products it is only attached as metadata information. For

our purposes, we selected L2C products, as the images are available in raw matrix form and RPC coefficients can be derived from metadata, allowing users to perform an independent geometric correction to achieve higher geometric accuracy.

The PRISMA products are released in an HDF-EOS5 format, then to export the panchromatic data in GeoTIFF format several solutions have been tested, including the following: ENVI software (from version 5.5.3 it supports the PRISMA data), Erdas Imagine, the open-source software QGis, the "prismaread" method accessible from R [12] and MATLAB. In the data export phase, it is important to ensure that the raster has not undergone any preliminary geocoding, since this would return altered data incongruent with the "Geocoding Model" parameters provided. To verify the absence of geocoding, the extracted data can be imported into any GIS software to verify that the graphic restitution of the raster corresponds to its matrix coordinates (internal coordinate reference system), that is, the coordinates of the top-left corner must be 0, 0.

The geocoding model information (PRISMA Products Specification Document) is contained in the metadata but it is not attached to the exported GeoTIFF product and, as a consequence, it was attached by means of a text file in the RPC00B format. In fact, as reported in the documentation, the geocoding model adopted for L2 products is the Rational Polynomial Coefficient model: RPC00B—Rapid Positioning Capability, as defined in the National Imagery and Mapping Agency standard [29]. For PRISMA panchromatic products, the matrix dimension is a 6000 × 6000 pixel, without any projection.

A fundamental aspect for the correct application of polynomial rational coefficients is the export of raw data, which is presented with the North direction rotated 90° counter-clockwise (Figure 2). The application of RPCs to exported raw images that are correctly oriented North produced final orthorectified images that are rotated with respect to the real geographic position, as shown in Figure 3, where the orthorectified image presents a wrong rotation with respect to the Isle of Ischia (in green).

(**a**)

(**b**)

(**c**)
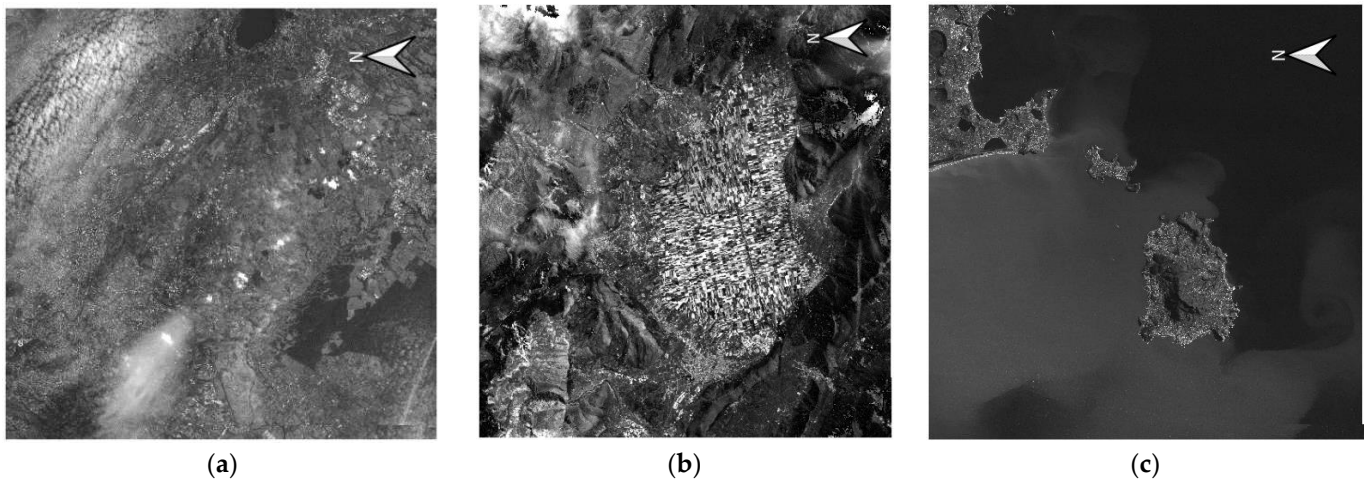
Figure 2. Correct export of the panchromatic product, test field of Rome (**a**), Fucino (**b**) and Ischia (**c**).
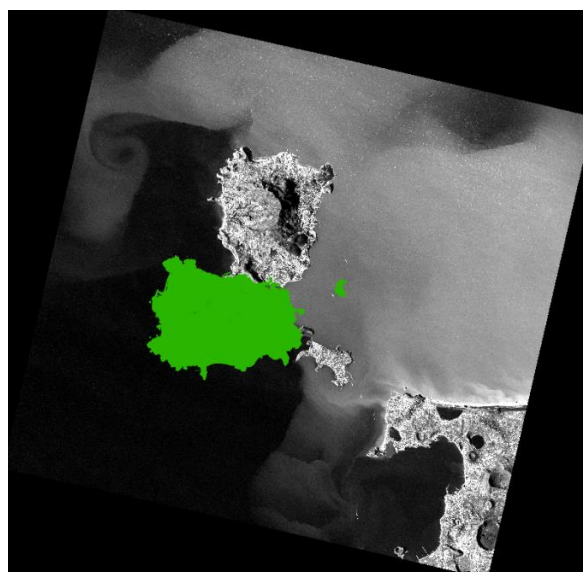
Figure 3. Superimposition between the "orthorectified" image, obtained using a north-correct raw image, and the actual position of the isle of Ischia (in green).

2.2. Orthorectification of PRISMA Images

The photogrammetric processing of pushbroom satellite images is usually based on the application of the following three methods: the rigorous approach and the polynomial function method with RPCs provided with the image or estimated image on the basis of a large set of GCPs. In this experimentation, we tried to test all three methods to provide a broader view of the geometric elaboration of PRISMA images.

Currently, a specific rigorous model for PRISMA images has not yet been implemented, only the commercial software OrthoEngine provides a function, named "Read Generic Image File", that can reconstruct the orbital parameters starting from information available in the metadata file. Only a few tests have been carried out using the function "Read Generic Image File" because some information (such as information related to the across-track and along-track angles) is not provided in the format required and documentation with an explanation of the parameter's physical meaning is still unavailable [19].

For this reason, the authors believe that the experimentation of the rigorous model reported below should be considered preliminary due to the uncertainties mentioned regarding the validity of the orbital parameters used (some of which were estimated before launch) and the interpretation of them. Unfortunately, these uncertainties also depend on the known lack of standardisation of the orbital and orientation parameters already observed in previous works in the literature [19].

Therefore, the authors underline that the experiments must be viewed as garnering the best result currently achievable with the data and means that could be found, but they are open to advice and suggestions from the scientific community.

The results obtained with the RPF and RPC models have instead been widely analysed.

The RPF empirical model is generally based on third-degree polynomials that relate an object and image coordinates, using 78 rational polynomial coefficients estimated with a least-square process based on an adequate number of GCPs. The RPF model can be given as:

$$
\begin{aligned}
I &= \frac{a_0 + a_1\lambda + a_2\varphi + a_3h + a_4\lambda\varphi + a_5\lambda h + a_6\varphi h + a_7\lambda^2 + a_8\varphi^2 + a_9h^2}{b_0 + b_1\lambda + b_2\varphi + b_3h + b_4\lambda\varphi + b_5\lambda h + b_6\varphi h + b_7\lambda^2 + b_8\varphi^2 + b_9h^2} \\
J &= \frac{c_0 + c_1\lambda + c_2\varphi + c_3h + c_4\lambda\varphi + c_5\lambda h + c_6\varphi h + c_7\lambda^2 + c_8\varphi^2 + c_9h^2}{d_0 + d_1\lambda + d_2\varphi + d_3h + d_4\lambda\varphi + d_5\lambda h + d_6\varphi h + d_7\lambda^2 + d_8\varphi^2 + d_9h^2}
\end{aligned}
\tag{1}
$$

where a_j, b_j, c_j, d_j are the polynomial coefficients, I and J are the image coordinates and λ, φ, h are the corresponding object point coordinates. The RPC model is based on the RPF

approach, but the coefficients are known and supplied in the imagery metadata. An RPC model with third-order polynomials, in the format RPC00B, is generally used, but the order of the terms may differ for different applications [29]. The orientation given by RPCs can be improved by estimating the parameters of a polynomial transformation on the basis of a set of GCPs; the polynomial order can vary from 0 to 2 [17]. Table 2 shows the strictly necessary GCP number for parameter estimation, but in our elaboration, several redundancy conditions have been achieved to reduce the risk of errors due to outliers or a strong dependence on the chosen GCPs.

Table 2. Parameters and minimum GCP numbers for RPC refinement in OrthoEngine.

	RPC Parameters	**Min Number of GCPs**
RPC adjustment order = 0	X0, Y0	1
RPC adjustment order = 1	X0, X1, X2, Y0, Y1, Y2	3
RPC adjustment order = 2	X0, X1, X2, X3, X4, X5, Y0, Y1, Y2, Y3, Y4, Y5	6

The PRISMA Geocoding Model data include the RPC coefficients and parameters for normalizing the row, column, latitude, longitude and ellipsoidal height values. The parameters provided together with PRISMA imagery comply with NIMA standards, but they include a total of only 40 non-zero coefficients, which are sufficient only for the calculation of second order rational polynomials. Moreover, the Geocoding Model parameters are extracted from metadata and transcribed into a file with the "RPB" extension, following the RPB00B format, in order to create the standard format for processing in the most commonly used software.

RPC and RFP models were performed with OrthoEngine software and an extensive analysis was conducted.

For the application of the RPC model, 20 points were collimated for each image; initially all of them were set as Check Points (CPs) for the estimation of the geopositioning accuracy given only by the application of the RPC provided; progressively some points were chosen as GCPs for the estimation of refinement parameters. Several tests have been performed on each image, by increasing the number of GCPs used for orientation parameters estimation, starting from 2 GCPs and 18 CPs, up to a configuration with 10 GCPs and 10 CPs. The RMSE values for each test, for each test field and for each transformation starting from order 0, up to order 2, are reported.

The RPF method has been applied on all test fields and a total of 60 points for each image have been collimated: 47 used as GCPs for coefficients estimation and 13 used as CPs for validation of the oriented image.

3. Results and Discussion

The experiments conducted on the three field tests (Rome, Ischia Island and Fucino) were replicated using the following three models: rigorous, RPC and RPF. All the results are reported below except for some results from tests with the RPC model, which are reported in the Appendix A for completeness but which are not reported here in the main text because they do not provide exhaustive results and so were deemed to unnecessarily burden the text.

3.1. Rigorous Model
3.1.1. Results of Rigorous Model

The "Read Generic Image File" function available in OrthoEngine software allows for the creation of an orbital model for image formats, whose ephemeris data are not read automatically by the software itself, usually because the satellite has just been released as in the case under study. This function allows for the satellite image and orbit information to be entered manually. Table 3 shows the parameters that are required by the application and the orbital and sensor information includes the IFOV, flight height, orbit period and inclination,

and eccentricity; for the PRISMA product, this information is derived from pre-launch data available in the literature [30–32]. Unfortunately, the across-track angle, i.e., the angle between the vertical and the observation direction during the side scan, and the along-track angle, i.e., the angle between the vertical and the forward or backward observation direction, are different for each image and they are not clearly stated. The only information reported in the PRISMA image metadata is the Observing Angle values attached in a matrix form (Swaths-> PRS_L2C_HCP-> Geometric Fields-> Observing Angle), from which the View zenith angle of the image is derived by considering the value of the central pixel (500 × 500).

The values of Table 3 are reported for the repeatability of the experiment; as already mentioned, the lack of standardization [19] of this information could have led to incorrect interpretations or the use of outdated parameters, and the authors are therefore open to suggestions and contributions from the scientific community.

Table 3. Orbital and image information required for "Read Generic Image File" function.

Parameter	Value	Source
Across-track angle	0.42 deg	Observing Angle
Along-track angle	0 deg	Observing Angle
IFOV	48 mrad	[32]
Altitude	615 km	[30]
Period	97 m	[30]
Semi-major axis	6992.935 km	[31]
Eccentricity	0.0011403	[33]
Inclination	97.851°	[32]

The rigorous model is estimated from the use of seven GCPs, although we used a set of 60 points and tested the different combinations reported in Table 4.

Table 4. Results of rigorous model for Rome test field.

N. of GCPs (N. of CP)	RMSE Value of Ground Checkpoint Discrepancies. Units Are in Metres	
	E	N
7 GCP	13.322	30.662
10 GCP	13.699	27.117
15 GCP	12.533	23.704
20 GCP	12.925	22.046

3.1.2. Discussion of Rigorous Model

The results show a constant trend for the residuals in the E direction, while the residuals in the N direction improve when the GCP number increases. Surely, a full knowledge of the required parameters could improve the quality of the results obtained. It has to be underlined that, curiously, these results are obtained with an image partly already geometrically processed (2d level) while the same model does not converge if we use the raw image, which in theory should give the best results with this model. The authors are also open to suggestions by the scientific community on this specific topic.

3.2. Results of RPC Model

The results obtained with RPC for the panchromatic image of Ischia are reported in Table 5 where the image accuracy is calculated, ranging from 20 (0 GCP) to 10 CPs (10 GCP). The first row of the table shows the RMSE value of residuals obtained by applying the RPC coefficients provided with the image, i.e., the value of geolocation accuracy achieved after correction with only the parameters provided by the PRISMA image; in this case, the accuracy is very poor (tens of metres). Then, the RPC method was refined after considering

different polynomial orders and different GCP numbers. The translation parameters of the 0-order transformation, estimated with 2 GCPs, leads to a clear increase in accuracy, while as the order of the estimated transformation increases, the achieved accuracy improves slightly, to 1–2 pixels.

Table 5. Results of RPC bundle adjustment with bias compensation for Ischia test field.

RPC Bundle Adjustment Solution	N. of GCPs (N. of CP)	RMSE Value of CP Discrepancies. Units Are in Metres	
		E	N
Spatial Intersection	None (20)	59.43	35.922
RPC order 0: X0, Y0	2 (18)	8.156	6.268
RPC order 0: X0, Y0	7 (13)	7.821	5.766
RPC order 1: X0, X1, X2, Y0, Y1,Y2	4 (16)	6.697	6.257
RPC order 1: X0, X1, X2, Y0, Y1,Y2	7 (13)	6.434	5.586
RPC order 1: X0, X1, X2, Y0, Y1,Y2	10 (10)	6.397	5.703
RPC order 2: X0, X1, X2, X3, X4, X5, Y0, Y1, Y2, Y3, Y4, Y5	7 (13)	5.489	5.489
RPC order 2: X0, X1, X2, X3, X4, X5, Y0, Y1, Y2, Y3, Y4, Y5	10 (10)	6.183	5.593

The same procedure was performed for the Rome and Fucino plain test fields (Tables 6 and 7, respectively). The accuracy trend achieved in these two test fields is similar, even though they present different values in the E and N directions. In both cases, the RPC order 0 solution led to a notable accuracy improvement and, in addition, increasing the order of estimated transformation improved the positioning accuracy. Note that in the case of Rome the improvement affects only the residuals in the E direction, at up to 2 pixels, while for the other test field similar residuals are reached in both directions, at about 3–4 pixels.

**Table 6.** Results of RPC bundle adjustment with bias compensation for Rome.

RPC Bundle Adjustment Solution	N. of GCPs (N. of CP)	RMSE Value of CP Discrepancies. Units Are in Metres	
		E	N
Spatial Intersection	None (20)	130.762	80.972
RPC order 0: X0, Y0	2 (18)	30.077	30.783
RPC order 0: X0, Y0	7 (13)	23.423	35.518
RPC order 1: X0, X1, X2, Y0, Y1, Y2	4 (16)	22.884	32
RPC order 1: X0, X1, X2, Y0, Y1, Y2	7 (13)	12.004	35.091
RPC order 1: X0, X1, X2, Y0, Y1, Y2	10 (10)	11.368	27.62
RPC order 2: X0, X1, X2, X3, X4, X5, Y0, Y1, Y2, Y3, Y4, Y5	7 (13)	11.173	34.684
RPC order 2: X0, X1, X2, X3, X4, X5, Y0, Y1, Y2, Y3, Y4, Y5	10 (10)	10.553	26.68

Considering the results obtained, the accuracy achieved by applying the RPC method with bias compensation is acceptable for applications of the hyperspectral data, whose spatial resolution is 30 m per pixel, while it is inappropriate for the correction of panchromatic data, whose spatial resolution is 5 m. Furthermore, the accuracy values obtained in the Ischia test field are decidedly better than in the other two cases. The reason for these different behaviours can be due to the different extension of areas; in fact, the Isle of Ischia occupies only a portion of the whole image with limited extension in latitude and longitude, unlike the other two cases. To further investigate this behavior, a test was

carried out in which a 10 km E-W × 8 km N-S portion of the images of the other test-fields was considered (Figure 4).

Table 7. Results of RPC bundle adjustment with bias compensation for Fucino plain.

RPC Bundle Adjustment Solution	N. of GCPs (N. of CP)	RMSE Value of CP Discrepancies. Units Are in Metres	
		E	N
Spatial Intersection	None (20)	127.618	83.365
RPC order 0: X0, Y0	2 (18)	36.77	32.052
RPC order 0: X0, Y0	7 (13)	30.873	22.698
RPC order 1: X0, X1, X2, Y0, Y1, Y2	4 (16)	39.267	34.575
RPC order 1: X0, X1, X2, Y0, Y1, Y2	7 (13)	17.276	16.441
RPC order 1: X0, X1, X2, Y0, Y1, Y2	10 (10)	15.31	18.439
RPC order 2: X0, X1, X2, X3, X4, X5, Y0, Y1, Y2, Y3, Y4, Y5	7 (13)	15.38	17.263
RPC order 2: X0, X1, X2, X3, X4, X5, Y0, Y1, Y2, Y3, Y4, Y5	10 (10)	14.46	19.386

(**a**)　　　　　　　　　　　　　(**b**)　　　　　　　　　　　　　(**c**)
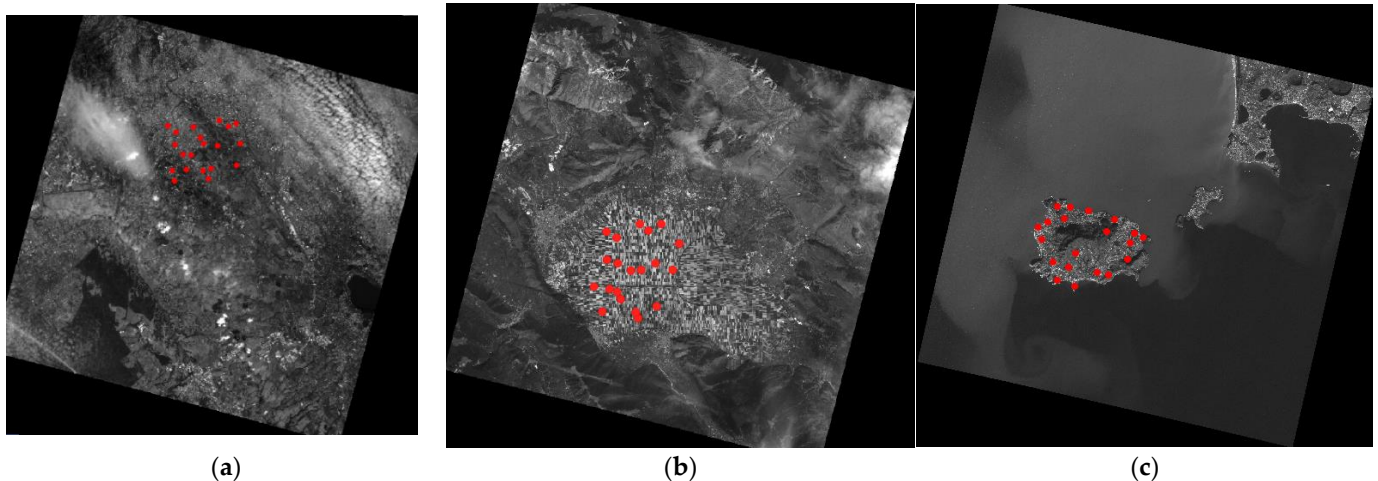
Figure 4. Ground point distribution for a central area of the image, test field of Rome (**a**), Fucino (**b**) and Ischia (**c**).

The results obtained in the test concentrated in an area of limited extension are reported in Tables 8 and 9. Similarly to the case of Ischia, acceptable accuracies have already been obtained, starting from the estimation of the RPC order 0 solution with only two GCPs. A further observation is the slight improvement of the accuracy values as the order of the transformation increases. The case study of Rome reached the highest accuracy, especially in the E direction, while the cases of Ischia and Fucino reached an accuracy in the order of 1–2 pixels overall.

Finally, a small non-central area of the Fucino test field was selected to complete the accuracy analysis as a function of the image extension and GCP distribution (Figure 5). To complete the analysis, four GCPs and four CPs were collimated in the lower right area of test field. The results (Table 10), computed only for RPC order 0 and order 1 solutions, show a clear deterioration in accuracy compared to the solution obtained in the central area of the test field.

Table 8. Results of RPC bundle adjustment with bias compensation for small-central area of Rome.

RPC Bundle Adjustment Solution	N. of GCPs (N. of CP)	RMSE Value of CP Discrepancies. Units Are in Metres	
		E	N
Spatial Intersection	None (20)	138.763	102.29
RPC order 0: X0, Y0	2 (18)	5.857	5.231
RPC order 0: X0, Y0	7 (13)	4.361	4.68
RPC order 1: X0, X1, X2, Y0, Y1, Y2	4 (16)	4.234	5.847
RPC order 1: X0, X1, X2, Y0, Y1, Y2	7 (13)	4.335	4.753
RPC order 1: X0, X1, X2, Y0, Y1, Y2	10 (10)	3.168	4.99
RPC order 2: X0, X1, X2, X3, X4, X5, Y0, Y1, Y2, Y3, Y4, Y5	7 (13)	4.325	4.786
RPC order 2: X0, X1, X2, X3, X4, X5, Y0, Y1, Y2, Y3, Y4, Y5	10 (10)	3.157	5.014

Table 9. Results of RPC bundle adjustment with bias compensation for small-central area of Fucino.

RPC Bundle Adjustment Solution	N. of GCPs (N. of CP)	RMSE Value of CP Discrepancies. Units Are in Metres	
		E	N
Spatial Intersection	None (20)	144.924	108.254
RPC order 0: X0, Y0	2 (18)	5.194	4.08
RPC order 0: X0, Y0	7 (13)	4.38	5.001
RPC order 1: X0, X1, X2, Y0, Y1, Y2	4 (16)	5.142	4.3
RPC order 1: X0, X1, X2, Y0, Y1, Y2	7 (13)	4.222	4.938
RPC order 1: X0, X1, X2, Y0, Y1, Y2	10 (10)	4.329	4.373
RPC order 2: X0, X1, X2, X3, X4, X5, Y0, Y1, Y2, Y3, Y4, Y5	7 (13)	4.116	4.902
RPC order 2: X0, X1, X2, X3, X4, X5, Y0, Y1, Y2, Y3, Y4, Y5	10 (10)	4.201	4.315
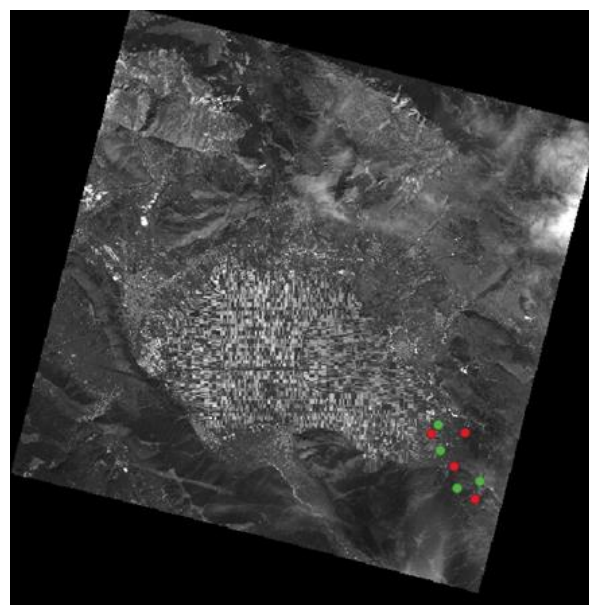
Figure 5. Ground point distribution for a small area of the image in the lower right corner, test field of Fucino (in red the GCPs, in green the CPs).

Table 10. Results of RPC bundle adjustment with bias compensation for small area of the image in the lower right corner, test field of Fucino.

RPC Bundle Adjustment Solution	RMSE Value of CP Discrepancies. Units Are in Metres	
	E	**N**
RPC order 0	18.012	23.486
RPC order 1	17.824	23.327

A trend analysis of the results (Figures 6–8) was conducted by considering the RMSE of both GCPs and CPs as a function of the GCP number used for orientation model computation. The figures show that both the model precision (RMSE of GCP) and the image accuracy (RMSE of CP) values follow the expected behaviour, that is the former increases while the latter decreases, as the number of GCPs increases. For the test fields of Rome and Fucino, a trend variation between the RPC order 0 and order 1 solutions was observed, while the trends recorded for the test field of Ischia remained unchanged in cases where the order transformation varied, a behavior already noted in the results in Table 5.
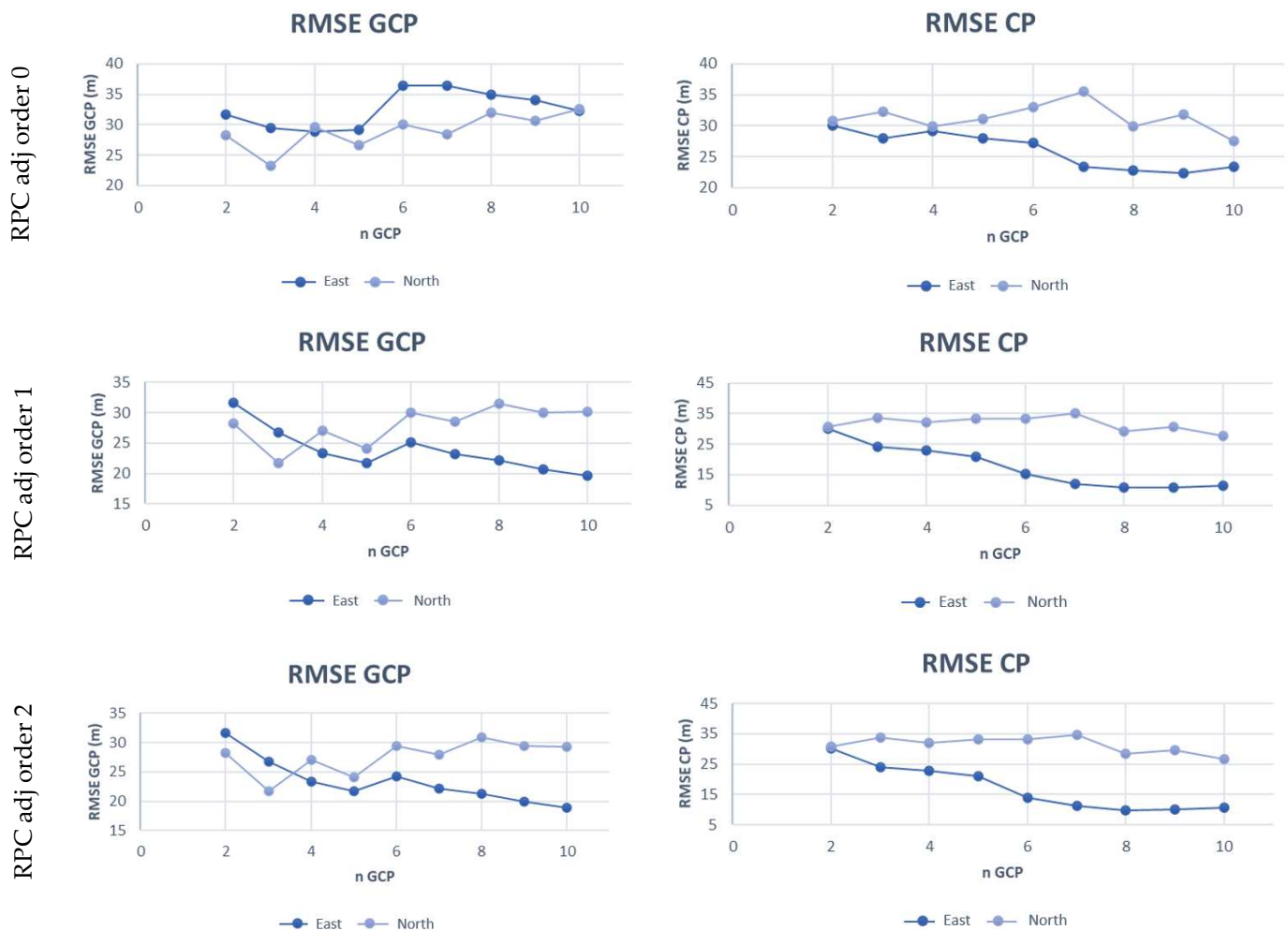
Figure 6. Precision and accuracy trends for Rome image.
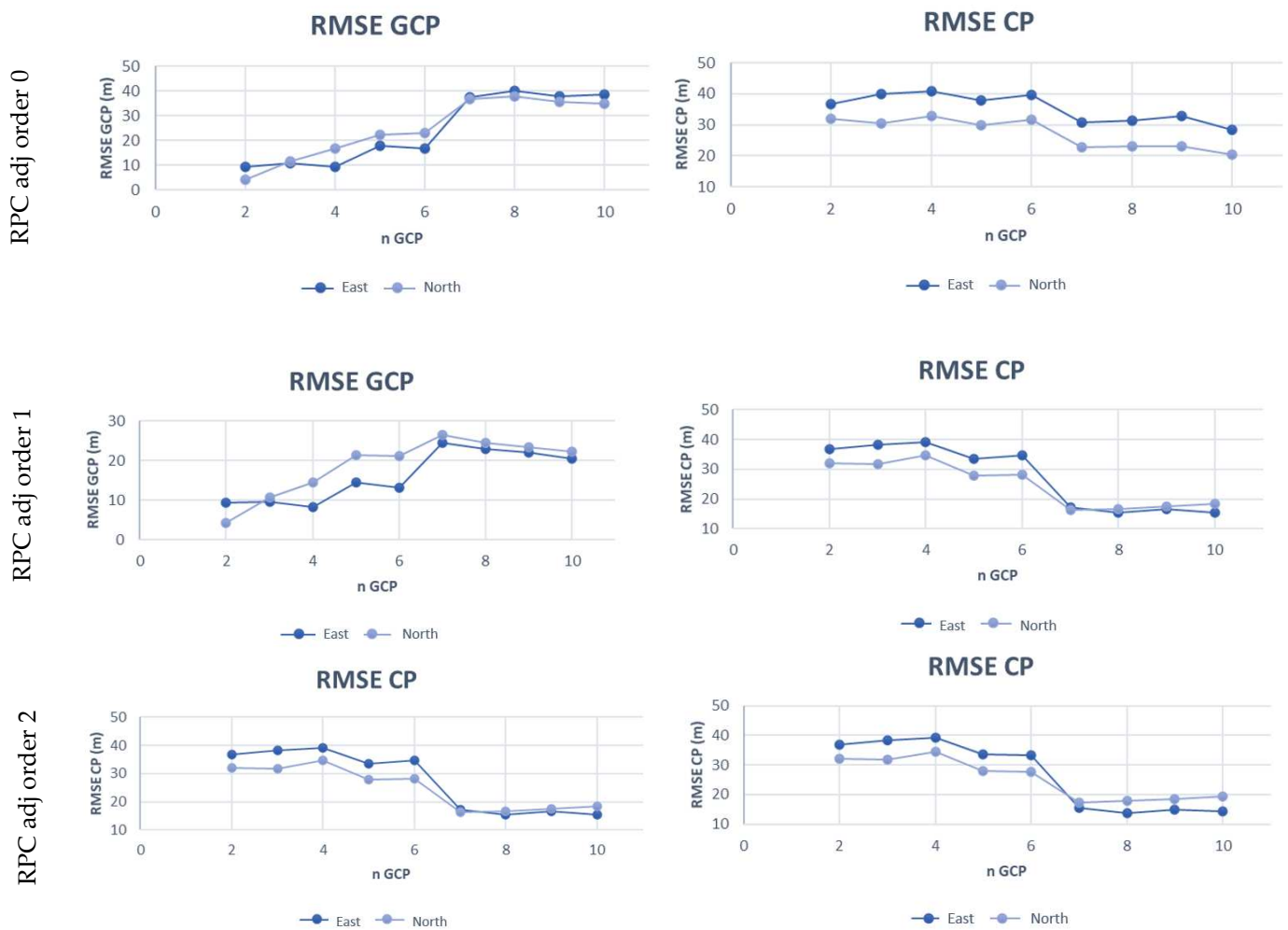
Figure 7. Precision and accuracy trends for Fucino image.

Considering the results obtained in all tests, the best performance for the orientation with the RCP model of whole images was obtained with RPC order 1 or order 2 transformations, as evidenced by the improvement recorded for the accuracy values in the E direction, while for the orientation with the RCP model of the central area of the image, the RPC order 0 solution with few GCPs reached a constant accuracy.

Moreover, the precision and accuracy trends tend to stabilize as the number of GCPs increases, as is described in the literature [13,22], which in our study started from about 7–8 GCPs. The results shown for the orientations estimated on the basis of a few GCPs, in fact, are affected by the distribution of the GCPs chosen.

The graphs of the vectors representing the residuals in the E and N directions are shown below. The graphs allow us to highlight the characteristics of the RPC errors; in fact, a random distribution can be interpreted as the absence of the influence of time-dependent drift effects. On the contrary, residuals aligned in the along-track direction show the presence of drift effects and an influence of the scan velocity [15]. A further analysis can be carried out by studying the residuals on individual CPs, and Figure 9 shows the results obtained by applying the RPC model without any refinement. The error is clearly systematic and is partially corrected by RPC order adjustment = 0, which only allows for the estimation of translation parameters (Figure 10a,c,e). Figure 10 shows the residuals of each point (in red the GCPs, in green the CPs) for the different test fields, and for RPC refinement order 0 (Figure 10a,c,e) and order 2 (Figure 10b,d,f). Despite the refinement of RPC parameters, it is still possible to observe a systematic behaviour in the test-fields of Rome and the Fucino plain. The residual vectors of the points distributed on the image

perimeter decreased after increasing the order of the transformation, while the errors in the image center remained essentially unchanged. The Isle of Ischia, on the other hand, shows a slight improvement in errors with the RPC bundle adjustment order = 2.
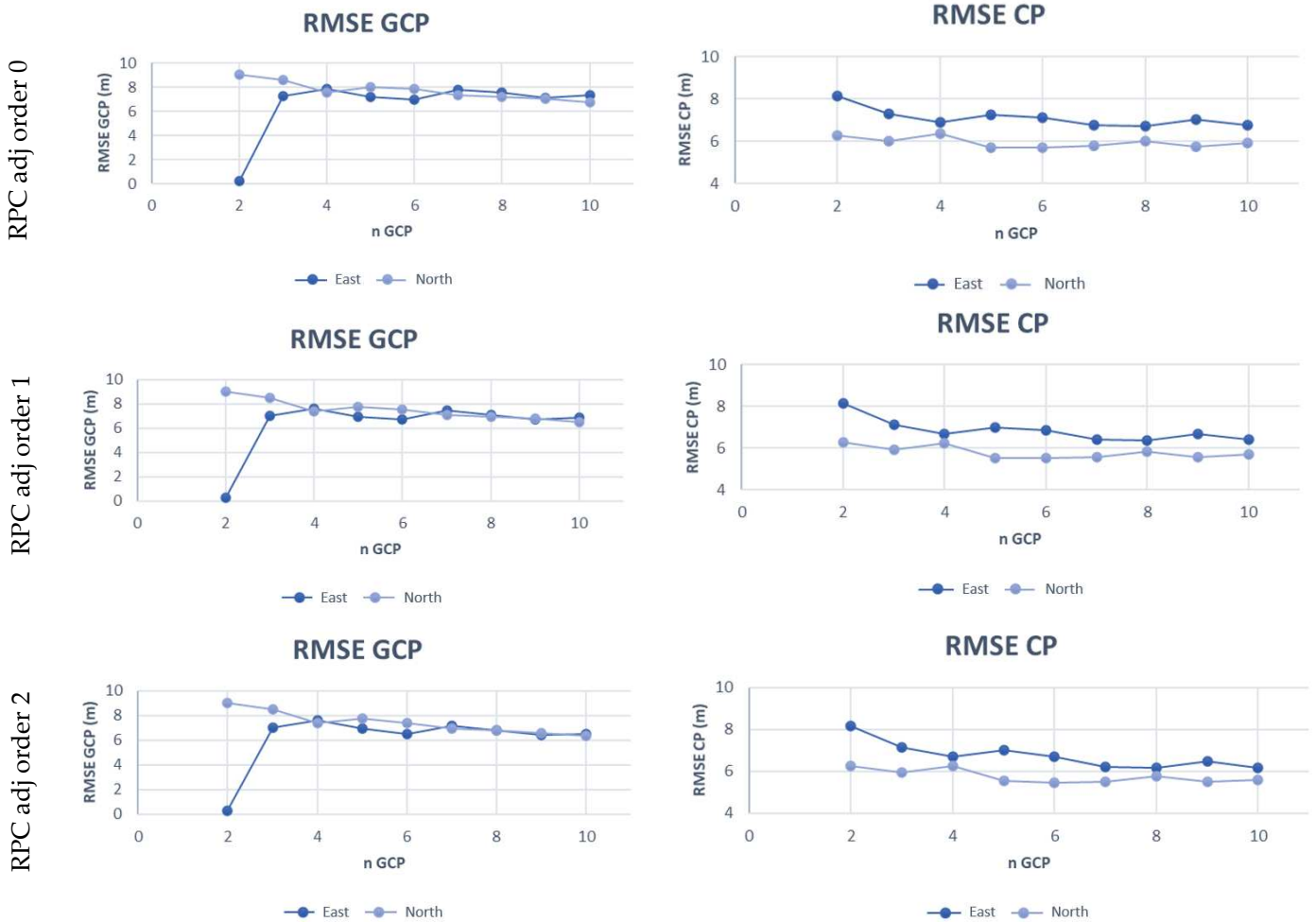

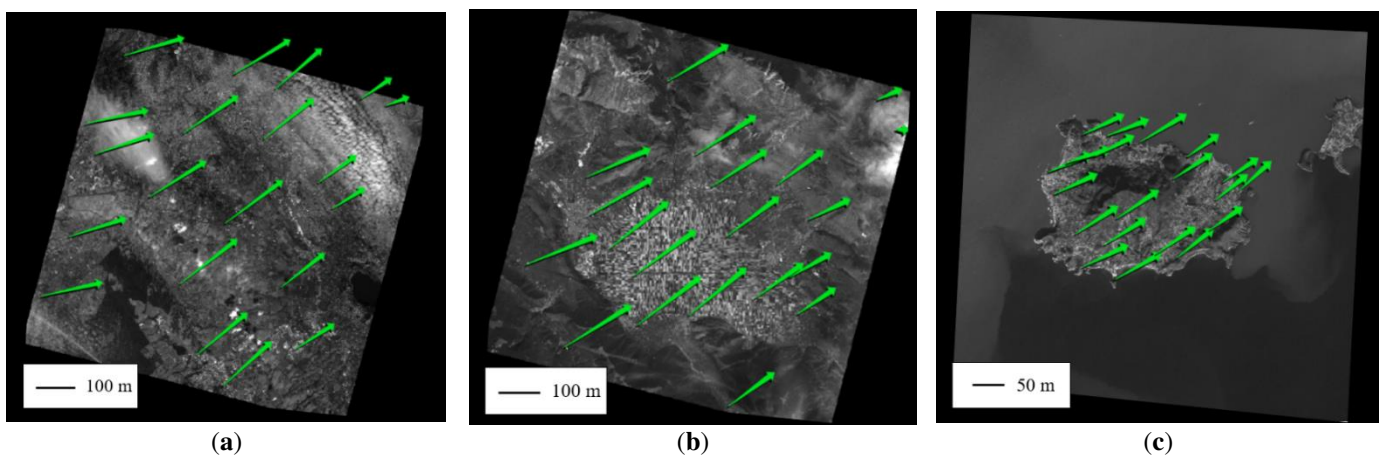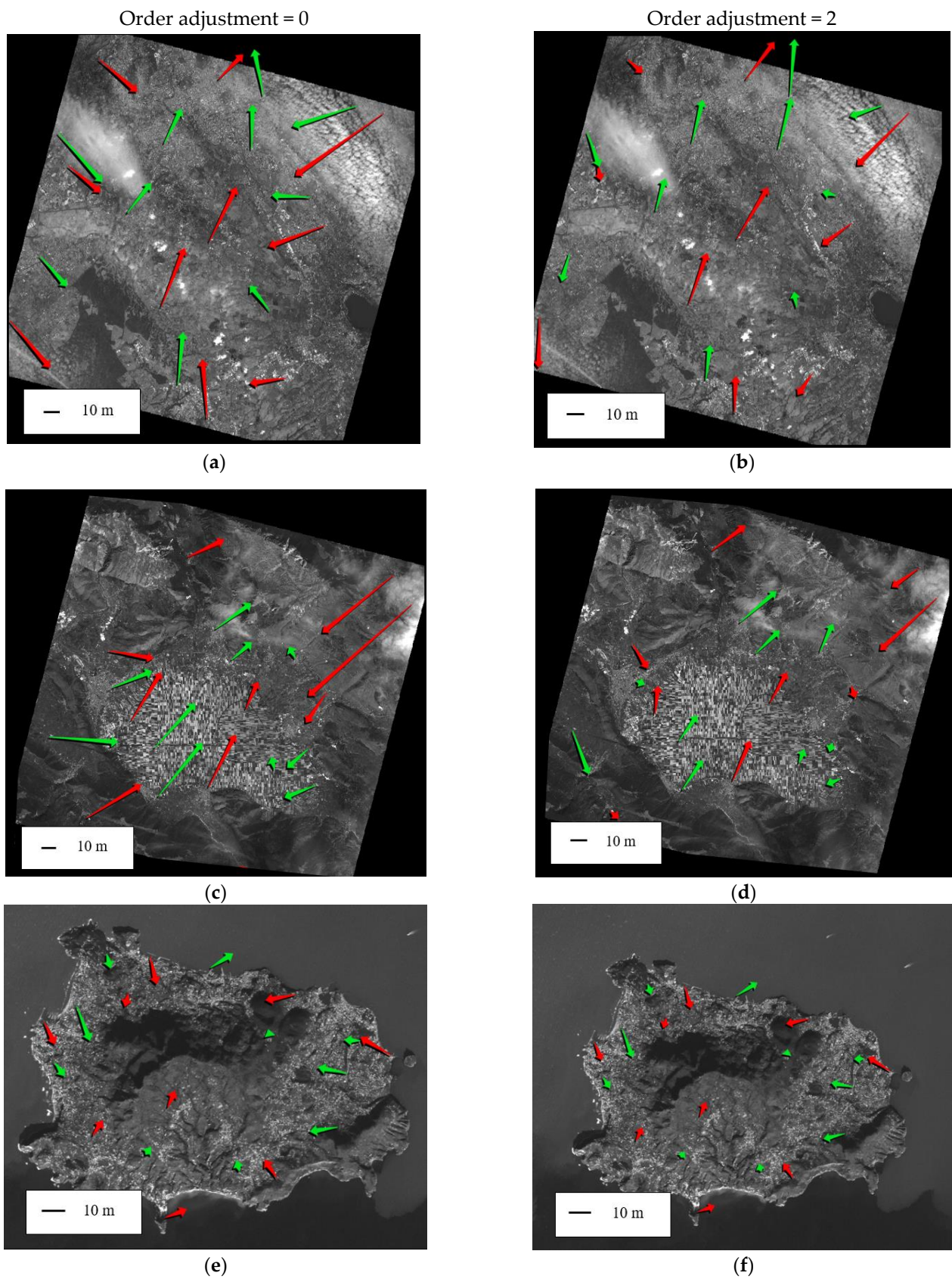**Figure 8.** Precision and accuracy trends for Ischia image.

Figure 9. The planimetric errors—RPC model with no refinements applied, test field of Rome (**a**), Fucino (**b**) and Ischia (**c**).

Order adjustment = 0

Order adjustment = 2

Figure 10. Planimetric errors for RPC order 0 and order 2 solution—test field of Rome (**a**,**b**), Fucino (**c**,**d**) and Ischia (**e**,**f**).

The results of the accuracies obtained using the RPC models were in agreement with the hypothesis that dividing the image by stripes (E-W direction) or by columns (N-S direction) could improve the results as was the case for highly asynchronous satellites studied previously (e.g., EROS-A); however, these tests did not achieve reliable and unambiguous results and are therefore only reported in Appendix A for completeness.

3.3. RPF Model

3.3.1. Results of RPF Model

The Rational Polynomial Functions without RPCs were analysed to complete the overview of PRISMA performance. In the RPF empirical method, the coefficients were estimated on the basis of a large set of collimated GCPs. The method has been applied on all test fields and a total of 60 points for each image were collimated. Of these, 47 were used as GCPs for coefficients estimation and 13 were used as CPs for validation of the oriented image.

The analysis was performed in OrthoEngine, in which it is possible to set the number of RPF coefficients that need to be estimated. Figure 11 shows the accuracy trend as a function of coefficient numbers, whereby the accuracy decreases as the number of coefficients increases. In particular, the Rome and Fucino test fields show similar behaviour, reaching the best accuracy in the E and N directions when six polynomial coefficients were estimated (Table 11); it should also be noted that the accuracy trends tend to worsen from the estimation of second-degree polynomials function. The results obtained for Ischia show that maximum accuracy was achieved when using five polynomial coefficients (Table 11).
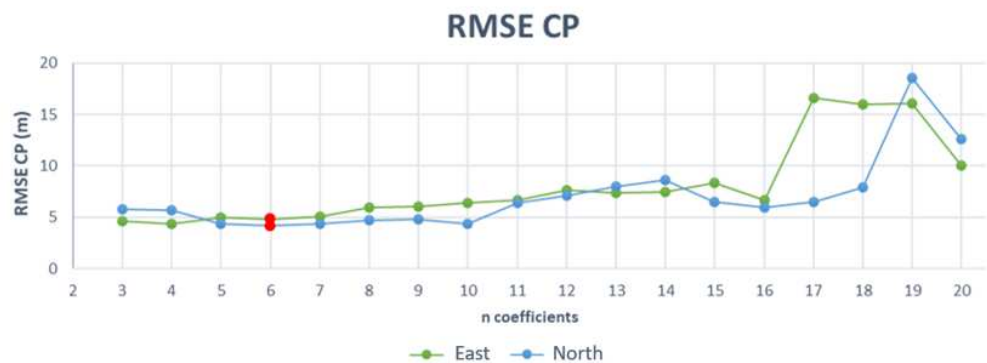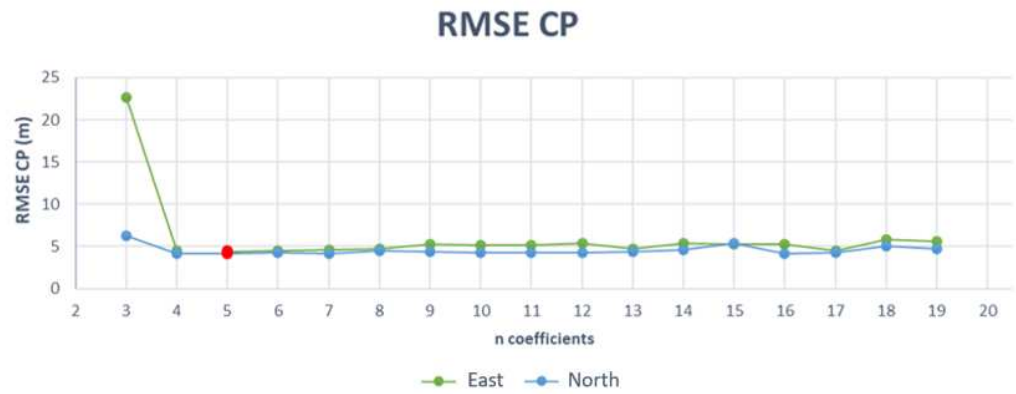

(**a**)
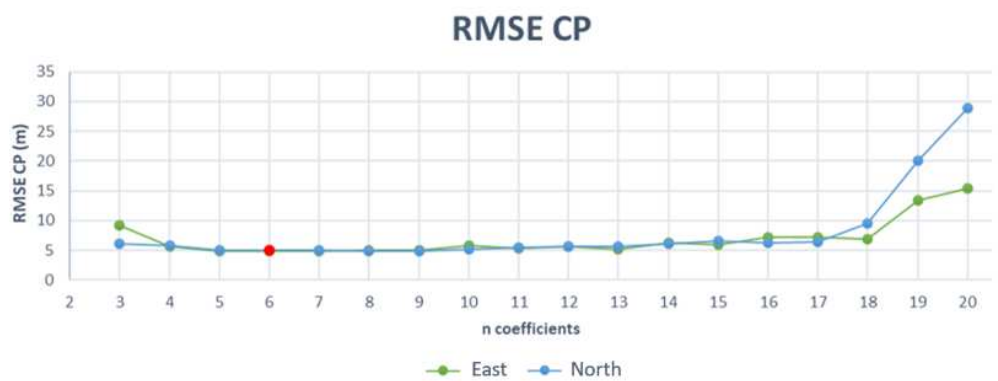
(**b**)

Figure 11. *Cont.*

(**c**)

Figure 11. Accuracy trend as a function of RPC coefficients—test field Rome (**a**), Fucino (**b**) and Ischia (**c**).

**Table 11.** Maximum accuracy achieved.

Test Field	N. of GCPs (N. of CP)	RMSE Value of CP Discrepancies. Units Are in Metres	
		E	N
Rome	6 (54)	4.811	4.173
Fucino	6 (54)	4.792	5.009
Ischia	5 (55)	4.404	4.105

3.3.2. Discussion of RPF Model

Considering that the most efficient application of RPFs for PRISMA images were reached with six polynomial coefficients, a further investigation was carried out to investigate the necessary number of GCPs to achieve adequate precision and accuracy, considering the resolution of the panchromatic image as a reference (5 m).

The Rome and Fucino images were considered to be representative because the GCPs can be distributed over the entire image, then they were oriented after considering an RPF model with six polynomial coefficients. The model precision (RMSE of GCP, Figures 12a and 13a) and image accuracy (RMSE of CP, Figures 12b and 13b) are analysed as a function of the GCP number.
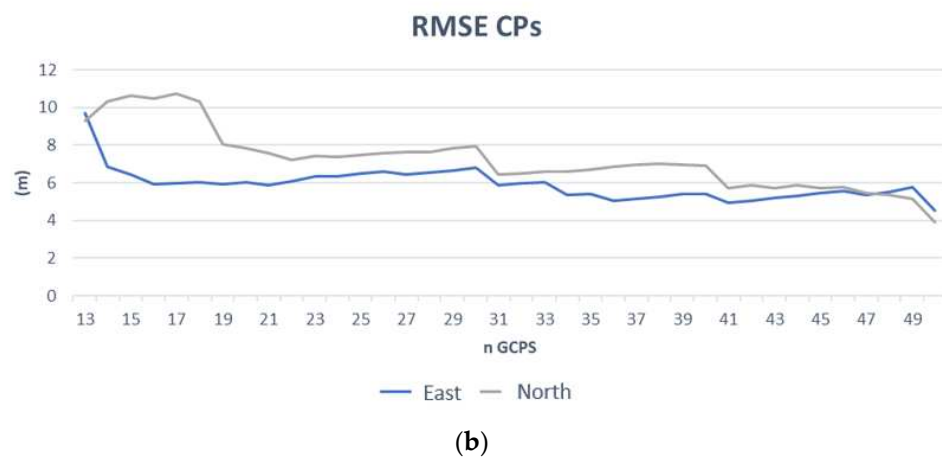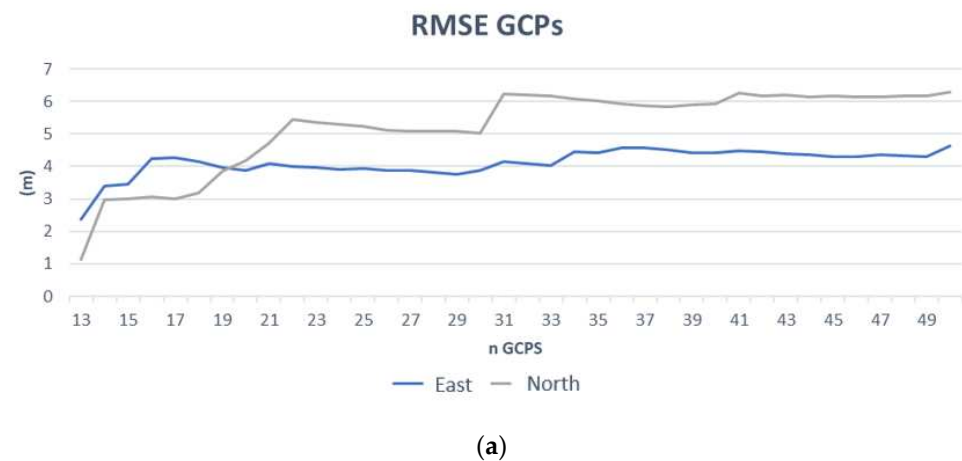

(**a**)

Figure 12. *Cont.*

(**b**)
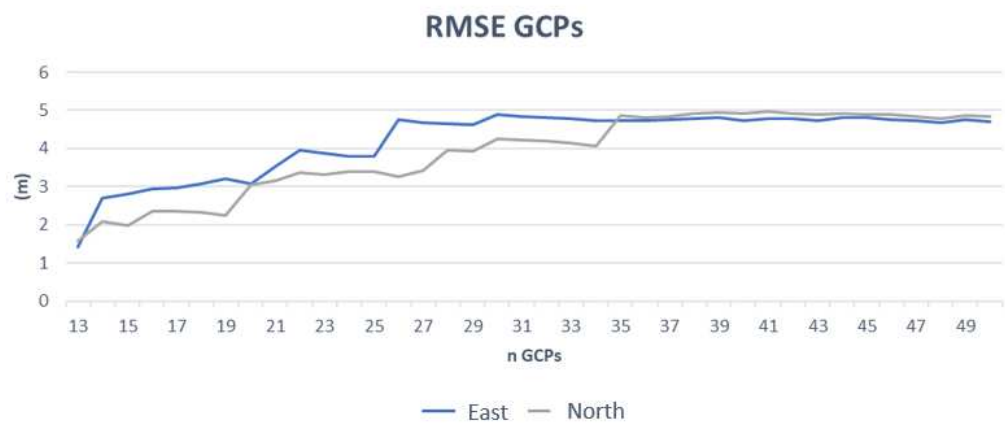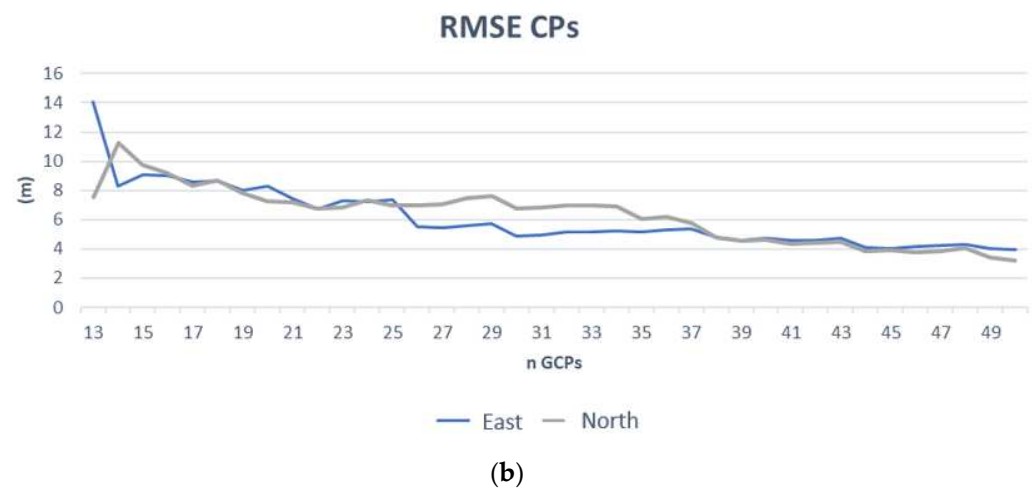
Figure 12. Trend of precision (**a**) and accuracy (**b**) in relation to the number of collimated GCPs, referred to the Rome test field.

(**a**)

(**b**)

Figure 13. Trend of precision (**a**) and accuracy (**b**) in relation to the number of collimated GCPs, referred to the Fucino test field.

It can be observed that adequate accuracy was reached with 40 GCPs (Table 12) which is certainly a high value of GCPs compared to the 12–20 usually necessary for rigorous models or the 2–4 required for RPCs. Nevertheless, it is important to underline that the panchromatic resolution (5 m) of PRSIMA images does not necessarily require GCPs with decimetre or centimetre precision, so the ground points can be quickly acquired from maps at a scale of 1:10,000 or larger making the process much faster.

Table 12. Accuracy achieved with 40 GCPs.

Test Field	N. of GCPs (N. of CP)	RMSE Value of CP Discrepancies. Units Are in Metres	
		E	N
Rome	40	4.74	4.635
Fucino	40	5.408	6.904

4. Conclusions

This study on the possible methods of geometric correction of the PRISMA images provided different results depending on the type of orientation model used.

The tests were carried out on data that had the highest resolution, i.e., the panchromatic image (5 m), while the hyperspectral images were found to have lower resolutions (generally 30 m). The spatial resolution of the images is a fundamental piece of information because the accuracies required to best orthorectify a certain image depend on their specific resolution.

The rigorous model, as we previously estimated, in the OrthoEngine function, has an accuracy of about 20 m with about 12 GCPs over the entire image.

It has to be underlined that, curiously, these results were obtained with an image that was already partly geometrically processed (2d level) while the same model does not converge if we use the raw image, which in theory should provide the best results with this model. This model can be used to orientate, using a small number of points, the hyperspectral layers of the image because it provides accuracies that are compatible with the specific resolutions.

The RPC-based model, whose parameters are declared compliant with the NIMA standard, can achieve accuracies close to the resolution of the panchromatic image (5 m) but only for limited and central areas, as observed in the island example. In such a case, few GCPs are needed to obtain accuracies that are compatible with panchromatic images but, as mentioned, only for limited and centred areas.

Finally, the RPF model seems to achieve the best results; in particular, the six-parameter formulation was the most efficient when using panchromatic PRISMA images. Considering this model, the entire scene can be oriented and consequently orthorectified with an accuracy of around 5 m which is equal to the maximum resolution of the image itself. Since the disadvantage of RPFs with respect to previous models is the high number of GCPs required, the number of GCPs required to provide adequate accuracy was also evaluated. Optimal results seem to be obtained from 40 GCPs; however, GCPs can also be inserted with an accuracy of 2.5 m on the ground, and these accuracies are also easily attainable from high- to medium-scale maps (1:5000–1:10,000) available in many areas, making time-consuming surveying with geodetic class GPS unnecessary. This procedure can therefore be used advantageously on entire scenes even for panchromatic images, as long as a large set of GCPs with metric accuracy is available which can be rapidly obtained, as already mentioned, if cartography (at least at 1:10,000 scale) is available.

For the rigorous model, we are still waiting for the release of some specific functions on commercial software and when they become available, they will be widely tested. In our tests with the rigorous model, the orbital and external orientation parameters used and their sources were specified. These parameters have been included in the OrthoEngine function according to best practices established in the literature. However, the authors are open to suggestions and contributions from the scientific community or platform operators for possible refinements of the model itself.

With regard to the RPC models, the authors expect the possible realization of automatic procedures in commercial software or possible refinements of the RPC sets themselves by the satellite operator.

RPFs, on the other hand, can already be used, even on open-source software, with 40 or more GCPs.

Appendix A

The orientation of the panchromatic images of Rome and the Fucino plain shows critical results for the accuracy values in the N direction (Tables 6 and 7). Considering the pushbroom acquisition mode of the PRISMA satellite, we decided to perform tests by analysing the image of Rome for strips distributed in the North–South and East–West directions (Figure A1). In the case of strips in the North–South direction, a reduced number of image columns was considered, while in the case of East–West strips, a reduced number of image rows was considered. In both cases, a strip extension of approximately 6 km was set and 20 ground points were collimated. Table A1 shows the results obtained by orienting the image with a point distribution in the E-W direction, and the values are similar to those obtained for the whole image. Finally, Table A2 shows the results obtained with a point distribution in the N-S direction; in this case, a substantial improvement of the residuals in the N direction can be seen.

(**a**)   (**b**)
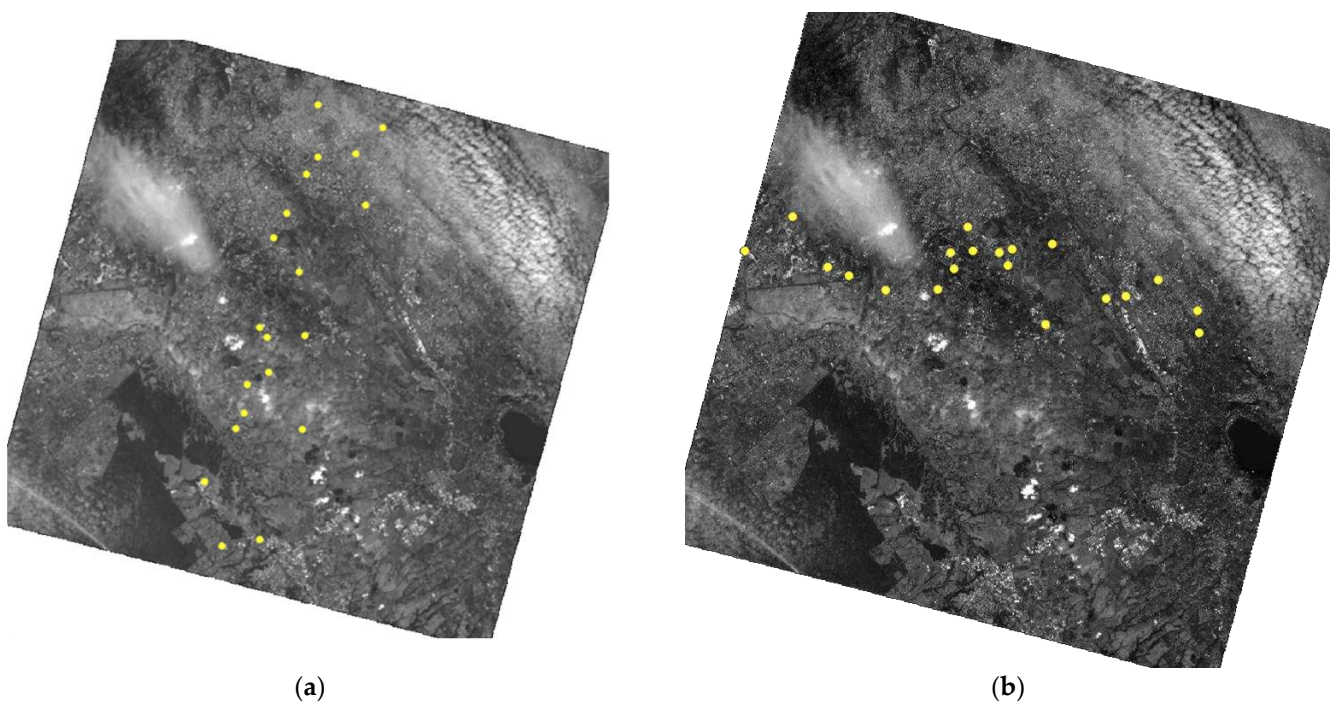
Figure A1. Ground point distribution in N-S (**a**) and E-W (**b**) direction, test field of Rome.

Table A1. Results of RPC bundle adjustment with bias compensation for strip in E-W direction, Rome test field.

RPC Bundle Adjustment Solution	N. of GCPs (N. of CP)	RMSE Value of CP Discrepancies. Units Are in Metres	
		E	**N**
Spatial Intersection	None (20)	135.128	88.883
RPC order 0: X0, Y0	2 (18)	22.968	22.47
RPC order 0: X0, Y0	7 (13)	18134	23.208
RPC order 1: X0, X1, X2, Y0, Y1, Y2	4 (16)	14.668	23.068
RPC order 1: X0, X1, X2, Y0, Y1, Y2	7 (13)	12.96	23.177
RPC order 1: X0, X1, X2, Y0, Y1, Y2	10 (10)	9.139	22.769
RPC order 2: X0, X1, X2, X3, X4, X5, Y0, Y1, Y2, Y3, Y4, Y5	7 (13)	12.058	22.866
RPC order 2: X0, X1, X2, X3, X4, X5, Y0, Y1, Y2, Y3, Y4, Y5	10 (10)	8.106	22.467

Table A2. Results of RPC bundle adjustment with bias compensation for strip in N-S direction, Rome test field.

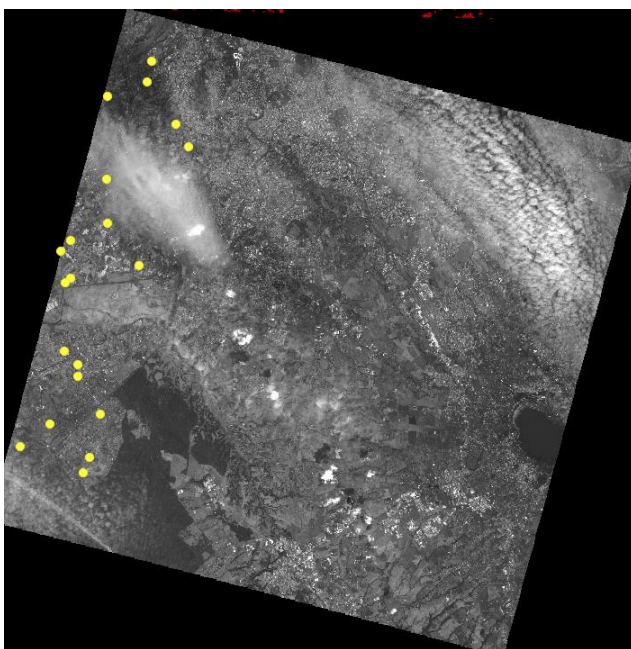| RPC Bundle Adjustment Solution	N. of GCPs (N. of CP)	RMSE Value of CP Discrepancies. Units Are in Metres	
		E	**N**
Spatial Intersection	None (20)	137.997	106.319
RPC order 0: X0, Y0	2 (18)	7.842	14.759
RPC order 0: X0, Y0	7 (13)	7.881	7.355
RPC order 1: X0, X1, X2, Y0, Y1, Y2	4 (16)	7.338	7.726
RPC order 1: X0, X1, X2, Y0, Y1, Y2	7 (13)	7.827	5.9
RPC order 1: X0, X1, X2, Y0, Y1, Y2	10 (10)	7.63	5.98
RPC order 2: X0, X1, X2, X3, X4, X5, Y0, Y1, Y2, Y3, Y4, Y5	7 (13)	7.836	5.824
RPC order 2: X0, X1, X2, X3, X4, X5, Y0, Y1, Y2, Y3, Y4, Y5	10 (10)	7.722	5.809

The best result was obtained by analysing a central area of the image distributed in the N-S direction. For completeness, tests were also repeated for the lateral areas (Figures A2 and A3a,c), to highlight possible dependencies on variable sensor orientation conditions. The behaviors shown by the test fields of Rome and the Fucino plain are very similar; in fact, for the central area, the highest accuracy in both directions E and N, was equal to 1–2 px. On the contrary, the results for the lateral area of the image are worse (Tables A3–A7), specifically for the right side that reaches an accuracy of 3–4 px in both directions.

Table A3. Results of RPC bundle adjustment with bias compensation for strip in N-S direction in the left side, Rome test field.

RPC Bundle Adjustment Solution	N. of GCPs (N. of CP)	RMSE Value of CP Discrepancies. Units Are in Metres	
		E	**N**
Spatial Intersection	None (20)	156.498	57.906
RPC order 0: X0, Y0	2 (18)	5.911	21.938
RPC order 0: X0, Y0	7 (13)	5.719	19.891
RPC order 1: X0, X1, X2, Y0, Y1, Y2	4 (16)	6.422	26.909

Table A3. *Cont.*

RPC Bundle Adjustment Solution	N. of GCPs (N. of CP)	RMSE Value of CP Discrepancies. Units Are in Metres	
		E	N
RPC order 1: X0, X1, X2, Y0, Y1, Y2	7 (13)	5.601	19.708
RPC order 1: X0, X1, X2, Y0, Y1, Y2	10 (10)	6.017	20.066
RPC order 2: X0, X1, X2, X3, X4, X5, Y0, Y1, Y2, Y3, Y4, Y5	7 (13)	5.461	19.254
RPC order 2: X0, X1, X2, X3, X4, X5, Y0, Y1, Y2, Y3, Y4, Y5	10 (10)	5.854	19.507

(**a**)   (**b**)

Figure A2. Ground point distribution in N-S direction in the side areas of the image, Rome test field, west side area in (**a**) and east side area in (**b**).

Table A4. Results of RPC bundle adjustment with bias compensation for strip in N-S direction in the right side, Rome test field.

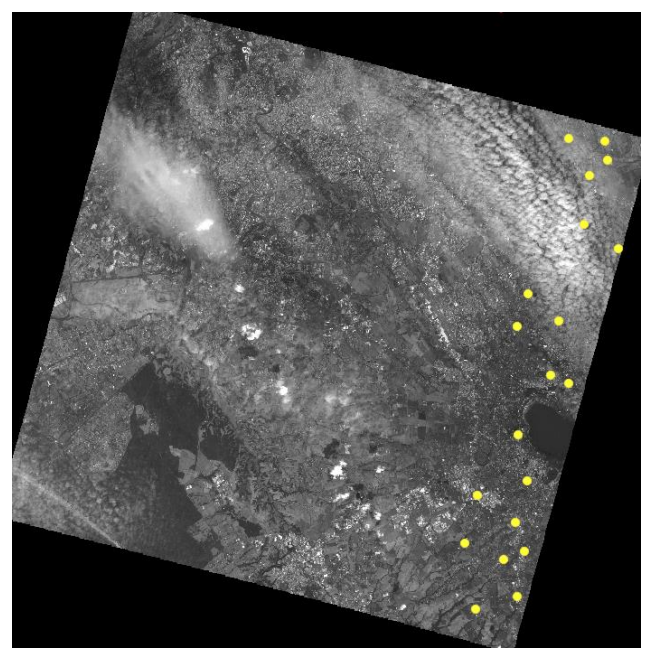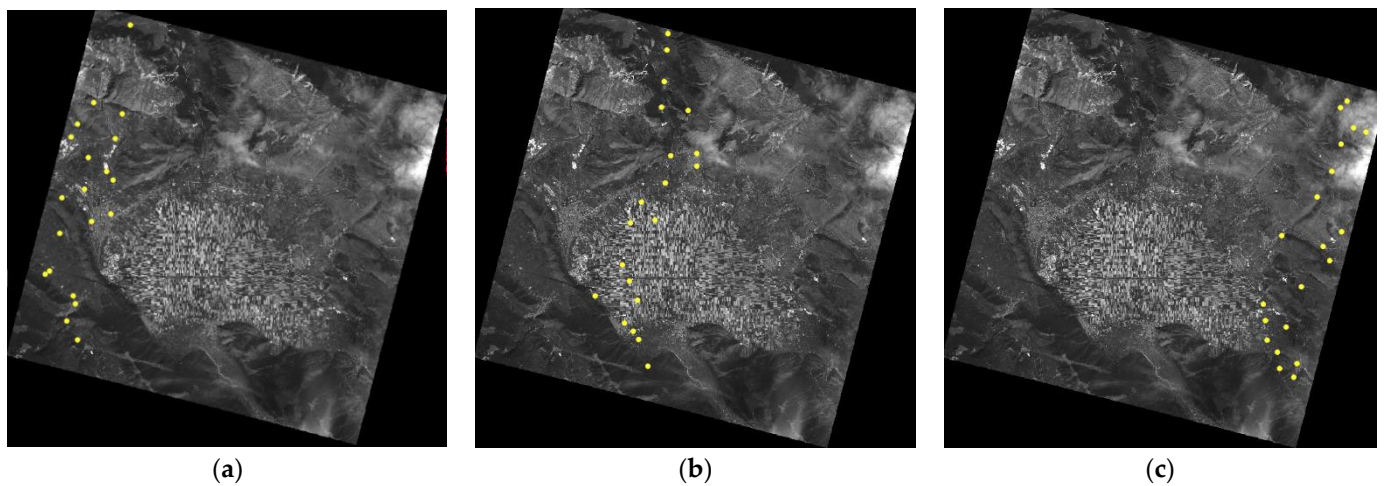| RPC Bundle Adjustment Solution	N. of GCPs (N. of CP)	RMSE Value of CP Discrepancies. Units Are in Metres	
		E	N
Spatial Intersection	None (20)	61.103	30.784
RPC order 0: X0, Y0	2 (18)	22.488	21.314
RPC order 0: X0, Y0	7 (13)	17.95	18.11
RPC order 1: X0, X1, X2, Y0, Y1, Y2	4 (16)	20.433	18.245
RPC order 1: X0, X1, X2, Y0, Y1, Y2	7 (13)	18.934	17.415
RPC order 1: X0, X1, X2, Y0, Y1, Y2	10 (10)	17.157	17.141
RPC order 2: X0, X1, X2, X3, X4, X5, Y0, Y1, Y2, Y3, Y4, Y5	7 (13)	19.231	17.627
RPC order 2: X0, X1, X2, X3, X4, X5, Y0, Y1, Y2, Y3, Y4, Y5	10 (10)	17.212	17.099

(**a**) (**b**) (**c**)

Figure A3. Ground point distribution in N-S direction in the central (**b**) and side areas (**a**) and (**c**) of the image, Fucino test field.

Table A5. Results of RPC bundle adjustment with bias compensation for central strip in N-S direction, case (b).

RPC Bundle Adjustment Solution	N. of GCPs (N. of CP)	RMSE value of CP Discrepancies. Units Are in Metres	
		E	N
Spatial Intersection	None (20)	145.989	99.858
RPC order 0: X0, Y0	2 (18)	5.439	14.128
RPC order 0: X0, Y0	7 (13)	5.478	15.798
RPC order 1: X0, X1, X2, Y0, Y1, Y2	4 (16)	5.359	11.891
RPC order 1: X0, X1, X2, Y0, Y1, Y2	7 (13)	5.365	12.217
RPC order 1: X0, X1, X2, Y0, Y1, Y2	10 (10)	4.759	11.402
RPC order 2: X0, X1, X2, X3, X4, X5, Y0, Y1, Y2, Y3, Y4, Y5	7 (13)	5.317	11.414
RPC order 2: X0, X1, X2, X3, X4, X5, Y0, Y1, Y2, Y3, Y4, Y5	10 (10)	4.833	10.582

Table A6. Results of RPC bundle adjustment with bias compensation for left strip in N-S direction, case (a).

RPC Bundle Adjustment Solution	N. of GCPs (N. of CP)	RMSE Value of CP Discrepancies. Units Are in Metres	
		E	N
Spatial Intersection	None (20)	158.24	71.255
RPC order 0: X0, Y0	2 (18)	11.925	24.684
RPC order 0: X0, Y0	7 (13)	9.409	26.421
RPC order 1: X0, X1, X2, Y0, Y1, Y2	4 (16)	11.043	22.122
RPC order 1: X0, X1, X2, Y0, Y1, Y2	7 (13)	8.672	24.179
RPC order 1: X0, X1, X2, Y0, Y1, Y2	10 (10)	8.37	21.756
RPC order 2: X0, X1, X2, X3, X4, X5, Y0, Y1, Y2, Y3, Y4, Y5	7 (13)	8.818	23.152
RPC order 2: X0, X1, X2, X3, X4, X5, Y0, Y1, Y2, Y3, Y4, Y5	10 (10)	8.667	20.454

Table A7. Results of RPC bundle adjustment with bias compensation for right strip in N-S direction, case (c).

RPC Bundle Adjustment Solution	N. of GCPs (N. of CP)	RMSE Value of CP Discrepancies. Units Are in Metres	
		E	N
Spatial Intersection	None (20)	66.662	32.143
RPC order 0: X0, Y0	2 (18)	21.436	29.653
RPC order 0: X0, Y0	7 (13)	18.004	17.514
RPC order 1: X0, X1, X2, Y0, Y1, Y2	4 (16)	17.631	20.029
RPC order 1: X0, X1, X2, Y0, Y1, Y2	7 (13)	17.41	16.395
RPC order 1: X0, X1, X2, Y0, Y1, Y2	10 (10)	17.071	15.243
RPC order 2: X0, X1, X2, X3, X4, X5, Y0, Y1, Y2, Y3, Y4, Y5	7 (13)	17.369	16.287
RPC order 2: X0, X1, X2, X3, X4, X5, Y0, Y1, Y2, Y3, Y4, Y5	10 (10)	17.022	15.102

References

1. Koçal, A.; Duzgun, H.S.; Karpuz, C. *Discontinuity Mapping with Automatic Lineament Extraction from High Resolution Satellite Imagery*; ISPRS XX: Istanbul, Turkey, 2004; pp. 12–23.
2. Chen, T.; Trinder, J.C.; Niu, R. Object-Oriented Landslide Mapping Using ZY-3 Satellite Imagery, Random Forest and Mathematical Morphology, for the Three-Gorges Reservoir, China. *Remote Sens.* **2017**, *9*, 333. [CrossRef]
3. Lu, H.; Ma, L.; Fu, X.; Liu, C.; Wang, Z.; Tang, M.; Li, N. Landslides Information Extraction Using Object-Oriented Image Analysis Paradigm Based on Deep Learning and Transfer Learning. *Remote Sens.* **2020**, *12*, 752. [CrossRef]
4. Rostami, M.; Kolouri, S.; Eaton, E.; Kim, K. Deep Transfer Learning for Few-Shot SAR Image Classification. *Remote Sens.* **2019**, *11*, 1374. [CrossRef]
5. Baiocchi, V.; Brigante, R.; Dominici, D.; Milone, M.V.; Mormile, M.; Radicioni, F. Automatic three-dimensional features extraction: The case study of L'Aquila for collapse identification after April 06, 2009 earthquake. *Eur. J. Remote Sens.* **2014**, *47*, 413–435. [CrossRef]
6. Transon, J.; D'Andrimont, R.; Maugnard, A.; Defourny, P. Survey of Hyperspectral Earth Observation Applications from Space in the Sentinel-2 Context. *Remote Sens.* **2018**, *10*, 157. [CrossRef]
7. Pignatti, S.; Acito, N.; Amato, U.; Casa, R.; Bonis, R.d.; Diani, M.; Laneve, G.; Matteoli, S.; Palombo, A.; Pascucci, S.; et al. Development of algorithms and products for supporting the Italian hyperspectral PRISMA mission: The SAP4PRISMA project. In Proceedings of the 2012 IEEE International Geoscience and Remote Sensing Symposium, Munich, Germany, 22–27 July 2012; pp. 127–130.
8. Guarini, R.; Loizzo, R.; Facchinetti, C.; Longo, F.; Ponticelli, B.; Faraci, M.; Dami, M.; Cosi, M.; Amoruso, L.; de Pasquale, V.; et al. Prisma Hyperspectral Mission Products. In Proceedings of the IEEE International Geoscience and Remote Sensing Symposium, IGARSS '18, Valencia, Spain, 22–27 July 2018; pp. 179–182.
9. Loizzo, R.; Daraio, M.; Guarini, R.; Longo, F.; Lorusso, R.; Dini, L.; Lopinto, E. Prisma Mission Status and Perspective. In Proceedings of the IEEE International Geoscience and Remote Sensing Symposium, IGARSS '19, Yokohama, Japan, 28 July–2 August 2019; pp. 4503–4506.
10. Giardino, C.; Bresciani, M.; Braga, F.; Fabbretto, A.; Ghirardi, N.; Pepe, M.; Gianinetto, M.; Colombo, R.; Cogliati, S.; Ghebrehiwot, S.; et al. First Evaluation of PRISMA Level 1 Data for Water Applications. *Sensors* **2020**, *20*, 4553. [CrossRef] [PubMed]
11. Vangi, E.; D'Amico, G.; Francini, S.; Giannetti, F.; Lasserre, B.; Marchetti, M.; Chirici, G. The New Hyperspectral Satellite PRISMA: Imagery for Forest Types Discrimination. *Sensors* **2021**, *21*, 1182. [CrossRef] [PubMed]
12. Busetto, L.; Ranghetti, L. Prismaread: A Tool for Facilitating Access and Analysis of PRISMA L1/L2 Hyperspectral Imagery v1.0.0. 2020. Available online: https://lbusett.github.io/prismaread/ (accessed on 22 February 2022).
13. Toutin, T. Review article: Geometric processing of remote sensing images: Models, algorithms and methods. *Int. J. Remote Sens.* **2004**, *25*, 1893–1924. [CrossRef]
14. Poli, D. A Rigorous Model for Spaceborne Linear Array Sensors. *Photogramm. Eng. Remote Sens.* **2007**, *73*, 187–196. [CrossRef]
15. Mikhail, E.M.; Bethel, J.S.; McGlone, J.C. *Introduction to Modern Photogrammetry*; Wiley: Hoboken, NJ, USA, 2001; ISBN 978-0-471-30924-6.
16. Fraser, C.S.; Hanley, H.B. Bias-compensated RPCs for Sensor Orientation of High-resolution Satellite Imagery. *Photogramm. Eng. Remote Sens.* **2005**, *71*, 909–915. [CrossRef]
17. Tong, X.; Liu, S.; Weng, Q. Bias-corrected rational polynomial coefficients for high accuracy geo-positioning of QuickBird stereo imagery. *ISPRS J. Photogramm. Remote Sens.* **2010**, *65*, 218–226. [CrossRef]

18. Meguro, Y.; Fraser, C.S. Georeferencing accuracy of Geoeye-1 stereo imagery: Experiences in a Japanese test field. *Int. Arch. Photogramm. Remote Sens. Spat. Inf. Sci.* **2010**, *38*, 1069–1072.

19. Poli, D.; Toutin, T. Review of developments in geometric modelling for high resolution satellite pushbroom sensors. *Photogramm. Rec.* **2012**, *27*, 58–73. [CrossRef]

20. Rupnik, E.; Deseilligny, M.P.; Delorme, A.; Klinger, Y. Refined satellite image orientation in the free open-source photogrammetric tools apero/micmac. *ISPRS Ann. Photogramm. Remote Sens. Spat. Inf. Sci.* **2016**, *III-1*, 83–90. [CrossRef]

21. Hanley, H.B.; Fraser, C.S. Sensor orientation for high-resolution satellite imagery: Further insights into bias-compensated RPCs. *Photogramm. Eng. Remote Sens.* **2004**, 71. Available online: https://www.researchgate.net/publication/228806 391_Sensor_orientation_for_high-resolution_satellite_imagery_Further_insights_into_bias-compensated_RPCs (accessed on 22 February 2022).

22. Jacobsen, K. Systematic geometric image errors of very high resolution optical satellites. *ISPRS Int. Arch. Photogramm. Remote Sens. Spat. Inf. Sci.* **2018**, *XLII-1*, 233–238. [CrossRef]

23. Zhou, G.; Li, R. Accuracy Evaluation of Ground Points from IKONOS High-Resolution Satellite imagery. *Photogramm. Eng. Remote. Sens.* **2000**, *66*, 1103–1112.

24. Baiocchi, V.; Giannone, F.; Monti, F.; Vatore, F. ACYOTB plugin: Tool for accurate orthorectification in open-source environments. *ISPRS Int. J. Geo Inf.* **2019**, *9*, 11. [CrossRef]

25. Poli, D.; Remondino, F.; Angiuli, E.; Agugiaro, G. Radiometric and geometric evaluation of GeoEye-1, WorldView-2 and Pléiades-1A stereo images for 3D information extraction. *ISPRS J. Photogramm. Remote Sens.* **2015**, *100*, 35–47. [CrossRef]

26. Agugiaro, G.; Poli, D.; Remondino, F. Testfield Trento: Geometric Evaluation Of Very High Resolution Satellite Imagery. *ISPRS Int. Arch. Photogramm. Remote Sens. Spat. Inf. Sci.* **2012**, *XXXIX-B1*, 191–196. [CrossRef]

27. Zheng, X.; Huang, Q.; Wang, J.; Wang, T.; Zhang, G. Geometric Accuracy Evaluation of High-Resolution Satellite Images Based on Xianning Test Field. *Sensors* **2018**, *18*, 2121. [CrossRef] [PubMed]

28. Tarquini, S.; Isola, I.; Favalli, M.; Battistini, A. *TINITALY, a Digital Elevation Model of Italy with a 10 Meters Cell Size (Version 1.0) [Data Set]*; Istituto Nazionale di Geofisica e Vulcanologia (INGV): Rome, Italy, 2007. [CrossRef]

29. National Imagery and Mapping Agency. "The Compendium of Controlled Extensions (CE) for the National Imagery Transmission Format (NITF)", VERSION 2.1, 16 November 2000. Available online: http://geotiff.maptools.org/STDI-0002_v2.1.pdf (accessed on 22 February 2022).

30. Loizzo, R.; Ananasso, C.; Guarini, R.; Lopinto, E.; Candela, L.; Pisani, A.R. The prisma hyperspectral mission. In Proceedings of the Living Planet Symposium, Prague, Czech Republic, 9–13 May 2016; pp. 9–13.

31. PRISMA: La Missione Iperspettrale Nazionale, Conferenza 2018. Available online: http://conferenzecisam.it/convegni/c-i-s-a-m-2018-1/documenti/Loizzo_PRISMA%20La%20missione%20iperspettrale%20nazionale.pdf (accessed on 22 February 2022).

32. IFAC CNR, Progetto Optima. 2014. Available online: http://www.ifac.cnr.it/corsari/meteors/private/OPTIMA%20-%20 PRISMA%20Products%20and%20Applications%20-%2020140930.pdf (accessed on 22 February 2022).

33. Guarini, R.; Loizzo, R.; Longo, F.; Mari, S.; Scopa, T.; Varacalli, G. Overview of the PRISMA space and ground segment and its hyperspectral products. In Proceedings of the IEEE International Geoscience and Remote Sensing Symposium (IGARSS), Fort Worth, TX, USA, 23–28 July 2017; pp. 431–434. [CrossRef]

2 CHAPTER II RECONSTRUCTING THE LATE PLEISTOCENE – ANTHROPOCENE INTERACTION BETWEEN THE NEOTECTONIC AND ARCHAEOLOGICAL LANDSCAPE EVOLUTION IN THE APENNINES (LA SASSA CAVE, ITALY)

(published in *Quaternary science reviews*)

Reconstructing the Late Pleistocene − Anthropocene interaction between the neotectonic and archaeological landscape evolution in the Apennines (La Sassa cave, Italy)

L. Alessandri [a, 1, *], G.L. Cardello [b, c, 1], P.A.J. Attema [a], V. Baiocchi [d], F. De Angelis [e], S. Del Pizzo [f], F. Di Ciaccio [f], A. Fiorillo [g], M. Gatta [g, h], F. Monti [d], M. Onori [d], M.F. Rolfo [g], M. Romboni [e], G. Sottili [c], S. Troisi [f]

[a] University of Groningen, GIA, Poststraat 6, 9712ER, Groningen, the Netherlands
[b] Department of Chemistry and Pharmacy, University of Sassari, Italy
[c] Sapienza University of Rome, Earth Sciences Department, Piazzale Aldo Moro 5, 00185, Roma, Italy
[d] Sapienza University of Rome, DICEA, Via Eudossiana 18, 00184, Rome, Italy
[e] University of Tor Vergata, Centre of Molecular Anthropology for Ancient DNA Studies, Via Della Ricerca Scientifica 1, 00133, Rome, Italy
[f] Parthenope University of Naples, Centro Direzionale Isola C4, Naples, Italy
[g] University of Tor Vergata, Department of History, Culture and Society, Via Columbia 1, 00133, Rome, Italy
[h] University of York, Department of Archaeology, King's Manor, Exhibition Square, York, YO1 7EP, UK

ARTICLE INFO

ABSTRACT

Caves are one of the most conservative environments on Earth, where archaeological, anthropological, climatic and tectonic data can be well-preserved. Here, we present the results of a multidisciplinary method that allowed us to recognize, for the first time in this area, the interaction between Late Pleistocene to Anthropocene neotectonic and archaeological evolutionary stages of a cave of the Apennines (La Sassa cave), that encompass also its surroundings (Volsci Range and Pontina Plain). Both structural and 3D survey highlighted a step-wise shape of the cave due to normal fault steps that allowed the localized formation of concretions also enveloping archaeological layers. Sixteen ^{14}C ages on fauna and human bones and thousands of archaeological finds provided chronological constraints of faulting in the Late Pleistocene and possibly also after the Middle Bronze Age. In the frame of a region that was not previously recognized as tectonically active, the structural evidence is relevant for understanding the speleogenesis of the cave from the Late Pleistocene and its human occupation. Burial and ritual activities in the cave from the Copper Age to the Middle Bronze Age have been recognized with implications on possible settlement pattern schemes with the La Sassa cave as a "persistent place" in the prehistoric human landscape. The analyses of the ceramic style in a regional framework also suggests the presence of a cultural boundary near La Sassa, which becomes highly osmotic just after the beginning of the Middle Bronze Age. The La Sassa findings provide as well implications for the seismic hazard assessment in a region inhabited by about 0.4 million people.

1. Introduction

The Late Pleistocene − Anthropocene transition is one of the most intriguing time ranges that allow to understand the human dispersal and cultural evolution (Fukasawa and Akasaka, 2019; Rick and Sandweiss, 2020; Smith et al., 2019; Stephens et al., 2019). A process that occurred during geological times through thousands of years and that thus had interacted with changing landscapes (e.g., Allen et al., 2000; Gatta et al., 2019; van Gorp and Sevink, 2019), that are affected by tectonic and volcanic activity, sea-level and

* Corresponding author.
E-mail addresses: l.alessandri@rug.nl (L. Alessandri), glcardello@uniss.it (G.L. Cardello), p.a.j.attema@rug.nl (P.A.J. Attema), valerio.baiocchi@uniroma1.it (V. Baiocchi), flavio.de.angelis@uniroma2.it (F. De Angelis), silvio.delpizzo@uniparthenope.it (S. Del Pizzo), fabiana.diciaccio@uniparthenope.it (F. Di Ciaccio), angelica.fiorillo@uniroma2.it (A. Fiorillo), maurizio.gatta@uniroma2.it (M. Gatta), Monti.1614926@studenti.uniroma1.it (F. Monti), matteo.onori@uniroma1.it (M. Onori), rolfo@uniroma2.it (M.F. Rolfo), marco.romboni@uniroma2.it (M. Romboni), gianluca.sottili@uniroma1.it (G. Sottili), salvatore.troisi@uniparthenope.it (S. Troisi).
[1] These authors contributed equally to this work.

climate changes (e.g., the Apennines; Marra et al., 2020, 2021). In such changing context, caves are one of the most conservative environments, where archaeological, anthropological, climatic and tectonic data can be well-preserved. Their study allows the understanding of the interplay between geological processes and human use of the natural and persistent habitats in an ecosystem such as that around the cave. Today, the Apennines are a densely inhabited and seismically active mountain belt (Fig. 1) (Frepoli et al., 2017; Stucchi et al., 2004), where its axial part in Central Italy recorded earthquakes that reached magnitude up to ~ Mw 7.2, and bear evidence of neotectonics (Galadini and Galli, 2000; Galli, 2020; Roberts and Michetti, 2004; Schlagenhauf et al., 2011). By contrast, near the coast of *Latium*, despite the reports on some historical earthquakes, like the 1170 CE Ceccano Earthquake (Mw 5.5; Fig. 1) (Locati et al., 2021; Rovida et al., 2020), and the occurrence of large Quaternary fault systems, little is known about the seismogenic structures capable of destructive earthquakes (Basili et al., 2008; Faure Walker et al., 2020). At the edge of the coastal Pontina Plain and within the Volsci Range (VR), the southwestern and most internal mountain chain of the central Apennines, Quaternary monogenetic volcanic centres emplaced between ca. 800 and 350 ka are aligned with Quaternary fault zones that facilitated fast magma ascent (Cardello et al., 2020). A few tens of kilometres offshore in the Tyrrhenian Sea, Middle Pleistocene faults were recognized associated with submarine volcanoes (Cuffaro et al., 2016). Despite the well-recognized Pleistocene regional uplift and tectonic evolution affecting the southern Apennines and Tyrrhenian Basin (Bordoni and Valensise, 1999; Curzi et al., 2020), tectonic stability along the Tyrrhenian Sea coast comprised between Anzio and Gaeta during middle-Late Pleistocene has been hypothesized (Castagnino Berlinghieri et al., 2020; Ferranti et al., 2006), as opposed to a multi-phased tectonic uplift affecting the coast north of Anzio (Karner et al., 2001; Marra et al., 2016, 2019a).

However, recent work (Marra et al., 2019b, 2020) suggested that differential uplift affected the coastal ridge between Anzio and Circeo promontories (Fig. 1), coeval with subsidence of the inner sector of the Pontina Plain ("Pontina Graben", Sevink et al., 2020) during the last 250 ka. The uplift rate, its precise timing and areal extension are still the subject of debate, while a total differential uplift in the order of 30 m is documented by terraces elevation (Marra et al., 2020, and ref. Therein).

Despite the occurrence of well-known paleontological and archaeological records in the area (Alessandri, 2013; Gatta et al., 2019), no direct neotectonic evidence was either reported from the speleological exploration of the VR (Agostini and Forti, 1982). A few tens of kilometres away, some caves of the more north-eastern ranges of the central Apennines, provided evidence of co-seismic activity (Di Domenica and Pizzi, 2017; Ferranti et al., 2015; Forti and Postpischl, 1984; Pace et al., 2020; Postpischl et al., 1991).

In this work, we report on neotectonics in the Central Apennines constrained by geological, paleontological and archaeological evidence at La Sassa cave (Sonnino, about 100 km southeast of Rome, Fig. 1), by providing a methodological example for geo-archaeological exploration in caves. The cave was first investigated in 2014 during a survey of the natural caves in the Ausoni Mounts (Alessandri et al., 2020; Alessandri and Rolfo, 2015), which constitute the central mountain group of the Volsci Range. Since 2016, four archaeological campaigns were carried out at La Sassa. In the cave, between 2016 and 2019, a rich stratigraphic sequence, ranging from Late Pleistocene to the Second World War, when the cave was used by the Sonnino inhabitants as a shelter, was discovered and investigated. Our finds, constrained by a set of sixteen ^{14}C ages and numerous archaeological time markers, show that the cave was used in the Late Pleistocene (32,930-30,6744 calBC) as hyena den and bear winter shelter. Much later, during the

Copper Age (CA; ca 3400-2000 calBC) and the Bronze Age (ca 1900-1400 calBC), as a burial place. The upper portion of the archaeological deposit in rooms 1, 2 and 3 also shows some medieval and renaissance activities which partially reworked the Bronze Age layers. Starting from 2018, an almost complete 3D model of the cave merged with the outside ground surface was obtained to support the archaeological interpretations and the multiscale geological survey performed in the surroundings. As later discussed, this work bears implication for seismic hazard assessment in the region, setting the ground for further investigation in the Quaternary and Holocene/Anthropocene units and other caves of the region and elsewhere. This work aims also at bridging the current interest in the Anthropocene with landscape evolution before and after the impact of human use of a cave began as it well shows the interplay between geological processes and human use of the natural and persistent habitats. A speleogenic comparison with karst systems worldwide is presented in the discussion as well as a contextualization of the archaeological finds in the frame of the regional landscape evolution.

2. Regional setting

2.1. The geological and palaeontological setting

The La Sassa cave occurs (Fig. 1) in the Quaternary lithified breccia deposited in a valley of the Volsci Range (VR), the most extensive mountain range of the Central Apennines (Carminati et al., 2012; Cardello and Doglioni, 2015; Cardello et al., 2021). The VR is mostly composed of carbonate rocks and it comprises three major mountain groups, Lepini, Ausoni and Aurunci Mounts, located between the Colli Albani Volcanic District (0.6−0.04 Ma) to the northwest and the Roccamonfina volcano (0.5−0.1 Ma) to the southeast (Marra et al., 2021 and references therein). In the Ausoni Mounts, Cretaceous shallow-water carbonates crop out while discontinuous Cenozoic temperate ramp deposits occur in the Latin Valley (Centamore et al., 2007; Consorti et al., 2017). At the top of the carbonate succession, middle to upper Miocene syn-orogenic siliciclastic rocks and marls are locally found at the footwall of the thrusted carbonate units (Angelucci, 1966; Cosentino et al., 2002; Cardello et al., 2021). During the Messinian salinity crisis, between 5.96 e 5.33 Ma, the area was exposed to fluvial erosion followed by the deposition of early Pliocene sandy gravels ranging between 5.33 and 4 Ma (Centamore et al., 2010). Near our study area, according to the averaged uplift history of the nearby Simbruini Mounts (Fig. 1; Delchiaro et al., 2020), which are just north of VR, about 2.4 Myr of Quaternary uplift are recorded. In particular, from 2.4 to 1.65 Ma, the baselevel fall rate constantly reached the highest value of about 690 m Ma^{-1}. Then, from 1.65 Ma to 0.75 Ma it temporarily decreases at around 1.3 Ma. As at 0.75 Ma, the baselevel fall rate reaches its minimum of about 370 m Ma^{-1}, the uplift rate raised again until the present day with a value of about 660 m Ma^{-1}. From the occurrence of deposits of early Pliocene deposits at the bottom of the valleys (Centamore et al., 2010), also our study area experienced regional Quaternary uplift from at least the Middle Pliocene. After emersion, erosional terraces were displaced by tectonics that brought them to different elevations (Centamore et al., 2007). During the late Pliocene, the VR was uplifted together with the rest of the Apennines, while the Pontina Plain was invaded by seawater (Boni et al., 1980). In the VR, from the Early Pleistocene, crustal uplift was accompanied by normal faulting, which generated a horst-and-graben structure with fault-bounded marine to continental basins towards the inland. The oldest Quaternary deposits recorded in the hinterland, suggest that atop the downthrown normal fault blocks, lacustrine to fluvial sedimentary conditions occurred, bearing geomorphological
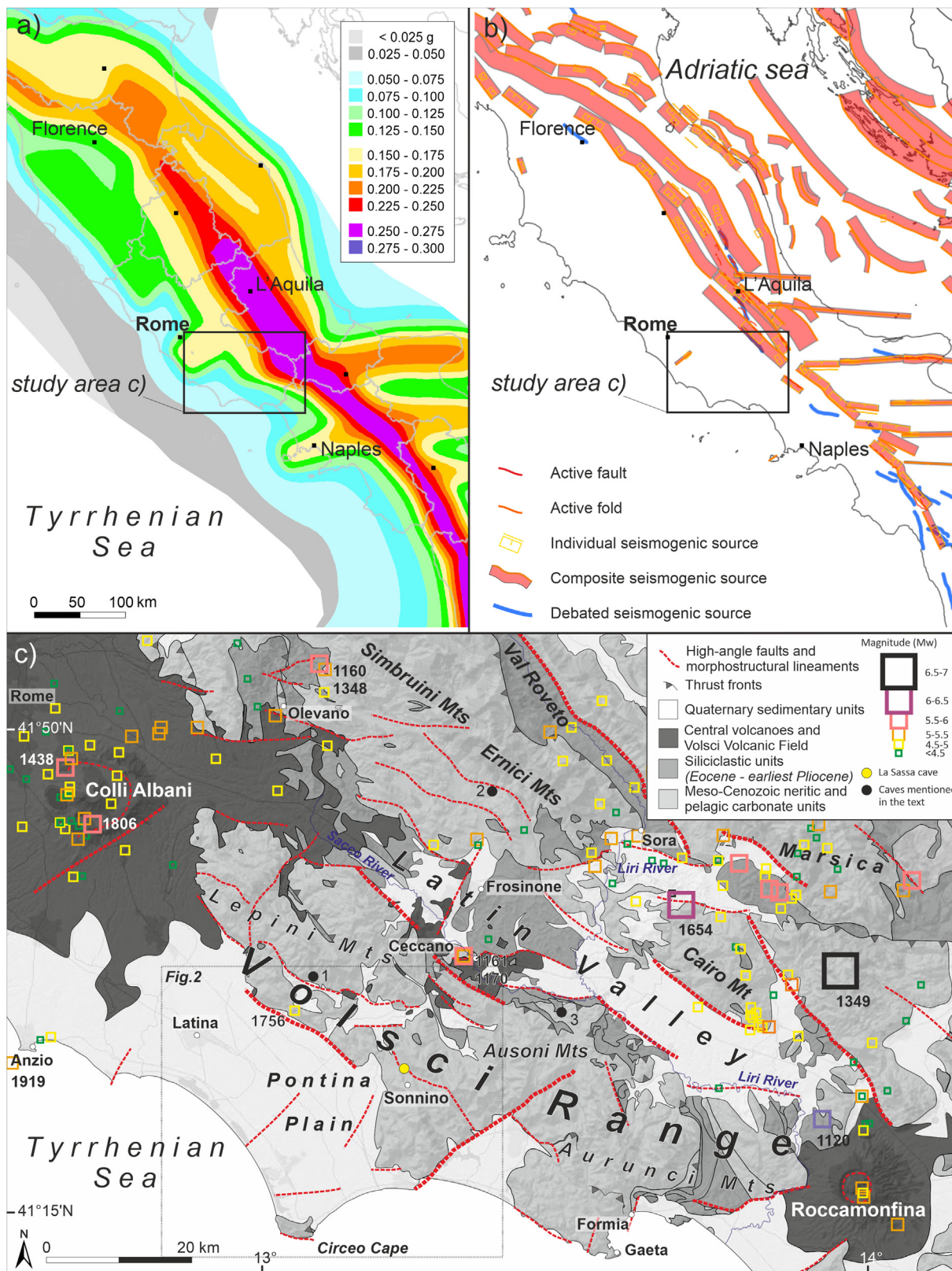
Fig. 1. Geological setting. (a) Seismic hazard map of central Italy (Stucchi et al., 2004). (b) Individual seismogenic sources of central Italy (Basili et al., 2008). (c) Reviewed sketch geological map of the Volsci Range (modified after Cardello et al., 2021) with the location of La Sassa cave (yellow dot, coordinates of the entrance: WGS84, 41°25′30″N, 13°14′11″E), other caves mentioned in the text (1, Vittorio Vecchi; 2, Regina Margherita; 3, Pastena) and the historical earthquakes (Rovida et al., 2020). (For interpretation of the references to colour in this figure legend, the reader is referred to the Web version of this article.)

evidence of ongoing tectonics (Centamore et al., 2010). Until the Middle Pleistocene, volcanic terrains comprise distal tephra from nearby potassic volcanoes recognized within continental successions in the Latin Valley and in the Pontina Plain (Alessandri, 2019; Centamore et al., 2010; Sevink et al., 2020). In the VR intermontane depressions of the Lepini and Ausoni Mounts and the Latin Valley are punctuated by volcanic occurrences of Pleistocene age also from local eruptive centres (Fig. 1) (Cardello et al., 2020; Marra et al., 2021). Notably, lower to upper Pleistocene slope, river and lacustrine deposits are preserved within depressions determined by high-angle NW-, ENE- and (N)NE-striking normal faults that dissected the inherited fold-and-thrust fabric, influencing the distribution of 1) Quaternary deposits; 2) karst form and 3) the fluid circulation. Quaternary slope deposits occur as breccia formed after the dismantling of mountain chains during glacial periods (Blanc and Segre, 1953; Hughes and Woodward, 2008; Petronio et al., 2007). In the nearby, Circeo Mt continental reddish breccia occurs at the seaside. In the VR, similar rocks occur at an altitude comprised between about 150 and 50 m. While in the Circeo Mount they were attributed to the last ice age (between 55 and 33 ka, Blanc and Segre, 1953), in the VR area, they are still undetermined. After their deposition, these breccia units were karstified and the caves were occupied.

During the Late Pleistocene, the Pontina Plain (also known as Pontine swamps or plain in the Archaeological literature) was characterized by a varied landscape. Its high biodiversity and ecology turned it into refugial environment during the rapid and severe climatic fluctuations of the Marine Isotope Stage (MIS) 3 and 2 (57−11.7 ka BP) (Allen et al., 2000; Gatta et al., 2019). It consisted of at least three coexisting temperate ecosystems including humid and swampy coastlines, a vast steppe-grassland plain with numerous streams and extensive Mediterranean woods populated by a broad spectrum of large and small vertebrates, reptiles and amphibians (Gatta et al, 2016, 2019).

Archaeological and paleontological sites in the Pontina Plain (among others Canale delle Acque Alte and Cava Muracci; Blanc, 1935; Farina, 2011; Gatta et al., 2019; Gatta and Rolfo, 2017) and the many caves of Mount Circeo (e.g., Grotta Guattari, Grotta del Fossellone, Grotta Breuil; Blanc, 1954; Stiner, 1991) have yielded important data on human presence, distribution of fauna and climate variability during the MIS 3−2 transition covering the time frame from 35 to 33 ka. After the last Holocene transgression (6ka BP; van Gorp et al., 2020), marine terraces underwent soil formation and created a gully landscape in the Fondi plain and in the south-eastern Pontina Plain (Fig. 2) (see also van Gorp and Sevink, 2019).

At around 1900 BCE (van Gorp and Sevink, 2019), the dune ridges closed the south-eastern marine lagoons at the foot of the Volsci Range near present-day Terracina, forming a lacustrine to marshy environment. The infilling lacustrine to marsh deposits are thicker where the effects of subsidence were enhanced (i.e., after the 1919−29 reclamation of the Pontine swamps; Serva and Brunamonte, 2007). Nowadays, the main VR hydrogeologic unit has a piezometric head below 125 m above sea level (Boni et al., 1980), making the whole area still subjected to karst. Similar to what observed elsewhere in the Central Apennines (e.g., Barberio et al., 2021), springs are associated to mixing deep fluids along the main normal faults.

As shown in Fig. 1, the distribution of historical earthquakes in the region is mostly clustering far from our study area (i.e., in the Colli Albani, and Sora-Marsica; Fig. 1). However, earthquakes also cluster at the edge of the Latin Valley graben, while in the Pontina Plain their occurrence was sporadically recorded near Anzio (also offshore) and along the foot of the Volsci Range (Fig. 1) (Sezze earthquake 1756, Mw 4.4; Rovida et al., 2020), where a major WNW-striking normal fault bounds the plain.

Being at the edge of the more seismic Apennine backbone (Frepoli et al., 2017; Stucchi et al., 2004), a large part of the study area was traditionally considered inactive because of the lack of volcanic and seismic historical events. For this reason, this area was chosen in the 1950s as an ideal setting to install two nuclear power plants. Unexpectedly, two seismic sequences in 2011 and 2012 shook the Pontina Plain with earthquakes of moderate magnitude (Mw ≤ 3.8; http://iside.rm.ingv.it), demonstrating that tectonic faulting may suddenly occur. On http://terremoti.ingv.it/search the distribution of recent earthquakes is kept up-to-date.

2.2. The archaeological setting

Despite systematic archaeological research (Fig. 2a), almost all evidence for the Copper Age (CA) and Bronze Age human activity comes from either un-systematic surveys or has been found by chance. Therefore, the CA and the Early Bronze Age (EBA) landscape is poorly known. The few CA pottery sherds in the area (Carboni, 2002, 2019 and references therein) (Fig. 2b) point to a material culture influenced by the southern Italian facies. The EBA has been recently targeted by the Avellino Project, which aimed at reconstructing the landscape and human occupation around the time of the Avellino Eruption (around 1900 BCE, Alessandri et al., 2019; Attema et al., 2019; van Gorp et al., 2020, Sevink et al., 2020). Since only few EBA potsherds have been retrieved during systematic and targeted surveys, it is likely that the Pontina Plain and the VR in the EBA were very scarcely populated (Fig. 2c). A different picture emerges from the beginning of MBA (Fig. 2d), when the northwestern portion of the Ausoni Mounts and the coastal strip were more densely occupied (Alessandri, 2013 and references therein). At the beginning of MBA (subphases 1−2), the material culture of the Tyrrhenian side of the peninsula was characterised by two widespread ceramic styles: the Grotta Nuova facies, in the central part, and the Protoappenninico facies in the southern part (for a definition of the facies see Damiani, 1995 and Cocchi Genick, 2002). Already in 1995, Cocchi Genick (1995) and Damiani (1995) placed their boundary in the Pontina Plain (Fig. 2d, upper right).

Using natural caves as places for burial are typical of CA, EBA and MBA. In the surroundings of the La Sassa cave, a good example is the Vittorio Vecchi cave (Fig. 2), where the disarticulated human remains of more than 40 people were recovered together with a considerable number of potsherds dated from CA to MBA (Guidi and Rosini, 2019). According to the authors, the potsherds belonging to the MBA1A subphase resemble the Grotta Nuova facies, while in the next subphase (MBA1B) some typical stylistic traits of the Protoappenninico facies are also present. As supported by recent investigations, also the La Sassa cave was used for human burial between the Copper Age and the Middle Bronze Age.

3. Material and methods

3.1. The geological methods

In the La Sassa cave, an additional geological-structural survey of the rocky substrate was carried out, integrating the previous work (Accordi et al., 1966). Field work aimed to re-define the general stratigraphic and structural architecture of the La Sassa area and identifying the main structural trends of the area. To this end, as shown in Fig. 3, faults and fractures have been described at key localities. Also, the morpho-structural interpretation is based on both field checks and the analysis of the orientation of river and valley segments and relieves characterized by break-in-slopes and near-surface fault traces cutting through Cretaceous carbonate and Quaternary deposits. In these units, the analysis of break-in-slopes
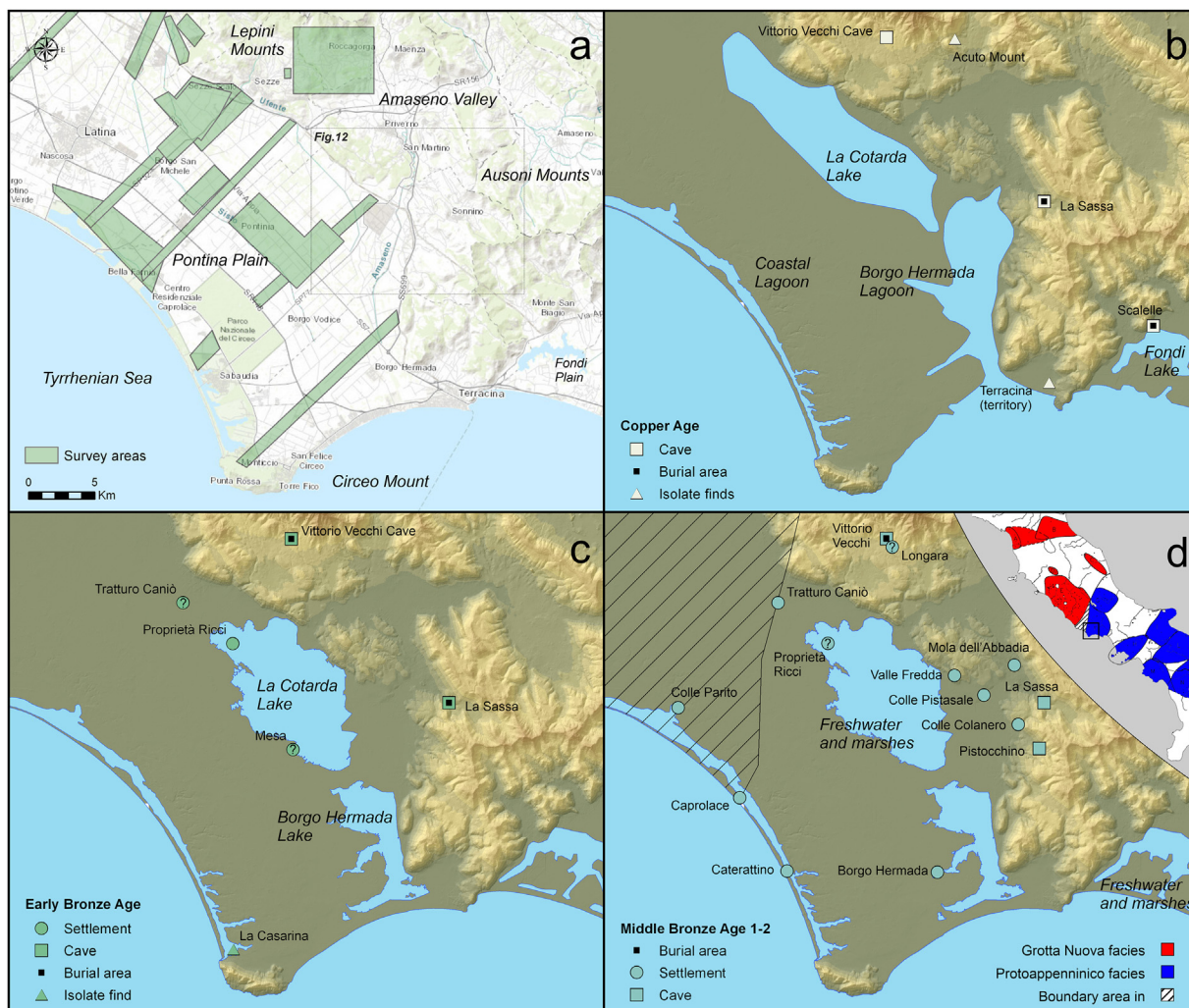
Fig. 2. Archaeological setting. (a) Areas in which archaeological surveys have been carried out. Background from Esri, DeLorme, HERE, TomTom, Intermap, increment P Corp., GEBCO, USGS, FAO, NPS, NRCAN, GeoBase, IGN, Kadaster NL, Ordnance Survey, Esri Japan, METI, Esri China (Hong Kong), Swisstopo, MapmyIndia, and the GIS User Community. (b, c, d) Copper Age (CA), Early Bronze Age (EBA) and Middle Bronze Age (MBA 1−2) evidence around La Sassa cave. In the top right corner of (d), the areas characterised by Grotta Nuova and Protoapenninico facies, modified after Damiani (1995). CA sites from Carboni (2019), 2002; EBA and MBA sites from Alessandri (2013). Background DEM from TINITALY/01 (Tarquini et al., 2007). Reconstruction of the lakes and lagoons modified after Alessandri (2013), van Gorp and Sevink (2019) and van Gorp et al. (2020).

>20% recognized on the LiDAR Digital Terrain Model (e.g. Cardello et al., 2020) allowed tracing morphostructural lineaments crossing and bounding the Cretaceous carbonate relieves and the Quaternary units. The collected geological data support inferences on the sub-surface deeper geometry of faults schematically represented in the cross-sections and in a block diagram, which allow to roughly determine the lateral extension of faults (fault length) and their related offset. Structural data (e.g., faults, fractures, bedding) were measured in the field and plotted by using TectonicsFP (Ortner et al., 2002).

3.2. The archaeological methods

During the four archaeological campaigns, the cave was subdivided into rooms and soundings were carried out in most of them. Both rooms and soundings were named by alphanumeric code. All the finds and layers described in this paper were carefully recorded in a local coordinate system and then transformed into EPSG (European Petroleum Survey Group): 32,633, which corresponds to the World Geodetic System 84, Universal Transverse of Mercator projection, zone 33 N. The finds received a unique

number and are now stored at the Laboratory of Prehistory at the University of Rome Tor Vergata along with all the original datasets, recorded in a digital database. The relative chronology of contexts was assessed by ceramic typo-chronological parallels; the absolute chronology by radiocarbon date on human and animal bone. The demographic parameters were estimated according to several consolidated methods based on the available skeletal districts (Bruzek, 2002; Houdaille et al., 1972; İşcan, 1985; Lovejoy et al., 1985; Meindl et al., 1985; Ubelaker, 1989).

The walking-time distances from the settlements to the necropoleis were calculated using the path-distance function in ESRI ArcGis. The movements were simulated following the so-called Naismith (1892) rule with the Langmuir (1984) correction.

Excavation and study permits were received yearly from the Soprintendenza Archeologia, Belle Arti e Paesaggio per le Province di Frosinone, Latina e Rieti (2016: n. 4888 Class 34 31. C7/328.1; 2017: n. 9559 Class 34.31.07/74; 2018: n. 0013261-P Class 34.31.07/7.January 11, 2018; 2019: n. 0016086-P Class 34.31.07/7.January 11, 2018).
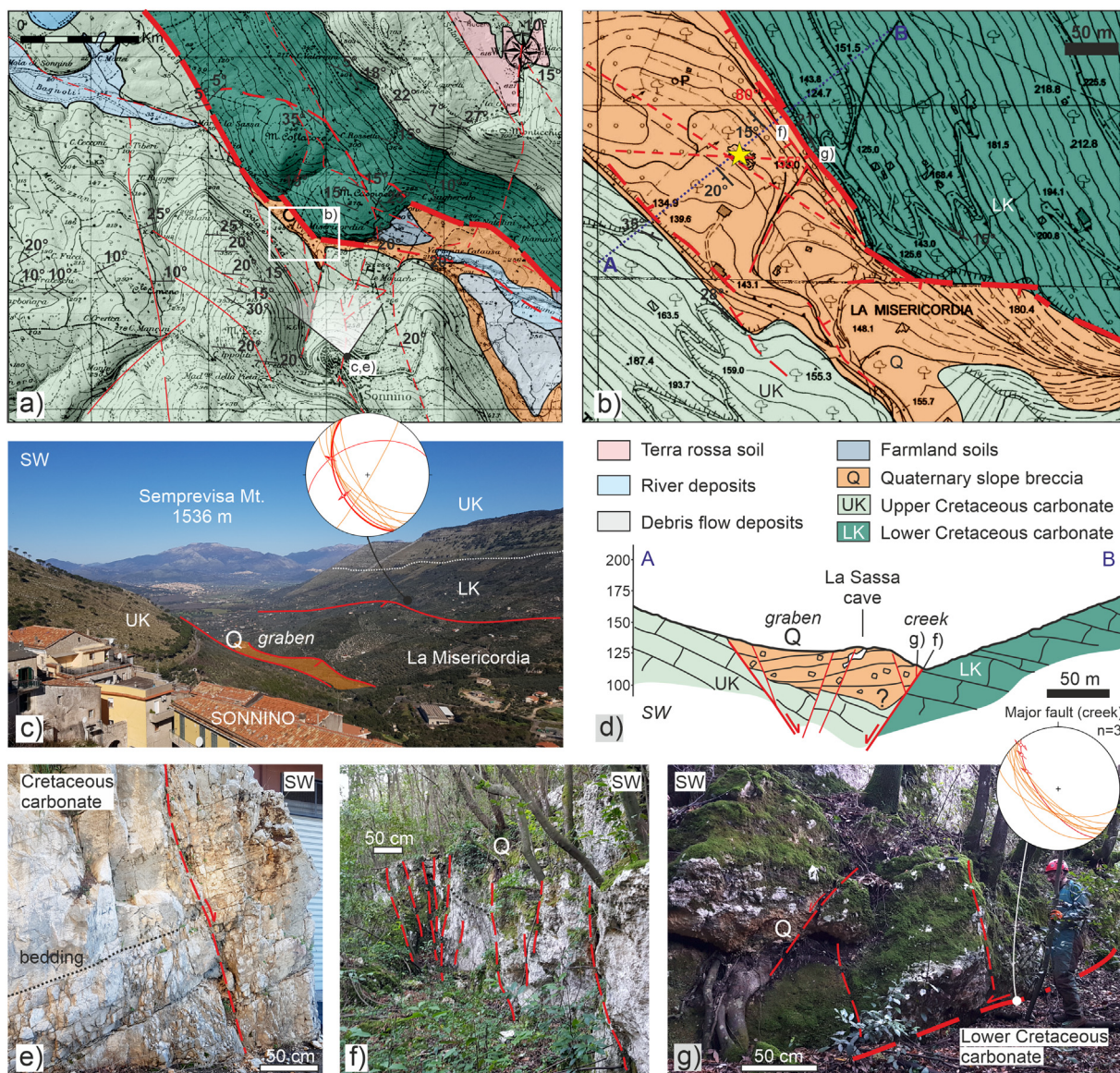
Fig. 3. Geology of the surroundings of the La Sassa cave. (a) Geological map modified after (Accordi et al., 1966) and https://sit.provincia.latina.it/. (b) Structural detailed map of the surroundings of the La Sassa cave showing cross-section AB (blue dashed line) and location of the La Sassa valley and cave (yellow star). (c) Panoramic view of the La Sassa valley from Sonnino village with stereoplot of lower hemisphere projection of fractures (orange) and faults with slickenfibers (red) measured on the Carbonate ridge to the north (Le Camminate locality, WGS84, 41°26′4″N, 13°14′39″E). (d) Geological cross-section AB of the graben with the location of geological evidence below. The cross-section is supported by field data and it has been drawn along the mean direction of transport towards the northeast during the Apennine collision. (e) NW-striking fractured carbonates at Sonnino. (f) North-west striking fractured Quaternary breccia and (g) fault contact with Cretaceous carbonates in the La Sassa at the northern edge of the graben (WGS84, 41°23′32″N, 13°14′11″E) with stereoplot of lower hemisphere projection of fractures (orange) in the breccia (f) and faults with slickenfibers (red) measured at (g). (For interpretation of the references to colour in this figure legend, the reader is referred to the Web version of this article.)

3.3. Three-dimensional internal and external modelling with geomatic techniques

The 3D model of the cave is the result of two distinct photogrammetric surveys performed during the excavations. Different cameras and light dispositions were used. Due to the narrow environment, the most complex and inaccessible areas (e.g., Branch and Room RA) were surveyed using the camera and the light of a smartphone Xiaomi Mi 9. The remainder of the cave was modelled by processing images extracted from videos recorded by a Nikon D800E camera with a fisheye lens, following a procedure already employed successfully in the survey of other underground environments (Troisi et al., 2017).

The photogrammetric model was georeferenced and scaled using three Ground Control Points (GCPs), previously obtained by a Global Navigation Satellite System (GNSS) survey. Double frequency Topcon Legacy-e receivers were employed to acquire the points, which were further differentiated according to the permanent stations of the Lazio Region, obtaining almost 25 mm horizontal estimated accuracy and 40 mm estimated vertical accuracy. Since these points could only be placed in the external part of the cave, further constraints were necessary to minimise the deformations of the most inner parts. For this reason, some targets were placed on the internal walls and their relative distances were measured.

Unfortunately, at branch RA, these constraints were not applied due to the very narrow space. Consequently, the survey was conducted about 1 year after the first photogrammetric survey. To

update the 3D model including the new Room RA, a 3D-Helmert transformation was carried out taking the first survey as reference. The alignment was then refined using the ICP technique, providing a Root-Mean-Square Error (RMSE) of 12 mm. The complete 3D model was then linked to the Rete Dinamica Nazionale 2008 (RDN, 2008; EPSG: 7792).

Outside, a drone photogrammetry survey was performed with a quadcopter DJI Phantom 4 equipped with its standard camera to obtain a high-density 3D model of the terrain surrounding the cave. The flight planning was conducted to assure a 15 mm Ground Sample Distance on the ground. During the flight the drone acquired 343 nadiral images with a geometric resolution of 5472×3648 pixels, to cover a zone of 30,000 m^2. At the end of the processing, a Digital Surface Model (DSM) was obtained on the basis of a dense point cloud of about 25 million points. To correctly orient the model, a further ground survey was carried out to estimate the coordinates of ten GCPs using the same GNSS receiver with the same accuracy. The obtained result was referred as well to the EPSG: 7792 reference system, with an RMSE of 30 mm on the GCPs and an RMSE of 90 mm on the Check Points (CPs).

3.4. Radiocarbon dating

The human and fauna bones were sampled according to their stratigraphical position. Two samples were analyzed at the CIO (Centre for Isotope Research, code GrA) of the University of Groningen (methodology details in Dee et al., 2019; Mook and Streurman, 1983). Eleven samples were analyzed at the CEDAD (Centro di Datazione e Diagnostica, code LTL) of the University of Salento (methodology details in Calcagnile et al., 2019). Three more samples were analyzed at the ORAU (Oxford Radiocarbon Accelerator Unit, code OxA) by using the ultrafiltration protocol AF (see details in Brock et al., 2010; Higham et al., 2006). Finally, all the radiocarbon dates were calibrated with OxCAL4.3 using the IntCal13 curve (Reimer et al., 2013).

4. Results

4.1. Large-scale geological evidence

The mesoscopic geological setting of the area surrounding the La Sassa cave is dominated by several kilometres long normal faults (Fig. 3) that cross-cut Lower to Upper Cretaceous carbonate units. Overall, the Cretaceous carbonate groups have a total minimum thickness of about 1 km, being the Upper Cretaceous group characterized by channelized rudist fragments-rich limestones, while the Lower Cretaceous group is richer in dolomites. Both Cretaceous carbonate units and Quaternary breccia are affected by linear karstic incisions, which often occur at fault zones rich in fractures (both in the footwall and in the hanging wall of major faults). In the area, occasionally speleothemes were found associated with areas with higher fracture density. As reported on the map of Fig. 3, the valleys are infilled by Pleistocene to Holocene deposits. By comparing the orientation of our structural data with these linear forms, retrieved from the combined analysis of LIDAR field and field data along the most evident fault traces (see section 3.1), we distinguished between major (thick dashed lines) and minor fault lineaments (thin dashed lines) in the area (Fig. 3). Overall, we observe a 10−12 km long segmented fault-arrangement disposed along a dominant NW-striking fault set, being the longest segment up to 3−4 km each.

Nearby NE-striking faults can reach comparable lengths. Minor faults are NNW- to NNE-striking and are of limited lateral extent (i.e.,1.3 km on average). In places (e.g., at La Misericordia Fig. 3b), the NW-striking segments are connected and locally crosscut by

ENE-to WNW-striking cross-faults with oblique kinematics. These fault sets occur as high-angle faults with dip ranges between 50° and 85°. The cumulative fault offset associated with this extensional system along the main NW-striking system is in the order of about 0.8−1 km distributed on about 2−3 major fault branches down-stepping towards the SW. In this frame, the La Sassa valley has been recognized as a graben bounded by antithetic normal faults clearly dissecting at least a 0.5 km thick pile of upper Cretaceous carbonate that is locally well-fractured near the major graben-bounding faults (Fig. 3). The major fault bounding the north-western edge of the valley is an oblique normal fault with a left lateral component (Fig. S1). The morphology of this localities is characterized by with vertical shafts and sinkholes (i.e., Voragine Catausa; La Sassa). Their elongation corresponds to a well-incised valley that connects two different basins placed northwest and northeast of Sonnino, La Sassa valley being the northwesternmost (Fig. 3). Close to the north-eastern bounding fault, the breccia occurring at the top are affected by dominant near-vertical NW- and ENE-striking fractures that overall run parallel to the master fault. At La Sassa locality, the bedding of the deposits, that partially fill the valley is constituted by a succession of Quaternary breccia deposits that gently dips towards the SW. The morphological evidence suggests that the Quaternary slope breccia deposits are topped by an erosive surface generating a fluvial terrace (e.g., north and east of Sonnino; Fig. 3). Supported by a more detailed field survey and geomorphic analysis on the LiDAR dataset, we report that the NW-striking fractures affecting the breccia in the surroundings of the La Sassa cave (Fig. S1) are associated with NW-striking topographic breaks of the slopes with jumps in the elevation in the order of a few meters (Fig. 3). These fractured zones bound cultivated depressions that are some meters across, and are filled by Quaternary to more recent soil deposits.

4.2. Geology of the La Sassa cave

Underground fieldwork allowed to recognize that the bedrock mostly crops out on the roof of the north-western part of the cave (Fig. 4), where it is constituted of clast-supported and cemented continental breccia with rare soil-derived matrix arranged in irregular layers that dip about 15−30° to the southwest (Fig. 5). The clasts contained within represent the Cretaceous carbonates (often with rudists). On the roof, at the edge between rooms 1−2 and rooms 3−7 and in room RA, dm-scale stalactites and sails of calcite abound near areas where fractures are more abundant. On the floor, a collapse-derived deposit of fallen blocks of breccia bedrock and more recent soil occur at the present-day entrance, in the NE portion of Room 1, between the latter and Room 3, the Branch and Room RA. On the fallen blocks limiting the southwestern walls of the rooms of the cave, fossil stalagmites and coalescences of columns occur. The fossil concretions bound the internal terraces that constitute 2−4 m large and some decimetric to centimetric thick ponds. Within these depressions, soils rich in archaeological materials are preserved. Active concretioning is limited to the deepest and southwesternmost part of the cave.

Two sets of faults with faint slickenlines were found at the old entry, indicating NE-striking dip-slip and (W)NW-striking right-lateral faults (Fig. 5c). On the south-western wall of Room1 normal to oblique right-lateral kinematics were found. Overall, the structural analysis of the fractures accompanying faults and concretioned lineaments of the cave allows identifying three major morpho-structural lineaments representative of NW-, E (NE)- and (N)NE-striking fault sets (Fig. 5d). The fault sets recognized in the cave can be compared with the faults and fracture recognized outside the cave (Fig. S1). No clear cross-cutting relationships could be established between the different fault sets.
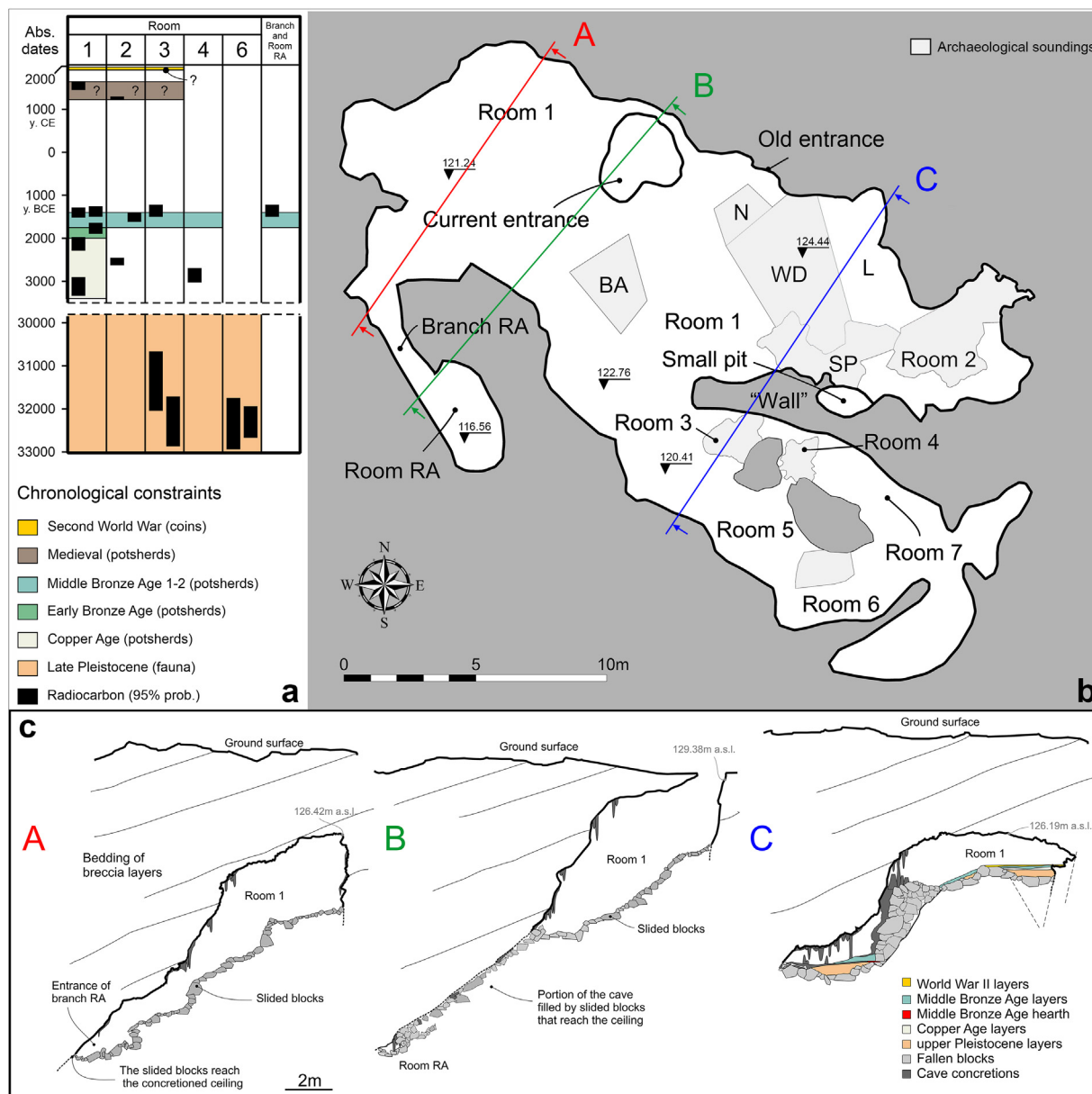
Fig. 4. Chronology and map of the archaeological soundings at La Sassa cave. Different portions of the cave have been labelled rooms and branches and named with alphanumeric codes. (a) Chronological (relative) phases and radiocarbon (absolute) dates. (b) Schematic map of the La Sassa Cave with the archaeological soundings and the cross-sections A, B and C decorated with speleothems, concretions, collapsed blocks and debris. The "wall" made of rocks and concretions between rooms 1–2 and 3–7 is also indicated. The cross-sections of the cave have been extracted from the photogrammetric 3D model. Structural data projection is shown in Fig. 5.

With regards to the structure within the cave, the roof of Room 1 is flat in the inner part while it abruptly dips towards the southwest of about 75°. There, near the most intensely fractured zones, concretions occur on the roof as well as on the floor. In Room 1, ENE- and WNW-striking concretion lineaments occur, while the NW- and (N)NE-striking sets bound the longest edges of the cave. Of note, about 1.5 m across large loose blocks of breccia occur at the entrance between room 1 and 3. Also, the ENE-striking set runs along a concreted fallen-rock assemblage, dividing Room 1 from rooms 3–7. Approaching this wall, fractures are healed by sail-type concretions that get coalescent and share the same orientation as the wall.

This clearly marks the limit between the area with a few or free of concretions (northeastern side of Room 1) and the rooms rich in concretions (rooms 3–7) (Fig. 5, S1). As the ENE-striking lineament

is locally interrupted by NNE-striking and NE-striking concretions, fractures with different orientations occur.

Between rooms 1 and 3, a column is crosscut by a SW dipping fracture, which is partially healed by later speleothems (smaller size columns) (Fig. 5f). Three geological cross-sections obtained from the 3D model of the cave allow quantifying the observed height offset between the flat parts of the roof of Room 1 and Room 3, which is 4.75 m high. This topographic step is accompanied by blocks and concretions that, depending on the sector of the cave, together with soil of different ages healed or partially sealed the break in offsets in the cave. Worthy of note, between Room 3 and Room RA, the vertical offset is about 3.64 m, where a massive concretioned collapse breccia is almost wholly sealing the scarp. At Branch RA, a further NW-striking abrupt termination is observed to the south-west. As shown in the map (Fig. 5), minor NE-striking
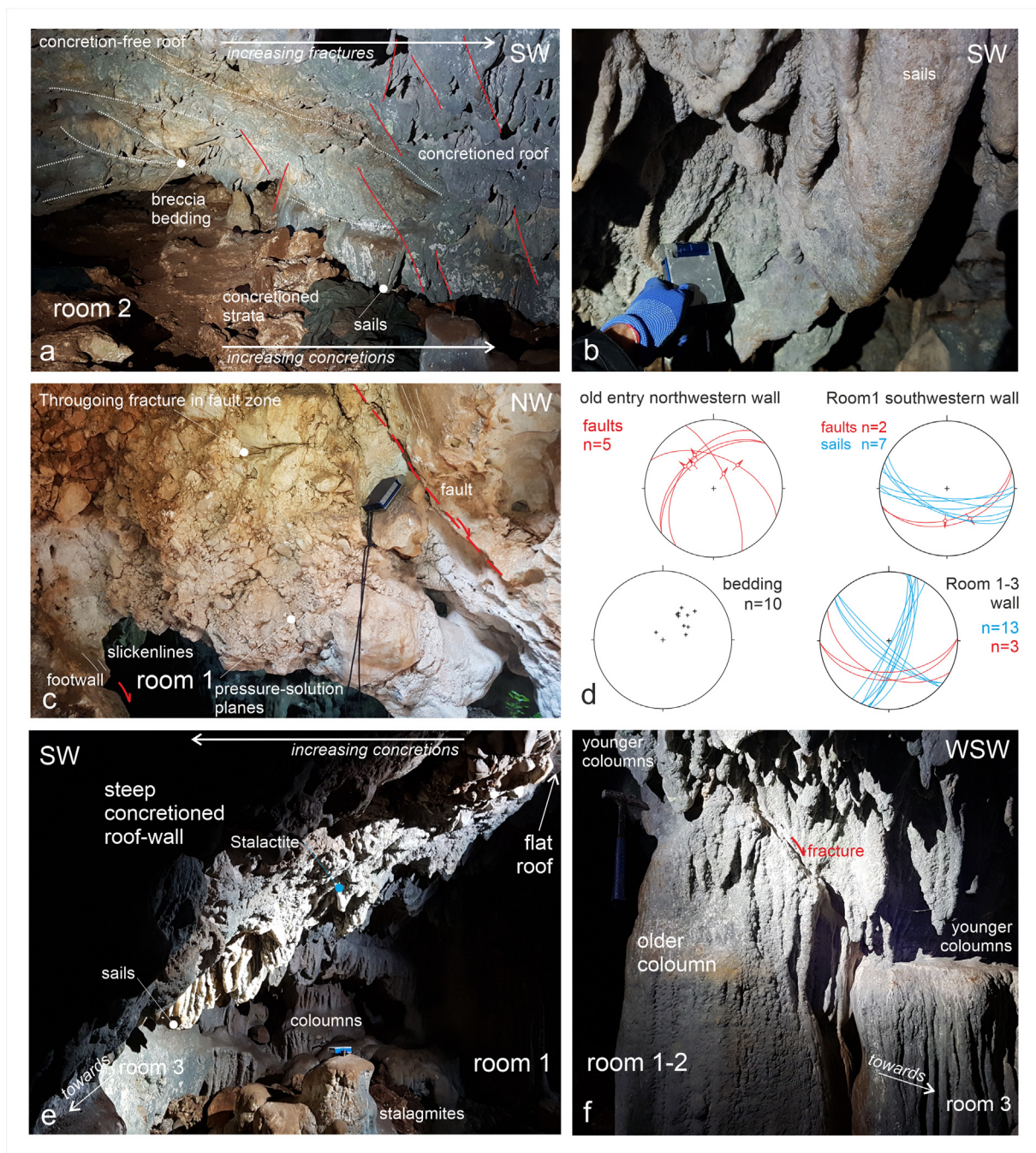
Fig. 5. Structural evidence in the La Sassa cave. (a) Room 2, increase of fractures and sealing concretions towards the SW. (b) Detail of NW striking calcitic elonged sail concretions. (c) Old entry of Room 1, fault core breccia within NE striking fault. (d) Lower hemisphere stereo-plot projections of key fractured and concreted areas. SW wall of Room 1 with increasing concretions towards the fault wall. (f) Detail of the syn-tectonic column concretion characterised by through-going fracture within a column later healed by younger columns.

lineaments occur between different rooms and at the room edges.

4.3. The late pleistocene finds and chronological constraints

Variably thick upper Pleistocene layers have been identified in Rooms 1, 2, 3 and 6. These yielded hundreds of coprolites and almost 5000 bone remains belonging to at least 23 different faunal taxa. Bone remains with gnawing traces by at least one large carnivore and hyena coprolites were found in primary position in Rooms 1 and 2. Faunal remains from Room 3 were collected from a partially concreted layer sealing the (almost) 4 m-thick deposit, composed of fallen blocks of breccia (up to 1.5 m across each) relatively free of concretions and which probably lie directly on some blocks on the cave floor. In this deposit, we found bone remains in often vertical position. In room 6 (Figs. 5 and 6), a well-preserved adult skeleton of a brown bear (*Ursus arctos*) in partial anatomical connection and a few other isolated bones belonging to a second specimen were found. Most of the bone remains were covered and partially embedded in the stratigraphic unit SU 16, a highly concreted calcitic crust 5–7 cm thick (Fig. 6). A small number

Fig. 6. The bear from Room 6. (a) The bear bones covered by concretions before the start of the excavations. (b) The radiocarbon dated right radius (LS 35). (c) A left tibia. (d) SU 16, Astragalus almost completely embedded by concretions; remains of macro and micro fauna are visible.

of bones lay on a soft brownish clay layer underneath (SU 17). As in Room 3, also in Room 6, the lower stratigraphic unit is free of concretions. No cutmarks and gnawing traces occur on the bones of the bears.

The four radiocarbon dates on hyena and bear bones from Rooms 1, 3 and 6 (Table 1) constrain these deposits between 32,930-30,6744 calBC (Fig. 7b).

Table 1
Radiocarbon dates from La Sassa. Calibration done with OxCal 4.3, IntCal13.

| Lab code	Sample code	Context	Sample	14C age	STD	Calibrated age (OxCal4.3, IntCal13, 95.4%)
GrA64830	LS 35	Room 6, SU 16	*Ursus arctos*, right radius	30,210	180	32,665−31,945 calBC
OxA-37283	LS 3	Room 6	*Ursus arctos*, right radius	30,220	360	32,930−31,755 calBC
OxA-37219	LS 516°	Room 3	*Crocuta crocuta*, mandible	30,150	350	32,862−31,722 calBC
OxA-37218	LS 516b	Room 3	*Crocuta crocuta*, mandible	29,190	310	32,037−30,674 calBC
LTL19066A	LS 2993	Room 1, SU 97	Human femur	4409	45	3327−2911 calBC
LTL18164	LS 1014	Room 4, SU 25	Indeterminate, vertebra	4271	45	3019−2701 calBC
GrA64828	LS 418	Room 2, SU 19	Human femur	4000	35	2619−2462 calBC
LTL19064	LS 605	Room 1, SU 55	Human femur	3722	40	2278−1980 calBC
LTL19065A	LS 873	Room 1, SU 78	Human femur	3451	45	1888−1646 calBC
LTL18166	LS 1047	Room 2, SU 31	Ovis sp., right humerus	3205	45	1611−1406 calBC
LTL20395A	LS 2176	Area RA	Human femur	3165	40	1519−1306 calBC
LTL17395A	LS 430	Room 1, SU 9	Sus sp., right ulna	3148	45	1506−1293 calBC
LTL18165	LS 1040	Room 1, SU 26	Sus sp., radius	3112	40	1492−1266 calBC
LTL17393A	LS 425	Room 3, SU 7	Sus sp., left radius	3101	45	1492−1233 calBC
LTL18163A	LS 921	Room 2, SU 18	*Canis familiaris*, right radius	745	30	1222−1290 calAD
LTL17396A	LS 431 + LS 432	Room 1, SU 9	*Canis familiaris*, third left metatarsal and left heel	347	45	1456−1641 calAD
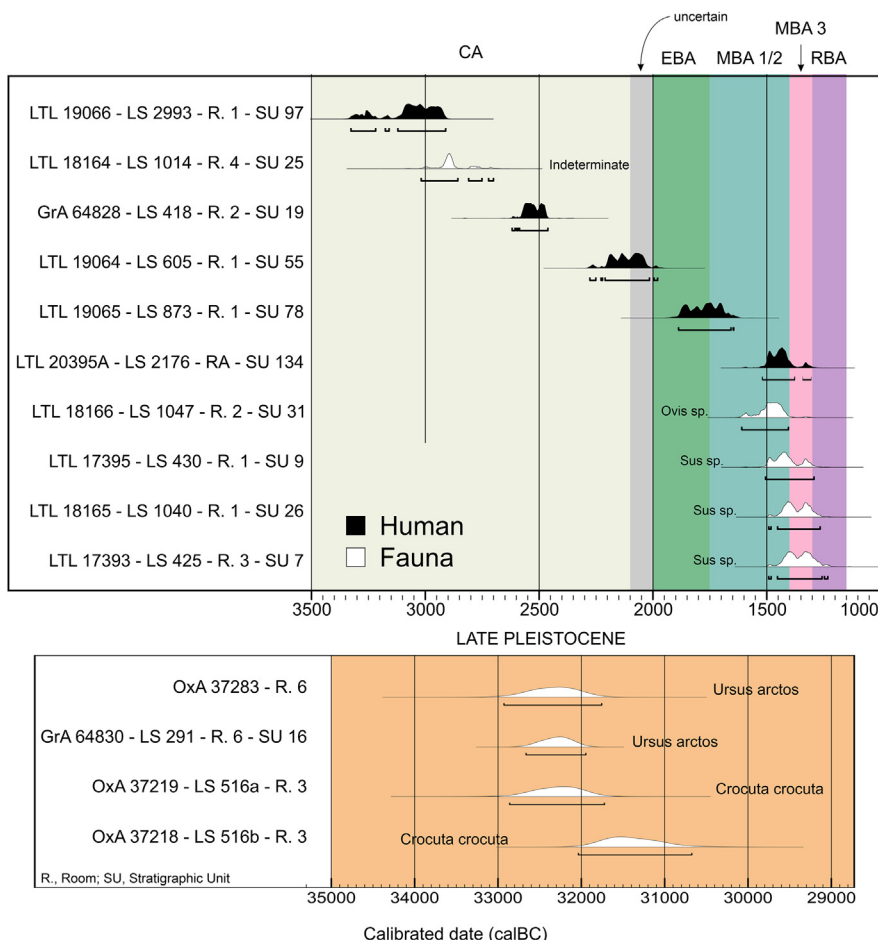
Fig. 7. The radiocarbon dates (a) Copper Age and Bronze Age. (b) Pleistocene. R., Room; RA, Room RA; SU, Stratigraphic Unit. Calibration done with OxCal 4.3, IntCal 13.

4.4. The Copper Age and Bronze Age finds and chronological constraints

In rooms 1 and 2, hundreds of disarticulated human bones were found just above the upper Pleistocene deposits. Their distribution could be due both to naturally occurring sliding and intentional reductions (Fig. 8a and c).

The osteological evaluation allows to determine a Minimum Number of Individuals of 20, including adults and at least three skeletally immature individuals. The osteological and osteometric analysis showed that adults buried in the cave were both males and females (four men and four women were osteologically identified), ranging from young (20–25 years) to senile individuals (over 50 years), showing that access to the funerary area was not restricted by age or sex. A few potsherds were found together with the human bones. However, none of them was diagnostic for time or cultural constraining, as it was not possible to reconstruct the shape of the vessels. The radiocarbon dates (Fig. 7 and Table 1) on some human femurs range from the CA to the EBA.

In Room RA, several meters away from the other disarticulated bones, an infant (1–2 years old) was recovered and radiocarbon dated to 1519–1306 calBC (Middle Bronze Age; Table 1; Fig. 7). The infant bones were collected at the front of a rock-debris unit that was cemented by concretions. About one meter away from the burial, a complete baby-bottle was found partially concretioned on the room floor (Fig. 9). Furthermore, a complete pyx lid and other well-preserved burial-related jug fragments were found in the Branch RA between the block slide and the southwestern wall of the cave (Fig. 8b, e).

In rooms 1 and 2, just above the CA and EBA deposits, some layers yielded potsherds dated to the MBA 1–2 based on typo-chronologically parallels, but without human remains in primary deposition. Radiocarbon dates ranging from 1611 to 1231 calBC were obtained from fauna remains collected from these layers (Fig. 7 and Table 1). No typical settlement features (e.g., post holes, small ditches) were detected in these deposits. On top of the CA and of the partially concreted MBA layers, loose and reworked layers rich in MBA potsherds and dog bones were found. Two bones of dogs found within these layers, SU 18 in Room 2 and SU 9 in Room 1, were radiocarbon dated respectively to the Middle Age and Renaissance (Table 1).

In Room 3, MBA 1 potsherds were found as well (Fig. 6). Some come from layers reworked between medieval times and the present day (Fig. 9, SU 1, 3 and 5). Just below these layers, an MBA layer (SU 6) partly covers the remains of a hearth, containing charcoal, ashes and charred animal bones (SU 7). Inside the ashes, a left radio of a Sus sp., (LS 425) was found and radiocarbon dated to 1493–1231 calBC (Fig. S7a and Table 1).

The hearth was half-covered by a large (40–60 cm) collapsed block that constitutes the base of a concreted fallen-rock assemblage, dividing Room 1 from rooms 3–7 (the "wall" in Fig. 4).

Fig. 8. Excavation and finds. (a) and (c) Human bones from the Copper Age layers, in Room 1. (b) Collecting the potsherds in Branch RA (d). The baby-bottle found in Room RA. (e) The pyx lid and some burial-related potsherds from Branch RA. (Pictures by A. Ferracci and M. F. Rolfo).

5. Discussion

We discuss the results presented above, in the following order: 1) the morphostructural evolution of the La Sassa surroundings; 2) the speleogenesis and neotectonics of the Sassa cave; 3) the seismogenic potential of the studied structures and; 4) the interaction between Protoappenninico and Grotta Nuova facies in the MBA; 5) the utilisation of the cave and 6) the settlement and necropolis patterns.

5.1. Morpho-structural evolution of the La Sassa surroundings

The surroundings of the La Sassa Cave are characterized by a major fault system that was active during the Plio-Quaternary extension. The major faults are NW- and NE-striking and present minor strike undulations resulting in a cumulative minimum displacement of about 0.8−1 km. This is in the order of the major normal faults reported elsewhere in the Volsci Range (e.g., Cardello et al., 2020, 2021 and references therein). Overall, the fault segmentation pattern accounts for E-W and N−S transfer zones (e.g., Morley et al., 1990), which segment the master faults. The fault kinematics recorded both within the Cretaceous carbonate units of the footwall of the major NW-striking fault, and in the Quaternary

breccia in the hanging wall are transtensive. However, they generally accommodate a NE-directed extension. Despite the low deformation rates, i.e., within the Latin Valley (Marra et al., 2021), the focal mechanisms from the earthquakes shaking the region account for the re-activation of the Plio-Pleistocene faults with transtensive kinematics. Besides dip-slip NW-striking faults, of NNE-striking faults with oblique-slip kinematics, our data are consistent with a prevailing NE-oriented sigma-3, as typical of the Apennines (Montone and Mariucci, 2016). As shown elsewhere in the axial zone of the central-southern Apennines, the NW-striking intramontane basins record active NE-directed extension (e.g., Bernard and Zollo, 1989; Montone et al., 1999; Galadini and Galli, 2000; Galadini and Messina, 2004; Chiarabba et al., 2009; Falcucci et al., 2016). However, little is known about active tectonics and the structural control on the distribution of Quaternary sediments and karst development in the internal and coastal part of the Apennines.

As shown in Fig. 10, the fault arrangement controls the location of structural depressions and karstic forms, i.e. the La Sassa graben. In particular, during the Quaternary, NW-striking faults guided the deposition of continental breccia units at the edge of the La Sassa valley. The so formed graben contains Quaternary breccia that, according to our reconstructions based on the present-day tectonic
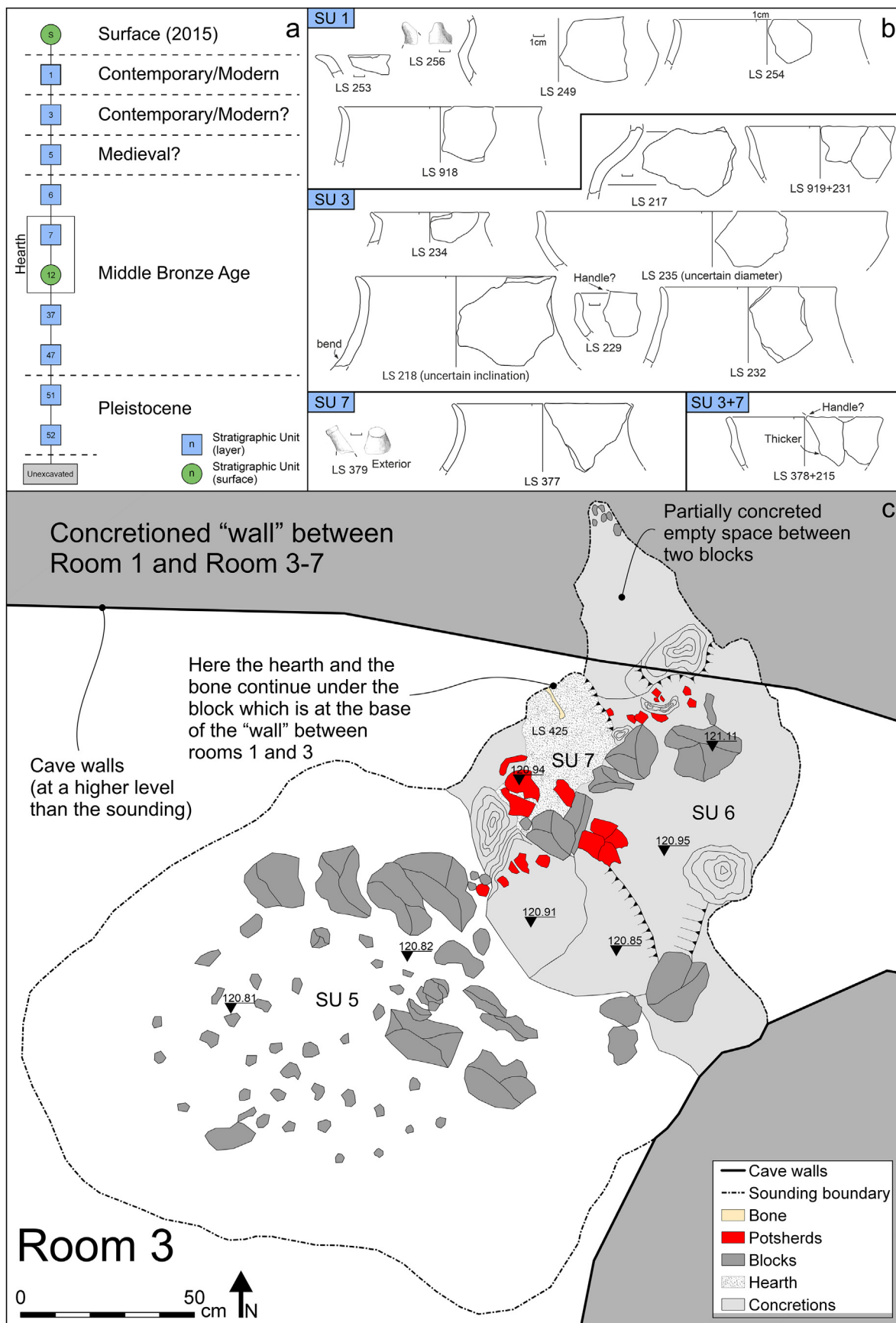
Fig. 9. Archaeological finds in Room 3. (a) Matrix of the sounding in Room 3. (b) Diagnostic potsherds collected in Room 3 (drawings by L. Alessandri), for the parallels see Table S1 (c) Map of the sounding in Room 3. SU 5, soil layer with few MBA impasto potsherds, most of them in a sloping NS positions. One potsherd made of depurated clay, possibly roman

and stratigraphic setting, we consider as syn-tectonic (Fig. 10). As demonstrated by Serva and Brunamonte (2007), the infilling lacustrine to marsh-lagoon deposits are thicker where the effects of subsidence were enhanced. Further, this occurs at the foothill of the Volsci Range, where Quaternary normal faults are reported (Milia and Torrente, 2015) and seismicity localizes (see Section 5.3).

Elsewhere in fold-and-thrust belts, it has reported the effect of tectonics on controlling the paleogeographic and sedimentary environment both in marine (e.g., Cardello and Mancktelow, 2014) and continental hypogeous conditions, which guided the speleogenesis (Ekmekçi, 2005, 2003; Miller, 1996). In particular, Miller (1996) relates the extent and position of karst systems in Belize to a control by major bounding faults with a situation that shares some similarity with the La Sassa Valley. Generally, the architecture of fault zones typically exerts control on fluid flow in the upper crust (Bense et al., 2013; Caine et al., 1996; Rawling et al., 2001; Doglioni et al., 2015) also, from examples exhumed from the seismogenic depth that can affect both thrust (e.g., Perfettini et al., 2010; Dal Zilio et al., 2018; Cardello et al., 2019; Menant et al., 2019) and normal faults (e.g., Clemenzi et al., 2015). The relationships between karst processes and tectonics have been well-explored in the review work of Shanov and Kostov (2015). The role of tectonic elements as fractures and faults on guiding the underground karst systems has been recognized (Goldscheider, 2005; Klimchouk et al., 2012; Klimchouk and Ford, 2000; Pepe and Parise, 2014; Stafford et al., 2005; Šušteršič, 2006).

Similar to our context, in the Ligurian Alps (Antonellini et al., 2019) and a number of other localities, regional tectonic uplift and neotectonics triggered karst development (e.g., Ekmekçi, 2003). For example, small-scale poljes develop along the depression related to the axis of a syncline fold in the Northern Alps (Goeppert et al., 2011). In tectonically-controlled karst contexts with localized fractured zones, the cave shape and the distribution of underground and landscape forms are guided by major faults (Pepe and Parise, 2014; Tîrlă and Vijulie, 2013) (c.f. section 5.6). The control of tectonics on karst development occurs both in epigene (Silva et al., 2017) and hypogene conditions (Cazarin et al., 2019; Ennes-Silva et al., 2016; Klimchouk et al., 2016). The relations among fractures, bedding and faults were established also in a gypsum cave in the Northern Apennines, where they guided the karst epigenesis of a cave (Pisani et al., 2019). However, the constraints provided by the archaeological and paleontological findings and datings are rarely reported in the literature concerning underground neotectonics. In our interpretation, during and after the Quaternary Breccia deposition, the Sonnino surroundings were affected by karstic (e.g., possibly periglacial thermokarst), fluvial and tectonic processes. In this study, we could not constrain the age of the host-rock breccia nor detail the steps of evolution before the CA, however U/Th or C-14 dating on speleothems could better assess the progression of Quaternary tectonics in the area. Yet, we remark that the La Sassa cave could have undergone multiple phases of formation related to the regionally recorded climatic variations (Bini et al., 2020; Boschin et al., 2021), that must be older than our oldest dated bone (i.e., pre- 32,930 calBC) in the upper Pleistocene deposits found within the cave (Fig. 7).

5.2. Speleogenesis stages and neoctectonics of La Sassa cave

In light of the 3D speleological and structural surveys of the La Sassa cave, we propose an interpretation that explains the speleogenesis of the cave. As shown in Fig. 11, the drop-in height level between the averaged roof height of Room 1 and the roof of rooms 3−7, corresponds with the occurrence of morphostructural aligned steps dipping towards the SW and thus of NW- and E-striking thoroughgoing faults that offset the morphology of the cave and its outside (Figs. 3 and 4). As documented, the NW-striking normal faults in the breccia associated with metric-scaled offset, crop out associated with major NW-striking regional faults recording larger offsets (Figs. 4 and 11). In the surroundings of the cave, dm-to metric amount of topographic offset can also be recognized in the topographic articulations of the Quaternary terrace. Those forms can be compared with the structures observed within the cave. In particular, the morphologic offset (4.75 m) is likely to be due to a fault offset related to the E-striking and NW-striking high-angle fault zones with similar orientations as documented on the surface in the surroundings of the cave affecting both the Quaternary rocks and the Cretaceous carbonate groups (Fig. 3, S1). In this perspective, as reported, most of the morphostructural lineaments in the cave can be considered near-surface fault branches of the major normal to oblique normal faults bounding the La Sassa graben. Thus, in our interpretation, we consider the present-day step-wise shape of the cave as resulting from fractured zones and faults prone to roof collapses and concretioning.

Radiocarbon dates on human and fauna remains, together with relative ages based on potsherd typo-chronology, have been used to constrain the ages of the infilling deposits. By correlating this information with the structural data we could indirectly reconstruct the timing of faulting. In the cave, the evolutionary steps retrieved from the interpretation of the events were obtained by analysing the cross-section AB in Fig. 3b,d, which was extracted from the 3D model (Figs. 4 and 11). This has provided the basis for a sketched reconstruction, which aims at establishing the evolution steps related to the development of the cave during the Late Pleistocene, the Copper Age, the Middle Bronze Age and present day.

The resulting structure has been manually restored in Fig. 11 by applying a kinematic inversion of movement along faults, according to their amount of displacement. This is done because a 2D restoration is schematic and implicitly assumes that there is no movement of material into or out of the plane of the section. Besides the structural aspects, our multidisciplinary approach, including the taphonomic and spatial distribution of the entire assemblage, allows to reconstruct the animal and human occupation stages of the cave (Fig. 11; cf. Section 5.5). The upper Pleistocene as well as the CA and MBA sediments are preserved within depositional pockets bounded by fallen blocks constituting rocky concreted walls or concreted fault zones. At the same time, the roof of the cave, far from these edges, is flat and relatively free of concretions. The ages of the infilling deposits are constrained by the sixteen absolute ages and other relative ages presented in this work between the Late Pleistocene and the Renaissance (Table 1), therewith dating the timing of faulting.

During the Late Pleistocene, in a time period corresponding to 32,930 and 30,674 calBC, Rooms 1 and 2 together constituted an ample cave hyena den that allowed a free circulation of the fauna in the cave prior to the onset of concretioning. The lenticular shape of the cave possibly followed a more erodible layer within the Quaternary breccia which dips towards the SW around 20°. As we will discuss later, concretioning is triggered and enhanced by the onset of faulting, which, based on taphonomic data, shortly postdated the

---

or medieval, has been collected from this layer. SU 6 is a calcite floor with several MBA potsherds. The latter were embedded in the concretions and slightly sloping from north to south. SU 7 consists of ashes, charcoal and charred animal bones. The deposit fills an artificial cavity (cut) in the calcite floor. At the bottom of this cavity, just below the ashes, a layer of potsherds was intentionally placed in flat position. (Drawing by E. Fazi, A. Ferracci and R. Malinconico).
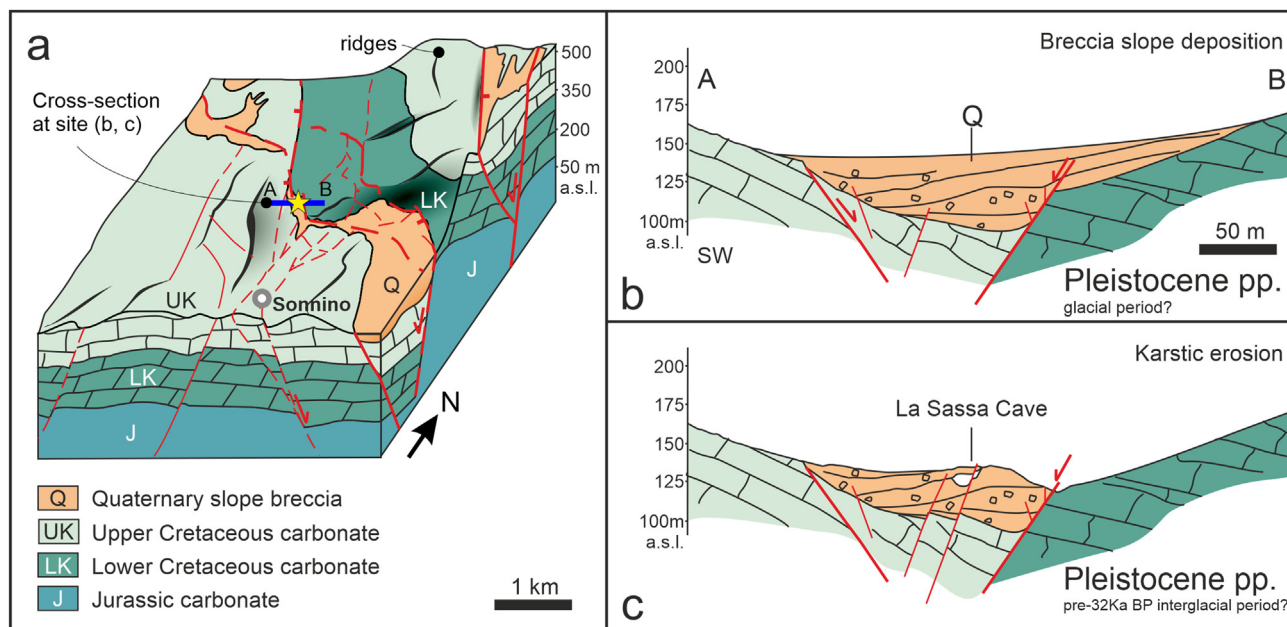
Fig. 10. Reconstruction of the La Sassa Valley. A) Sketch of the 3D setting of the La Sassa Valley and surrounding areas characterized by an articulated horst and graben structure. b-c) 2D schematic restoration of the cross-section presented in Fig. 3d B) The infill breccia layers of the La Sassa graben is likely coeval with the erosion of the mountain ridges made of Cretaceous carbonates during the syn-tectonic evolution of the graben. c) pre-32.9 ka karstic erosion affected the breccia generating the La Sassa cave.

death of the bears in Room 6. Further, as the bear(s) were found in a space that is much smaller (20−30 cm in hight; Fig. 6) than the size of a living-brown bear (70−150 cm), this implies that the accommodation space for a winter shelter was compartmentalized and reduced by concretioning after their death. From a structural and speleological point of view we conclude that the concretion process started after the death of the bear and during the use of the cave as a hyena den. The radiocarbon dates suggest that concretioning started after 32,930 calBC. Considering that the bear bones found in Room 6 are free of cutmarks and gnawings, they have naturally died in this inner area of the cave, where they probably retreated to hibernate (Fiorillo, 2016). Thus, although the radiocarbon date of hyenas and bears overlap in geologic time, it is unlikely that they actually made use of the cave at the same time. In our interpretation, we suppose that the rejuvenated shape of the cave triggered the partial remobilization of the upper Pleistocene deposits, that were not yet concreted. In particular, in Room 3, the chaotic distribution and the vertical position of the hyena bones point at a reworked deposit, that possibly did slide from the upper Room 1. However, close to the faults, concretioning of the Pleistocene hyena-bearing deposits shows that this process started already during their presence, suggesting that faulting and remobilization could have onset in the cave during this stage.

During the Copper Age (CA), in a time period comprised between 3300 and about 2000 calBC, the cave had already experienced much of the offset of the normal faults as it was already compartmentalized in progressively smaller rooms towards the SW with the footwall of faults possibly exposing the upper Pleistocene rocks. Meantime those fault walls could have already been concretioned. In the CA, as constrained by the archaeological finds and four radiocarbon ages, the cave was used as a burial place (see section 5.4).

In the Middle Bronze Age (MBA), between 1900 and 1200 BCE, the cave was experiencing widespread concretioning on both the floor and along the major fault-steps (i.e., Room 3 and 1). In other areas of the La Sassa Cave, where the rock debris was not completely "frozen" by the concretions, the rocks filled the lower

portion of the cave, possibly reworking finds of CA and EBA. Remobilization of the fallen blocks occurred before concretioning set on, as suggested by the disposition of the MBA baby burial in Room RA. The four radiocarbon age constraints from this period derive from the finds of a hearth leftover and possibly cultic activities whose implications are discussed in Section 5.5.

In more recent times, comprised between the Bronze Age (1233 calBC) and the Middle Age (1222 calAD), we highlight the presence of a fracture crosscutting a column belonging to the post-MBA concretioned "wall" between Room 1 and Room 3−7. This fracture, also schematically reported in Fig. 11 is partially healed by the growth of new speleothems representing a relatively recent effect of faulting, which could either be due to local activity or represent a coseismic effect of nearby earthquakes. The rock fall and concretioning at fault zones progressively generated a series of walls that hampered the rock debris to slide further downward and completely fill the space, acting as a dam (e.g., covering the MBA hearth in Room 3). Accordingly, we interpret the fault healing documented in rooms 1−3 on the post-MBA dividing wall as the most recent faulting effect in the cave. Further, the collapses near the fault zones had occurred before the emplacement of the concretioned "wall" between Room 1 and Room 3−7, which formed slightly after the MBA 1−2. In particular, we recognize that the fault intersection occurring at the cave entrances and the coexistence of increasing fracturing with concretioning at the southwestern edges of the rooms of the cave, intimately tighten the relationship between tectonic processes (faulting and fracturing) and the internal karst development. This "dam" has prevented the medieval unconsolidated debris to fall in the lower rooms. This suggests that the latest concretioning, to which we can possibly date the most recent healing event on the faulted column, could have occurred in a time comprised between the Middle Bronze Age and the Middle Age (cf. Table 1 and Fig. 4).

5.3. Seismogenic potential

The La Sassa morphostructural evolution during the Late
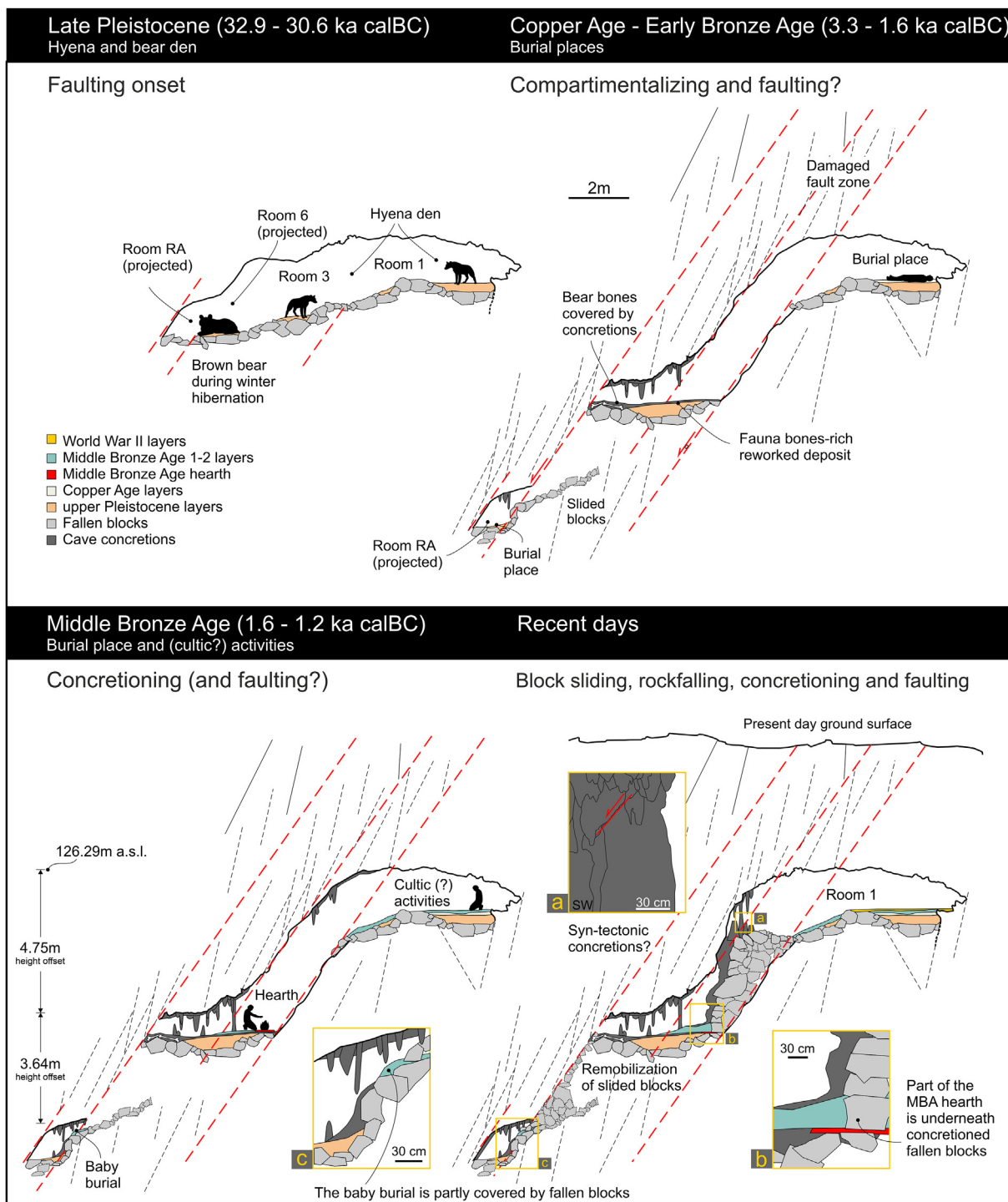
Fig. 11. Evolution of La Sassa cave. Reconstruction of the morphologic and structural evolution of the La Sassa cave from the Late Pleistocene up to the present day. The cross-section of the cave (C in Fig. 4) has been extracted from the photogrammetric 3D model, that identifies a step-wise shape of the cave due to normal fault steps, with the projected add of Room RA. The room for bears and hyena is reconstructed as virtually free of large concretions with a less prominent shape of the cave. In its Copper Age-Early Bronze Age, Middle Bronze Age and present-day shape, the cave has become affected by faulting and progressively infilled by collapsed blocks, concretions. Layer trends are schematic but describe the different steps of the syn-sedimentary evolution related to normal faulting in the cave. Details in the yellow bounded insets are referred to important finds (i.e., CA baby burial on MBA remobilized and concretioned debris; column cross-cut by a fault and later partially healed; MBA hearth underneath a fault-related concretioned-wall). (For interpretation of the references to colour in this figure legend, the reader is referred to the Web version of this article.)

Pleistocene to more recent times can possibly be used to provide constraints to the paleogeographic evolution of the Pontina Plain (van Gorp et al., 2020) and nearby areas (cf. section 5.6). In particular, by contextualizing and scaling our faults into a present-day dynamic context, we can attempt to estimate the seismogenic potential of the La Sassa faults.

In the vicinity of our study area, within the Pontina Plain (about 15–25 km to the west, Fig. 1), the distribution of the instrumentally

recorded earthquakes clearly shows (W)NW- and NNE-striking 7−10 km elongated clusters with major events up to Mw 3.8 (cf. http://terremoti.ingv.it/search). As also reported by Marra et al. (2021), despite the localization error of the seismic source, the two strongest earthquakes seem to have occurred at the intersection between the two above mentioned seismic alignments. Similar to what hereby described on the transfer faults of La Sassa (see section 4.1), the main earthquakes in the Pontina Plain also show a significant strike-slip component. Further, concerning their depth, most hypocentres occur in the first 10 km and, as typical of karst settings, a complex pattern of water flow occurs (Boni et al., 1981). This information contributes scaling the active faults near Sonnino (Figs. 1 and 2), which can be compared with the Quaternary faults cropping out in the Volsci Range (Fig. 1). The latter accumulated an estimated offset in the order of 1 km and along strike fault length in the order of 10−12 km occur (Cardello et al., 2020), which is geometrically and compositionally similar to what studied in the exhumed examples of seismogenic faults in carbonates elsewhere in the Apennines and in the Helvetic Alps (Cardello and Tesei, 2013; Cardello and Mancktelow, 2015; Clemenzi et al., 2015), where as demonstrated by groundwater studies deep fluids are involved (Barberio et al., 2021). As shown at La Sassa, considering that Quaternary faults are subdivided into segments that rarely exceed the length of about 3−4 km, we attribute for the Wells and Coppersmith (1994) empirical correlation line a possible maximum expected earthquake of about 5.1 Moment Magnitude (Mw). However, considering the total fault displacement along the whole length of the major normal fault, if the fault offset is explained as a cumulative coseismic slip, then earthquakes with a magnitude up to 5.8 Mw could be expected. This estimate is comparable with the magnitude of the most relevant regional earthquakes of Anzio and Ceccano that reached respectively a reconstructed magnitude of Mw 5.2 and 5.6 (Fig. 1) (Rovida et al., 2020). Also, these findings support the model of a multi-phased tectonic uplift affecting the coast of Latium (Karner et al., 2001; Marra et al., 2016, 2019a) with differential uplift between the Anzio-Circeo coastal ridge and the subsiding inner sector of the Pontina Plain (Marra et al., 2019b, 2020; Sevink et al., 2020) during the last 250 ka. Recent findings in low-seismicity sectors of the western Mediterranean Sea show that Late Pleistocene to Holocene tectonics are supported by significant regional uplift (e.g., Sardinia; Casini et al., 2020), which has been recently detected in zones/areas near our study area (cf., Section 2; Delchiaro et al., 2020) and attributed to slab break-off (San Jose et al., 2020).

5.4. Interaction between Protoappenninico and Grotta Nuova facies in the MBA 1

The potsherds recovered in the sounding of Room 3 can be all dated to the subphase MBA 1 (Table S1), with only one exception (LS 234). They all have close parallels with the Protoapenninico facies, thus confirming the presence of this facies in our study area (Damiani, 1995). The ceramic record was similar in sounding SP, in Room 1 (Fig. 4), but here some potsherds could be dated more precisely either to a very early moment of the Protoappenninico facies, likely in the MBA1A, or to the MBA1B (Alessandri et al., 2018). While the more ancient potsherds canbe exclusively attributed to the Protoappenninico facies (from the South), a few MBA1B potsherds show parallels with the Grotta Nuova facies (from the North). Synthesising, the potsherds from both soundings point to an exclusive Protoappenninico ceramic culture at the beginning of the MBA, while in the MBA1B traces of contacts with the northern facies are evident. In the near-by Vittorio Vecchi cave (Fig. 1 and) the situation is reversed. Here, according to the authors, the MBA1A potsherds exclusively belong to the Grotta Nuova facies and the

MBA1B potsherds show the first traces of contact with the Protoappenninico facies (Guidi, Rosini, 2019). The ceramic record therefore suggests that in the MBA1A the Amaseno valley, which runs between the Lepini and Ausoni Mounts (Figs. 1 and 2) constituted the boundary between the two facies. This would imply that in the MBA1B the populations south and north of the valley maintained cultural contacts. To test the hypothesis of exchange of goods and/or people isotopic (Sr) analyses on the human remains of La Sassa are underway. Unfortunately, potsherds from Colle Colanero, Mola dell'Abbadia and Valle Fredda (Fig. 2) remain unpublished, so their stylistic traits cannot be checked (Anastasia, 2007). Although potsherds from Colle Pistasale (Cancellieri, 1986) show some Protoappenninco influence, at least during MBA 1, they are too few to infer a chronological development. The overall picture fits with the progressive increase in the mixture of stylistic traits, already observed during the MBA in all of central-south Italy: in the subsequent MBA 3 (around 1400-1300 BCE) the entire area will be characterised by the same Appenninico facies (Macchiarola, 1995; Pacciarelli, 2001).

5.5. The utilisation of the cave

The evidence about the use of the La Sassa cave during the Bronze Age is discussed below, in order to both contextualize our archaeological finds and to constrain the tectonic of the cave. The utilisation of caves in Bronze Age central Italy has been long debated (Cazzella and Guidi, 2016; Cocchi Genick, 1998, 2002; Guidi, 1992; Guidi and Rosini, 2019; Ricciardi, 2012). Hypotheses range from water cults to practical uses related to burials, temporary shelters, or economy (e.g., sheepfolds), to name a few. In our case, the CA and EBA evidence from La Sassa points to a funerary use of the cave. It must be noted that in central Europe, the presence of Bronze Age items in caves, including human remains, has often been interpreted as the results of ritual offering. The missing anatomical connections, which is also quite common in Italy (including La Sassa), was one of the main points which led the authors to interpret them as the results of human sacrifice, sometimes associated with cannibalism (Orschiedt, 2012). However, during the excavation of the Vittorio Vecchi Cave (Fig. 2c and d) (Guidi and Rosini, 2019), the authors noticed that the potsherds and the bones were better preserved along the wall of the cave, compared to those found in the centre of the main room. This evidence led the author to hypothesise that the corpses were first put along the walls of the cave and later transferred to the centre of the room to make space for new burials. This process would explain the loss of anatomical integrity of most of the human skeletons. The evidence from La Sassa points to the same process. The presence in the skeletal record of all the anatomical districts, including the smaller bones, indicates a primary deposition in the cave, subsequently manipulated in the same place or in the immediate proximity. Besides, as for sex and age, the record in La Sassa is the expected outcome of several extended family in a contemporary village. Finally, in La Sassa no traces of cannibalism or ritual sacrifices, like cut-marks and perimortal breakage patterns have been detected on human bones.

In MBA 1−2, the layers in rooms 1 and 2 show very few human remains, that moreover originate from the lower CA and EBA layers. Thus, a funerary context can be easily ruled out. Moreover, as shown by the geological reconstruction, the hearth discovered in the Room 3 was likely at the same level or just a little beneath the MBA 1−2 deposits and certainly was in use when rooms 1, 2 and 3 formed a unique space (Fig. 11). In central Italy, hearths are a common discovery in MBA cave contexts. Since the current Italian interpretative framework almost excludes a residential use of the caves in the Bronze Age (Cazzella and Guidi, 2016), these features

are usually considered traces of ritual activities. Nearby, they have been found in the Vittorio Vecchi (Sezze, Guidi and Rosini, 2019), Regina Margherita (Figs. 1 and 2) (Collepardo, Angle et al., 2010) and Pastena (Figs. 1 and 3) (Pastena, Angle et al., 2014) caves. In the Vittorio Vecchi cave, the presence of hearths and charred seeds in the main room, close to the human remains, led the author to hypothesise the presence of ritual activities (Guidi and Rosini, 2019). In the case of Regina Margherita and Pastena, the zooarchaeological record has been carefully studied and proved to be a fundamental proxy to interpret the archaeological deposits (Silvestri et al., 2018). In the Pastena cave, the fire and cut marks and the kill-off patterns of the domesticated fauna bones indicate recurring meat consumption. According to the authors, this evidence, together with the depositional context, a small and quite inaccessible and dark room, points to a ritual activity. In the Regina Margherita cave, the hearths were found near the entrance and associated with domesticated animal bones. The area was slightly separated from the burial area, which is located in the inner portion of the cave, thus the authors hypothesise that offerings took place related to the mortuary contexts.

In the rest of Europe, like in Italy, hearths were found to be often associated with burial areas and often interpreted as traces of ritual activity (Harding, 2000) like in the cases of the Duffaits cave, in France (Gomez de Soto, 1973) and the Bezdanjača cave in Croatia (Drechsler-Bizic, 1980). On the other hand, especially in France, Bronze Age caves are mainly considered dwellings or dwelling annexes (Orschiedt, 2012; Treffort, 2005), thus hearths in caves have also been considered as related to domestic activities. It has already been noted that these opposite interpretations, rather than originating from different archaeological records, seem to be the effect of diverse scholarly traditions (Silvestri, 2017). However, as Brück (1999) pointed out, the dichotomy between ritual and domestic activities might well be a Western perception grounded in the post-Enlightenment rationalism which opposes the functional (secular) to the non-functional and irrational (ritual). The issue is also interwoven with the definition of the word "ritual" about which there is no general consensus among anthropologists. The definition of rituality ranges from the expression of fundamental propositions linked with religious beliefs (focusing on the message) (Rappaport, 1999) to performances according to precise conventions (focusing on the procedure) (Turner, 1969).

In 2005, Bradley tried to overcome the methodological deadlock. Following Brück's arguments, he suggested that rituality might be considered a performance defined by its own conventions where certain parts of life are selected and given particular emphasis (Bradley, 2005). In such a way, the distinction between domestic and ritual activity would eventually disappear and archaeologists can monitor the development of ritualization as part of social and political trajectories.

From this perspective, the MBA layers and the hearth in rooms 1–3, can be considered the outcome of a ritual that involved food consumption just above or close to the human bone deposit. The human bones were likely visible, since there was no additional soil between the CA/EBA and the MBA deposit. The ongoing study on the associated fauna remains (more than 5000 bones) and on the complete potsherd assemblages would certainly shed new light on this issue, helping to unveil the social framework.

At the end of this phase (MBA 2), the burial area shifted to the inner portion of the cave (Room RA) and perhaps in other non-yet investigated areas, like the north-west portion of Room 1, still occupied by a more recent block-debris. In Room RA, a single MBA (infant) burial has been recovered. In particular, these remains were found dispersed in a very small area, with no traces of other individuals. This latter evidence points to a single deposition in Room RA that later, during the remobilization of the underlying sliding blocks, was partly disturbed.

5.6. Settlement and necropolis patterns

So far, no CA or EBA settlements have been reported in the La Sassa valley. The nearest MBA known settlement is Mola dell'Abbadia, which is at around 46 min walking-time (Fig. 12). Colle Colanero and Colle Pistasale are at 50–60 min (Fig. 12a).

The reciprocal distance between the settlements is quite regular, with an average of about 50 min walking-time, thus enclosing territories with a radius of about 25 min. In southern Lazio, in MBA 1, territories with a similar radius (around 26 min) have also been identified near Anzio (Fig. 1) (Alessandri, 2013). The 2–3 km radius territories, which equals 24–36 min in level terrain, is recognized as a recurrent worldwide catchment radius, in a package that also includes a maximum of 5 km and a minimum of 1–2 km. Already in 1976, in his study about the early Mesoamerican villages, Flannery provided an elegant explanation for these values, arguing that they were the results of successive divisions (tessellation) of the available area (Flannery, 1976). Colonising a new area, farmers tend to develop their activities in a radius of around 5 km (60 min walking-time). Thus, a progressive infill of the available area tends to produce a network of settlements about 10 km apart. In a context of demographic growth, when all the available soil was already occupied, new settlements must carve out their territories at the expense of the older villages. A 5 km radius fragmented by 2 gives a 2–3 km territory radius and, if the process goes on, a subsequent 1–2 km radius. As Flannery pointed out, the settlements with a 5 km radius had likely more land and, consequentially, resources than needed. The 1 km radius could instead be interpreted as a symptom of unusual pressure on the land. In this regard, the 2–3 km radius seems to be balanced and sustainable. Not surprisingly, this value can be found in Europe, in different periods. Territories with a 2 km radius (which equals 24 min in level terrain) were proposed by Ellison and Harris (1974) for southern England between the Bronze Age and the early medieval period. A radius between 1 and 2 km (12–24 min in level terrain) also characterised the Early Neolithic villages in Thessaly (Perlès, 1999). Slightly wider territories (2.5 km, around 30 min walk) have been reconstructed for the Bulgarian Neolithic tells (Dennel, Webley, 1975), and the Classical period in Boeotia and Attica (Bintliff, 1999, 2009). Later, the same radius was proposed for medieval settlements in the Netherlands, France and Britain (Davies, 1988; Heidinga, 1987; Pounds, 1974). In 1999, Bintliff began to apply the conceptual tools of the Complexity Theory (Bintliff, 1999) to the archaeological interpretation. The Complexity Theory aims to explain how complex biological and physical systems tend to converge on stable or semi-stable configurations, named Strange Attractors (Lewin, 1992). In the general process of successive land tessellation described above, he identified three Strange Attractors: the first is the tendency of dry farmers to concentrate their activity in a 5 km, or 1 h walking-time, as already noted by Flannery. The second is the tendency of settlements to split up when they reach about 150 individuals. This seems to be a critical threshold for the so-called face-to-face communities both in social (Forge, 1972) and physical anthropology (Dunbar, 1996). In face-to-face communities the social relations are direct and divisions in subgroups or social classes are not necessary to preserve internal cohesion; when this number is surpassed, the community tends to differentiate internally or to split up (fission). The third Strange Attractor is the tendency to converge to territories with a 2–3 km radius, like in the case of the La Sassa cave, which enclose adequate resources to sustain the settlement needs also in the case of resource restraints. In 2013, Alessandri already suggested that the fission phenomenon could explain the MBA settlement pattern in the study area (Fig. 2;
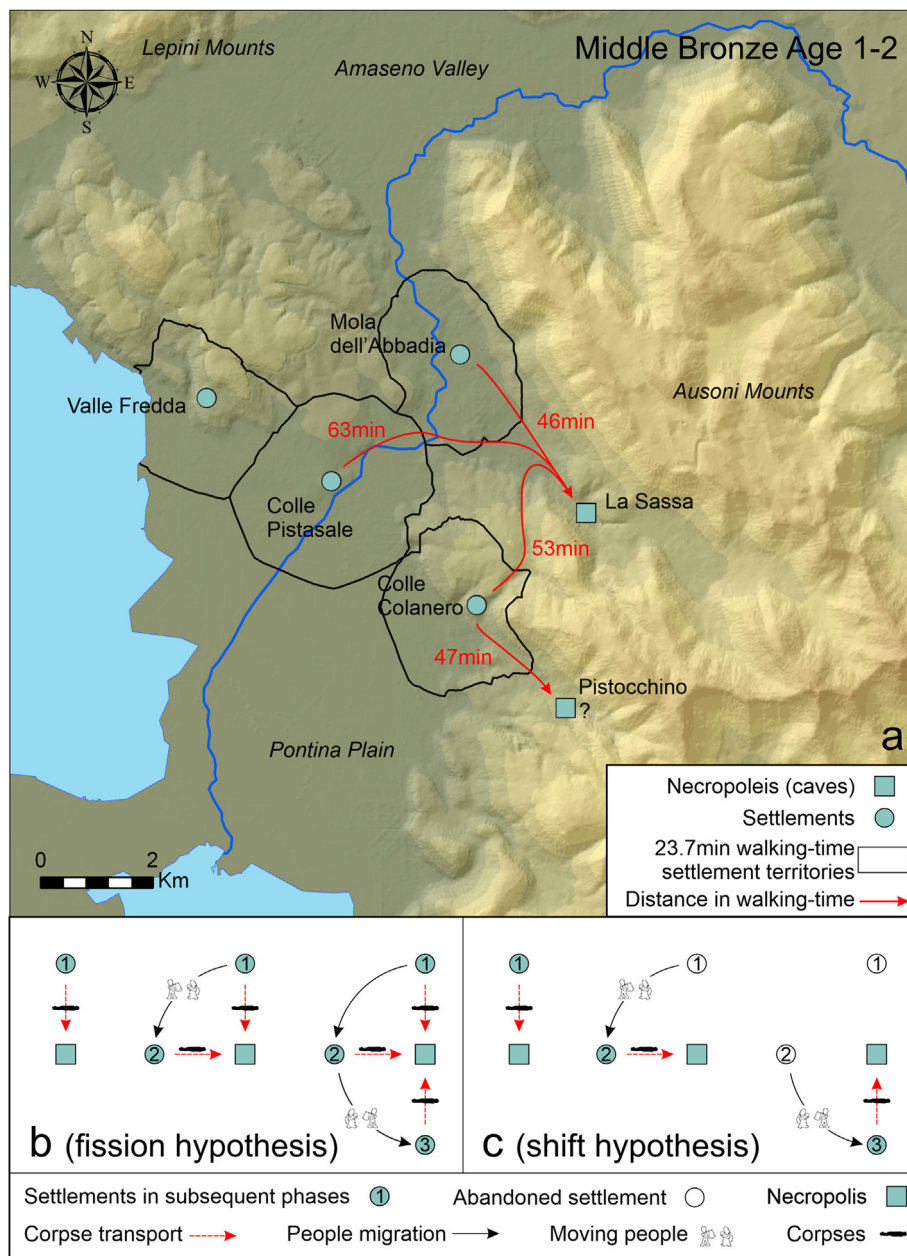
Fig. 12. Settlement patterns in the Middle Bronze Age 1–2 around La Sassa cave. A) Reconstruction of the territories of the settlements near La Sassa cave and their mutual distances. b-c) Two hypotheses about the development of the settlement patterns (moving people symbol from Cavazzuti et al., 2019).

Fig. 12b). However, he also suggested an alternative hypothesis: these villages could have periodically shifted in search of "fresh" terrains, that were not impoverished by agricultural use (Fig. 12c). In this perspective, Colle Colanero, Colle Pistasale and Mola dell'Abbadia (Fig. 12a) might have been the archaeological footprints of the same community moving to unexploited lands, caught at different times although all included in the MBA 1–2 (Alessandri, 2013). To this model, we can now propose the existence of a fourth Strange Attractor. The radiocarbon dates suggest that, even in a settlement pattern scheme where one or more villages periodically move around, the necropolis of La Sassa continued to be used for at least 1400 years, both as a burial place or as a site where to perform possible ritual activities. This should not be surprising since the presence of caves with an easy entrance and a considerable amount of space available such as La Sassa is rare and at the

moment the CA to MBA funerary practices seem to be restricted only to natural or artificial (smaller) caves. Further, the distance between the settlements and the cave remained quite stable, with an average of 54 min. MBA potsherds, in reworked Roman layers with Republican ex-voto objects, have also been found in the Pistocchino cave (Alessandri and Rolfo, 2015), which is about 47 min from the settlement of Colle Colanero. The cave has not been further investigated, but it is likely that it previously? served as a ritual or burial place, like the majority of central Italian caves. A partly similar situation, based on Sr and O isotope analyses, has been proposed for the EBA necropolis of Sant'Eurosia (Cavazzuti et al., 2019) in the Po Plain, where the dispersed isotope ratios indicate that the buried people were rather mobile and their provenance had to be placed in a hinterland of about 20–50 km radius, which in a flat terrain equals 4–10 h of walking-time. In this

case, the necropolis was used for a much shorter time, but it still worked as a "persistent place" in the settlement pattern.

6. Conclusions

We hereby synthetize the outcomes of a novel investigation method comprehensive of geomatic, structural geology, palaeontological, archaeologic and radiometric data applied to solve the morphostructural evolution of a cave in an area with unconstrained Quaternary evidence. This method enabled us to recognize:

- a step-like shape of the cave that is associated with normal faults with similar orientation also occurring in the surroundings;
- Late Pleistocene (32,930-30,6744 calBC) hyena and bear bones, which were partially to fully embedded in concretions near the wall of a major fault marking the onset of syn-sedimentary faulting in the cave;
- syn-sedimentary pockets generated within small step-like metric-scaled basins preserving rich archaeological finds belonging to the Copper Age (CA, 3300-2000 calBC) and the Early and Middle Bronze Age (EBA-MBA, 1900-1200 calBC);
- Middle Bronze Age to Medieval collapse of blocks and concretions occurring at approaching fault zones.

In our interpretation, the CA deposits progressively infill rooms, while the concretioned collapse covering the MBA hearth is evidence of crack-and-seal processes along a secondary fault zone of a segmented major normal fault of the Volsci Range with cumulative subsurface rupture length reaching up to 10–12 km and displacement in the order of 0.8–1 km, which could possibly be capable of generating an earthquake of magnitude M_w comprised between 5.1 and 5.8 depending on the fault segmentation. The structural evidence is relevant for understanding the speleogenesis from the Late Pleistocene and the human occupation of the cave.

The archaeological evidence suggests that in the area:

- the boundary between the Protoappenninico and Grotta Nuova facies might be placed along the Amaseno valley;
- The long-lasting process of stylistic melting between Protoappenninico and Grotta Nuova facies starts in the MBA1B;
- The cave was used as a burial place from CA to MBA 1–2 and possibly to perform ritual activities in the MBA 1–2;
- In the MBA, the cave acted as a "persistent place" within a developing settlement pattern.

Overall, these results set the timing of faulting and thus represent the first neotectonic evolution ever documented in the internal Central Apennines nearby Rome. The outcome is of regional relevance as Late Pleistocene to Holocene/Anthropocene neotectonics were poorly constrained by the structural studies of the Tyrrhenian coast of Latium, due to the rarity of outcrops of syntectonic rocks and possibly to a less active seismic context. As a result, the La Sassa findings provide temporal constraints to the recent regional tectonic evolution. This study sets the ground for further seismic hazard assessment in a region inhabited by about 0.4 million people.

The specific attention for post-depositional processes improved our understanding of the interplay between geological processes and human use of the cave and allow us to put forward some hypotheses on the local to regional development of the human landscape. We believe that the methodology adopted in this study has the potential to unveil (pre)historical processes and to constrain neotectonic evolution also in similar contexts worldwide.

Author contributions

L.A. and G.L.C. were involved equally in designing the study, acquiring and analysing the data, writing the manuscript and preparing figures. L.A. and M.G. contributed to fund acquisition. V.B., S.D.P., F.D.C., F.M., M.O., S.T., designed, executed and processed the network necessary for the geodetic framing of the 3d model. They have also carried out the surveys and calculations necessary for the realisation of the model. A.F., M.G., M.F.R. studied the palaeontological remains. P. AJ.A. and G.S. reviewed all the manuscript. All authors contributed substantially to drafts and gave approval for publication.

Data and materials availability

All data needed to evaluate the conclusions in the paper are present in the paper and the Supplementary Materials. The finds from La Sassa cave are stored in the Archaeology Laboratory of the University of Tor Vergata, Department of History, Culture and Society (Rome, Italy).

Appendix A. Supplementary data

Supplementary data to this article can be found online at https://doi.org/10.1016/j.quascirev.2021.107067.

References

Accordi, B., Segre, A.O., Cocozza, T., Angelucci, A., Sirna, G., Farinacci, A., 1966. Sheet 159 Frosinone of the Geological Map of Italy at L:100'000, second ed. Servizio Geologico d' Italia, Roma.

Agostini, S., Forti, P., 1982. Indagine sismotettonica dell'area carsica a Sud Est di Latina (M. Ausoni e M. Ernici) con metodi speleologici - contributi alla realizzazione della Carta Neotettonica d'Italia. Progetto Finalizzato Geodinamica pubb 513 (CNR).

Alessandri, L., 2013. Latium Vetus in the Bronze Age and Early Iron Age/Il Latium Vetus nell'età del Bronzo e nella prima età del Ferro. BAR Int. Ser. 2565 (Oxford).

Alessandri, L., 2019. The early and Middle Bronze Age (1/2) in South and central Tyrrhenian Italy and their connections with the Avellino eruption: an overview. Quat. Int. 499, 161–185. https://doi.org/10.1016/j.quaint.2018.08.002.

Alessandri, L., Rolfo, M.F., 2015. L'utilizzo delle cavità naturali nella media età del Bronzo: nuovi dati dal Lazio meridionale. Boll. Unione Stor. e Arte 10, 109–126.

Alessandri, L., Achino, K.F., Gatta, M., Rolfo, M.F., Silvestri, L., 2018. Grotta La Sassa

(Sonnino). Poster presented at: siti chiave tra antico e inizi medio Bronzo nel Lazio e in Campania. Nuovi dati e nuove date, 28.6.2018, Naples (Italy).

Alessandri, L., Achino, K.F., Attema, P.A.J., de Novaes Nascimento, M., Gatta, M., Rolfo, M.F., Sevink, J., Sottili, G., van Gorp, W., 2019. Salt or fish (or salted fish)? The Bronze Age specialised sites along the Tyrrhenian coast of Central Italy: new insights from Caprolace settlement. PLoS One 14.

Alessandri, L., Baiocchi, V., Del Pizzo, S., Di Ciaccio, F., Onori, M., Rolfo, M.F., Troisi, S., 2020. A flexible and swift approach for 3D image–based survey in a cave. Appl. Geomatics. https://doi.org/10.1007/s12518-020-00309-4.

Allen, J.R.M., Watts, W.A., Huntley, B., 2000. Weichselian palynostratigraphy, palaeovegetation and palaeoenvironment; the record from Lago Grande di Monticchio, southern Italy. Quat. Int. 73–74, 91–110. https://doi.org/10.1016/S1040-6182(00)00067-7.

Anastasia, C., 2007. L'evoluzione dell'insediamento nelle valli dell'Amaseno e dell'Ufente nell'età del Bronzo e del Ferro. In: Atti Della XL Riunione Scientifica Dell'Istituto Italiano Di Preistoria e Protostoria, Strategie Di Insediamento Fra Lazio e Campania in Età Preistorica e Protostorica, pp. 877–881.

Angelucci, A., 1966. La serie miocenica della Media Valle Latina. Geol. Rom. 5, 425–452.

Angle, M., Catracchia, F., Cavazzuti, C., Celletti, P., Malorgio, M., Mancini, D., 2010. La grotta Regina Margherita a collepardo (Frosinone). Lazio e Sabina 6, 381–393.

Angle, M., Rolfo, M.F., Fusco, I., Silvestri, L., 2014. New investigations at the cave of Pastena (Frosinone). Report 2012. Lazio e Sabina 10, 205–211.

Antonellini, M., Nannoni, A., Vigna, B., De Waele, J., 2019. Structural control on karst water circulation and speleogenesis in a lithological contact zone: the Bossea cave system (Western Alps, Italy). Geomorphology 345, 106832. https://doi.org/10.1016/j.geomorph.2019.07.019.

Attema, P.A.J., Alessandri, L., Bakels, C., Doorenbosch, M., Field, M., Van Gorp, W., De Haas, T., Van Leusen, M., Tol, G.W., Sevink, J., 2019. Vecchie e nuove ricerche multidisciplinari nel territorio di Sezze e nelle zone adiacenti (Agro Pontino, Lazio). IpoTESI di Preist 11, 103–118. https://doi.org/10.6092/issn.1974-7985/9902.

Barberio, D., Gori, F., Barbieri, M., Boschetti, T., Caracausi, A., Cardello, G.L., Petitta, M., 2021. Understanding origin and mixing of deep fluids in shallow aquifers and possible implications for crustal deformation studies: san Vittorino Plain. Central Appennines Appl. Sci.

Basili, R., Valensise, G., Vannoli, P., Burrato, P., Fracassi, U., Mariano, S., Tiberti, M.M., Boschi, E., 2008. The Database of Individual Seismogenic Sources (DISS), version 3: summarizing 20 years of research on Italy's earthquake geology. Tectonophysics 453, 20–43. https://doi.org/10.1016/j.tecto.2007.04.014.

Bense, V.F., Gleeson, T., Loveless, S.E., Bour, O., Scibek, J., 2013. Fault zone hydrogeology. Earth Sci. Rev. 127, 171–192.

Bernard, P., Zollo, A., 1989. The Irpinia (Italy) 1980 earthquake: detailed analysis of a complex normal faulting. J. Geophys. Res.: Solid Earth 94 (B2), 1631–1647.

Bini, M., Zanchetta, G., Drysdale, R.N., Giaccio, B., Stocchi, P., Vacchi, M., Hellstrom, J.C., Couchoud, I., Monaco, L., Ratti, A., Martini, F., Sarti, L., 2020. An end to the last interglacial highstand before 120 ka: relative sea-level evidence from infreschi cave (southern Italy). Quat. Sci. Rev. 250, 106658. https://doi.org/10.1016/j.quascirev.2020.106658.

Bintliff, J.L., 1999. The origins and nature of the Greek city-state and its significance for World settlement history. In: Actes de La Table Ronde Internationale Organisée Par Le Centre Jean Bérard et l'Ecole Française de Rome Naples, pp. 27–29. Octobre 1994.

Bintliff, J.L., 2009. Catchments, settlement chambers and demography: case studies and general theory in the Greek landscape from Prehistory to Early Modern times. In: Favory, F., Nuninger, L. (Eds.), pp. 107–117.

Blanc, A.C., 1935. Stratigrafia del canale Mussolini nell'Agro Pontino. Atti della Soc. Toscana di Sci. Nat. Process. Verbali 44, 52–56.

Blanc, A.C., 1954. Resti fossili neandertaliani nella Grotta del Fossellone al Monte Circeo: Circeo IV. Quaternaria 1, 171–175.

Blanc, A.C., Segre, A., 1953. Excursion au mont Circé. In: IV Congrés International, Guide INQUA (International Union for Quaternary).

Boni, C., Bono, P., Calderoni, G., Lombardi, S., Turi, B., 1980. Indagine idrogeologica e geochimica sui rapporti tra ciclo carsico e circuito idrotermale nella Pianura Pontina. Geol. Appl. Idrogeol. 15, 204–247.

Bordoni, P., Valensise, G., 1999. Deformation of the 125 ka marine terrace in Italy: tectonic implications. Geol. Soc. London, Spec. Publ. 146, 71–110.

Boschin, F., Columbu, A., Spagnolo, V., Crezzini, J., Bahain, J.J., FalguèRes, C., Benazzi, S., Boscato, P., Ronchitelli, A., Moroni, A., Martini, I., 2021. Human occupation continuity in southern Italy towards the end of the Middle Palaeolithic: a palaeoenvironmental perspective from Apulia. J. Quat. Sci. https://doi.org/10.1002/jqs.3319.

Bradley, R., 2005. Ritual and Domestic Life in Prehistoric Europe. Routledge, London.

Brock, F., Higham, T., Ditchfield, P., Ramsey, C.B., 2010. Current pretreatment methods for AMS radiocarbon dating at the oxford radiocarbon accelerator unit (orau). Radiocarbon 52, 103–112. https://doi.org/10.1017/S0033822200045069.

Brück, J., 1999. Ritual and rationality: some problems of interpretation in European archaeology. Eur. J. Archaeol. 2, 313–344.

Bruzek, J., 2002. A method for visual determination of sex, using the human hip bone. Am. J. Phys. Anthropol. 117, 157–168. https://doi.org/10.1002/ajpa.10012.

Caine, J.S., Evans, J.P., Forster, C.B., 1996. Fault zone architecture and permeability structure. Geology 24, 1025–1028. https://doi.org/10.1130/0091-7613(1996)024<1025:FZAAPS>2.3.CO;2.

Calcagnile, L., Maruccio, L., Scrimieri, L., delle Side, D., Braione, E., D'Elia, M., Quarta, G., 2019. Development and application of facilities at the centre for applied physics, dating and diagnostics (CEDAD) at the university of Salento during the last 15 years. Nucl. Instrum. Methods Phys. Res. Sect. B Beam Interact. Mater. Atoms 456, 252–256. https://doi.org/10.1016/j.nimb.2019.03.031.

Cancellieri, M., 1986. Le vie d'acqua dell'area pontina. Archeol. Laz VII, 143–156.

Carboni, G., 2002. Territorio aperto o di frontiera? Nuove prospettive di ricerca per lo studio della distribuzione spaziale delle facies del Gaudo e di Rinaldone nel Lazio centro-meridionale. Origini XXIV 235–299.

Carboni, G., 2019. "Territorio Aperto o di Frontiera?" quindici anni dopo. Conferme e nuove evidenze dell'età del Rame nel Lazio centro-meridionale. IpoTESI di Preist 11. https://doi.org/10.6092/issn.1974-7985/9899.

Cardello, G.L., Doglioni, C., 2015. From mesozoic rifting to apennine orogeny: the gran sasso range (Italy). Gondwana Res. 27, 1307–1334. https://doi.org/10.1016/j.gr.2014.09.009.

Cardello, G.L., Mancktelow, N.S., 2014. Cretaceous syn-sedimentary faulting in the wildhorn nappe (SW Switzerland). Swiss J. Geosci. 107, 223–250. https://doi.org/10.1007/s00015-014-0166-8.

Cardello, G.L., Mancktelow, N.S., 2015. Veining and post-nappe transtensional faulting in the SW Helvetic Alps (Switzerland). Swiss J. Geosci. 108, 379–400. https://doi.org/10.1007/s00015-015-0199-7.

Cardello, G.L., Tesei, T., 2013. Transtensive faulting in carbonates at different crustal levels: examples from SW Helvetics and Central Apennines. Rendiconti online della Società Geologica Italiana 29, 20–23. https://doi.org/10.3301/GFT.2016.04. Socgeol.net.

Cardello, G.L., Di Vincenzo, G., Giorgetti, G., Zwingmann, H., Mancktelow, N., 2019. Initiation and development of the Pennine Basal Thrust (Swiss Alps): a structural and geochronological study of an exhumed megathrust. J. Struct. Geol. 126, 338–356. https://doi.org/10.1016/j.jsg.2019.06.014.

Cardello, G.L., Consorti, L., Palladino, D.M., Carminati, E., Carlini, M., Doglioni, C., 2020. Tectonically controlled carbonate-seated maar-diatreme volcanoes: the case of the Volsci Volcanic Field, central Italy. J. Geodyn. 139, 101763. https://doi.org/10.1016/j.jog.2020.101763.

Cardello, G.L., Vico, G., Consorti, L., Sabbatino, M., Carminati, E., Doglioni, C., 2021. Constraining the passive to active margin tectonics of the internal central Apennines: insights from biostratigraphy, structural, and seismic analysis. Geosciences 11 (4), 160. https://doi.org/10.3390/geosciences11040160.

Carminati, E., Lustrino, M., Doglioni, C., 2012. Geodynamic evolution of the central and western Mediterranean: tectonics vs. igneous petrology constraints. Tectonophysics 579, 173–192. https://doi.org/10.1016/j.tecto.2012.01.026.

Casini, L., Andreucci, S., Sechi, D., Huang, C.-Y., Shen, C.-C., Pascucci, V., 2020. Luminescence dating of Late Pleistocene faults as evidence of uplift and active tectonics in Sardinia, W Mediterranean. Terra. Nova 32, 261–271. https://doi.org/10.1111/ter.12458.

Castagnino Berlinghieri, E.F., Antonioli, F., Bailey, G., 2020. Italy: the archaeology of palaeoshorelines, coastal caves and seafaring connections. In: Bailey, G., Galanidou, N., Peeters, H., Jöns, H., Mennenga, M. (Eds.), The Archaeology of Europe's Drowned Landscapes. Springer International Publishing, Cham, pp. 321–340. https://doi.org/10.1007/978-3-030-37367-2_16.

Cavazzuti, C., Skeates, R., Millard, A.R., Nowell, G., Peterkin, J., Bernabò Brea, M., Cardarelli, A., Salzani, L., 2019. Flows of people in villages and large centres in Bronze Age Italy through strontium and oxygen isotopes. PLoS One 14, e0209693.

Cazarin, C.L., Bezerra, F.H.R., Borghi, L., Santos, R.V., Favoreto, J., Brod, J.A., Auler, A.S., Srivastava, N.K., 2019. The conduit-seal system of hypogene karst in Neoproterozoic carbonates in northeastern Brazil. Mar. Petrol. Geol. 101, 90–107. https://doi.org/10.1016/j.marpetgeo.2018.11.046.

Cazzella, A., Guidi, A., 2016. Aspetti simbolici connessi con le grotte nell'Italia centro-meridionale dal Neolitico alla prima età del ferro. Quad. di Stud. e Mater. di Stor. delle Relig. supp. 82, 47–63.

Centamore, E., Di Manna, P., Rossi, D., 2007. Kinematic evolution of the Volsci Range: a new overview. Boll. della Soc. Geol. Ital. 126, 159–172.

Centamore, E., Dramis, F., Di Manna, P., Fumanti, F., M, S., Rossi, D., Palombo, M.R., Palladino, D.M., Trigila, R., Zanon, V., Chiocchini, M., Didaskalou, P., Potetti, M., Nisio, S., 2010. Note illustrative del Foglio 402 Ceccano. Carta Geologica d'Italia 1:50.000. Servizio Geologico d'Italia (Firenze).

Chiarabba, C., Amato, A., Anselmi, M., Baccheschi, P., Bianchi, I., Cattaneo, M., Cecere, G., Chiaraluce, L., Ciaccio, M.G., De Gori, P., De Luca, GI, Di Bona, M., Di Stefano, R., Faenza, L., Govoni, A., Improta, L., Lucente, F.P., Marchetti, A., Margheriti, L., Mele, F., Michelini, A., Monachesi, G., Moretti, M., Pastori, M., Piana Agostinetti, N., Piccinini, D., Roselli, P., Seccia, D., Valoroso, L., 2009. The 2009 L'Aquila (central Italy) MW6. 3 earthquake: main shock and aftershocks. Geophys. Res. Lett. 36 (18) https://doi.org/10.1029/2009GL039627.

Clemenzi, L., Storti, F., Balsamo, F., Molli, G., Ellam, R., Muchez, P., Swennen, R., 2015. Fluid pressure cycles, variations in permeability, and weakening mechanisms along low-angle normal faults: the Tellaro detachment, Italy. GSA Bulletin 127 (11–12), 1689–1710.

Cocchi Genick, D., 1995. La facies di Grotta Nuova. In: Cocchi Genick, D. (Ed.), Aspetti Culturali Della Media Età Del Bronzo in Italia Centro-Meriidonale, pp. 364–397.

Cocchi Genick, D., 1998. L'antica età del Bronzo nell'Italia centrale. Profilo di un'epoca e di un'appropriata strategia metodologica (Firenze).

Cocchi Genick, D., 2002. Grotta Nuova : la prima unità culturale attorno all'Etruria protostorica. M. Baroni, Viareggio Lucca [Italy].

Consorti, L., Frijia, G., Caus, E., 2017. Rotaloidean foraminifera from the Upper Cretaceous carbonates of Central and Southern Italy and their chronostratigraphic age. Cretac. Res. 70, 226–243. https://doi.org/10.1016/

j.cretres.2016.11.004.

Cosentino, D., Cipollari, P., Di Donato, V., Sgrosso, I., 2002. The Volsci Range in the kinematic evolution of the northen and southern Apennine orogenetic system. Ital. J. Geosci. Volume spe 209–218.

Cuffaro, M., Martorelli, E., Bosman, A., Conti, A., Bigi, S., Muccini, F., Cocchi, L., Ligi, M., Bortoluzzi, G., Scrocca, D., Canese, S., Chiocci, F.L., Conte, A.M., Doglioni, C., Perinelli, C., 2016. The ventotene volcanic ridge: a newly explored complex in the central Tyrrhenian Sea (Italy). Bull. Volcanol. 78, 86. https://doi.org/10.1007/s00445-016-1081-9.

Curzi, M., Billi, A., Carminati, E., Rossetti, F., Albert, R., Aldega, L., Cardello, G.L., Conti, A., Gerdes, A., Smeraglia, L., Van der Lelij, R., Vignaroli, G., Viola, G., 2020. Disproving the presence of Paleozoic-Triassic metamorphic rocks on the Island of Zannone (central Italy): implications for the early stages of the Tyrrhenian-Apennines tectonic evolution. Tectonics N/a, e2020TC006296. https://doi.org/10.1029/2020TC006296.

Dal Zilio, L., van Dinther, Y., Gerya, T.V., Pranger, C.C., 2018. Seismic behaviour of mountain belts controlled by plate convergence rate. Earth Planet Sci. Lett. 482, 81–92.

Damiani, I., 1995. La facies protoappenninica. In: Cocchi Genick, D. (Ed.), Aspetti Culturali Della Media Età Del Bronzo in Italia Centro-Meridionale, pp. 398–428.

Davies, W., 1988. Small Worlds: the Village Community in Early Medieval Brittany. University of California Press, Berkeley.

Dee, M.W., Palstra, S.W.L., Aerts-Bijma, A.T., Bleeker, M.O., de Bruijn, S., Ghebru, F., Jansen, H.G., Kuitems, M., Paul, D., Richie, R.R., Spriensma, J.J., Scifo, A., van Zonneveld, D., Verstappen-Dumoulin, B.M.A.A., Wietzes-Land, P., Meijer, H.A.J., 2019. Radiocarbon dating at groningen: new and updated chemical pretreatment procedures. Radiocarbon 62, 63–74. https://doi.org/10.1017/RDC.2019.101.

Delchiaro, M., Fioramonti, V., Della Seta, M., Cavinato, G.P., Mattei, M., 2020. Fluvial inverse modelling for inferring the timing of Quaternary uplift in the Simbruini range (Central Apennines, Italy). In: Massimiliano, A., Marchesini, I., Melelli, L., Guth, P. (Eds.), Proceedings of the Geomorphometry 2020 Conference. https://doi.org/10.30437/GEOMORPHOMETRY2020_58.

Dennel, R.W., Webley, D., 1975. In: Higgs, E.S. (Ed.), Prehistoric Settlement and Land Use in Southern Bulgaria, Palaeoeconomy. Cambridge University Press, Cambridge, pp. 97–109. https://doi.org/10.1017/S0079497X00011026.

Di Domenica, A., Pizzi, A., 2017. Defining a mid-Holocene earthquake through speleoseismological and independent data: implications for the outer Central Apennines (Italy) seismotectonic framework. Solid Earth 8, 161–176. https://doi.org/10.5194/se-8-161-2017.

Doglioni, C., Barba, S., Carminati, E., Riguzzi, F., 2015. Fault on-off versus strain rate and earthquakes energy. Geosci. Front. 6 (2), 265–276.

Drechsler-Bizic, R., 1980. Bronze age necropolis in the cave Bezdanjaca near Vrhovine. Bull. Arch. Museum Zagreb 3/XIII-XII, 27–28.

Dunbar, R.I.M., 1996. Grooming, Gossip, and the Evolution of Language. Faber and Faber Limited.

Ekmekçì, M., 2003. Review of Turkish karst with special emphasis on tectonic and climatic controls. Acta Carsol. 32, 205–218.

Ekmekçì, M., 2005. Karst in Turkish thrace: compatibility between geological history and karst type. Turk. J. Earth Sci.

Ellison, A., Harriss, J., 1974. Settlement and land use in the prehistory and early history of southern England: a study based on locational models. In: Clarke, D.L. (Ed.), Models in Archaeology. Methuen, London, pp. 911–962.

Ennes-Silva, R.A., Bezerra, F.H.R., Nogueira, F.C.C., Balsamo, F., Klimchouk, A., Cazarin, C.L., Auler, A.S., 2016. Superposed folding and associated fracturing influence hypogene karst development in Neoproterozoic carbonates, São Francisco Craton, Brazil. Tectonophysics 666, 244–259. https://doi.org/10.1016/j.tecto.2015.11.006.

Falcucci, E., Gori, S., Galadini, F., Fubelli, G., Moro, M., Saroli, M., 2016. Active faults in the epicentral and mesoseismal MI 6.0 24, 2016 Amatrice earthquake region, central Italy. Methodological and seismotectonic issues. Ann. Geophys. 59.

Farina, S., 2011. Late pleistocene-holocene mammals from "canale delle Acque Alte (canale mussolini)" (agro pontino, Latium). Boll. della Soc. Paleontol. Ital. 50, 11–22.

Faure Walker, J., Boncio, P., Pace, B., Roberts, G., Benedetti, L., Scotti, O., Visini, F., Peruzza, L., 2020. Fault2SHA Central Apennines Database. Institute for Risk and Disaster Reduction. PANGAEA. https://doi.org/10.1594/PANGAEA.922582.

Ferranti, L., Antonioli, F., Mauz, B., Amorosi, A., Dai Pra, G., Mastronuzzi, G., Monaco, C., Orrù, P., Pappalardo, M., Radtke, U., Renda, P., Romano, P., Sansò, P., Verrubbi, V., 2006. Markers of the last interglacial sea-level high stand along the coast of Italy: tectonic implications. Quat. Int. 145–146, 30–54. https://doi.org/10.1016/j.quaint.2005.07.009.

Ferranti, L., Pace, B., Vasta, M., Colella, A., Ramondini, M., Calcaterra, D., Di Bianco, S., Valentini, A., De Massis, J., Teodoro, P., Berardi, D., La Rocca, N., 2015. Evaluation of the seismogenic potential in key areas of the central and southern Apennines through analysis of speleothem vulnerability. In: 6th International INQUA Meeting on Paleoseismology, Active Tectonics and Archaeoseismology.

Fiorillo, A., 2016. Il rapporto uomo-orso nelle grotte italiane del tardo Pleistocene. Università degli Studi di Roma Tor Vergata.

Flannery, K.V., 1976. The Early Mesoamerican Village. Academic Press, New York.

Forge, A., 1972. Normative factors in the settlement size of neolithic cultivators (New Guinea). In: Ucko, P.J., Dimbleby, G.W., Tringham, R. (Eds.), Man, Settlement and Urbanism (London).

Forti, P., Postpischl, D., 1984. Seismotectonic and paleoseismic analyses using karst sediments. Mar. Geol. 55, 145–161. https://doi.org/10.1016/0025-3227(84)90138-5.

Frepoli, A., Cimini, G.B., De Gori, P., De Luca, G., Marchetti, A., Monna, S., Montuori, C., Pagliuca, N.M., 2017. Seismic sequences and swarms in the Latium-Abruzzo-Molise Apennines (central Italy): new observations and analysis from a dense monitoring of the recent activity. Tectonophysics 712–713, 312–329. https://doi.org/10.1016/j.tecto.2017.05.026.

Fukasawa, K., Akasaka, T., 2019. Long-lasting effects of historical land use on the current distribution of mammals revealed by ecological and archaeological patterns. Sci. Rep. 9, 10697. https://doi.org/10.1038/s41598-019-46809-1.

Galadini, F., Galli, P., 2000. Active tectonics in the central Apennines (Italy) − input data for seismic hazard assessment. Nat. Hazards 22, 225–268. https://doi.org/10.1023/A:1008149531980.

Galadini, F., Messina, P., 2004. Early−middle Pleistocene eastward migration of the abruzzi apennine (central Italy) extensional domain. J. Geodyn. 37 (1), 57–81.

Galli, P., 2020. Recurrence times of central-southern Apennine faults (Italy): hints from palaeoseismology. Terra. Nova. https://doi.org/10.1111/ter.12470 n/a.

Gatta, M., Rolfo, M.F., 2017. Cava Muracci: a new middle-upper palaeolithic site in west-central Italy. Mediterr. Archaeol. Archaeom. 17, 105–116. https://doi.org/10.5281/zenodo.581729.

Gatta, M., Sinopoli, G., Giardini, M., Giaccio, B., Hajdas, I., Pandolfi, L., Bailey, G., Spikins, P., Rolfo, M.F., Sadori, L., 2016. Pollen from Late Pleistocene hyena (Crocuta crocuta spelaea) coprolites: an interdisciplinary approach from two Italian sites. Rev. Palaeobot. Palynol. 233, 56–66. https://doi.org/10.1016/j.revpalbo.2016.07.005.

Gatta, M., Kotsakis, T., Pandolfi, L., Petronio, C., Salari, L., Achino, K.F., Silvestri, L., Rolfo, M.F., 2019. The late Pleistocene faunal assemblage from Cava Muracci (Latium, Italy): palaeoenvironmental implications for coastal central Italy during MIS 3. Comptes Rendus Palevol 18, 51–71. https://doi.org/10.1016/j.crpv.2018.04.006.

Goeppert, N., Goldscheider, N., Scholz, H., 2011. Karst geomorphology of carbonatic conglomerates in the folded molasse zone of the northern Alps (Austria/Germany). Geomorphology 130, 289–298. https://doi.org/10.1016/j.geomorph.2011.04.011.

Goldscheider, N., 2005. Fold structure and underground drainage pattern in the alpine karst system Hochifen-Gottesacker. Eclogae Geol. Helv. 98, 1–17. https://doi.org/10.1007/s00015-005-1143-z.

Gomez de Soto, J., 1973. La grotte sépulcrale des Duffaits (La Rochette, Charente). Bull. la Société Préhistorique Française 70, 401–444.

Guidi, A., 1992. Recenti ritrovamenti in grotta nel Lazio: un riesame critico del problema dell'utilizzazione delle cavità naturali. Rass. di Archeol. X, 427–437.

Guidi, A., Rosini, L., 2019. Materiali protostorici dalla grotta Vittorio Vecchi (sezze romano, LT), 2919. BAR International Series, Oxford.

Religion and ritual. In: Harding, A.F. (Ed.), 2000. European Societies in the Bronze Age, Cambridge World Archaeology. Cambridge University Press, Cambridge, pp. 308–351. https://doi.org/10.1017/CBO9780511605901.010.

Heidinga, H.A., 1987. Medieval settlement and economy north of the lower rhine. In: Archaeology and History of Kootwijk and the Veluwe (the Netherlands). Van Gorcum, Assen-Maastricht.

Higham, T.F.G., Jacobi, R.M., Ramsey, C.B., 2006. AMS radiocarbon dating of ancient bone using ultrafiltration. Radiocarbon 48, 179–195. https://doi.org/10.1017/S0033822200066388.

Houdaille, J., Acsadi, G., Nemeskeri, J., 1972. History of human life span and mortality. Ann. Demogr. Hist., Paris, pp. 377–379.

Hughes, P.D., Woodward, J.C., 2008. Timing of glaciation in the Mediterranean mountains during the last cold stage. J. Quat. Sci. 23, 575–588. https://doi.org/10.1002/jqs.1212.

İşcan, Y., 1985. Osteometric analysis of sexual dimorphism in the sternal end of the rib. J. Forensic Sci. 30, 1090–1099. https://doi.org/10.1520/JFS11050J.

Karner, D.B., Marra, F., Florindo, F., Boschi, E., 2001. Pulsed uplift estimated from terrace elevations in the coast of Rome: evidence for a new phase of volcanic activity? Earth Planet Sci. Lett. 188, 135–148.

Klimchouk, A., Ford, D., 2000. Lithologic and structural controls of dissolutional cave development. In: Klimchouk, A., Ford, D.C., Palmer, A.N., Dreybrodt, W. (Eds.), Speleogenesis. Evolution of Karst Aquifers. National Speleological Society, pp. 54–64.

Klimchouk, A., Tymokhina, E., Amelichev, G., 2012. Speleogenetic effects of interaction between deeply derived fracture-conduit flow and intrastratal matrix flow in hypogene karst settings. Int. J. Speleol. 41, 161–179. https://doi.org/10.5038/1827-806X.41.2.4.

Klimchouk, A., Auler, A.S., Bezerra, F.H.R., Cazarin, C.L., Balsamo, F., Dublyansky, Y., 2016. Hypogenic origin, geologic controls and functional organization of a giant cave system in Precambrian carbonates, Brazil. Geomorphology 253, 385–405. https://doi.org/10.1016/j.geomorph.2015.11.002.

Langmuir, E., 1984. Mountaincraft and Leadership. The Scottish Sports Council/MLTB, Cordee, Leicester.

Lewin, R., 1992. Complexity. Life at the Edge of Chaos. Macmillan Pub. Co., New York.

Locati, M., Camassi, R., Rovida, A., Ercolani, E., Bernardini, F., Castelli, V., Caracciolo, C.H., Tertulliani, A., Rossi, A., Azzaro, R., D'Amico, S., Antonucci, A., 2021. Database Macrosismico Italiano (DBMI15), Versione 3.0. Istituto Nazionale di Geofisica e Vulcanologia (INGV). https://doi.org/10.13127/DBMI/DBMI15.3.

Lovejoy, C.O., Meindl, R.S., Pryzbeck, T.R., Mensforth, R.P., 1985. Chronological metamorphosis of the auricular surface of the ilium: a new method for the determination of adult skeletal age at death. Am. J. Phys. Anthropol. 68, 15–28. https://doi.org/10.1002/ajpa.1330680103.

Macchiarola, I., 1995. La facies appenninica. In: Cocchi Genick, D. (Ed.), Aspetti

Culturali Della Media Età Del Bronzo in Italia Centro-Meridionale, pp. 441–463.

Marra, F., Florindo, F., Anzidei, M., Sepe, V., 2016. Paleo-surfaces of glacio-eustatically forced aggradational successions in the coastal area of Rome: assessing interplay between tectonics and sea-level during the last ten interglacials. Quat. Sci. Rev. 148, 85–100. https://doi.org/10.1016/j.quascirev.2016.07.003.

Marra, F., Gaeta, M., Jicha, B.R., Nicosia, C., Tolomei, C., Ceruleo, P., Florindo, F., Gatta, M., La Rosa, M., Rolfo, M.F., 2019a. MIS 9 to MIS 5 terraces along the Tyrrhenian Sea coast of Latium (central Italy): assessing interplay between sea-level oscillations and tectonic movements. Geomorphology 346, 106843. https://doi.org/10.1016/j.geomorph.2019.106843.

Marra, F., Bahain, J.-J., Jicha, B.R., Nomade, S., Palladino, D.M., Pereira, A., Tolomei, C., Voinchet, P., Anzidei, M., Aureli, D., Ceruleo, P., Falguères, C., Florindo, F., Gatta, M., Ghaleb, B., La Rosa, M., Peretto, C., Petronio, C., Rocca, R., Rolfo, M.F., Salari, L., Smedile, A., Tombret, O., 2019b. Reconstruction of the MIS 5.5, 5.3 and 5.1 coastal terraces in Latium (central Italy): a re-evaluation of the sea-level history in the Mediterranean Sea during the last interglacial. Quat. Int. 525, 54–77. https://doi.org/10.1016/j.quaint.2019.09.001.

Marra, F., Rolfo, F.M., Gaeta, M., Florindo, F., 2020. Anomalous last interglacial Tyrrhenian Sea levels and neanderthal settling at Guattari and moscerini caves (central Italy). Sci. Rep. 10, 11929. https://doi.org/10.1038/s41598-020-68604-z.

Marra, F., Cardello, G.L., Gaeta, M., Jicha, B.R., Montone, P., Niespolo, E.M., Nomade, S., Palladino, D.M., Pereira, A., De Luca, G., Florindo, F., Frepoli, A., Renne, P.R., Sottili, G., 2021. The Volsci Volcanic Field (central Italy): eruptive history, magma system and implications on continental subduction processes. Int. J. Earth Sci. https://doi.org/10.1007/s00531-021-01981-6.

Meindl, R.S., Lovejoy, C.O., Mensforth, R.P., Walker, R.A., 1985. A revised method of age determination using the os pubis, with a review and tests of accuracy of other current methods of pubic symphyseal aging. Am. J. Phys. Anthropol. 68, 29–45. https://doi.org/10.1002/ajpa.1330680104.

Menant, A., Angiboust, S., Gerya, T., 2019. Stress-driven fluid flow controls long-term megathrust strength and deep accretionary dynamics. Sci. Rep. 9 (1), 1–11.

Milia, A., Torrente, M.M., 2015. Tectono-stratigraphic signature of a rapid multistage subsiding rift basin in the Tyrrhenian-Apennine hinge zone (Italy): a possible interaction of upper plate with subducting slab. J. Geodyn. 86, 42–60. https://doi.org/10.1016/j.jog.2015.02.005.

Miller, T.E., 1996. Geologic and hydrologic controls on karst and cave development in Belize. J. Cave Karst Stud. 58, 100–120.

Montone, P., Mariucci, M.T., 2016. The new release of the Italian contemporary stress map. Geophys. J. Int. 205 (3), 1525–1531. https://doi.org/10.1093/gji/ggw100.

Montone, P., Amato, A., Pondrelli, S., 1999. Active stress map of Italy. J. Geophys. Res.: Solid Earth 104 (B11), 25595–25610.

Mook, W.G., Streurman, H.J., 1983. Physical and chemical aspects of radiocarbon dating. PACT 8, 45–53.

Morley, C.K., Nelson, R.A., Patton, T.L., Munn, S.G., 1990. Transfer zones in the East African rift system and their relevance to hydrocarbon exploration in rifts. AAPG Bull. 74 (8), 1234–1253.

Naismith, W.W., 1892. Excursions. Cruach ardran, stobinian, and ben more. Scottish Mountain. Club J. 2, 136.

Orschiedt, J., 2012. Cave burials in prehistoric central Europe. In: Bergsvik, A.K., Skeates, R. (Eds.), Caves in Context. The Cultural Signifi Cance of Caves and Rockshelters in Europe. Oxbow books, pp. 212–224.

Ortner, H., Reiter, F., Acs, P., 2002. Easy handling of tectonic data: the programs TectonicVB for mac and TectonicsFP for Windows™. Comput. Geosci. 28, 1193–1200. https://doi.org/10.1016/S0098-3004(02)00038-9.

Pacciarelli, M., 2001. Dal villaggio alla città. La svolta protourbana del 1000 a.C. nell'Italia tirrenica (Firenze).

Pace, B., Valentini, A., Ferranti, L., Vasta, M., Vassallo, M., Montagna, P., Colella, A., Pons-Branchu, E., 2020. A large paleoearthquake in the central Apennines, Italy, recorded by the collapse of a cave speleothem. Tectonics 39. https://doi.org/10.1029/2020TC006289.

Pepe, M., Parise, M., 2014. Structural control on development of karst landscape in the Salento Peninsula (Apulia, SE Italy). Acta Carsol. 43 https://doi.org/10.3986/ac.v43i1.643.

Perfettini, H., Avouac, J.P., Tavera, H., Kositsky, A., Nocquet, J.M., Bondoux, F., Chlieh, M., Sladen, A., Audin, L., Farber, L.H., Soler, P., 2010. Seismic and aseismic slip on the Central Peru megathrust. Nature 465 (7294), 78.

Pèrles, C., 1999. In: Halstead, P. (Ed.), The Distribution of Magoules in Eastern Thessaly. Neolithic Society in Greece, pp. 42–56.

Petronio, C., Di Canzio, E., Salari, L., 2007. The Late Pleistocene and Holocene Mammals in Italy: new biochronological and paleoenvironmental data. Palaeontograph. Abteilung 279, 147–157. https://doi.org/10.1127/pala/279/2007/147.

Pisani, L., Antonellini, M., De Waele, J., 2019. Structural control on epigenic gypsum caves: evidences from Messinian evaporites (Northern Apennines, Italy). Geomorphology 332, 170–186. https://doi.org/10.1016/j.geomorph.2019.02.016.

Postpischl, D., Agostini, S., Forti, P., Quinif, Y., 1991. Palaeoseismicity from karst sediments: the "Grotta del Cervo" cave case study (Central Italy). Tectonophysics 193, 33–44. https://doi.org/10.1016/0040-1951(91)90186-V.

Pounds, N.J.G., 1974. An Economic History of Medieval Europe. Longman, London ; New York.

Rappaport, R.A., 1999. Ritual and Religion in the Making of Humanity. Cambridge University Press, Cambridge.

Rawling, G.C., Goodwin, L.B., Wilson, J.L., 2001. Internal architecture, permeability structure, and hydrologic significance of contrasting fault-zone types. Geology

29, 43–46. https://doi.org/10.1130/0091-7613(2001)029<0043:IAPSAH>2.0.CO;2.

Reimer, P.J., Bard, E., Bayliss, A., Beck, J.W., Blackwell, P.G., Bronk Ramsey, C., Buck, C.E., Cheng, H., Edwards, R.L., Friedrich, M., Grootes, P.M., Guilderson, T.P., Haflidason, H., Hajdas, I., Hatté, C., Heaton, T.J., Hoffmann, D.L., Hogg, A.G., Hughen, K.A., Kaiser, K.F., Kromer, B., Manning, S.W., Niu, M., Reimer, R.W., Richards, D.A., Scott, E.M., Southon, J.R., Staff, R.A., Turney, C.S.M., Van der Plicht, J., 2013. IntCal13 and Marine13 radiocarbon age calibration curves 0–50,000 years cal BP. Radiocarbon 55, 1869–1887.

Ricciardi, A.B., 2012. Utilizzazione delle cavità naturali dell'Italia centrale nell'età del Bronzo. Università degli Studi Roma Tre.

Rick, T.C., Sandweiss, D.H., 2020. Archaeology, climate, and global change in the Age of Humans. Proc. Natl. Acad. Sci. Unit. States Am. 117, 8250–8253. https://doi.org/10.1073/pnas.2003612117.

Roberts, G.P., Michetti, A.M., 2004. Spatial and temporal variations in growth rates along active normal fault systems: an example from the Lazio–Abruzzo Apennines, central Italy. J. Struct. Geol. 26, 339–376. https://doi.org/10.1016/S0191-8141(03)00103-2.

Rovida, A., Locati, M., Camassi, R., Lolli, B., Gasperini, P., 2020. The Italian earthquake catalogue CPTI15. Bull. Earthq. Eng. 18, 2953–2984. https://doi.org/10.1007/s10518-020-00818-y.

San Jose, M., Caves Rugenstein, J.K., Cosentino, D., Faccenna, C., Fellin, M.G., Ghinassi, M., Martini, I., 2020. Stable isotope evidence for rapid uplift of the central Apennines since the late Pliocene. Earth Planet Sci. Lett. 544, 116376. https://doi.org/10.1016/j.epsl.2020.116376.

Schlagenhauf, A., Manighetti, I., Benedetti, L., Gaudemer, Y., Finkel, R., Malavieille, J., Pou, K., 2011. Earthquake supercycles in Central Italy, inferred from 36Cl exposure dating. Earth Planet Sci. Lett. 307, 487–500. https://doi.org/10.1016/j.epsl.2011.05.022.

Serva, L., Brunamonte, F., 2007. Subsidence in the Pontina Plain. Italy. Bull. Eng. Geol. Environ. 66, 125–134. https://doi.org/10.1007/s10064-006-0057-y.

Sevink, J., van Gorp, W., Di Vito, M.A., Arienzo, I., 2020. Distal tephra from campanian eruptions in early late Holocene fills of the agro pontino graben and Fondi basin (southern Lazio, Italy). J. Volcanol. Geoth. Res. 107041 https://doi.org/10.1016/j.jvolgeores.2020.107041.

Shanov, S., Kostov, K., 2015. Dynamic Tectonics and Karst. Springer-Verlag Berlin Heidelberg. https://doi.org/10.1007/978-3-662-43992-0.

Silva, O.L., Bezerra, F.H.R., Maia, R.P., Cazarin, C.L., 2017. Karst landforms revealed at various scales using LiDAR and UAV in semi-arid Brazil: consideration on karstification processes and methodological constraints. Geomorphology 295, 611–630. https://doi.org/10.1016/j.geomorph.2017.07.025.

Silvestri, L., 2017. Caves and Human Lifeways in Middle Bronze Age Central Italy: a Social Bioarchaeology Approach. Durham University.

Silvestri, L., Rolfo, M.F., Angle, M., Skeates, R., Salari, L., 2018. Faunal remains and ritualisation: case studies from Bronze age caves in Central Italy. In: Livarda, A., Magdwick, R., Riera Mora, S. (Eds.), The Bioarchaeology of Ritual and Religion. Oxbow Books, Oxford, pp. 129–147.

Smith, F.A., Elliott Smith, R.E., Lyons, S.K., Payne, J.L., Villaseñor, A., 2019. The accelerating influence of humans on mammalian macroecological patterns over the late Quaternary. Quat. Sci. Rev. 211, 1–16. https://doi.org/10.1016/j.quascirev.2019.02.031.

Stafford, K., Mylroie, John, Taboroši, D., Jenson, J., Mylroie, Joan, 2005. Karst development on tinian, commonwealth of the Northern Mariana Islands: controls on dissolution in relation to the carbonate island karst model. J. Cave Karst Stud. 67, 14–27.

Stephens, L., Fuller, D., Boivin, N., Rick, T., Gauthier, N., Kay, A., Marwick, B., Armstrong, C.G., Barton, C.M., Denham, T., Douglass, K., Driver, J., Janz, L., Roberts, P., Rogers, J.D., Thakar, H., Altaweel, M., Johnson, A.L., Sampietro Vattuone, M.M., Aldenderfer, M., Archila, S., Artioli, G., Bale, M.T., Beach, T., Borrell, F., Braje, T., Buckland, P.I., Jiménez Cano, N.G., Capriles, J.M., Diez Castillo, A., Çilingiroğlu, Ç., Negus Cleary, M., Conolly, J., Coutros, P.R., Covey, R.A., Cremaschi, M., Crowther, A., Der, L., di Lernia, S., Doershuk, J.F., Doolittle, W.E., Edwards, K.J., Erlandson, J.M., Evans, D., Fairbairn, A., Faulkner, P., Feinman, G., Fernandes, R., Fitzpatrick, S.M., Fyfe, R., Garcea, E., Goldstein, S., Goodman, R.C., Dalpoim Guedes, J., Herrmann, J., Hiscock, P., Hommel, P., Horsburgh, K.A., Hritz, C., Ives, J.W., Junno, A., Kahn, J.G., Kaufman, B., Kearns, C., Kidder, T.R., Lanoë, F., Lawrence, D., Lee, G.-A., Levin, M.J., Lindskoug, H.B., López-Sáez, J.A., Macrae, S., Marchant, R., Marston, J.M., McClure, S., McCoy, M.D., Miller, A.V., Morrison, M., Motuzaite Matuzeviciute, G., Müller, J., Nayak, A., Noerwidi, S., Peres, T.M., Peterson, C.E., Proctor, L., Randall, A.R., Renette, S., Robbins Schug, G., Ryzewski, K., Saini, R., Scheinsohn, V., Schmidt, P., Sebillaud, P., Seitsonen, O., Simpson, I.A., Słtysiak, A., Speakman, R.J., Spengler, R.N., Steffen, M.L., Storozum, M.J., Strickland, K.M., Thompson, J., Thurston, T.L., Ulm, S., Ustunkaya, M.C., Welker, M.H., West, C., Williams, P.R., Wright, D.K., Wright, N., Zahir, M., Zerboni, A., Beaudoin, E., Munevar Garcia, S., Powell, J., Thornton, A., Kaplan, J.O., Gaillard, M.-J., Klein Goldewijk, K., Ellis, E., 2019. Archaeological assessment reveals Earth's early transformation through land use. Science 80– (365), 897–902. https://doi.org/10.1126/science.aax1192.

Stiner, M.C., 1991. The faunal remains from grotta Guattari: a taphonomic perspective. Curr. Anthropol. 32, 103–117.

Stucchi, M., Meletti, C., Montaldo, V., Akinci, A., Faccioli, E., Gasperini, P., Malagnini, L., Valensise, G., 2004. Pericolosità sismica di riferimento per il territorio nazionale MPS04 [Data set]. Istituto Nazionale di Geofisica e Vulcanologia (INGV). https://doi.org/10.13127/sh/mps04/ag.

Šušteršič, F., 2006. Relationships between deflector faults, collapse dolines and

collector channel formation: some examples from Slovenia. Int. J. Speleol. 35, 1–12. https://doi.org/10.5038/1827-806X.35.1.1.

Tarquini, S., Isola, I., Favalli, M., Battistini, A., 2007. TINITALY, a Digital Elevation Model of Italy with a 10 M-Cell Size. Istituto Nazionale di Geofisica e Vulcanologia (INGV). https://doi.org/10.13127/TINITALY/1.0 [Data set], Version 1.0.

Tîrlă, L., Vijulie, I., 2013. Structural−tectonic controls and geomorphology of the karst corridors in alpine limestone ridges: southern Carpathians, Romania. Geomorphology 197, 123−136. https://doi.org/10.1016/j.geomorph.2013.05.003.

Treffort, J.-M., 2005. La fréquentation des cavités naturelles du Jura méridional au Bronze final : état de la question, nouvelles données et perspectives. Bull. la Société préhistorique française 401−416.

Troisi, S., Baiocchi, V., Del Pizzo, S., Giannone, F., 2017. A prompt methodology to georeference complex hypogea environments. Int. Arch. Photogramm. Remote Sens. Spat. Inf. Sci. XLII-2/W3 639−644. https://doi.org/10.5194/isprs-archives-XLII-2-W3-639-2017.

Turner, V., 1969. The Ritual Process. Aldine, Chicago.

Ubelaker, D.H., 1989. The estimation of age at death from immature human bone. In: İşcan, Y. (Ed.), Age Markers in the Human Skeleton. Charles C. Thomas, Springfield, pp. 55−70.

van Gorp, W., Sevink, J., 2019. Distal deposits of the Avellino eruption as a marker for the detailed reconstruction of the early Bronze age depositional environment in the agro pontino and Fondi basin (Lazio, Italy). Quat. Int. 499B, 245−257. https://doi.org/10.1016/j.quaint.2018.03.017.

van Gorp, W., Sevink, J., van Leusen, P.M., 2020. Post-depositional subsidence of the Avellino tephra marker bed in the Pontine plain (Lazio, Italy): implications for Early Bronze Age palaeogeographical, water level and relative sea level reconstruction. Catena 194, 104770. https://doi.org/10.1016/j.catena.2020.104770.

Wells, D.L., Coppersmith, K.J., 1994. New empirical relationships among magnitude, rupture length, rupture width, rupture area, and surface displacement. Bull. Seismol. Soc. Am. 84, 974−1002.

3 CHAPTER III SOLUTIONS AND LIMITATIONS OF THE GEOMATIC SURVEY OF AN ARCHAEOLOGICAL SITE IN HARD TO ACCESS AREAS WITH A LATEST GENERATION SMARTPHONE: THE EXAMPLE OF THE INTIHUATANA STONE IN MACHU PICCHU (PERU)

(published in *Acta imeko*)

Solutions and limitations of the geomatic survey of an archaeological site in hard to access areas with a latest generation smartphone: the example of the Intihuatana stone in Machu Picchu (Peru)

Valerio Baiocchi[1], Silvio Del Pizzo[2], Felicia Monti[1], Giovanni Pugliano[3], Matteo Onori[1], Umberto Robustelli[4], Salvatore Troisi[2], Felicia Vatore[1], Francisco James León Trujillo[5]

[1] *Dipartimento Ingegneria Civile, Edile ed Ambientale(DICEA), Sapienza Università di Roma, Via Eudossiana 18, I00184, Italy*
[2] *Dipartimento di Scienze e Tecnologie, Università degli Studi di Napoli "Parthenope", Centro Direzionale Isola C4, I80143 Napoli, Italy*
[3] *Dipartimento Ingegneria Civile, Edile ed Ambientale, Università degli Studi di Napoli "Federico II", Via Claudio 21, I80125 Napoli, Italy*
[4] *Dipartimento di Ingegneria, Università degli Studi di Napoli "Parthenope", Centro Direzionale Isola C4, I80143 Napoli, Italy*
[5] *Carrera de Ingeniería Civil, Facultad de Ingeniería y Arquitectura, Universidad de Lima, Perù*

ABSTRACT
Archaeological remains need to be geometrically surveyed and set in absolute reference systems in order to allow a "virtual visit" and to create "digital twins" useful in case of deterioration for proper restoration. Some countries (e.g., Peru) have a vast archaeological heritage whose survey requires optimized procedures that allow high productivity while maintaining high standards of geometric accuracy. A large part of Peru's cultural heritage is located in remote areas, at high altitudes and not easily accessible. For this reason, it is of great interest to study the possible applications of easily transportable instruments. In this study it was verified how the capabilities of the latest smartphones in terms of absolute differential positioning and photogrammetric acquisition can allow the acquisition of a geometrically correct and georeferenced three-dimensional model. The experimentation concerned a new survey of the Intihuatana stones at Machu Picchu and its comparison with a previous survey carried out with a much more complex laser scanning instrumentation. It is important to note that both the photogrammetric survey and the GPS/GNSS survey were carried out with the same smartphone taking full advantage of both features of the same mobile phone. Relative comparison to an existing point cloud provided differences of 2 millimeters in mean with an RMSE of 2 cm. The absolute positioning accuracy compared to a very large-scale cartography appears to be of the order of one metre as was expected mainly due to the high distance of the GPS/GNSS permanent stations.

Corresponding author: Valerio Baiocchi, e-mail: valerio.baiocchi@uniroma1.it

1. INTRODUCTION

The geomatic survey of archaeological remains is always a difficult task due to the complex accessibility of sites whether they are located in urban or more remote areas. In fact, remains in densely populated areas have problems of accessibility because they are often located in underground areas with limited space [1]. On the other hand, remains in sparsely populated areas are often remote and difficult to reach with bulky equipment [2]-[6]. In the present work we wanted to test the geometric accuracy that can be obtained by creating a three-dimensional point cloud model from images acquired using a latest generation smartphone (Xiaomi Mi9). The three-dimensional model was framed in the geodetic datum WGS84 by means of differential measurements performed with the same smartphone thanks to the recent possibility of writing GNSS RINEX observation files made possible by the Android operating system (from version 7).

1.1. What are Intihuatana stones?

All the important Inca cities had an Intihuatana (or Intiwatana) stone, whose most accredited translation is "the place where the sun binds", it is believed that they indicated in some way the dates of the solstices.

There are many theories concerning the history of the city of Machu Picchu and the meaning of the Intihuatana stone itself, but scholars are yet to reach a consensus. Giulio Magli [7], an Italian archaeological astronomer, proposes that the Inca ritualistically travelled from Cusco to Machu Picchu. The Inca took this pilgrimage to replicate the mythical journey that the first Inca thought their ancestors took from the Island of the Sun in Lake Titicaca. Magli believes that the pilgrimage concluded at the highest peak in the main ruins, the steps leading to the Intihuatana stone.

In any case, the Spanish invaders, wanting to abolish the Inca religious beliefs, soon after their arrival in Peru in the fourteenth century destroyed almost all the Intihuatana stones they found in the various cities except for some of them, including Machu Picchu, probably because of the city's difficult accessibility (Figure 1). This last theory, however, contrasts with the fact that the city of Machu Picchu was never really completely "lost" but only abandoned, the inhabitants of the area have always known its existence and led the first scientific research missions at the beginning of the twentieth century [8].

1.2. Latest smartphone geomatic capabilities

Mobile phone technology is producing cameras with increasing resolution, with some of the latest smartphone models reaching 100 megapixels [9]. It is important to consider that resolution alone is no guarantee of correct photogrammetric reconstruction; the limited size of a mobile phone's camera does not allow to achieve the geometric characteristics of a Digital Single Lens Reflex as well as of a photogrammetric camera. Liquid lens technology is also soon to be released, which will make the optical sensors of smartphones much more versatile but, on the other hand, calibration or self-calibration of the optics will be more complex. In any case, smartphone images have provided interesting results, especially considering their easy transportation [10], [11].

In these and other works in the literature on the use of smartphones for photogrammetry, quite variable precision and accuracy have been observed, ranging from tens of centimetres [10] to a few centimetres [11], the causes of this variability are still being studied by the scientific community. A very important factor is the use of Ground Control Points (GCPs) without which there are poor and uncontrolled results [12], [13]. Other factors that influence the final results can be: the size and shape of the object to be detected, the acquisition distance and, obviously, the quality of the camera optics; it is precisely because of this last factor that it seems that the most recent smartphones are getting closer and closer to the classic professional cameras, which in any case almost always give more accurate results [10].

At the same time the Android operating system has recently (August 2016) released the possibility to access to raw Global Navigation Satellite Systems (GNSS) measurements on several (but not all) Android devices, allowing to write phase and/or code observations in a Rinex file similar to the procedure employed by professional receivers, such as it happens for geodetic measurements [14]. Mobile phone manufacturers, stimulated by this availability, have made terminals containing dual frequency capable chips which potentially allow for improved accuracy due to the possibility of estimating, as is

known, the delay of the satellite signal due to the crossing of the ionosphere. Unfortunately, till now, double frequency GNSS chips embedded in mobile phone limit this possibility to GPS ("L1/L5" frequencies) and Galilelo constellations ("E1/E5" frequencies) while GLONASS and Beidou, can be observed only in single frequency. This limitation combined with GNSS smart phone antennas once again of reduced dimensions, and other hardware limitations, do not allow to reach the millimetric accuracies of the geodetic receivers but metric and decimetric accuracies are possible [15], [16].

The combined use of these two features of modern mobile terminals is of particular interest, because what most affects the quality of three-dimensional models from photogrammetry is the presence and accuracy of control points that are needed to improve the intrinsic geometry of the camera, to georeference the model and scale it correctly. In other words, without GCPs, the model is generally deformed and only roughly georeferenced and scaled. Structure from Motion (SfM) algorithms typically use the positions that they read on the single frames that are acquired by the cameras through the built-in GPS/GNSS receivers in point positioning mode which produces accuracies in the range of tens of meters.

The possibility to acquire ground control points (GCPs) and SfM images from one single device with potentially decimetric or centimetric accuracy disclose new possibilities for prompt surveys, especially in areas with access difficulties such as archaeological ones.

2. MATERIALS AND SURVEYS PERFORMED

As already mentioned, the Intihuatana stone of Machu Picchu is one of the few that can still be observed, however, given its historical and cultural importance as well as damages caused by tourists in the past, access is restricted.

Furthermore, the site of Machu Picchu is, as is well known, not easy to reach, since it is an entire Inca city within which the accessibility routes are those of the time and obviously cannot be modified. It should be noted (again Figure 1) that the Intihuatana stone is practically at the highest and most central point of the site, and therefore at the most difficult point to reach with heavy instruments. All of the above shows that the survey of such an archaeological remain may require a complex logistical and authorisation process to be carried out using traditional techniques. The interest in studying the geometric characteristics of the Intihuatana stone, and in particular its alignment with respect to the geographic North, suggested that it would be advantageous to use a recently released smartphone, which has photographic and positioning characteristics useful for the reconstruction of an accurate three-dimensional model.

In particular, smartphones with up to five different focal lengths have recently become popular, allowing surveyors to select the most suitable optics for the survey at hand without having to use optical zooms, which require varying calibration parameters, making the process much more complex.

Nevertheless, it is necessary to calibrate the terminal for each of the optics in use and care must be taken to ensure that the specific calibration for that smartphone lens is applied to each acquisition. It is actually quite simple to change the optics, for example in the Android operating system, in the "pro" mode of the camera application, it can be changed instantly between the various optics available (three in the smartphone used in this test, but up to five in more recent smartphones) much more quickly than with traditional cameras.

Figure 1. The Intihuatana stone location in Machu Picchu.

quality of leisure photography by allowing different focuses to be used in the same image, but these same features could create difficulties for the correct use of the photogrammetric equations that have traditionally been written for solid-state optics.

Anyway, the latest generation devices allow to set the camera focus mode as well as the aperture and the shooting time like a professional camera, furthermore the latest generation high-end smartphone are equipped with several cameras characterized by different focal length. Such configuration allows to conduct a survey using an adaptive and swift approach, specifically the user can easily modify the focal length switching from a camera to another, in order to choose the suitable one in according to the environment conditions.

The focal length is an important parameter, since it set the Field of View of the camera, moreover, even others camera calibration parameters such as distortion coefficients are strictly related to the focal length [17].

A Xiaomi Mi9 terminal was used for this experiment, which is equipped with Sony 48 MPix ultra wide-angle AI triple camera: a 48 Mpix primary camera with a pixel size of 0.8 μm $f/1.75$ aperture, 12 Mpix telephoto camera with a pixel size of 1.0 μm $f/2.2$ aperture and a16 Mpix Ultra wide-angle lens with a pixel size of 1.0 μm $f/2.2$ aperture [18].

At the time of the present experimentation (April 2019) this camera was considered at the top range of mobile phone cameras, although it has been overtaken by other models in recent months [9]. Its size (157.5 x 74.7 x 7.6 mm) and weight (173 g.) do not generate any transportation problems and it is even possible to take more than one terminal with you for specific needs. At the time of experimentation its cost was that of an average mobile phone, just over 500 euros, but now it is possible to buy it refurbished for less than 300 euros, to give an idea of the investment required, which is certainly lower than that of other instruments that could be certainly more accurate.

In the present experiment, the feature of interest was recorded

In this regard, it is perhaps worth mentioning the announced (by Xiaomi company) imminent release of the first smartphones with liquid lenses, which promise to significantly improve the

Figure 2. Three-dimensional model of Intihuatana stone, acquired and georeferenced with Xiaomi Mi9 smart phone.
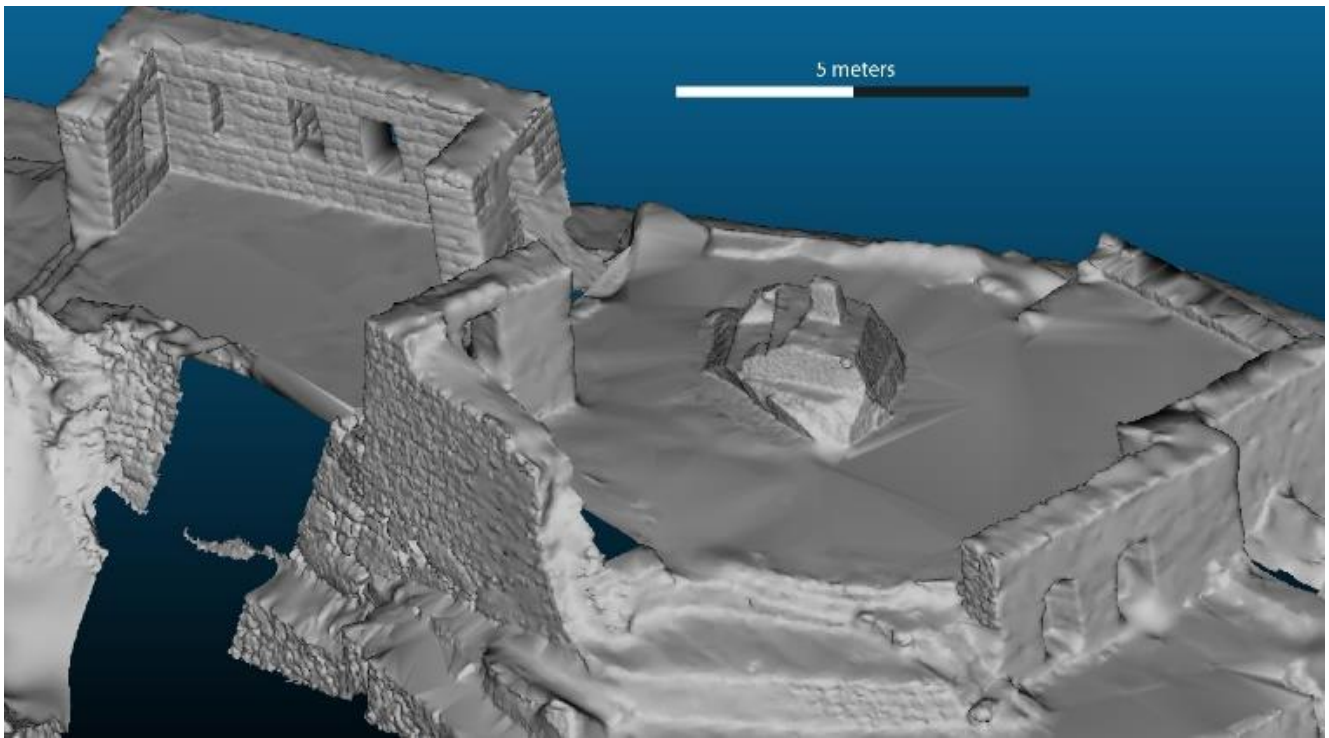
Figure 3. Reference laser scanning model.

in its entirety with intermediate optics. Additional images were acquired using wide angle optics for comparison. The geometry and sequence of the images to be acquired for correct photogrammetric reconstruction using smartphones is the subject of lively debate in the scientific community, which has also developed useful guidelines [19]. For this experiment, the authors have decided to proceed according to their experience gained in previous experiments [1], [2], [10] and therefore to use mainly the intermediate focal length with a single horizontal strip, maintaining an overlap between one frame and the next never minor than 60 % in the longitudinal direction.

The images taken from different points of view, along the entire accessible area near the Intihuatana stone, were subsequently processed with Agisoft Metashape software version 1.5.0 [20], obtaining a complete three-dimensional model of the visible part of the stone itself (Figure 2).
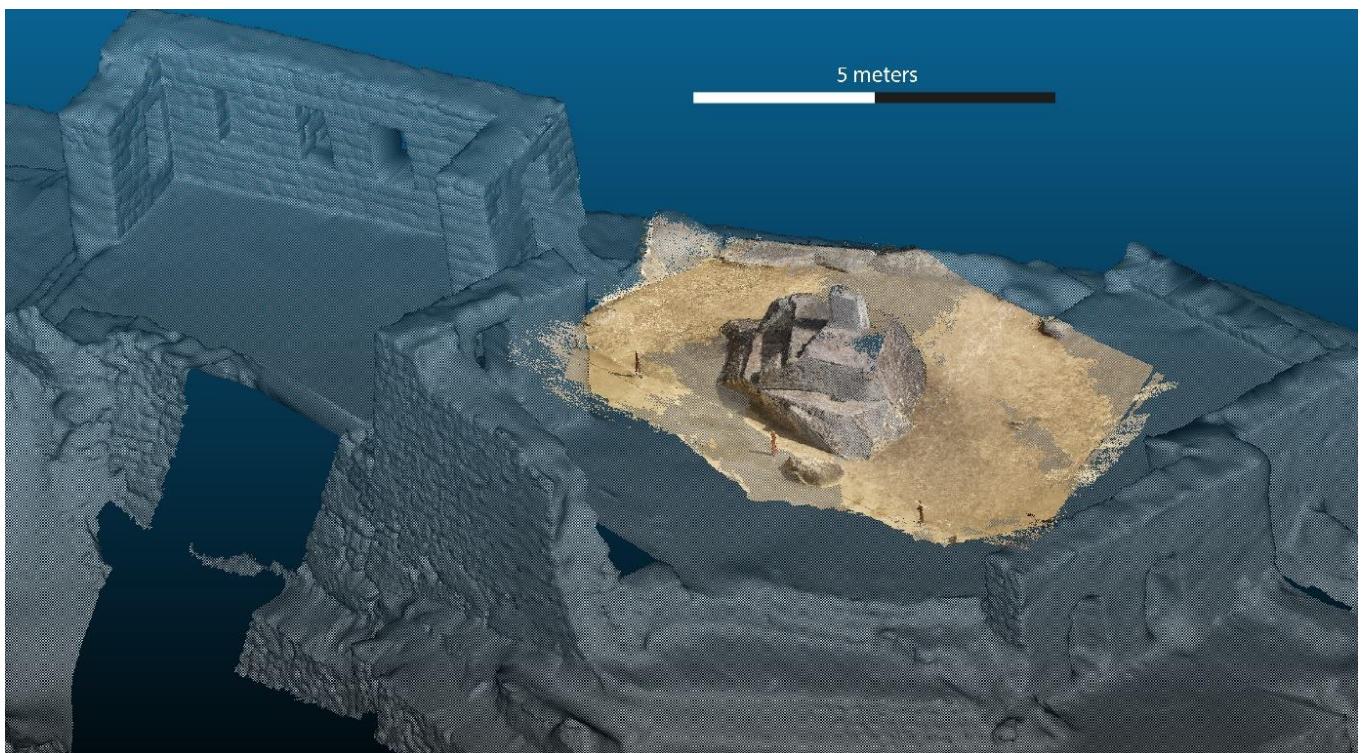

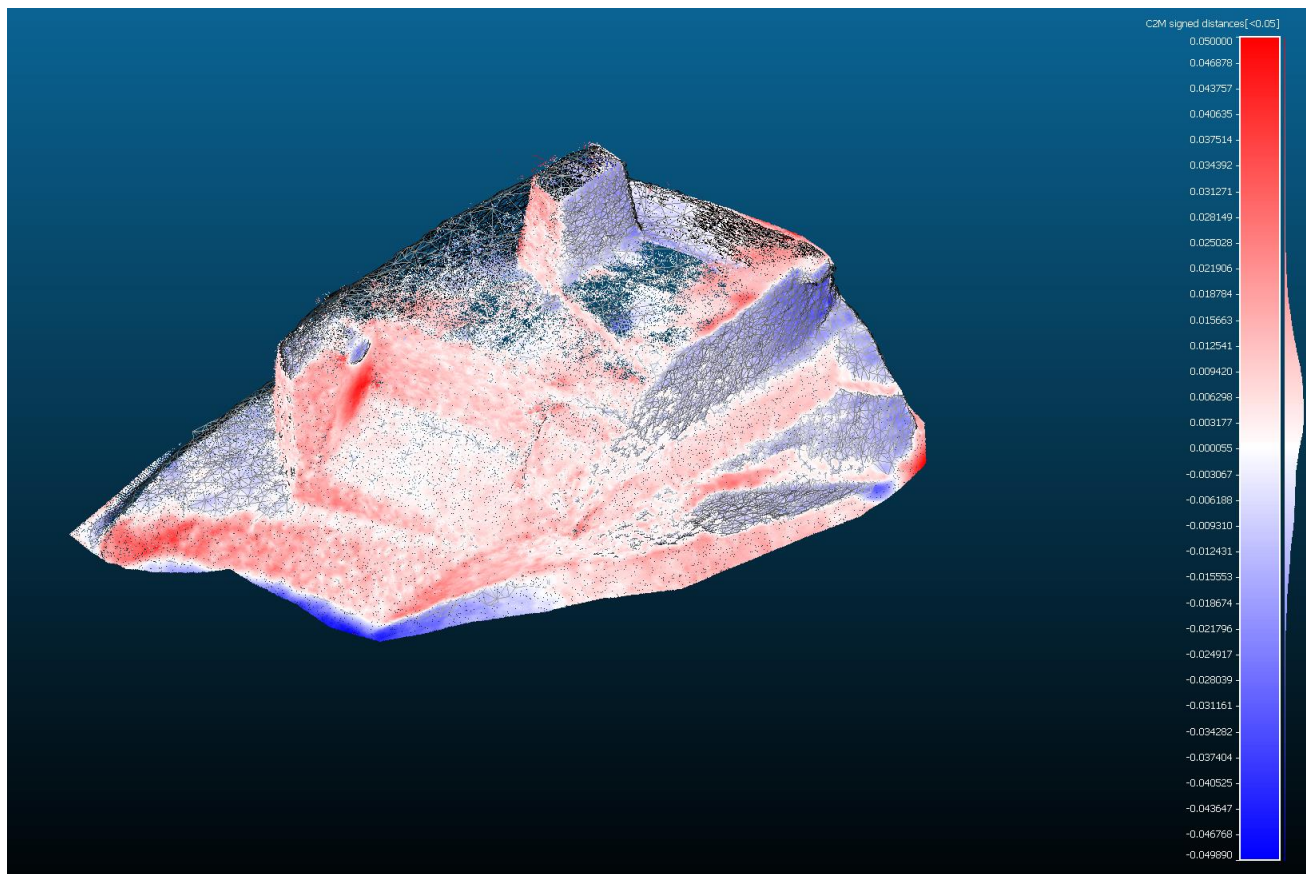Figure 4. Reference laser scanning model and photogrammetric model co-registered.

Figure 5. Reference laser scanning model and photogrammetric model compared with C2M distance signed tool (distances are in metres).

Image processing in the Metashape software requires personnel with at least basic photogrammetric knowledge, but many of the functions are automated, so the time required by the operator is reduced to a few hours, while processing time can be up to a few days on average performing hardware and for very detailed models. Obviously, one of the most important factors for processing time is the number and resolution of the images.

The smartphone itself was used in static mode to collect ground control points from the only natural points measurable on the 3D-model obtained by SfM which were the tops of the fence posts (Figure 2). We used three points on the fences; the fourth point had in fact a less extensive view of the sky and gave results that were not entirely congruent with the other three and is a likely outlier; it is therefore only included in the photogrammetric software as a Check Point (CP) and consequently not used to estimate the rototranslation of the model. We could not use artificially marked points because this would have required specific permissions and the blocking of tourist flow. Of course, from a photogrammetric point of view, it is much more correct to survey points all around the monument even with artificial targets but in this case, it was not possible. However, we decided to carry out the experimentation even in these unfavourable conditions because they are very similar to those encountered in real field situations due to access difficulties or morphologies that are unfavourable for GPS/GNSS surveying, such as the presence of steep slopes near the monuments to be surveyed due to excavation works. The results are nevertheless interesting despite the less-than-optimal geometry of the points.

The survey with raw GPS/GNSS data acquisition has been possible thanks to the app Rinex ON version 1.3; Rinex ON utilizes the measurements of the new Android Raw Measurements API to produce RINEX Observation and Navigation Message Files. The app was written by NSL as part of the FLAMINGO project [21]. It should be noted that, as mentioned above, the dual frequency is only observable for Galileo satellites (E5 frequency) and the latest generation GPS satellites (L5 frequency). In addition, at least on the terminal we used, the possibility of writing phase observations in the post-processing files seems to be disabled, limiting the possibilities of processing observations both in "classic" post-processing mode and in "Precise Point Positioning" (PPP) mode, which would be very useful in these areas given the great distance from the permanent stations of the Peruvian correction network. In other words, since only code observations can be recorded, acquisition times have to be prudently extended, the achievable accuracy is reduced to about 1 metre and the usefulness of the dual frequency is practically lost [22]. This limitation is even more incomprehensible given that it was possible to write phase observations with the previous model "Xiaomi Mi8" [23] of which the "Mi9" is the evolution. This determined the necessity to process the RINEX files in post processing code using the open-source software RTKLIB 2.4.2 [24], which would have potentially allowed to process all four GNSS constellations. Unfortunately, since it was only possible to operate the code difference relative to the permanent stations of the national geodetic network of Peru, it was necessary to limit ourselves to the use of only the GPS and GLONASS constellations. In particular, the observations were differentiated with respect to the stations of Abancay (AP01) and Cusco (CS01), both about 80 km away with significant differences in altitude [25]. By differentiating with respect to both stations, results were

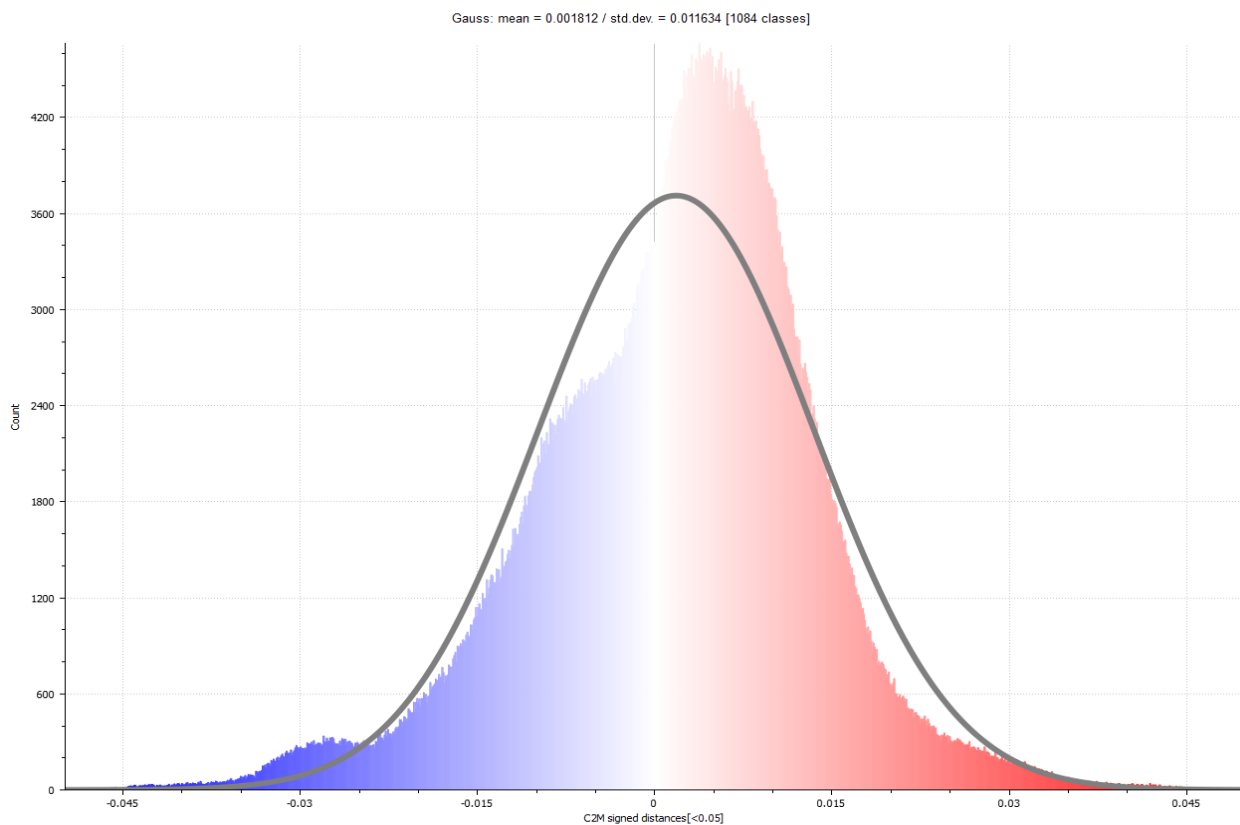Gauss: mean = 0.001812 / std.dev. = 0.011634 [1084 classes]

Figure 6. Histogram of differences between reference laser scanning model and photogrammetric model compared with C2M tool and the fitted gaussian curve computed (distances are in metres).

obtained with an estimated accuracy of 0.8 - 1 metre, which, considering the relatively short measurement sessions possible (so as not to hinder the flow of tourists) of about 20 minutes and the distance from the permanent stations can be considered absolutely satisfactory.

The whole survey took less than an hour and a half, most of which was spent surveying the GPS/GNSS points, while the photogrammetric survey took less than ten minutes. In this regard, it must be further specified that according to recent research [26] such times could be considerably shortened (about 5 minutes per point) if permanent real time GPS/GNSS stations (RTK) were available, as for example in Europe; on the other hand, in areas even more remote than those under study, it would be necessary to use PPP techniques [27] which require about one hour per point. All survey operations do not require any particular specialisation and can be carried out by one person.

3. RESULTS AND DISCUSSION

In order to check the results obtained from the smartphone device a comparison between the photogrammetric model and a 3D model from a LiDAR survey was performed. Indeed, the University of Arkansas [28] has released on the web a 3D model of the archaeological site of Machu Picchu performed using an Optech ILRIS-3D laser scanner, that is a long-range LiDAR (Figure 3). The laser scanner survey can be considered as reference, to estimate the accuracy as well as the completeness achieved by the photogrammetric solution.

Unfortunately, the LiDAR model (Figure 3) is not georeferenced, indeed, it is linked to a local reference system while the scale is correct. However, from the University of Arkansas web page for the specific project [29] it can be seen that

the scanning resolution was set at 3 cm and that at that distance the estimated accuracy is 7 mm.

Using the classical ICP (Iterative Closest Point) technique the two models have been registered in a common reference system (Figure 4). Therefore, a comparison between the two models was performed using the tool C2M present in the open-source software CloudCompare ver. 2.10.3 [30]. For each 3D point extracted by the photogrammetric procedure was computed the signed distance from the surface derived by the LiDAR survey. The result is reported in Figure 5 using a coloured map.

A statistical analysis, of the result obtained from the comparison between the two models, was conducted. The computed distance showed a remarkable agreement as reported in the histogram of the Figure 6. Specifically, a gaussian curve fitting was carried out to the signed distance, obtaining a curve with a mean of 2 millimetres and a standard deviation of 1 centimetre.

However, it can be observed that the average is very close to zero (although there is a small amount of systematic shift), that the maximum deviations are below 5 centimetres and that most of these are in the 2.5 cm range. These results are absolutely interesting, particularly when compared with previous research [10]-[12], but it should be noted that in our case the LiDAR cloud was adapted to the photogrammetric cloud because the lidar cloud was not georeferenced. These results can therefore confirm a relative coherence between the two clouds, but not absolute.

Finally, we wanted to evaluate the possibilities of some software to reconstruct missing parts, in particular SCANN3D [31] in Android environment and TRNIO [32] in IOS environment. This evaluation was interesting in this case because the accessibility to the monument was not complete all around

the monument itself due to the already mentioned protection needs. The 3D model obtained by the use of the first software was unsatisfactory and is not shown here; on the other hand, the result obtained with TRNIO is shown in Figure 4 where also some parts that are badly reconstructed can be easily detected.

It was much more complex to verify GNSS measurements accuracy, defined as the difference between the results obtained and the actual values of the same point coordinates. In order to be able to calculate this statistical parameter it is in fact, as is well known, necessary to know the true values with an accuracy higher than that expected for the measurement system on a suitable set of points. Usually, in geomatics and geodesy, such verifications are carried out using trigonometric points whose coordinates are known a priori with geodetic accuracy. Unfortunately, at the Machu Picchu site there is only one trigonometric point on maps, but it is not unambiguously identifiable in the field, which suggests that it may have been removed, as often happens at archaeological sites of considerable interest. It is obviously not possible to compare with the coverage available on the web such as Google Earth whose estimated planimetric accuracies are generally lower than those expected for our survey methodology [33].

Official large-scale cartographies of the area are not available, with the exception of a 1:750 nominal scale map produced by the Ministry of Culture of Peru in 2014 (Figure 7); considering a graphic error of 0.2 mm, its planimetric accuracy could be 15 cm, but since there are no metadata of the cartography itself, this must be considered only as a hypothesis. In any case, the
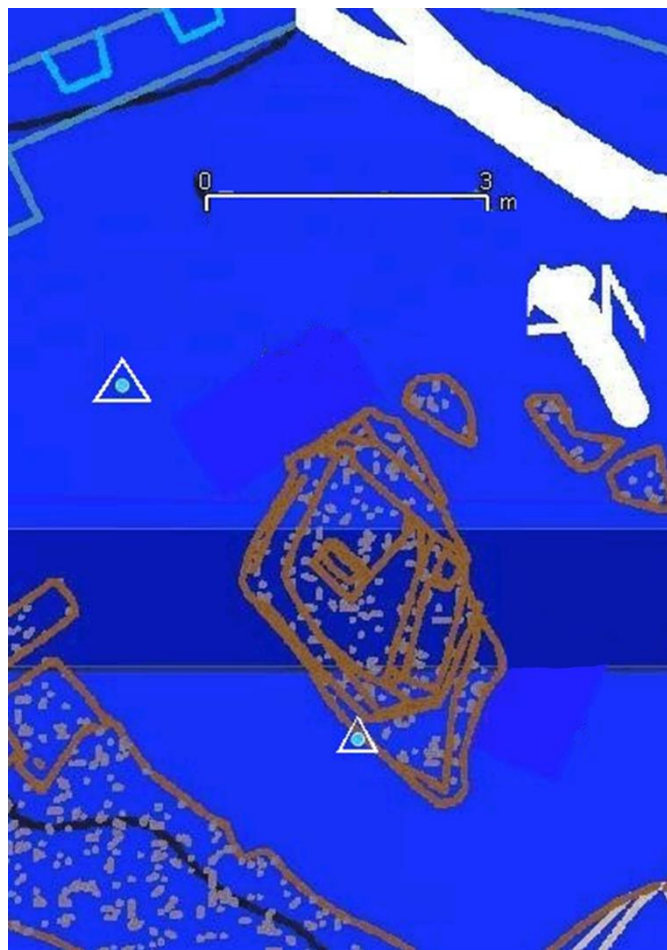
comparison with this cartography showed a good agreement in line with what was verified in previous experiments [10], [11], [12], [13] even if the measured points cannot be identified with certainty because they didn't exist in 2014 and so they are not reported on the map.

4. CONCLUSIONS AND FUTURE PERSPECTIVES

The present experimentation has shown that it is possible to carry out a complete and expeditious georeferenced geomatic survey with the latest generation smartphone. The ease of transport and the simplicity of the operations greatly facilitates the survey work both in terms of logistics and authorisation. The final results are at least comparable with those previously carried out on the same site with laser scanning. The possible applications of such surveys are numerous, ranging from rapid and efficient documentation to the valorisation of sites that are difficult for the general public to access, but also to true photogrammetric surveys where logistical situations make it very costly or impossible to survey with more rigorous instruments.

It is interesting to study in the future the possibilities offered by smartphones that also acquire dual frequency phase GNSS observations; this would also allow the application of PPP post-processing, which could prove to be the most appropriate in such remote sites. There is also interest in studying smartphones with even more advanced optics, with particular interest in liquid optics, which are expected to be released soon.

In this experiment, the GPS/GNSS sensor and the camera of the same mobile phone were used, which allowed the minimum possible encumbrance of the instrumentation. More generally, it is not necessary that the reference points and the photogrammetric survey are acquired by the same device, also considering that the overall dimensions of the mobile phones are very small and do not create any logistical or transport problems.

Figure 7. The Intihuatana stone location in 1:750 map and position of two of the four surveyed points (triangles).

REFERENCES

[1] V. Baiocchi, R. Brigante, S. Del Pizzo, F. Giannone, M. Onori, F. Radicioni, A. Stoppini, G. Tosi, S. Troisi, M. Baumgartner, Integrated geomatic techniques for georeferencing and reconstructing the position of underground archaeological sites: the case study of the Augustus Sundial (Rome), Remote Sens. 2020, 12, 4064.
DOI: 10.3390/rs12244064

[2] V. Baiocchi, G. Caramanna, D. Costantino, P. J. V. D'Aranno, F. Giannone, L. Liso, C. Piccaro, A. Sonnessa, M. Vecchio, First geomatic restitution of the sinkhole known as 'Pozzo del Merro' (Italy), with the integration and comparison of 'classic' and innovative geomatic techniques, Environmental Earth Sciences, no. 3, 2018, 77.
DOI: 10.1007/s12665-018-7244-6

[3] F. Radicioni, P. Matracchi, R. Brigante, A. Brozzi, M. Cecconi, A. Stoppini, G. Tosi, The Tempio Della Consolazione in Todi: Integrated Geomatic Techniques for a Monument Description Including Structural Damage Evolution in Time., International Archives of the Photogrammetry, Remote Sensing and Spatial Information Sciences - ISPRS Archives, 42(5W1), 2017, 433–440.
DOI: 10.5194/isprs-Archives-XLII-5-W1-433-2017

[4] D. Costantino, M. Pepe, A. G. Restuccia, Scan-to-HBIM for Conservation and Preservation of Cultural Heritage Building: The Case Study of San Nicola in Montedoro Church (Italy), Applied Geomatics, 2021.
DOI 10.1007/s12518-021-00359-2

[5] D. Ebolese, M. Lo Brutto, G. Dardanelli, The integrated 3d survey for underground archaeological environment, ISPRS Annals of the Photogrammetry, Remote Sensing and Spatial Information

Sciences, 2019, pp. 311-317.
DOI: 10.5194/isprs-archives-XLII-2-W9-311-201

[6] D. Dominici, E. Rosciano, M. Alicandro, M. Elaiopoulos, S. Trigliozzi and V. Massimi, Cultural heritage documentation using geomatic techniques: Case study: San Basilio's monastery, L'Aquila, Digital Heritage International Congress (DigitalHeritage), 2013, pp. 211-214.
DOI: 10.1109/DigitalHeritage.2013.6743735

[7] National geographic, Discover 10 secrets of Machu Picchu. Onloine [Accessed 15 December 2021]
https://www.nationalgeographic.com/travel/top-10/peru/machu-picchu/secrets/

[8] G. Magli, At the other end of the Sun's path: a new interpretation of Machu Picchu, Nexus Netw J 12, 2010, 321–341.
DOI: 10.1007/s00004-010-0028-2

[9] Xiaomi, MI11 Specifications. Online [Accessed 15 December 2021]
https://www.mi.com/global/mi11/specs

[10] L. Alessandri, V. Baiocchi, S. Del Pizzo, F. Di Ciaccio, M. Onori, M. F. Rolfo, S. Troisi, Three-dimensional survey of Guattari cave with traditional and mobile phone cameras, Int. Arch. Photogramm. Remote Sens. Spatial Inf. Sci. XLII-2/W11, 2019, 37-41.
DOI: 10.5194/isprs-archives-XLII-2-W11-37-2019

[11] E. Nocerino, F. Poiesi, A. Locher, Y. T. Tefera, F. Remondino, P. Chippendale, L. Van Gool, 3D reconstruction with a collaborative approach based on smartphones and a cloudbased server, International Archives of the Photogrammetry, Remote Sensing and Spatial Information Sciences – ISPRS Archives 42(2W8), 2017, 187-194.
DOI: 10.5194/isprs-archives-XLII-2-W8-187-2017

[12] A. Vinci, F. Todisco, R. Brigante, F. Mannocchi, F. Radicioni, A smartphone camera for the structure from motion reconstruction for measuring soil surface variations and soil loss due to erosion, Hydrol. Res., 48, 2017, pp. 673–685.
DOI: 10.2166/nh.2017.075

[13] A. Masiero, F. Fissore, M. Piragnolo, A. Guarnieri, F. Pirotti, A. Vettore, Initial evaluation of 3d reconstruction of close objects with smartphone stereo vision, Int. Arch. Photogramm. Remote Sens. Spatial Inf. Sci., XLII-1, 2018, 289–293.
DOI: 10.5194/isprs-archives-XLII-1-289-2018

[14] U. Robustelli, V. Baiocchi, L. Marconi, F. Radicioni, G. Pugliano, Precise Point Positioning with single and dual-frequency multi-GNSS Android smartphones, CEUR Workshop Proc. 2020, 2626. Online [Accessed 15 December 2021]
http://ceur-ws.org/Vol-2626/paper10.pdf

[15] Raw GNSS Measurements. Online [Accessed 15 December 2021]
https://developer.android.com/guide/topics/sensors/gnss

[16] U. Robustelli, V. Baiocchi, G. Pugliano, Assessment of dual frequency GNSS observations from a Xiaomi Mi 8 Android Smartphone and Positioning Performance Analysis, Electronics 8, 2019, 91.
DOI: 10.3390/electronics8010091

[17] C. S. Fraser, Automatic camera calibration in close range photogrammetry, Photogrammetric Engineering & Remote Sensing 79.4, 2013, 381-388.

[18] Xiaomi, MI9 Specifications. Online [Accessed 15 December 2021]
https://www.mi.com/global/mi9/specs

[19] P. Sapirstein, S. Murray, Establishing Best Practices for Photogrammetric Recording During Archaeological Fieldwork, Journal of Field Archaeology, 42:4 (2017) 337-350.
DOI: 10.1080/00934690.2017.1338513

[20] Agisoft, Discover intelligent photogrammetry with Metashape. Online [Accessed 15 December 2021]
https://www.agisoft.com

[21] Flamingo GNSS. Online [Accessed 15 December 2021]
https://www.flamingognss.com/

[22] M. Pepe, D. Costantino, G. Vozza, V. S. Alfio., Comparison of two approaches to GNSS positioning using code pseudoranges generated by smartphone device. Applied Sciences (Switzerland) 11, no. 11, 2021, 4787.
DOI: 10.3390/app11114787

[23] Dual-frequency GNSS on Android devices. Online [Accessed 15 December 2021]
https://barbeau.medium.com/dual-frequency-gnss-on-android-devices-152b8826e1c

[24] RTKlib. Online [Accessed 15 December 2021]
https://www.rtklib.com

[25] [Accessed 15 December 2021]
http://regpmoc.ign.gob.pe/rastreo_permanente/index.php

[26] P. Dabove, V. Di Pietra, Single-baseline RTK positioning using dual-frequency GNSS receivers inside smartphones, Sensors 19, 2019, 4302.
DOI: 10.3390/s19194302

[27] M. Barbarella, S. Gandolfi, L. Poluzzi and L. Tavasci, Precision of PPP as a function of the observing-session duration, IEEE Trans. Aerosp. Electron. Syst., vol. 54, no. 6, 2018, 2827-2836

[28] Instituto Nacional de Cultura, Center for Advanced Spatial Technologies, (University of Arkansas) and Cotsen Institute for Archaeology (UCLA). Online [Accessed 15 December 2021]
https://gmv.cast.uark.edu/scanning-2/data/machu-picchu-3d-data/

[29] Wayback. Online [Accessed 15 December 2021]
http://wayback.archive-it.org/6471/20150825200335/http://cast.uark.edu/home/research/archaeology-and-historic-preservation/archaeological-geomatics/archaeological-laser-scanning/laser-scanning-at-machu-picchu.html

[30] Cloudcompare. Online [Accessed 15 December 2021]
http://www.cloudcompare.orghttp://www.cloudcompare.org/

[31] Google Play. Online [Accessed 15 December 2021]
https://play.google.com/store/apps/details?id=com.smartmobilevision.scann3d&hl=it

[32] Trnio. The app that transforms your iPhone into a handheld 3D scanner. Online [Accessed 15 December 2021]
http://www.trnio.com

[33] G. Pulighe, V. Baiocchi, F. Lupia, Horizontal accuracy assessment of very high resolution Google Earth images in the city of Rome, Italy, Int. J. Digital Earth 9, 2015, 342-362.
DOI: 10.1080/17538947.2015.1031716

4 CHAPTER IV EFFICIENT THREE-DIMENSIONAL SURVEY TECHNIQUES AND THEIR COMPARISON IN OPEN SOFTWARE IN THE ARCHAEOLOGICAL TEST SITE OF NINFEO MAGGIORE AND NINFEO MINORE OF FORMIA (LATINA, ITALY)

EFFICIENT THREE-DIMENSIONAL SURVEY TECHNIQUES AND THEIR COMPARISON IN OPEN SOFTWARE IN THE ARCHAEOLOGICAL TEST SITE OF "NINFEO MAGGIORE" AND "NINFEO MINORE" OF FORMIA (LATINA, ITALY)

L. Alessandri[1], V. Baiocchi[2*], G. Melandri[3], F. Monti[2], A. Canu[4],
L. Ruzzi[5], G. Servodio[4]

[1] Groningen Institute of Archaeology, University of Groningen, Groningen, Netherlands- l.alessandri@rug.nl
[2] Sapienza University of Rome, DICEA, Rome, Italy – (valerio.baiocchi, felicia.monti)@uniroma1.it
[3] Soprintenza archeologica Belle arti e paesaggio per le Provincie di Frosinone e Latina, Italy- gianluca.melandri@beniculturali.it
[4] Microgeo S.r.l., Rome, Italy – (a.canu, g.servodio)@microgeo.it
[5] SITERRA STP S.r.l., Rome, Italy – info@siterra.it

Commission IV, WG IV/4

KEY WORDS: Formia, SLAM, CloudCompare, Ninfeo Maggiore, Villa Romana di Caposele, Ninfeo Minore.

ABSTRACT:

In Europe and beyond, the cultural and archaeological heritage may have considerable extensions of hundreds of square metres if not kilometres. It is then necessary to study highly efficient techniques able , at the same time, to maintain centimetric accuracy. In these contexts, the SLAM technique can be an efficient solution. We tested the latter in a survey of a portion of the so-called Roman Villa of Caposele, also known as Villa Rubino in Formia, (Italy): the "Ninfeo Maggiore" and "Ninfeo Minore" (Major and Minor *nymphaeum*). The two structures had to be surveyed for both conservation and study purposes and to allow a virtual visit, which is particularly important since they are located inside a private property. The structure is complex, with a succession of rooms and environments in an archaeological complex extending approximately 480 metres in an east-west direction and approximately 50 metres in a south-north direction. We decided to survey both *nymphaea* with the "GEOSLAM Zeb Horizon", also surveying all the internal connecting rooms and corridors between them. Both *nymphaea* were also surveyed with a "Faro" terrestrial laser scanning, to allow comparison. To verify the validity of the SLAM on the outside, a survey was carried out using a DJI Matrix drone with laser scanning. The comparison showed very limited deviations whose statistical validation is in progress, demonstrating that the SLAM technique can advantageously be used in such vast archaeological complexes where the efficiency and completeness of the survey is more important than the millimetric accuracy.

1. INTRODUCTION

The geomatic survey of cultural and archaeological heritage is currently at the centre of a fervent debate in the scientific world (Bitelli et al. 2019). The techniques used are very different from the most traditional to the most innovative, from terrestrial photogrammetry (Alessandri et al. 2022; Baiocchi et al. 2017; Del Pizzo et al. 2011) to terrestrial laser scanning (TLS) (Masiero et al. 2019; Angelini et al. 2017, Pirotti et al. 2013) to the numerous studies on the use of UAVs (Pan et al. 2019; Caroti et al. 2015; Lo Brutto et al. 2014). Very often all these techniques, in the case of complex archaeological structures, are used in an integrated manner (Dominici at al. 2013; Ebolese et al. 2019: D' Agostino et al. 2022; Radicioni et al. 2017). The survey of cultural heritage may require extensive measurement campaigns, especially when the remains extend over large areas and consist of very complex structures. Examples include the complexity and vastness of the Incan cities (Baiocchi et al. 2022), the archaeological deposits in caves (Alessandri et al. 2019) and the quarries and catacombs under the historic cities (Troisi et al. 2107). Surveys must be carried out thoroughly but also efficiently otherwise they become difficult to implement in practice. Without an available detailed survey, it is sometimes impossible to proceed with adequate restoration after heavy damage or structural failure, as happened in *Pompeii* (Sarhosis et al. 2016) or even in the *Domus Aurea* of the emperor Nero in the centre of Rome (Giavarini, 2001), to name but a few of the best-known examples. Developing and calibrating more or less

innovative geomatic techniques to identify the most suitable procedures for surveying large and complex structures in short time, maintaining accuracies of at least the order of a few centimetres has become a priority (Sanz-Ablanedo et al. 2018; Turneret al. 2012; Iheaturu et al. 2020). In the present paper, the SLAM technique was tested in the context of a real archaeological survey on a particularly complex site: the so-called Roman Villa of Caposele, also known as Villa Rubino (Giuliani & Guaitoli, 1972; Cassieri, 2015). The survey has been repeated using more established geomatic techniques to validate the times and geometric correctness characteristics. The Villa, built by the Dukes of Marzano and subsequently passed into the hands of Charles of Ligny, Prince of Caposele, was purchased by King Ferdinando II di Borbone in 1845, to make it a luxurious summer residence. The building overlooks the inlet of Caposele, where there must have been a small harbour, and it is squeezed between the Via Appia and the sea. To the west of the small port are the remains of an imposing structure with a central courtyard, datable to the 1st century B.C., which scholarly tradition has identified as Cicero's Academy or School, although it is probably a *horreum*, testifying to the utilitarian vocation of this area of the villa. In later phases, while retaining its intended use, the *horreum* would be incorporated into a residential building complex together with other structures further to the west that may have served as warehouses in the earlier phase. To the east of the marina is the residential area, the area in which the survey operations were concentrated. Here, on a front about 140 metres long, there are a

---

* Corresponding author

series of rooms with barrel vaults that were probably part of the *basis villae* of the building. In two of these rooms are the so-called minor and major *nymphaea*. The first consists of an almost quadrangular room with a roof supported by four doric brick columns; on the back wall, in a large niche, spring water gushes out. The wall decorations include stucco, shells and incrustations of glass paste and small stones. The main *nymphaeum* is divided into three naves and covered with a rounded coffered vault supported by doric columns. The large niche at the bottom of the *nymphaeum* contains a pool of spring water; the floor consists of a white mosaic with polychrome *tesserae*. These *nymphaea* constitute the focus of the intervention. In front of them there was a very large fishpond, which ran into the sea for about one hundred metres in length, with a width of over 200m.

The two *nymphaea* surveys had conservative and scientific purposes. One of the aim was to allow a virtual visit, which is particularly important since they are both located inside a private property. As already described, the structure is complex, with a succession of rooms and passageways in an archaeological complex extending approximately 480 metres in an east-west direction and approximately 50 metres in a south-north direction. The survey of such an extension and such an articulation with consolidated techniques such as terrestrial laser scanning would probably have required days, and for this purpose, we wanted to test the possible use of the most modern SLAM techniques, in particular using a GEOSLAM Zeb Horizon, totally transportable by an operator and with a range of up to 100 metres (GEOSLAM, 2022).

The software Cloud Compare 2.11.3 (64 bit) (Cloud Compare DT, 2022) has been used to compare times, modes, precision and accuracy of the point cloud obtained. Cloud Compare allows comparisons and it uses various methods to separately calculating distance and estimating precision and accuracy. It allows one cloud to be fitted to the other or to be compared while remaining within its absolute coordinates.

We decided to survey both *nymphaea* with the "GEOSLAM", also surveying all the internal connecting rooms and passageways between them. The whole survey was carried out in few tens of minutes and afterwards the survey continued over most of the exterior of the entire structure.

The survey of the entire complex was not carried out because the main interest of this project was to test the SLAM technology and validate its precision and accuracy in comparison with more consolidated techniques.

For comparison, both *nymphaea* were surveyed with a more consolidated "Faro" TLS instrument.

To verify the validity of the SLAM also on the external part, a survey was carried out using a DJI Matrix drone with laser scanning. Finally, the same survey was also carried out with an optical camera on the same Matrix drone and with the most widely used drone for photogrammetry, i.e. the "Phantom 4 pro", also by DJI.

All the surveys used the same ground control points, to refer them to the same reference system and to be able to assess their precision and accuracy.

It should be noted that SLAM was only able to station a few of the GCPs while, as can be easily guessed, the drones acquired almost all of them.

2. MATERIALS E METHODS

The instrumentation used in the survey consisted of the DJI Matrice 300 RTK drone to which the DJI P1 optical camera and the DJI L1 LiDAR sensor were attached, the DJI Phantom 4

drone (DJI, 2022), the TLS Faro (Faro, 2022) and the GEOSLAM Zeb Horizon (GEOSLAM, 2022) . The scanning mode of the LiDAR sensor was set to 480 points/m^2. For georeferencing and validation of the accuracy of the different survey types, ground control points were acquired with the E-Survey E300 Pro GNSS system. The photogrammetric reconstruction of the three-dimensional model from the DJI Matrice 300 images (flight with nadiral take and then 45° inclined take) was processed with the DJI Terra 3.4.4 software. The model was georeferenced according to the information obtained in RTK position correction mode, i.e. without the use of GCP. On the other hand, the three-dimensional model obtained from the DJI Phantom 4 images (flight with nadiral take-off) was created with the MicMac v. 1.1 (MicMac DT, 2022) software and oriented with the help of GCPs, achieving an average accuracy of 8.6 cm. This accuracy value was also achieved by correcting the altitude problem often encountered by DJI users. In fact, the 'Absolute Altitude', i.e. the height reported in the EXIF, is often incorrect. It is possible to correct the altitude information of all images.

It should be noted that the complexity of the area analysed by the external surveys of the entire complex (Fig. 1) allowed the acquisition of a small number of points, in a non-ideal conformation. However, all 5 points were used as Ground Control Points (GCPs) to orientate the three-dimensional model of the DJI Phantom 4 and the surveys of the Laser Scanner X and the GEOSLAM Zeb Horizon.
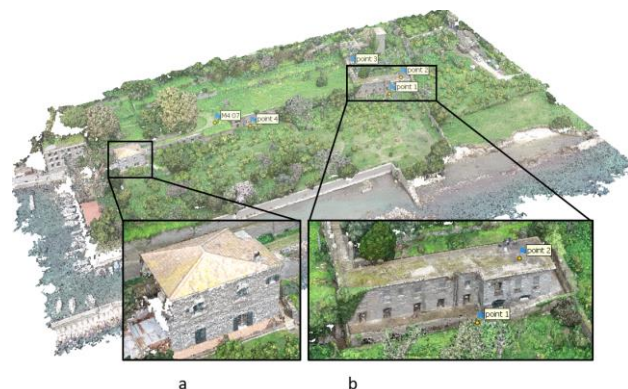
Figure 1. Overall area surveyed outside the complex and distribution of ground control points acquired. The detail boxes show the buildings a) and b) taken into consideration for the comparisons between the various survey methods, presented below.

The variety of instrumentation used for surveying is characterised by different sensors, mounted on different ground and aerial supports, using different positioning modes. Thus, the resulting three-dimensional models are characterised by both the different physical properties of the sensors and the different internal and external orientation parameters. However, we used CloudCompare's Cloud-to-Cloud algorithm (Cloud Compare DT, 2022), which allows us to estimate the distance between two point clouds. Distances are calculated on the cloud identified as 'compared' to the points in the 'reference' cloud. It is good practice to set the densest point cloud as the 'reference' cloud. At the end of the process, a new scalar field is applied to the "compared" cloud containing one scalar field describing the absolute distance and three scalar fields corresponding to the distance calculated along each dimension. In the tests conducted

with the Cloud-to-Cloud tool, the local nearest-neighbour matching model was used, as the tests were performed on the buildings shown in Figure 1, which are characterised by regular surfaces with low roughness. The choice of concentrating the tests on the buildings, rather than on the vegetation present, had the additional purpose of reducing the possibility of contaminating the results of the distances between points with outliers or erroneously highlighting shifts in the elements during the different acquisitions.

Due to the various positioning modes used during the surveys, it was decided to perform further tests with the Cloud-to-Cloud tool after applying Cloud Compare's Fine Registration (ICP) tool. This tool is capable of automatically fine registering two point clouds (or meshes) that have already been roughly registered and represent the same area, i.e. they are overlapping. The 'aligned' point cloud is recorded on the 'reference' cloud according to the set transformation parameters. In fact, shift and rotation with respect to a given axis can be constrained.

3. DISCUSSION

The Cloud-to-Cloud tool was applied to the calculation of the distance between the following point clouds representing the outdoor area:

- DJI Matrice 300 RTK L1/P1

- DJI Phantom 4/DJI Matrice 300 RTK P1

- DJI Matrice 300 RTK L1/DJI Phantom 4

Two sensors were used on the DJI Matrice 300/RTK drone, the DJI P1 optical and the DJI L1 LiDAR. In this case, both clouds obtained were oriented according to the RTK positioning information, without the use of GCPs. The comparison of the two point clouds circumscribed to the building a) depicted in Fig. 1 showed minimal absolute differences, due more to the distance in the z-direction and identified at the areas of discontinuity such as the part below the roof where the window canopies were acquired by LiDAR sensor differently than in the photogrammetric reconstruction (Fig. 2, bottom left and right box).

Distance direction	Gauss mean	St. dev.
	m	m
Absolute distance	0.0476	0.0570
x	0.0040	0.034
y	-0.0049	0.0482
z	-0.0234	0.0375

Table 1. Values obtained after application of the Cloud-to-Cloud tool between DJI Matrice 300 L1 (compared) and P1 (reference) clouds, without the application of Cloud registration.

The comparison of the two three-dimensional models obtained from the optical sensors mounted by the DJI Phantom 4 and the DJI Matrice 300/RTK was carried out by taking element b in Fig. 1 into consideration, as it is in a position that is better modelled by the GCPs than the total external area.
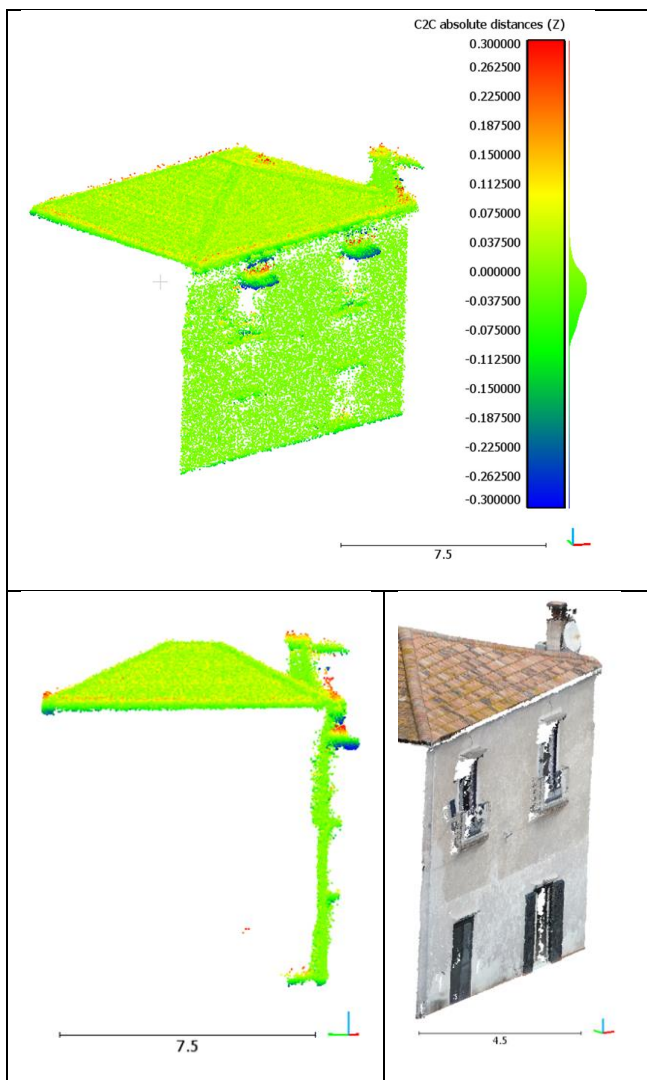
Figure 2. The largest distance values along z calculated are at the window canopies. Below you can see the different acquisition in the case of sensor L1 (left) and P1 (right).

This aspect ensures a lower deformation of the DJI Phantom 4 model, which was oriented on the basis of the GCPs. Also in this case, the greatest distances are detected along the z direction, as can be seen from Fig. 3 on the terrace there is a constant value of approximately 10 cm difference between the two point clouds (green/blue colouration corresponding to the value -0.1 m, negative as the point difference is calculated considering "compared" - "reference" altitude). In particular, the three-dimensional model of the DJI Matrice 300 RTK P1 has higher altitudes than the DJI Phantom 4, this difference could result from errors on the determination of the phase centre of the GPS/RTK antenna or the centre of the sensor acquisition. In this case, a post-registration comparison between the two point clouds was also performed with the 'Clouds registration' tool to highlight any differences between the geometries of the two clouds, disregarding positioning errors. Registration with constrained rotation around the z axis and shift along x,y, z returned no changes on the registered cloud. On the contrary, after applying registration with the possibility of rotation and shift along the three axes, the calculated distances are significantly smaller in all directions (Table 3). Thus, geometrically the clouds are congruent, despite the fact that the DJI Matrice works in RTK, thus, has a more robust frame block

than the Phantom 4 which has lower optical quality but relies on GCPs.

| Distance direction	Gauss mean	St. dev.
	m	m
Absolute distance	0.0815	0.0673
x	0.0057	0.0489
y	-0.0110	0.0496
z	-0.0464	0.0633

Table 2. Values obtained after the application of the Cloud-to-Cloud tool between DJI Phantom 4 clouds (compared) and DJI Matrice 300 RTK P1 (reference), without the application of Cloud registration.

Distance direction	Gauss mean	St. dev.
	m	m
Absolute distance	0.0342	0.0675
x	0.0001	0.0465
y	-0.00004	0.0426
z	0.0002	0.0419

Table 3. Values obtained after application of the Cloud-to-Cloud tool between DJI Phantom 4 clouds (compared) and DJI Matrice 300 RTK P1 (reference), after application of Cloud registration (shift and rotation with respect to X, Y, Z).
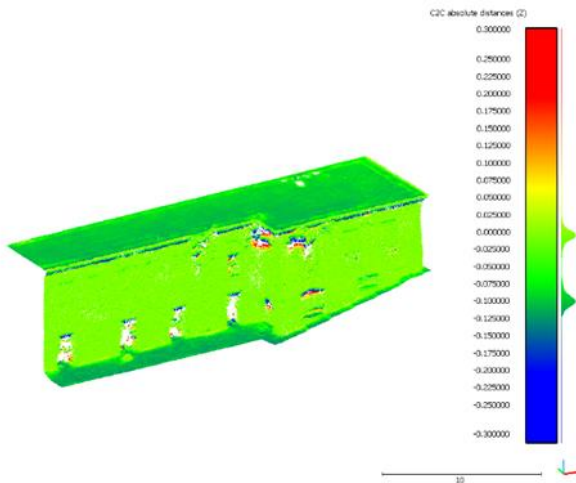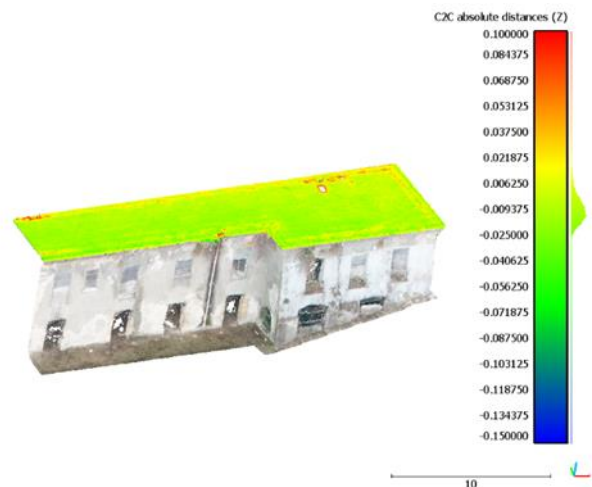

Figure 3. Distances along the z axis resulting from the Cloud-to-Cloud application without registration of the two clouds.
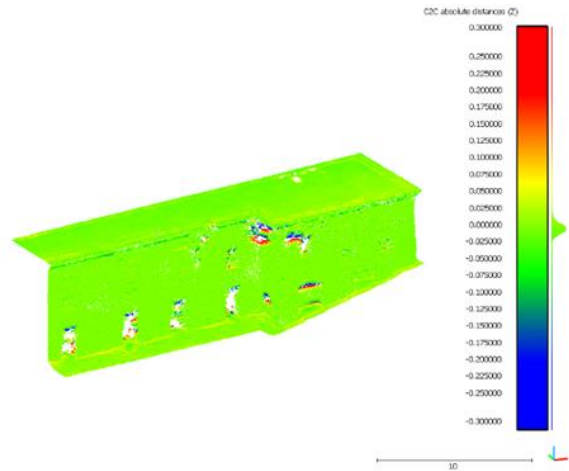
Figure 4. Distances along the z axis resulting from the Cloud-to-Cloud application after registration the two point clouds by setting shift and rotation in the three directions x,y,z.

Figure 5. Distances along the z axis resulting from the Cloud-to-Cloud application, without registration of the two clouds.

Figure 6. Distances along the Z axis resulting from the Cloud-to-Cloud application, after registration the two point clouds by setting shift in the three directions x,y,z and rotation with respect to the z axis.

To further test the registration with x,y,z shift and constrained rotation around the z axis, only the portion of the point cloud representing the terrace of building b) was taken into account (Fig. 1). In this case, the tool returned a better geometric congruence between the two point clouds.

Finally, with regard to the external models, the distance between the point clouds acquired by the DJI Matrice 300 RTK L1 and the DJI Phntom 4 was calculated. Note that, similarly to the first comparison, on the terrace there is a constant value of approximately 10 cm difference between the two point clouds (this time the difference in altitude is positive as it is calculated considering "compared" - "reference" altitude, the "compared" altitude is higher). Considering the similar working mode of position correction in RTK of the DJI Matrice 300 RTK drone, this difference could also result from errors in the determination of the phase centre of the GPS/RTK antenna or from the acquisition centre of the sensor.

Distance direction	Gauss mean	St. dev.
	m	m
Absolute distance	0.1009	0.1087
x	-0.0071	0.0542
y	0.0011	0.0593
z	0.0801	0.0951

Table 4. Values obtained after applying the Cloud-to-Cloud tool between DJI Matrice 300 RTK L1 (compared) and DJI Phantom 4 (reference) clouds, without Cloud registration.
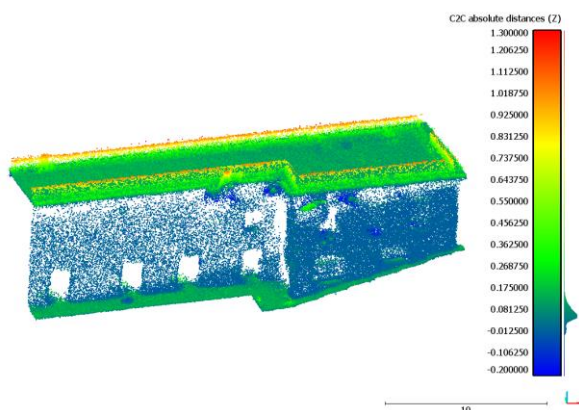
Figure 7. Distances along the z-axis resulting from the Cloud-to-Cloud application, the registration of the two point clouds was not applied.

The internal surveys of the Major Nymphaeum and the Minor Nymphaeum were carried out with the TLS Faro and the GEOSLAM Zeb Horizon. The entire environment was acquired with several stations with the TLS, but having worked in the absence of spherical markers, it was decided to use a single acuisition that was more representative of the actual geometry of the site, in order to perform comparisons on a robust point cloud. The scheme followed for calculating the distance between the point clouds representing the interior areas follows that used for the exterior. Thus, only comparisons were made between the original point clouds and tr recorded point clouds (with shift in x,y,z and rotation around z and then around x,y,z). The superposition of the original TLS and GEOSLAM point clouds representing the Nymphaeum Major shows an obvious shift. However, the cloud registration tool does not improve the superposition of the data, probably due to their complex three-dimensional structure (Fig. 8 a,b,c).

Then the geoslam was recorded on the laser cloud, with shifts in x,y,z, but rotation only on z (Fig. 10)

Figure 8. Cloud comparisons from Geoslam and TLS without registration (a), with registration with rotation along the z axis only (b) and with registration with rotation along the three axes x,y,z

The same registration was then tested with shifts in x,y,z and rotations in the three axes (fig. 11)
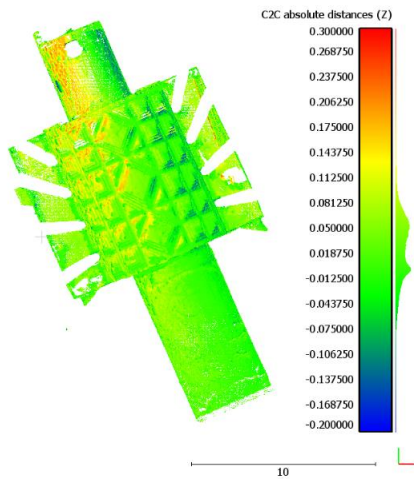
Figure 9. Distances along the z-axis resulting from the Cloud-to-Cloud application, the registration of the two point clouds was not applied.
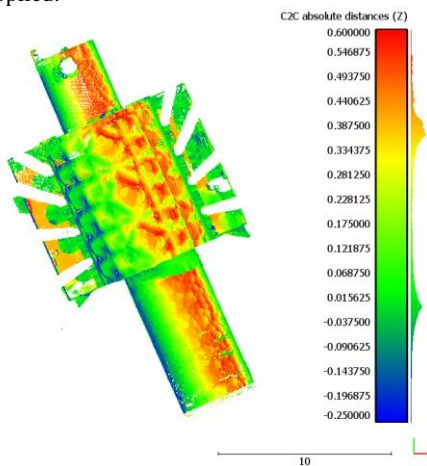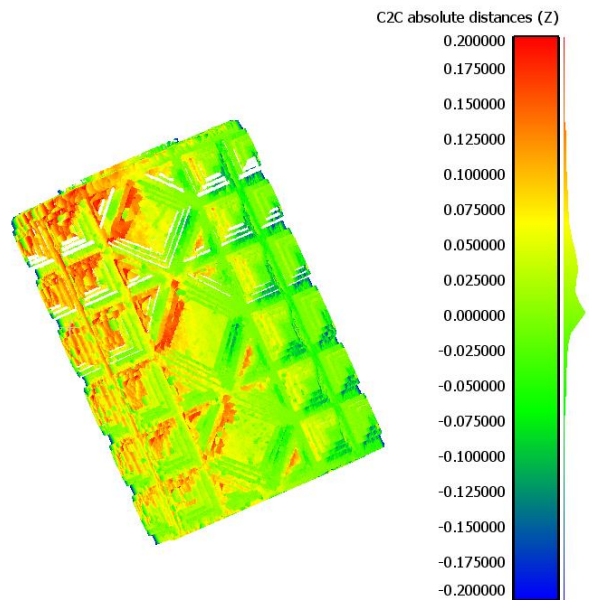

Figure 10. Distances along the Z axis resulting from the Cloud-to-Cloud application, registration was applied (by setting shift in the three directions x, y, z and rotation with respect to the z axis) of the two point clouds.
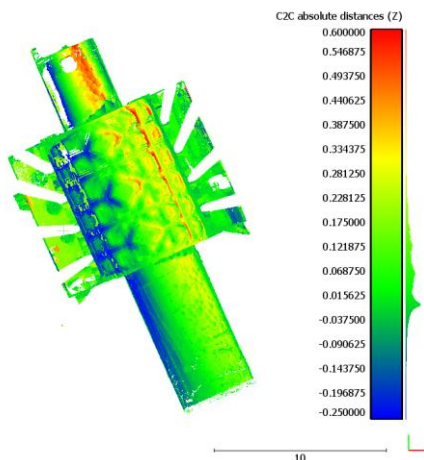
Figure 11. Distances along the z axis resulting from the Cloud-to-Cloud application, registration was applied by setting shift in the three directions x, y, z and rotation with respect to the z axis only.

a

b

Figure 12. Registration of the top part (a) and its distances (b) along the z axis resulting from the Cloud-to-Cloud application, registration was applied (by setting shift in the three directions x, y, z and rotation with respect to the z axis) of the two point clouds.

4. CONCLUSIONS

The present work made it possible to make some initial comparisons in a real archaeological survey operation. With regard to the survey of the internal parts, the possibility of surveying complex structures with Geoslam-type instrumentation was tested in comparison with more classic but costly and time consuming TLS surveys. In particular, it was verified that the survey of the entire internal structure and a large part of the external façade was carried out in less than 20 minutes, while the same survey of the internal parts alone with TLS took more than two hours. Assuming that the TLS is in any case more consistent in terms of maintaining the geometries (for the comparison, data obtained from a single TLS station were used), it would seem that Geoslam holds a good centimetric agreement for the first ten metres of the survey, subsequently increasing its "drift" as was to be expected. This effect would not seem to depend on incorrect georeferencing because even when calibrating one cloud over the other, the results do not seem to worsen. The Geoslam therefore proves to be a very interesting alternative for this type of survey where a large extension must be surveyed even without the accuracy of the more onerous (in terms of time) TLS. However, it is always possible to set up a network of reference points on the route, even in the interior with a classic terrestrial survey using a total station. As far as external clouds are concerned, the survey with RTK drone without ground reference points seems to give results very close to the more traditional use of the drone without RTK but with ground reference points of the GCPs application. The LIDAR survey from the same drone also seems very accurate. Only a systematism in altitude was observed between the RTK clouds and the other surveys all reverted to ground points, which could be due to the imperfect configuration of the height of the antennas on one of the GPS/GNSS receivers or to the use of different GNSS permanent stations and their materialisation. Further experimentation will be aimed at investigating these aspects more thoroughly with specific surveys.

REFERENCES

Alessandri, L., Baiocchi, V., Del Pizzo, S., Di Ciaccio, F., Onori, M., Rolfo, M.F. & Troisi, S., 2022: A flexible and swift approach for 3D image–based survey in a cave, *Applied Geomatics*, vol. 14, 5-19. https://doi.org/10.1007/s12518-020-00309-4

Alessandri, L., Baiocchi, V., Del Pizzo, S., Rolfo, M.F., Troisi, S., 2019: Photogrammetric survey with fisheye lens for the characterization of the la sassa cave, *ISPRS Annals of the Photogrammetry, Remote Sensing and Spatial Information Sciences*, 25. https://doi.org/10.5194/isprs-archives-XLII-2-W9-25-2019

Angelini, M. G., Baiocchi, V., Costantino, D., and Garzia, F., 2017: Scan to BIM for 3d reconstruction of the papal basilica of Saint Francis in Assisi in Italy. *Int. Arch. Photogramm. Remote Sens. Spatial Inf. Sci.,* XLII-5/W1, 47-54, DOI: 10.5194/isprsarchives-XLII-5-W1-47-2017.

Baiocchi, V., Giammarresi, V., Ialongo, R., Piccaro, C., Allegra, M. & Dominici, D., 2017: The survey of the basilica di collemaggio in L'Aquila with a system of terrestrial imaging and most proven techniques, *European Journal of Remote Sensing*, vol. 50, no. 1, 237-253. https://doi.org/10.1080/22797254.2017.1316523
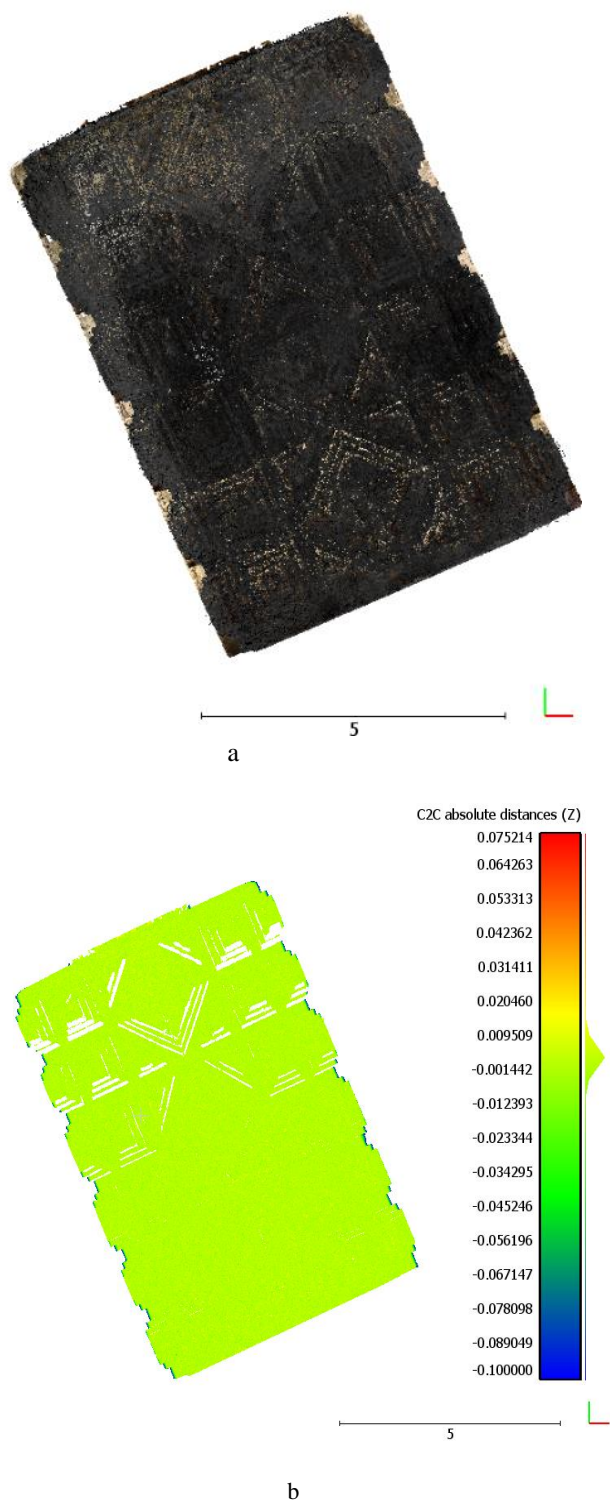
Figure 13. Registration of the top part (a) and its distances (b) along the z axis resulting from the Cloud-to-Cloud application, the registration of the two point clouds was applied (setting shift and rotation in the three directions x, y, z.

The same registration of the geoslam cloud on the laser was then performed, with shift along the x,y,z axes and rotation along all three x,y,z axes (fig. 13 a and b)

Baiocchi, V., Pizzo, S.D., Monti, F., Pugliano, G., Onori, M., Robustelli, U., Troisi, S., Vatore, F. & Trujillo, F.J.L., 2022: Solutions and limitations of the geomatic survey of an archaeological site in hard to access areas with a latest generation smartphone: the example of the Intihuatana stone in Machu Picchu (Peru), *Acta IMEKO*, vol. 11, no. 1. https://doi.org/10.21014/acta_imeko.v11i1.1117

Bitelli, G., Balletti, C., Brumana, R., Barazzetti, L., D'Urso, M.G., Rinaudo, F., Tucci, G., 2019: The gamher research project for metric documentation of cultural heritage: Current developments", *ISPRS Annals of the Photogrammetry, Remote Sensing and Spatial Information Sciences*, 239.

Caroti, G., Martinez-Espejo Zaragoza, I., Piemonte, A., 2015. Accuracy assessment in structure from motion 3D reconstruction from UAV-born images: The influence of the data processing methods. *Int. Arch. Photogramm. Remote Sens. Spat. Inf. Sci.,* XL-1/W4, 103–109. https://doi.org/10.5194/isprsarchives-XL-1-W4-103-2015.

Cassieri, N., 2015. Nuovi Risultati Di Indagine Dalle Ville Costiere Formiane. *Newsletter Di Archeologia* CISA 6: 67–93.

Cloudcompare development team, 2022, https://www.cloudcompare.org/ (last seen online: 10/06/2022)

D'Agostino, G., Figuera, M., Russo, G., Galizia, M., Militello, P.M., 2022: Integrated 3d survey for the documentation and visualization of a rock-cut underground built heritage, International Archives of the Photogrammetry, Remote Sensing and Spatial Information Sciences - ISPRS Archives, pp. 167.10.5194/isprs-archives-XLVI-2-W1-2022-167-2022

Del Pizzo, S., Troisi, S., 2011: Automatic orientation of image sequences in cultural heritage. *Int. Archives of Photogrammetry, Remote Sensing and Spatial Information Sciences*, 38(5/W16). https://doi.org/10.5194/isprsarchives-XXXVIII-5-W16-293-2011

DJI, 2022, http://www.dji.com (last seen online: 10/06/2022)

Dominici D., Rosciano E., Alicandro M., Elaiopoulos M., Trigliozzi S. and Massimi V., 2013. Cultural heritage documentation using geomatic techniques: Case study: San Basilio's monastery, L'Aquila, *Digital Heritage International Congress (DigitalHeritage)*, Marseille, 2013, 211-214. doi: 10.1109/DigitalHeritage.2013.6743735

Ebolese, D., Lo Brutto, M., Dardanelli, G., 2019: The integrated 3D survey for underground archeological environment. Int. Arch. Photogramm. Remote Sens. Spatial Inf. Sci., XLII-2/W9, 311– 317. doi.org/10.5194/isprs-archives-XLII-2-W9-311-2019.

Faro, 2002, https://www.faro.com/ (last seen online: 10/06/2022)

GEOSLAM, 2022, https://geoslam.com/solutions/zeb-horizon/ (last seen online: 10/06/2022)

Giavarini, C., 2001: Domus Aurea: The conservation project. *Journal of Cultural Heritage*, vol. 2, no. 3, 217-228. https://doi.org/10.1016/S1296-2074(01)01122-0

Giuliani, M., Cairoli, F., Guaitoli, M., 1972: Il Ninfeo Minore Della Villa Detta Di Cicerone a Formia. *Römische Mitteilungen*, 191–219. https://doi.org/10.1007/s10518-016-9881-z

Iheaturu, C., Ayodele, E., Okolie, C., 2020. An Assessment of the accuracy of Structure-from-Motion (SfM) Photogrammetry for 3D terrain mapping. *Geomatics, Landmanagement and Landscape*, 2, 65-82. http://dx.doi.org/10.15576/GLL/2020.2.65.

Lo Brutto, M., Garraffa, A., and Meli, P., 2014: UAV platforms for cultural heritage survey: first results. *ISPRS Ann. Photogramm. Remote Sens. Spatial Inf. Sci.*, Vol. II-5, 227-234. https://doi.org/10.5194/isprsannals-II-5-227-2014.

Masiero, A., Chiabrando, F., Lingua, A.M., Marino, B.G., Fissore, F., Guarnieri, A., Vettore, A., 2019: 3d modeling of Girifalco fortress. *Int. Arch. Photogramm. Remote Sens. Spatial Inf. Sci.*, XLII-2/W9, 473–478. https://doi.org/10.5194/isprsarchives-XLII-2-W9-473-2019.

MicMac Developer Team, 2022, https://micmac.ensg.eu/index.php/Install_MicMac_Windows (last seen online: 10/06/2022)

Pan, Y., Dong, Y., Wang, D., Chen, A., Ye, Z., 2019: ThreeDimensional Reconstruction of Structural Surface Model of Heritage Bridges Using UAV-Based Photogrammetric Point Clouds. *Remote Sens.*, 11, 1204. https://doi.org/10.3390/rs11101204.

Pirotti, F., Guarnieri, A., Vettore, A., 2013: State of the Art of Ground and Aerial Laser Scanning Technologies for High Resolution Topography of the Earth Surface. In *European Journal of Remote Sensing*, n. 46, 66-78.

Radicioni F., Matracchi P., Brigante R., Brozzi A., Cecconi M., Stoppini A., Tosi G., 2017: The Tempio della Consolazione in Todi: integrated geomatic techniques for a monument description including structural damage evolution in time. ISPRS - *Int. Arch. Photogramm. Remote Sens. Spat. Inf. Sci.,* XLII-5/W1, 433-440., https://doi.org/10.5194/isprs-archives-XLII-5-W1-433-2017

Sanz-Ablanedo, E., Chandler, J.H., Rodríguez-Pérez, J.R., Ordóñez, C., 2018. Accuracy of Unmanned Aerial Vehicle (UAV) and SfM Photogrammetry Survey as a Function of the Number and Location of Ground Control Points Used. *Remote Sens.*, 10, 1606. https://doi.org/10.3390/rs10101606.

Sarhosis, V., Asteris, P., Wang, T., Hu, W., Han, Y., 2016: On the stability of colonnade structural systems under static and dynamic loading conditions, *Bulletin of Earthquake Engineering*, vol. 14, no. 4, 1131-1152.

Troisi, S., Baiocchi, V., Del Pizzo, S., Giannone, F., 2017: A prompt methodology to georeference complex hypogea environments. *Int. Arch. Photogramm. Remote Sens. Spatial Inf. Sci.*, XLII-2/W3, 639–644. https://doi.org/10.5194/isprsarchives-XLII-2-W3-639-2017.

Turner, D., Lucieer, A., Watson, C., 2012. An Automated Technique for Generating Georectified Mosaics from UltraHigh Resolution Unmanned Aerial Vehicle (UAV) Imagery, Based on Structure from Motion (SfM) Point Clouds. *Remote Sens.*, 4, 1392-1410. https://doi.org/10.3390/rs4051392.

FINAL REMARKS

Geomatic techniques are currently experiencing a phase of significant innovation. According to some accredited researchers, many geomatic tools and techniques become outdated within two years. Therefore, it is necessary to investigate the most recently released techniques, as even within the timeframe of a doctoral thesis, some may prove to be no longer current. The experiments conducted throughout this thesis have allowed me to engage with the forefront of surveying technique development, verifying and understanding their advantages and limitations. While the latest satellite platforms provide free hyperspectral data worldwide, much work remains to be done on their geometric processing. Although the most advanced photogrammetry techniques simplify the entire processing workflow, greater attention must be paid to proper geometric framing. If laser scanning enables surveys at high speeds and from new perspectives, it is crucial to ensure that information about the sensor's geometry and its positioning sensors is accurate. We have learned much during this doctoral thesis, but we have also realized how much there is still to study.

APPENDIXES

Appendix 1- Additional Journal paper

Appendix 2- Notes on very preliminary results of ongoing research yet to be published

Article

ACYOTB Plugin: Tool for Accurate Orthorectification in Open-Source Environments

Valerio Baiocchi, Francesca Giannone, Felicia Monti and Felicia Vatore

Article

ACYOTB Plugin: Tool for Accurate Orthorectification in Open-Source Environments

Valerio Baiocchi [1,*](ID), Francesca Giannone [2], Felicia Monti [1] and Felicia Vatore [1]

[1]   Department of Civil, Constructional and Environmental Engineering, Sapienza University of Rome,
     I-00184 Rome, Italy; monti.1614926@studenti.uniroma1.it (F.M.); felicia.vatore@gmail.com (F.V.)
[2]   Niccolò Cusano University Via Don Carlo Gnocchi 3, 00166 Rome, Italy; francesca.giannone@unicusano.it
*   Correspondence: valerio.baiocchi@uniroma1.it; Tel.: +39-06-44585068

Abstract: High-resolution satellite images must undergo a geometric rectification process in order to be used for metrical purposes. This operation, called orthorectification, is necessary because of deformations mainly due to camera distortions and acquisition geometry. To correctly orthorectify an image, it is necessary to accurately reconstruct the photogrammetric-acquisition characteristics and the image position with respect to a reference system connected to the ground. This operation, called orientation, can be done using various mathematical models such as rigorous, rational polynomial function (RPF), and rational polynomial coefficient, or, according to some authors, rapid positioning coefficient (RPC) models. Orientation and orthorectification are usually performed within specific commercial software, but in QGIS, these complex operations can be performed using the open libraries of the Orfeo Tool Box (OTB). Unfortunately, instructions given by OTB developers lead to scarce results. In fact, the procedure proposed in OTB does not allow for the full exploitation of the potential of RPC models, on which OTB itself is based. As OTB is open-source software, a plugin was developed to overcome these limitations and exploit its full potential. In fact, OTB interfaces are unfortunately essential, and some necessary functions are missing. Therefore, a new QGIS plugin was developed in order to run the entire process in the most photogrammetrically and statistically correct way, and, at the same time, to simplify the relative procedures.

Keywords: QGIS; Orfeo Tool Box; RPC; accuracy; orthorectification; QuickBird; Ischia Island

1. Introduction

In the last twenty years, the availability of high- and very-high-resolution satellite images has stimulated methodological research for accurate geometric correction and the orientation of the images themselves. These corrections are necessary for accurate image orthorectification, an operation required to properly position the represented objects. Currently, the most established orthorectification models are based on the rigorous photogrammetric or the rapid positioning coefficient (RPC) approach; these models are almost exclusively available in closed-source commercial software. The possibility to orthorectify in free open-source software is necessary for the research world to disseminate the correct geometric management of the satellite images and to study possible improvements to the currently available models. We studied the possibilities of geometric correction made available by the Orfeo Tool Box (OTB), a library of open-source algorithms implemented within the GIS software QGIS, and we verified how some of the initial parameters of the RPC model could be improved to obtain results equal to or better than those of commercial software. This approach was implemented in a new QGIS plugin that was specifically developed by the authors and that allows for the entire process to be carried out, from data input to the estimation of the actual accuracy of the results, which is presently not possible. This paper describes the improvements that we propose to the OTB orthorectification process,

how they were implemented in our plugin, and the first obtained results, comparing them with those that could be obtained under the same condition using commercial software that is considered as a reference by the academic world.

2. Materials and Methods

The present experiment began from the verification of possibilities offered by the orthorectification module contained in open-source software OTB, an open library for processing and elaborating optical and radar images [1,2]. All OTB algorithms are accessible from Monteverdi, QGIS, and Python, and available through a command line or graphical interface. In this context, OTB QGIS functionalities, both command line and graphical interfaces, were checked: the former is more complex, even for experienced users, while not all functions are available in the latter.

The orthorectification of high-resolution satellite images is widely discussed in the literature [3,4], and several models have been developed for their orientation [5–7]. However, the availability of new images and models is always a reason for further research and development in search of increasingly optimized and efficient strategies [8,9]. Some commercial software have implemented rigorous, scientifically accredited models such as the well-known Toutin model [10], making such software [11,12] the reference for the most recently performed experiments.

The same cannot be said for open-source and freeware software packages for orthorectification: the available software is not user-friendly and is often poorly documented. Among these packages, the implementation of OTB in a QGIS environment up to the latest version, 3.x, is a matter of special interest.

OTB is built on the Insight Toolkit (ITK), a C++ library developed for image processing, and it manages raster and vector formats supported by the GDAL library, on which it relies for reading/writing data. As for sensor modeling and metadata reading, it is based on the OSSIM library and currently supports the Sentinel, Pléiades, SPOT6, SPOT5, and Digital Globe satellites. OTB is included in the standalone installation of QGIS for Windows, but it needs to be properly enabled and configured, defining the folder where the library was installed.

Once correctly installed, OTB applications can be directly accessed from the QGIS Processing Toolbox panel, and they provide a large number of useful functions to process remote-sensing images, from preprocessing to high-performance analysis such as orthorectification, sensor-model enhancement, segmentation, radiometric calibration, image fusion, pan-sharpening, and element extraction. Some functions, but unfortunately not all, are available with an intuitive graphical interface, simplifying data entry and input parameters, even for less experienced users, who could also take advantage of QGIS to edit, display, and compare different data formats (both raster and vector). As an alternative to the combined use of QGIS and OTB, the latter comes with Monteverdi, a satellite-image viewer that allows quick access to OTB functions, but not the editing and linking of data available with QGIS.

Subsequently, notwithstanding the knowledge of the correct application of photogrammetric models in the OTB, we analyzed the possibility of significantly improving the potential of the procedure, both from the simple point of view of its interface, and from the point of view of photogrammetric and statistical strictness of the operations.

In fact, OTB in QGIS currently does not allow for the accurate entry of measured ground control point (GCP) heights, which are always available when points are measured by differential GPS receivers.

At present, GCP heights in OTB are compulsorily estimated on a digital elevation model (DEM); the Shuttle Radar Topography Mission (SRTM) DEM is used if no DEM is available from the user. According to some authors, the SRTM DEM [13] has indeterminations of up to 10 m; in addition, the OTB only processes ellipsoidal heights, so the SRTM DEM must be corrected by the EGM96 geoid model, introducing further indetermination of the metric order.

Since the OTB is able to orthorectify decimetric ground resolution images (such as the QuickBird one used in this experiment), it is clear that metric approximations on the coordinates of input GCPs cannot provide optimal results. Moreover, in the OTB, it is currently only possible to insert GCPs,

but not check points (CPs), allowing us to only estimate precision, but not accuracy, as it is generally defined in statistics.

After a quick description of the experiments, the limits of the current procedure are explained in detail, and then possible solutions with the proposed plugin are illustrated. Finally, the experiment results using OTB with and without the plugin are shown in detail and compared with those obtained through the use of commercial software in rigorous and RPC mode.

2.1. Orientation Models

Aerial and satellite images must be oriented before they can be used for photogrammetric applications such as orthorectification and stereoscopic restitution [14,15].

In particular, for the orthorectification of satellite images, which is the subject of this research, the most widely used algorithms are based on two completely different approaches, generally defined as rigorous and RPC models.

Rigorous models are based on collinearity equations (photogrammetric approach) and describe the imagery acquisition considering geometrical and sensor characteristics. The reconstruction of the orbital segment during image acquisition is obtained by studying the acquisition mode, sensor features, satellite position, and attitude. Even though the rigorous model was not tested in this study, since OTB does not seem to support it with QuickBird images, it was considered quite important to briefly describe its characteristics in Appendix A.

A different type of orientation models is the rational polynomial functions (RPF) or the RPF with RPC. These types of models are completely independent from the physical and geometrical characteristics of the image acquisition. Their parameters can be directly estimated by GCPs by means of the least-squares estimation (RPF) or estimated a priori by the satellite provider, in which case the model is generally defined as RPC.

In the case of RPF, up to 30 uniformly distributed GCPs over the entire image are needed. With RPF, it is possible to obtain scarce accuracy if compared with RPC and the rigorous model. For this reason, RPF models calculated on GCPs are now rarely used. In contrast, RPC-based RPF models (generally referred to simply as RPC or RPC models) can orient the image even with very few GCPs, and with final accuracy close to that of the rigorous models.

In contrast with what is usually reported in the literature [5,6], we show in the discussion that, in this specific test, the RPC algorithms obtained slightly better results than those of the rigorous model of Toutin; for this reason, it was deemed that further tests should be carried out in order to understand the statistical significance of these specific results.

Both in the RPF and RPC models, the object coordinates (latitude, longitude, and ellipsoidal height) of a point are functions of pixel coordinates (I, J) using ratios of polynomial expressions:

$$
\begin{aligned}
I = \frac{P_1(\varphi,\lambda,h)}{P_2(\varphi,\lambda,h)} = \frac{a_0 + a_1\lambda + a_2\varphi + a_3h + a_4\lambda\varphi + \cdots + a_{17}\lambda^3 + a_{18}\varphi^3 + a_{19}h^3}{1 + b_1\lambda + b_2\varphi + b_3h + b_4\lambda\varphi + \cdots + b_{17}\lambda^3 + b_{18}\varphi^3 + b_{19}h^3} \\
J = \frac{P_3(\varphi,\lambda,h)}{P_4(\varphi,\lambda,h)} = \frac{c_0 + c_1\lambda + c_2\varphi + c_3h + c_4\lambda\varphi + \ldots + c_{17}\lambda^3 + c_{18}\varphi^3 + c_{19}h^3}{1 + d_1\lambda + d_2\varphi + d_3h + d_4\lambda\varphi + \ldots + d_{17}\lambda^3 + d_{18}\varphi^3 + d_{19}h^3}
\end{aligned}
\tag{1}
$$

where a_j, b_j, c_j, d_j are the coefficients; φ is latitude; λ is longitude; h is ellipsoidal height; I is the column of the pixel in the raster file; and J is the row.

The order of the RPF is generally less than or equal to 3, because a higher order does not substantially improve the results and it requires a very large number of GCPs. In particular, the National Imagery and Mapping Agency (NIMA) has defined a standardization for RPC contained in specific documentation, where the order of the polynomials is fixed at 3, all coordinates (image and terrain) are normalized in the range [+1; −1], using normalization parameters available in the metadata file. Normalized rather than actual values are used in order to minimize the introduction of errors during calculations [16].

The number of RPCs obviously depends on the polynomial order, so that for the third order, the maximum number of coefficients is 80 (20 for each polynomial), but it is reduced to 78 because

each equation is divided by the zero-order terms of the denominators. Within well-known GDAL libraries, direct transformation (1) and inverse transformation are available, where the former expresses image coordinates (I, J) as a function of 3D coordinates on the ground, and the latter expresses the 3D coordinates on the ground as a function of image coordinates (I, J). Both direct and inverse transformations of the ellipsoidal height of the points must be provided [17].

The orientation results obtained with RPC are usually refined introducing a 6-parameter 1st-order transformation in the RPF equation:

$$
\begin{aligned}
I &= A_0 + A_1 I + A_2 J + \frac{a_0 + a_1\lambda + a_2\varphi + a_3 h + a_4\lambda\varphi + \ldots + a_{17}\lambda^3 + a_{18}\varphi^3 + a_{19}h^3}{1 + b_1\lambda + b_2\varphi + b_3 h + b_4\lambda\varphi + \ldots + b_{17}\lambda^3 + b_{18}\varphi^3 + b_{19}h^3} \\
J &= B_0 + B_1 I + B_2 J + \frac{c_0 + c_1\lambda + c_2\varphi + c_3 h + c_4\lambda\varphi + \ldots + c_{17}\lambda^3 + c_{18}\varphi^3 + c_{19}h^3}{1 + d_1\lambda + d_2\varphi + d_3 h + d_4\lambda\varphi + \ldots + d_{17}\lambda^3 + d_{18}\varphi^3 + d_{19}h^3}
\end{aligned}
\tag{2}
$$

where the six parameters (A0, A1, A2, B0, B1, and B2) are estimated using a set of few GCPs [18–21].

We observed that OTB instead uses 5-parameter rototranslation [22] to refine RPC results:

$$
\begin{aligned}
I &= A_0 + s_\lambda \, \lambda \cos\alpha - s_\varphi \, \varphi \sin\alpha \\
J &= B_0 + s_\lambda \, \lambda \sin\alpha - s_\varphi \, \varphi \cos\alpha
\end{aligned}
\tag{3}
$$

This probably explains the different results that were obtained using the two software products, which are shown in detail below.

Currently, OTB supports RPC models for most high-resolution satellite images, while, according to the developers, "a more rigorous model is available for SPOT 5 and Sentinel" [23]. Having used a QuickBird image in this experiment, we were compelled to use the RPC model in OTB software. Despite this, details of the rigorous model are reported in Appendix A because it is important to precisely define what the meaning of the "rigorous model" is based on the photogrammetric approach, clarifying confusion on the subject that is sometimes found in the literature.

The accuracy of the final product strictly depends on the original image characteristics, on the quality of the measured coordinates of ground control points, and on the model chosen to perform the orientation.

Currently, the most used method to investigate the precision and the accuracy of the orientation models is residual analysis, which is based on known ground points that are partitioned into two sets: the first is used in the orientation model (GCPs) and is dedicated to model precision estimation; the second is used to validate the performance of the model itself (CPs) and to define the final accuracy of the product through the root mean square error (RMSE) of CP residuals [5,10].

Residual analysis is performed by comparing the image coordinates of the ground points collimated on the image with the image coordinates calculated through model equations and surveyed coordinates.

2.2. Experiment

The experiment was based on the study of a panchromatic image released by the QuickBird platform (0.7 m ground simple distance (GSD)) belonging to the ortho-ready standard category that was already corrected both radiometrically and geometrically, and also contained an approximate geographical transformation that provided a quick estimate of the image location, contained in the ".IMD" file, and also in the RPC parameters in the ".RPB" file.

There were 25 available ground points, but four of them were discarded because they were not univocally recognizable on the image (Figure 1). All of them were first used as GCPs because, as already explained, OTB does not currently allow the use of CPs. All points were measured with a double-frequency GPS/GNSS receiver and differentiated in postprocessing, and referred to the permanent ISCH station (yellow triangle in Figure 1), with baseline lengths always less than 6 km and a consequent centimeter accuracy for the 3D position. For each measured point, a descriptive monographic document was created to make their subsequent identification more certain for later studies; an example of a monograph is given in Appendix B.

Orthorectification of satellite images in OTB requires the succession of three independent applications. The first, *ReadImageInfo*, allows for the image metadata and sensor model to be read and writes them into a text file that becomes the input for the next application. The second, *RefineSensorModel*, adjusts the sensor model using a set of GCPs by calculating the five parameters of the double-scaled rototranslation that are exported to a new text file. The third is used as input, in addition to the raw satellite image and the digital terrain model, in the third and final step, *OrthoRectification*.

OTB can orthorectify by using different photogrammetric models including a "more rigorous" model [23]; here, the experiment focused on the RPC model that is currently the only one available for QuickBird images.
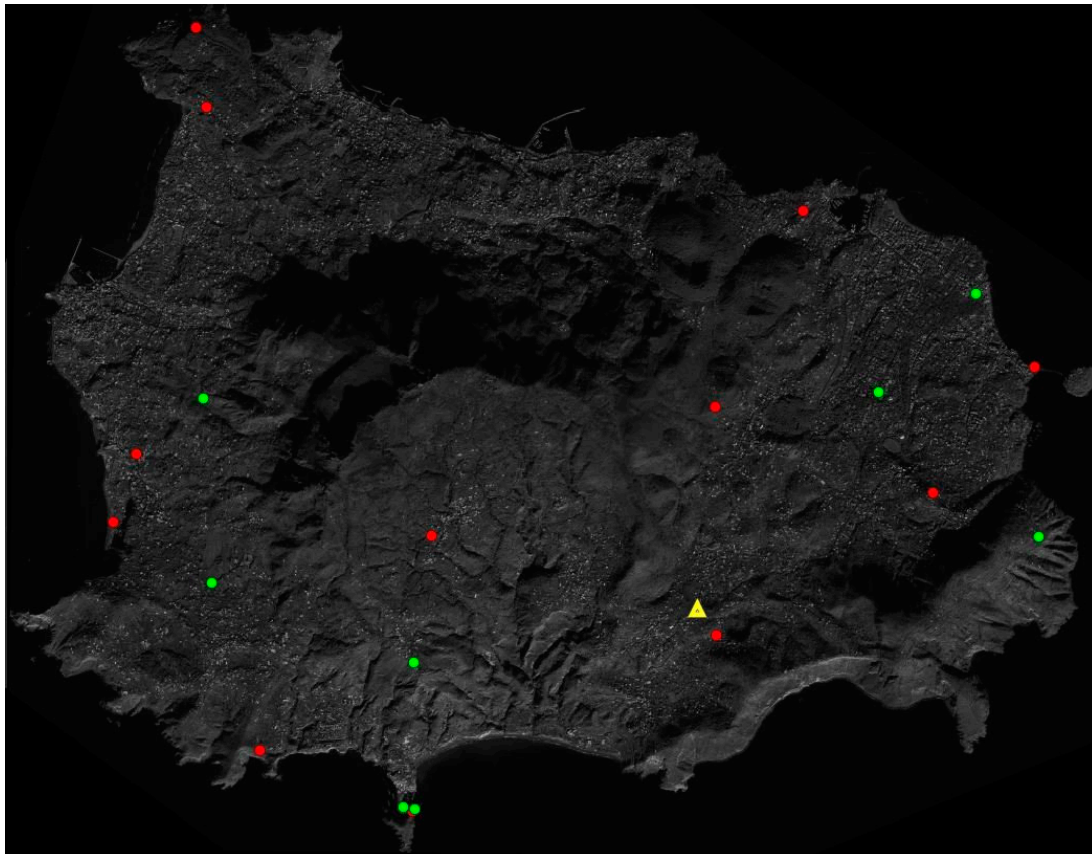
Figure 1. Ground control point (GCP) distribution used for the orthorectification process; the image is about 13 km wide. Red, GCPs; green, CPs; and yellow, permanent station "ISCH". Study area is the whole territory of Ischia Island, Italy.

2.2.1. Read Image Info

Command *otbgui_ReadImageInfo* provides a graphical interface to read the metadata of the image contained in the .IMD file; this command simultaneously reads even approximate positioning information of the image itself. By checking option "*Write the OSSIM keywordlist to a geom file*", the application allows for a ".geom" text file containing the information to be exported.

Currently supported sensors are GeoEye, Ikonos, Pleiades, QuickBird, RadarSat, Sentinel-1, SPOT5 (TIF format); as already mentioned, only for the last two satellites is a "more rigorous" model available according to the developers. It is not exactly clear what the meaning of a "more rigorous" model is, since orientation models in photogrammetry can be divided into rigorous (for example, the Toutin model) and not rigorous (such as the RPC and RPF models). For orthorectification purposes, the OTB needs a sensor model to reproject the image: if sensors are not supported, or the application does not detect any RPC model, the *otbgui_GenerateRPCSensorModel* command generates an RPC sensor

model from a list of GCPs by using the RPF approach. At least 20 points are required for estimation without DEM, and 40 points for estimation with height support. This function, which is actually an RPF model, was not tested here because RPF provided poor results in previous experiments [10].

2.2.2. RefineSensorModel

Command *RefineSensorModel* reads the previously exported ".geom" text file and a text file containing a list of GCPs as the input information, and provides a least-squares adjustment of the sensor model parameters as output. The application allows a new .geom text file that contains the five following transformation parameters to be exported:

- intrack_offset,
- crtrack_offset,
- intrack_scale,
- crtrack_scale, and
- map_rotation

2.2.3. DownloadSRTMTiles

If the user does not have an accurate DEM of the area, the software allows orthorectification, although with poor accuracy, by using the application otbgui_DownloadSRTMTiles, which allows the appropriate SRTM tiles covering the area of interest to be downloaded (Figure 2). SRTM tiles were downloaded from the USGS SRTM3 website [24]
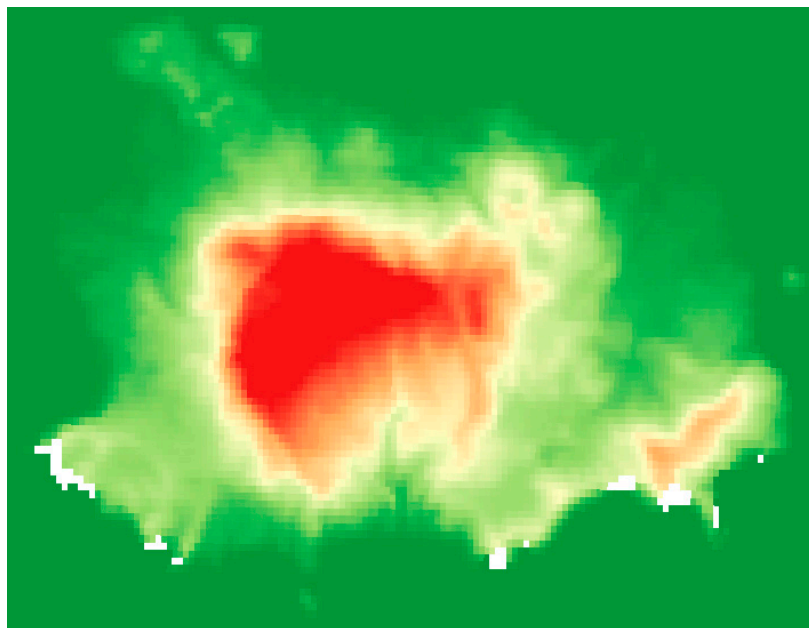
Figure 2. Shuttle radar topography mission (SRTM) tile; image is about 13 km wide. White pixels are "no data value" pixels.

The application downloads version 2.1 of DEM STRM with a 90 m resolution. As this DEM has indeterminations of up to 10 m, as previously mentioned, it is unsuitable for most experiments and applications with high- and very-high-resolution images. This DEM was tested to verify how much the use of the plugin improved the original results. The first verifications immediately showed unsatisfactory results because they were not accurate enough and because there were several void values (white pixels in Figure 2), mainly in the shoreline area. These inadequacies of the digital elevation model also influence the orthorectification process; in fact, the obtained orthophoto showed

discontinuities, as seen in Figure 3. For this reason, in the following orthorectification tests, a DEM obtained from the interpolation of a contour map on a 1:5000 scale was used; a planimetric cell size of 2 m was imposed on the final grid.

(**a**)   (**b**)
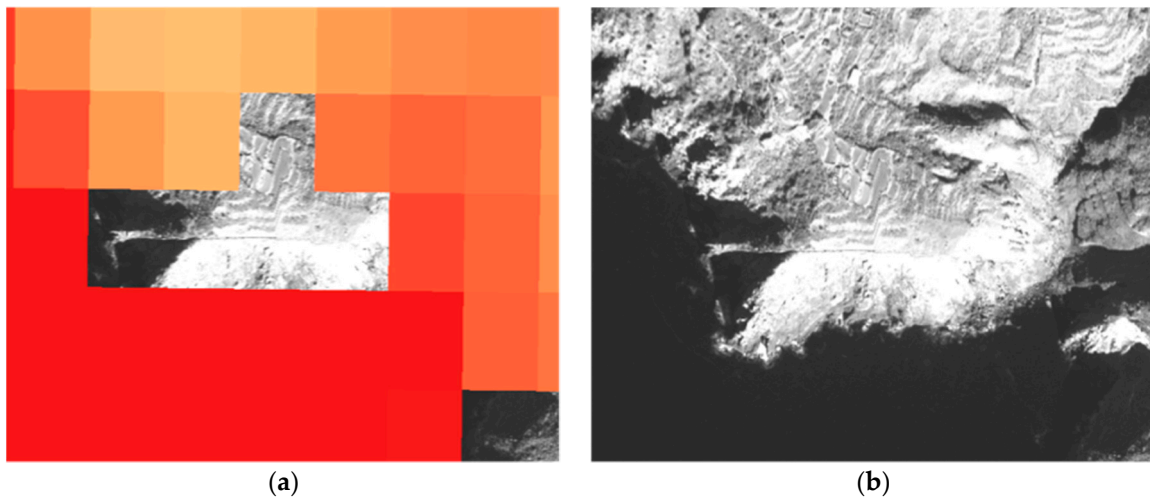
Figure 3. Detail of (**a**) "no data value" cells in SRTM and (**b**) obtained discontinuity in the orthorectified image.

2.2.4. OrthoRectification

This application allows the final orthorectified product to be obtained (i.e., the correction of the remotely sensed image from deformations that occurred during the acquisition phase. Command *otgui_OrthoRectification* opens a graphical interface that allows this process to be customized. In the experiment, as above-mentioned, we dealt with an Ortho-Ready QuickBird image (i.e., an image with georeferencing information). For an Ortho-Ready Standard product, according to OTB documentation, the software must be forced to omit approximate location information, inserting the path of the image in the input file, followed by the ?&skipcarto=true extension. A further constraint is to "force" the OTB to read the refined sensor model through the RefineSensorModel application, adding specific key &geom= to the input image path, followed by file path refine.geom (Figure 4).
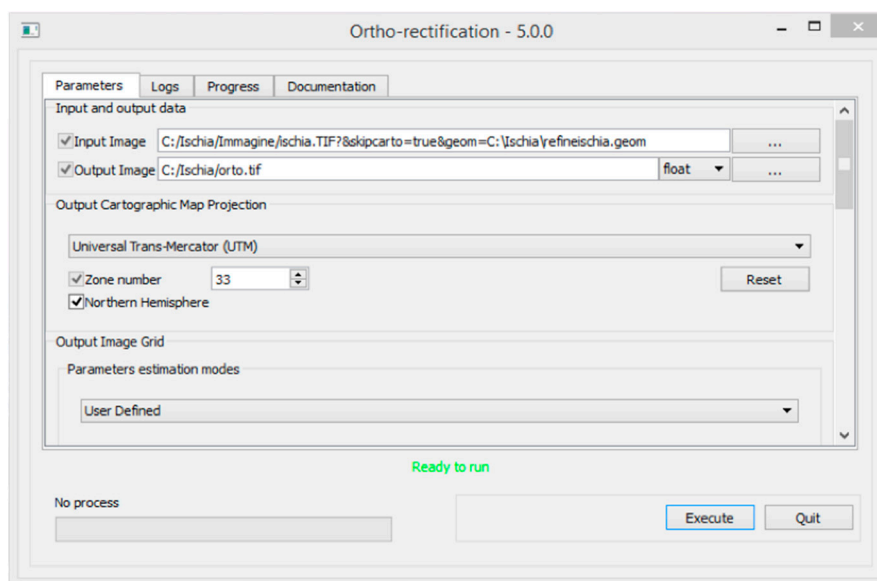
Figure 4. OrthoRectification module menu.

3. Results and Discussion

3.1. Current OTB Limits

OTB does not currently have a function for the collimation and management of GCPs and CPs, so in this experiment, the GCPs were collimated in the QGIS georeferencer, but image coordinates were not expressed according to OTB convention. Then, it was necessary to develop the first part of the plugin to further convert the image coordinates.

Moreover, in the OTB, as already mentioned several times, it is not possible to enter the value of the point heights, which are automatically obtained from the DEM uploaded in OTB by using the path of the folder that contains it. Since it is possible to only specify the path of the folder and not the name of the DEM file, it is advisable to insert a single file in the folder to avoid reading errors. In addition, the OTB performs all calculations with ellipsoidal heights; for this reason, if an orthometric DEM is used, a Geoid model is also needed. If, erroneously, an ellipsoidal DEM and Geoid file are introduced together, undulation is added anyway, providing incongruous results.

The impossibility of assigning a surveyed height to each ground point represents a serious fault of OTB in the orthorectification process because it does not allow the high precision of the coordinates of the ground control points acquired with a GPS/GNSS survey to be exploited. High-precision coordinates are necessary to obtain appropriate metric accuracy from high- and very-high-resolution images. At present, this inconvenience could be artificially circumvented by the creation of a "service DEM" (Figure 5) from the interpolation of the GCP heights; obviously, this DEM can only be used for this purpose because, moving away from the GCPs, heights become totally arbitrary.

Moreover, a further shortcoming of the OTB is its inability to select the type of collimated points as a check or ground control point, so that all of them are considered to be GCPs and used in the model estimation. For this reason, it is not possible to strictly estimate the accuracy of the final product, but only the precision of the orientation model; the latter usually shows lower values than those of the actual accuracy, so that confounding the two could lead to overestimation of the actual accuracy.

For this reason, the results indicated as "accuracy" in the *RefineSensorModel* (Figure 6) seem to be more model precision than accuracy, strictly defined according to the most accepted definition [25,26].
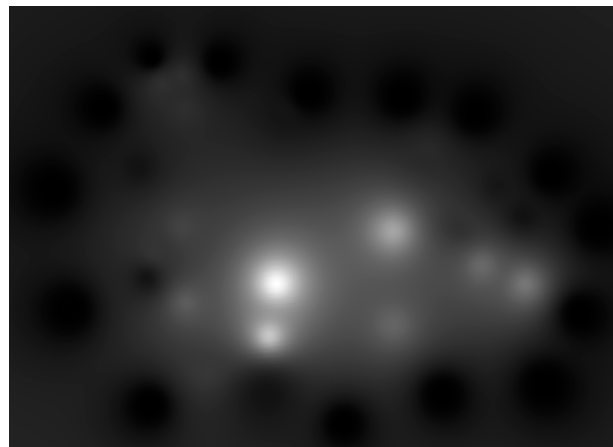
Figure 5. Fictitious digital elevation model (DEM) obtained from inverse distance weighted interpolation of GCP height values.
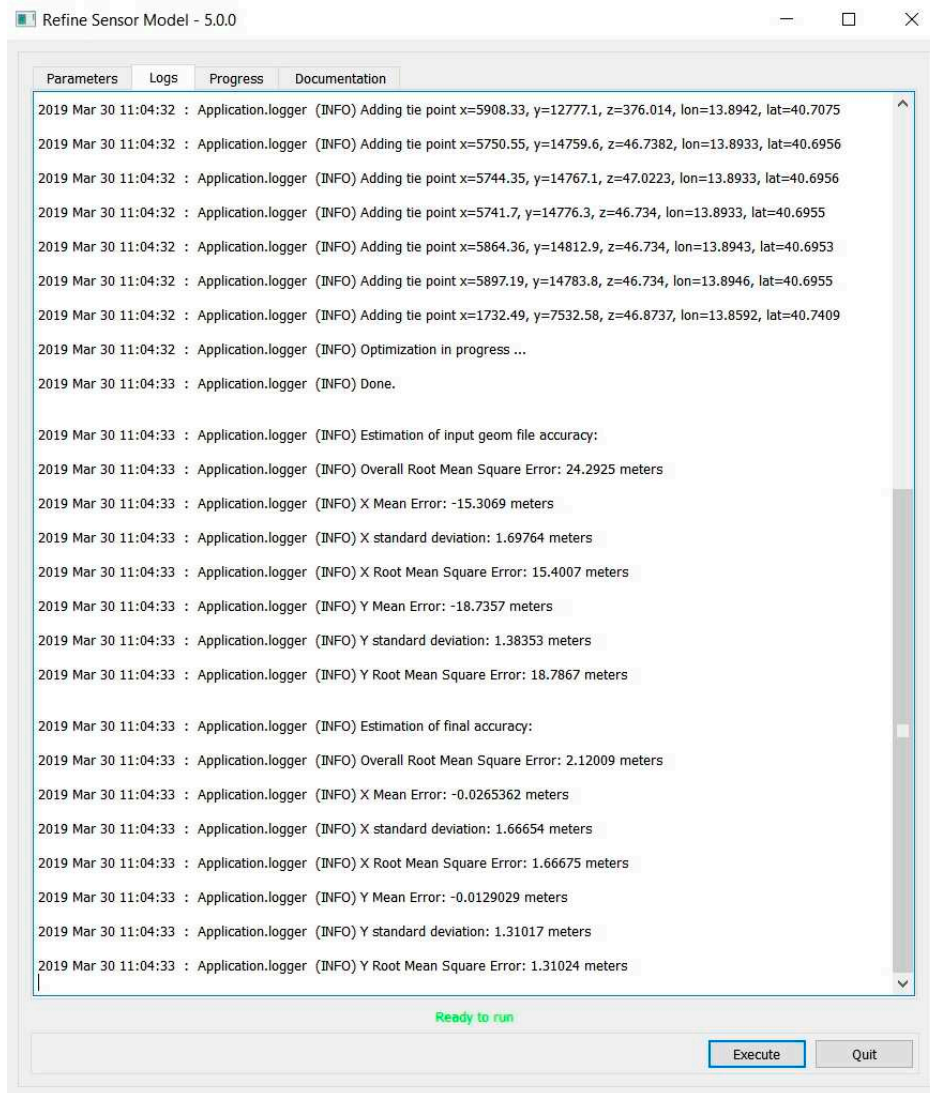
Figure 6. "Accuracy" report from *RefineSensorModel*.

3.2. ACYOTB Accuracy Estimation for OTB) Plugin

In order to facilitate orthorectification operations and to allow for real accuracy estimation, a QGIS plugin was implemented (Figure 7). First, the plugin can directly interface with the QGIS georeferencer; it is thus possible to directly collimate the points within the QGIS itself.

The OTB can only manage geographical coordinates and not projected coordinates; the ACYOTB plugin solves this problem because it can manage both. For any conversion between different projections, ACYOTB uses well-proven library PROJ.4 [27].

The previously described OTB criticality related to GCP height information, inserted only through a DEM, has been reported to the OTB development group. Waiting for a possible OTB development to fix this drawback, the ACYOTB plugin circumvents the problem by creating a "service DEM" by only using the three-dimensional coordinates of GPS GCPs (Figure 5). The service DEM is interpolated through the classical inverse distance weight (IDW) algorithm by using GPS-derived heights, and saved in a specific temporary directory. This DEM was used by the plugin only to estimate the GCP heights. For the final orthorectification step, a different DEM must be used.
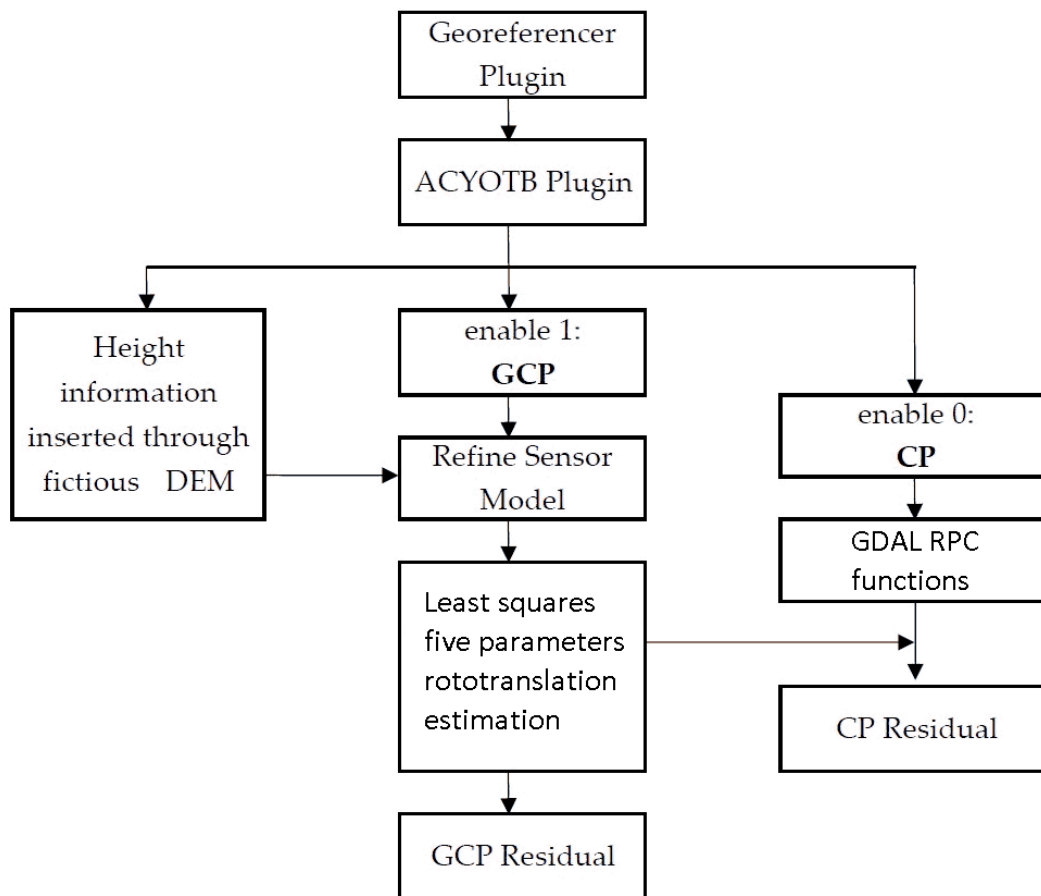
Figure 7. Flowchart of the accuracy estimation of the ACYOTB plugin. Ground points were divided into GCPs and CPs using the "enable" option of the QGIS georeferencing plugin.

In order to verify if interpolation of the service DEM decreases GCP height quality, the original GPS values of the heights were compared with those readable on the service DEM. Analysis showed that on only one point was the difference 1 mm, and on all other points it was less than 1 mm (Table A2). Considering that the height accuracy of the GNSS/GPS surveys is only a few centimeters, the error was always considered negligible.

The plugin also allowed the accuracy of the orientation model to be estimated considering a strict procedure based on CPs. In this way, it was possible to solve another OTB fault that currently does not allow CPs to be inserted, only GCPs (ground points used to refine the sensor model).

CPs are a set of ground points independent from GCPs, and they can be used to estimate the actual accuracy of the final results in terms of deviation from values measured on the ground. (Figure 8).

In order to estimate residuals on the CPs, it is necessary to calculate the predicted coordinates of the CPs themselves; residuals are in fact estimated by comparing the measured coordinates (for example, with the GPS) and corresponding predicted coordinates. OTB performs this calculation, but only on GCPs, so it is necessary to repeat the estimation for CPs.
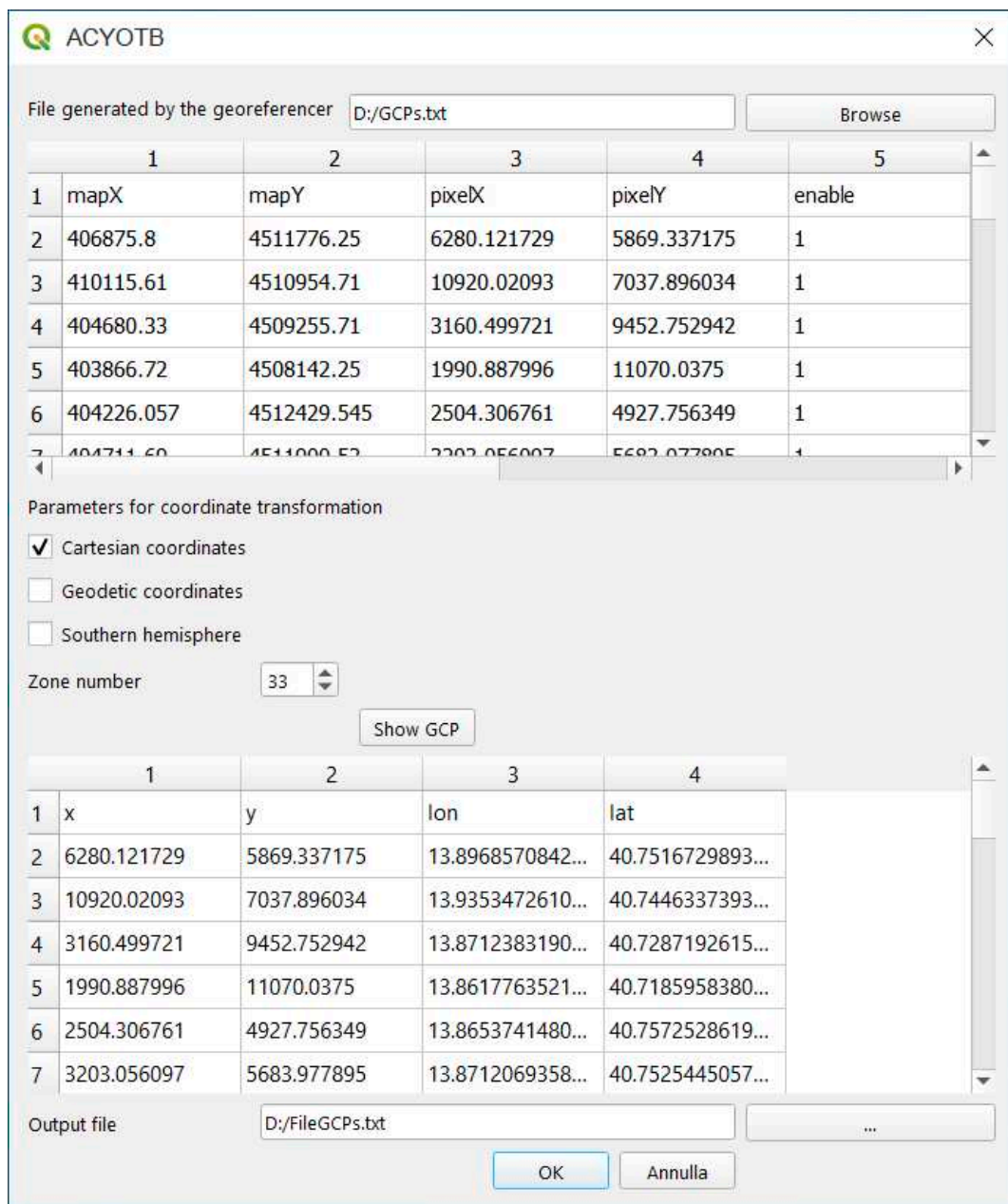
Figure 8. Graphical interface of the ACYOTB plugin. Input file was obtained from the QGIS georeferencer, while the output file is a text file in OTB format. If it is necessary, plugin automatically computes coordinate transformation.

The process takes place in two steps: first, image coordinates are transformed into ground coordinates using actual RPC transformations. This operation is carried out by using the appropriate functions of the GDAL libraries. These functions read RPCs directly from the header of the raw image tiff file that contains them, according to specifications defined by the NIMA. By using the RPCs of the raw image, they allow the ground coordinates of each point of the image to be recalculated. This first step allows for the recalculation of the coordinates of the various points with a bias that could be modeled by a rototranslation of the whole image. This rototranslation is necessary because RPCs are estimated by the owner of the satellite with only orbital data; to reach the accuracy of the ground-sample-distance (GSD) order, it is necessary to make corrections on the basis of some ground points. For this reason, the coordinates of the obtained points with the RPCs are then refined with a least-squares adjustment estimated rototranslation. Rototranslation is only estimated on the GCPs,

and rototranslation parameters thus obtained must then be applied to CPs to estimate the accuracy. The ACYOTB plugin uses the GDAL functions for the first step, and then uses a specially developed routine to estimate five-parameter transformation, starting from the coordinates of the GCPs in analogy with what OTB does.

It is assumed that other types of software such as PCI, perform the transformation in the same way, probably by using similar functions for the RPC; different results between PCI and the OTB with the plugin may be due to the fact that PCI uses six-parameter rototranslation. However, as PCI is closed commercial software, this is only a hypothesis.

3.3. Plugin Test Results

For a complete verification of the results that can be obtained with the plugin, we performed a series of tests using the same image and the same dataset in order to ensure the repeatability of the tests. First, a series of tests were carried out using all 21 points measured with GPS as GCPs; this series of tests was used to evaluate the precision of the different models. Residual analysis was performed by comparing the image coordinates of the ground point collimated on the image, with image coordinates calculated through model equations and surveyed coordinates. More specifically, the same points were used as GCP in the OTB by using different heights: elevations extracted from the SRTM DEM were corrected with the Geoid EGM96 model, and elevations obtained from the DEM were extracted from the 1:5000 contour map and the measured elevations (with GPS). The same GPS points were used in accredited commercial software PCI Geomatica 2018 (PCI). In this software, residuals on the 21 GCPs were estimated by using both the RPC model and the rigorous Toutin model. This last test was performed for a comparison with a model that is considered in the literature as representative of the state of the art for high- and very-high-resolution satellite images. The average residues separately calculated on 21 GCPs for 'across' and 'along track' components (x and y component, respectively) are shown in Table 1, while calculated values at each single point are shown in the complete table in Appendix C.

Table 1. Estimated precision on GCPs using different models and heights.

Orientation Model	PCI Rigorous		PCI RPC		OTB RPC		OTB RPC		OTB + Plugin RPC	
GCPs Height	h from GPS		h from GPS		h from SRTM +EGM96		h from 1:5000 Map		h from GPS	
DEM for Orthorectification	1:5000 Map DEM		1:5000 Map DEM		SRTM DEM + EGM96		1:5000 Map DEM		1:5000 Map DEM	
RMS Component	X RMS	Y RMS	X RMS	Y RMS	X RMS	Y RMS	X RMS	Y RMS	X RMS	Y RMS
RMS (meters)	0.540	0815	0.564	0.765	0.693	1.751	0.566	0.886	0.565	0.793

The indication of the used DEM for the final orthorectification is shown here only for greater clarity; in fact, actual orthorectification at this stage has not yet been done. In this regard, the use of an inaccurate DEM (such as SRTM) in the final orthorectification phase had the effect of further worsening the results compared to the already poor results reported in Tables 1 and 2. The precision of the results obtained with the plugin were absolutely equivalent if compared to the corresponding results of the PCI computed with both RPC and the rigorous model (slightly better in one component in the last case). From these first results, the precision of the OTB model seems even more balanced between the 'across' and 'along track' components if compared to the rigorous PCI model. Further tests with different image types are necessary to confirm this behavior.

A comparison between the obtained results considering the OTB with (column "OTB + plugin RPC") and without the plugin (column "OTB RPC/h from map" and "OTB RPC/ h from SRTM + geoid model EGM96") highlights clear residual improvement by using the plugin, especially in comparison with the heights from the SRTM DEM corrected with the EGM96.

Subsequently, to evaluate the actual accuracy of the final results, 10 out of the 21 points were only used as CPs; therefore, they were not used for the least-squares estimation of orientation parameters. The ten points were uniformly distributed over the area, as can be seen in Figure 1.

As already done for the precision estimation, tests were repeated by using the same points with different models: rigorous PCI, PCI RPC, and OTB RPC. In this case, the OTB RPC model was also tested with the GPS heights, DEM heights from the 1:5000 contour map, and SRTM + EGM96 heights in order to verify the OTB improvements by using the plugin. The average results can be seen in Table 2, while the complete results for each point can be verified in the Table A3.

Table 2. Estimated precision of 11 GCPs and accuracy of 10 CPs using different models and heights.

Orientation Model	PCI Rigorous		PCI RPC		OTB RPC		OTB RPC		OTB + Plugin RPC	
GCPs Height	h from GPS		h from GPS		h from SRTM +EGM96		h from 1:5000 Map		h from GPS	
DEM for Orthorectification	1:5000 Map DEM		1:5000 Map DEM		SRTM DEM + EGM96		1:5000 Map DEM		1:5000 Map DEM	
RMS Component	X RMS	Y RMS	X RMS	Y RMS	X RMS	Y RMS	X RMS	Y RMS	X RMS	Y RMS
Precision: GCPs RMS (meters)	0.435	0.904	0.459	0.700	0.589	1.609	0.492	0.890	0.519	0.706
Accuracy: CPs RMS (meters)	0.857	1.011	0.817	1.013	0.834	2.075	0.804	1.025	0.676	0.919

It can be observed that the accuracy results showed that the plugin (sixth column) significantly improved the OTB results without the plugin (fourth and fifth columns), up to twice on the along-track component. Comparing the obtained results with the plugin and with PCI (second and third columns), we can see that the accuracies were very similar for both the RPC and the rigorous model. Moreover, OTB results with the plugin seemed even better than the obtained results with the two PCI models; in this case, further tests must also be performed to validate this behavior.

4. Conclusions and Further Developments

The developed functions in OTB allow to orthorectify high- and very-high-resolution satellite images using several models. Currently, the OTB in QGIS has some limitations that significantly decrease the final achievable accuracy. Moreover, the interfaces of various operations are often complex to use, making it easier, in some cases, to use command-line functions. For this reason, the QGIS plugin described here was developed to simplify OTB usability and improve the accuracy of its results.

The described plugin made it possible to facilitate some operations including:

- capability of directly collimating the necessary points from the QGIS georeferencer without external software;
- feasibility to input GCP coordinates in different systems that are reprojected by the plugin;
- graphical interface for necessary options for proper orthorectification;
- input accurate heights for GCPs and CPs such as those measured with differential GPS; and
- ability to distinguish GCPs and CPs during the input step to evaluate the actual accuracy as defined in the statistics.

To verify the effectiveness of the ACYOTB plugin from the point of view of model precision and result accuracy, a complete set of tests were performed on an existing dataset. The results showed significant improvement in the accuracy and precision by performing the same operations in the OTB with and without the presented plugin. Using the RPC OTB model with the plugin, the results were practically the same (sometimes better) as the ones of accredited commercial software, both in comparison with the rigorous model and with the RPC model. The better results obtained from the OTB by using RPC with the plugin compared to PCI on the specific type of image could be due to the different rototranslation algorithms used. In fact, OTB uses five-parameter transformation, while

PCI instead uses the more widespread Affine transformation. The differences in the results could also be due to other causes, but since PCI, unlike OTB, is closed commercial software, it is difficult to understand them. On the other hand, open-source OTB functions could be further developed, expanded, and improved.

We plan to extend the plugin and experimentation to all other satellites available in the OTB in collaboration with its development team.

Author Contributions: Supervision, Valerio Baiocchi, Francesca Giannone, Felicia Monti and Felicia Vatore; Methodology, Valerio Baiocchi, Francesca Giannone, Felicia Monti and Felicia Vatore; Investigation, Valerio Baiocchi, Francesca Giannone, Felicia Monti and Felicia Vatore; Writing—Review and editing, Valerio Baiocchi, Felicia Monti and Felicia Vatore. All authors have read and agreed to the published version of the manuscript.

Conflicts of Interest: The authors declare no conflicts of interest.

Appendix A

Rigorous models are based on collinearity equations (photogrammetric approach), and describe imagery acquisition by considering geometrical and sensor characteristics. Reconstruction of the orbital segment during image acquisition is obtained by studying the acquisition mode, sensor features, satellite position, and attitude (Figure A1, Equation (A1)).

Collinearity equations relate the position of a point in the image space to the corresponding point in the object space, according to a central projection.
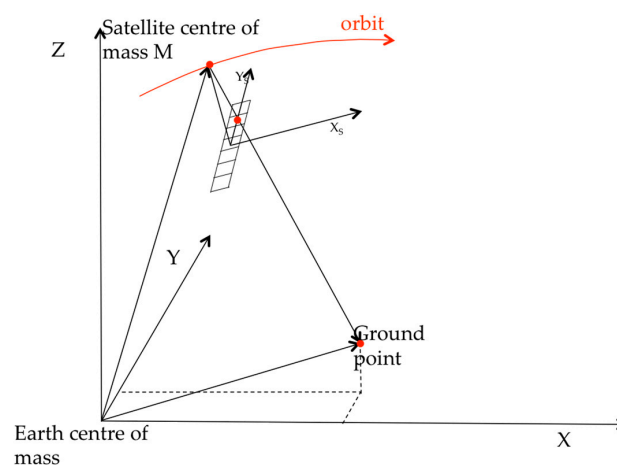
Figure A1. Rigorous photogrammetric model.

$$
\begin{cases}
\begin{cases}
\dfrac{x_s}{f} = \dfrac{R_{11}|X_t-X_S|+R_{12}|Y_t-Y_S|+R_{13}|Z_t-Z_S|}{R_{31}|X_t-X_S|+R_{32}|Y_t-Y_S|+R_{33}|Z_t-Z_S|} \\[2mm]
\dfrac{y_s}{f} = \dfrac{R_{21}|X_t-X_S|+R_{22}|Y_t-Y_S|+R_{23}|Z_t-Z_S|}{R_{31}|X_t-X_S|+R_{32}|Y_t-Y_S|+R_{33}|Z_t-Z_S|} \\[2mm]
f
\end{cases}
\end{cases}
\tag{A1}
$$

where

- f is the focal distance;
- R is the rotation matrix from ECI to the sensor system;
- x_s and y_s are the sensor system coordinates;
- X_t, Y_t, and Z_t are the ECI coordinates of the ground point, and
- X_s, Y_s, and Z_s are the ECI coordinates of the satellite.

The Earth-Centered Earth-Fixed (ECEF) system (E) is the origin is the Earth's center of mass, the X-axis is the intersection of equatorial plane and the plane of the reference meridian (transit meridian: close but not equal to the Greenwich meridian), the Z-axis is the mean rotational axis, and the Y-axis completes the right-handed coordinate system. The Earth Centered Inertial system (ECI) (I) is the origin of the Earth's center of mass, the X-axis points to vernal equinox (epoch J2000, 1 January 2000, ore 12 UT), the Z-axis points to the celestial North Pole (epoch J2000), and the Y-axis completes the right-handed coordinate system. The transformation matrix from the sensor to ECI system can be expressed as a function of Keplerian orbital parameters and attitude angles; approximate values for all parameters included in the model may be derived from metadata information released together with the image.

These approximate parameters must be corrected with least-squares estimation based on a suitable number of ground control points (GCPs), a set of points with object coordinates computed through a direct survey as a GNSS differential survey.

Usually, GCP coordinates are expressed in an ECEF reference frame (for example, RDN2008-ETRF2000 for Italy); so, in order to use them in collinearity equations, an ECEF–ECI transformation is needed. The ECI–ECEF rotation matrix is computed considering the motions of Earth in space: precession, nutation, polar motion, and Earth's rotation about its axis.

Even if rigorous models should theoretically provide the highest accuracy, they are complex models that require orbital parameters and sensor attitude information, and cannot be used when few or no GCPs are available; in fact, at least 10 GCPs are usually needed for each image.

Appendix B

Figure A2. Example of the GPS/GNSS surveyed point monography.

Appendix C

Table A1. Complete table for the model precision estimation on the GCPs.

Point ID	PCI Rigorous		PCI RPC		OTB h from Map		OTB h from GPS Measurements		OTB h from SRTM + EGM96 Geoid Model	
	Res X	Res Y	Res X	Res Y	Res X	Res Y	Res X	Res Y	Res X	Res Y
	m	m	m	m	m	m	m	m	m	m
1822	0.993	0.598	1.143	0.019	−0.959	0.627	−1.136	−0.052	−1.136	−0.052
391	−0.558	0.429	−0.825	1.400	0.523	−1.018	0.630	−0.903	0.630	−0.903
392	0.860	−0.457	0.691	−0.058	−0.919	1.143	−1.009	0.597	−1.009	0.597
sangel21	−0.583	0.060	−0.630	0.153	0.767	0.013	0.714	−0.165	0.714	−0.165
sangel31	−0.917	−0.115	−0.869	0.050	1.109	0.199	1.054	0.015	1.054	0.015
452	−0.325	−1.608	0.260	−0.200	−0.332	−0.192	−0.161	0.033	−0.161	0.033
molo arag1	0.350	0.967	0.139	0.210	−0.143	0.016	−0.168	−0.410	−0.168	−0.410
sangel11	0.767	−0.515	0.796	−0.568	−0.628	0.505	−0.655	0.405	−0.655	0.405
591	0.399	−0.314	0.269	0.786	−0.310	−0.795	−0.202	−0.430	−0.202	−0.430
822	0.326	−1.380	0.629	−1.474	−0.518	2.060	−0.588	1.796	−0.588	1.796
891	−0.636	1.439	−0.301	0.341	0.491	0.018	0.464	−0.136	0.464	−0.136
1852	0.194	−0.446	−0.210	0.265	0.033	−0.238	0.141	0.016	0.141	0.016
PC27075	−0.990	0.785	−0.929	0.159	0.648	−0.378	0.644	−0.702	0.644	−0.702
1851	−0.037	1.137	−0.124	0.993	0.411	−0.283	0.279	−0.830	0.279	−0.830
812	−0.042	0.803	−0.195	0.213	0.006	−0.147	0.094	0.113	0.094	0.113
482	−0.348	−1.127	−0.627	−0.833	0.762	1.227	0.566	0.421	0.566	0.421
471	0.460	−0.464	0.380	−0.025	−0.468	−0.015	−0.519	−0.522	−0.519	−0.522
sangel51	0.218	0.091	0.270	0.083	−0.012	0.072	−0.075	−0.140	−0.075	−0.140
muro sost1	0.038	0.396	0.093	0.292	−0.360	−1.141	−0.151	−0.879	−0.151	−0.879
811	−0.014	−0.803	0.345	−2.214	−0.301	2.307	−0.259	2.347	−0.259	2.347
sangel61	−0.156	0.525	−0.306	0.411	0.352	−0.311	0.281	−0.550	0.281	−0.550
	X RMS	Y RMS	X RMS	Y RMS	X RMS	Y RMS	X RMS	Y RMS	X RMS	Y RMS
	m	m	m	m	m	m	m	m	m	m
	0.540	0.815	0.564	0.765	0.566	0.886	0.565	0.793	0.693	1.751

Table A2. Complete table of different heights used; columns 1 and 3 do not show significant differences.

Ellipsoidal Heights in Metres			
Measured GPS Heights	Heights from Official Map + ITALGEO05 Geoid Model	"Fake" DEM Heights from GPS Measures	Heights from SRTM DEM + EGM96 Geoid Model
191.885	192.886	191.885	199.326
97.228	94.956	97.228	101.885
95.789	96.188	95.789	98.577
48.147	47.023	48.142	53.961
47.816	46.734	47.823	55.562
312.926	309.796	312.926	319.341
47.262	46.926	47.262	48.368
48.207	46.738	48.206	52.085
110.957	107.550	110.957	96.778
51.464	50.813	51.464	54.960
105.856	104.732	105.856	107.494
379.053	376.014	379.053	373.255
97.481	96.741	97.481	96.506
485.805	486.252	485.805	490.396
175.679	172.781	175.679	173.371
223.448	224.961	223.448	225.125
54.539	54.584	54.539	61.953
47.707	46.734	47.707	44.221
200.025	196.525	200.025	193.016
132.642	130.675	132.642	144.147
47.588	46.734	47.588	44.867

Table A3. Complete table for model precision estimation on 11 GCPs and accuracy on 10 CPs.

Point ID	Type	PCI Rigorous		PCI RPC		OTB h from Map		OTB h from GPS Measurements		OTB h from SRTM + EGM96 Geoid Model	
		Res X	Res Y	Res X	Res Y	Res X	Res Y	Res X	Res Y	Res X	Res Y
		m	m	m	m	m	m	m	m	m	m
1822	GCP	0.358	−0.042	0.745	−0.144	−0.525	0.860	−0.802	0.131	−0.135	2.274
391	GCP	−0.518	0.372	−0.663	1.067	0.320	−0.953	0.519	−0.793	0.499	−0.959
392	GCP	0.804	−0.535	0.801	−0.372	−1.063	1.204	−1.075	0.696	−1.169	0.275
452	GCP	−0.378	−1.753	0.003	−0.416	−0.058	0.066	0.044	0.259	0.468	1.595
molo aragonese 1	GCP	0.218	0.93	−0.212	0.006	0.239	0.420	0.085	−0.064	0.084	0.134
591	GCP	0.298	−0.067	−0.035	0.621	0.017	−0.779	0.102	−0.432	−0.743	−3.079
822	GCP	0.274	−1.239	0.518	−1.699	−0.410	2.034	−0.441	1.784	−0.195	2.583
891	GCP	−0.674	1.462	−0.378	0.101	0.560	0.010	0.577	−0.128	0.645	0.051
1851	GCP	0.218	0.961	−0.354	0.788	0.654	−0.165	0.494	−0.728	0.842	0.436
sangel51	GCP	−0.335	0.026	−0.127	−0.059	0.421	0.148	0.295	−0.100	0.253	−0.019
muro sost1	GCP	−0.266	−0.114	−0.297	0.11	0.065	−0.796	0.149	−0.592	−0.421	−1.844
sangel21	CP	1.778	−0.680	1.584	−0.798	1.389	0.293	0.589	−0.074	1.238	1.103
sangel31	CP	1.151	0.346	1.151	0.346	1.103	0.920	0.912	0.091	1.757	3.248
sangel11	CP	−0.731	−0.416	−0.731	0.183	−0.536	0.751	−0.580	−0.211	0.047	2.409
1852	CP	−0.472	−0.250	0.164	−0.837	0.518	−0.362	0.431	−0.590	0.383	−0.887
PC27075	CP	1.121	−1.118	0.505	−0.498	1.057	−0.029	1.073	−0.203	0.676	−0.720
812	CP	−0.123	−1.264	−0.172	−0.092	0.331	−0.104	0.220	−0.300	0.319	0.049
482	CP	0.553	2.463	1.125	1.874	1.071	1.391	1.071	1.391	1.214	0.962
471	CP	−0.138	0.066	0.473	0.085	−0.214	0.505	−0.214	−0.373	0.018	1.129
811	CP	−0.477	0.334	−0.491	2.148	−0.435	2.585	−0.582	2.395	0.283	4.681
sangel61	CP	0.519	−0.614	0.519	−0.614	0.401	−0.050	0.366	−0.312	0.282	0.246
	GCP	X RMS	Y RMS	X RMS	Y RMS	X RMS	Y RMS	X RMS	Y RMS	X RMS	Y RMS
		m	m	m	m	m	m	m	m	m	m
		0.435	0.904	0.459	0.700	0.492	0.890	0.519	0.706	0.589	1.609
	CP	X RMS	Y RMS	X RMS	Y RMS	X RMS	Y RMS	X RMS	Y RMS	X RMS	Y RMS
		m	m	m	m	m	m	m	m	m	m
		0.857	1.011	0.817	1.013	0.804	1.025	0.676	0.919	0.834	2.075

References

1. Grizonnet, M.; Michel, J.; Poughon, V.; Inglada, J.; Savinaud, M.; Cresson, R. Orfeo ToolBox: open source processing of remote sensing images. *Open Geospat. Data Softw. Stand.* **2017**, *2*. [CrossRef]
2. Teodoro, A.C.; Araujo, R. Comparison of performance of object-based image analysis techniques available in open source software (Spring and Orfeo Toolbox/Monteverdi) considering very high spatial resolution data. *J. Appl. Remote. Sens.* **2016**, *10*. [CrossRef]
3. Heipke, C.; Jacobsen, K.; Mills, J.P. High-resolution earth imaging for geospatial information, part II. *Photogramm. Rec.* **2008**, *23*, 351–352. [CrossRef]
4. Heipke, C.; Jacobsen, K.; Mills, J.P. High-resolution earth imaging for geospatial information, Part I. *Photogramm. Rec.* **2008**, *23*, 252–254. [CrossRef]
5. Baiocchi, V.; Crespi, M.; De Vendictis, L.; Giannone, F. A new rigorous model for the orthorectification of syncronous and asyncronous high resolution imagery. In *Proceedings of the 24th EARSel Symposium on New Strategies for European Remote Sensing, Dubrovnil, Croatia, 25–27 May 2004*; Oluić, M., Ed.; Millpress: Rotterdam, The Netherlands, 2005; ISBN 90 5966 003 X.
6. Toutin, T. State-of-the-art of geometric correction of remote sensing data: a data fusion perspective. *Int. J. Image Data Fusion* **2011**, *2*, 3–35. [CrossRef]
7. Jacobsen, K. Systematic geometric image errors of very high resolution optical satellites. *Int. Arch. Photogramm. Remote. Sens. Spat. Inf. Sci.* **2018**, *-XLII-1*, 233–238. [CrossRef]

8. Topan, H.; Jacobsen, K.; Cam, A.; Ozendi, M.; Oruc, M.; Bakioğlu, O.B.; Bayik, C.; Taşkanat, T. Comprehensive evaluation of Pléiades-1A bundle images for geospatial applications. *Arab. J. Geosci.* **2019**, *12*, 223. [CrossRef]

9. Zhang, R.; Zhou, G.; Zhang, G.; Zhou, X.; Huang, J. RPC-Based Orthorectification for Satellite Images Using FPGA. *Sensors* **2018**, *18*, 2511. [CrossRef] [PubMed]

10. Toutin, T. Review article: Geometric processing of remote sensing images: models, algorithms and methods. *Int. J. Remote. Sens.* **2004**, *25*, 1893–1924. [CrossRef]

11. Technical Specification-Technical Specification. Available online: www.pcigeomatics.com/pdf/geomatica/techspecs/2018/Satellite-Ortho-Suite.pdf (accessed on 28 March 2019).

12. ENVI Photogrammetry Module. Available online: www.harrisgeospatial.com/Portals/0/pdfs/HG_ENVI_Photogrammetry_module_data-sheet_WEB.pdf (accessed on 28 March 2019).

13. Mukul, M.; Srivastava, V.; Jade, S.; Mukul, M. Uncertainties in the Shuttle Radar Topography Mission (SRTM) Heights: Insights from the Indian Himalaya and Peninsula. *Sci. Rep.* **2017**, *7*, 41672. [CrossRef] [PubMed]

14. Fraser, C.S.; Yamakawa, T.; Hanley, H.B.; Dare, P.M. Geopositioning from high-resolution satellite imagery: experiences with the affine sensor orientation model. In Proceedings of the 2003 IEEE International Geoscience and Remote Sensing Symposium, Toulouse, France, 21–25 July 2003. [CrossRef]

15. Lei, Z.; Wang, M.; Li, D.; Lei, T.L. Stream Model-Based Orthorectification in a GPU Cluster Environment. *IEEE Geosci. Remote. Sens. Lett.* **2014**, *11*, 2115–2119. [CrossRef]

16. NIMA—National Imagery and Mapping Agency. The Compendium of Controlled Extensions (CE) for the National Imagery Transmission Format (NITF). Available online: http://geotiff.maptools.org/STDI-0002_v2.1.pdf (accessed on 28 March 2019).

17. GDAL. Available online: http://gdal.org/gdal.pdf (accessed on 18 October 2019).

18. Rupnik, E.; Pierrot Deseilligny, M.; Delorme, A.; Klinger, Y. Refined satellite image orientation in the free open-source photogrammetric tools apero/micmac. *ISPRS Ann. Photogramm. Remote. Sens. Spat. Inf. Sci.* **2016**, *III-1*, 83–90. [CrossRef]

19. Fraser, C.S.; Hanley, H.B. Bias-compensated RPCs for Sensor Orientation of High-resolution Satellite Imagery. *Photogramm. Eng. Remote. Sens.* **2005**, *7*, 909–915. [CrossRef]

20. Hanley, H.B.; Fraser, C.S. Sensor orientation for high-resolution satellite imagery: Further insights into bais-compensated RPCs. *Photogramm. Eng. Remote. Sens.* **2004**, *71*.

21. Zhou, G.; Li, R. Accuracy Evaluation of Ground Points from IKONOS High-Resolution Satellite imagery. *Photogramm. Eng. Remote. Sens.* **2000**, *66*, 1103–1112.

22. Greenfeld, J.S. Least squares weighted coordinate transformation formulas and their applications. *J. Surv. Eng.* **1997**, *123*, 147–161. [CrossRef]

23. OTB Users, Orectification Models. July 2019. Available online: http://otb-users.37221.n3.nabble.com/Orthorectification-models-td4031100.html (accessed on 19 December 2019).

24. SRTM Web Site. Available online: http://dds.cr.usgs.gov/srtm/version2_1/SRTM3/ (accessed on 19 December 2019).

25. Baiocchi, V.; Lelo, K. Accuracy of 1908 high to medium scale cartography of Rome and its surroundings and related georeferencing problems. *Acta Geodaetica et Geophysica Hungarica* **2010**, *45*, 97–104. [CrossRef]

26. Pulighe, G.; Baiocchi, V.; Lupia, F. Horizontal accuracy assessment of very high resolution Google Earth images in the city of Rome, Italy. *Int. J. Digit. Earth* **2016**, *9*, 342–362. [CrossRef]

27. PROJ Coordinate Transformation Software Library. Release 6.0.0. 21 January 2019. Available online: https://raw.githubusercontent.com/OSGeo/proj.4/gh-pages/proj.pdf (accessed on 19 December 2019).

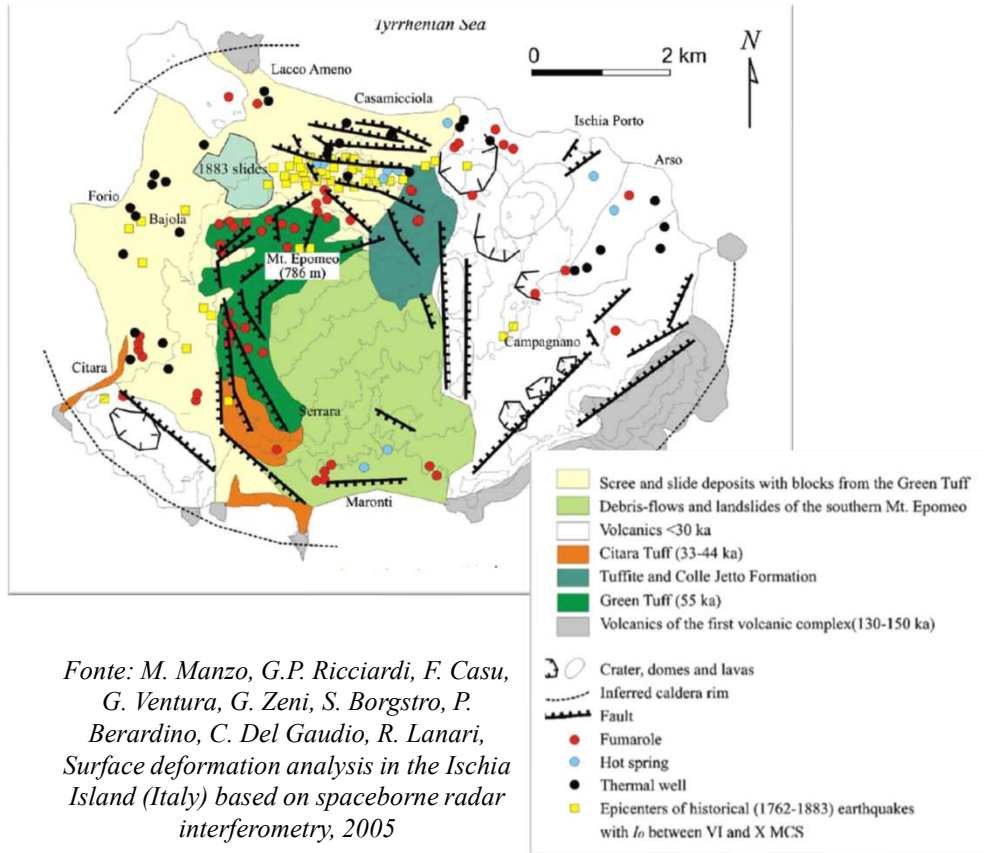Corso di Dottorato in Ingegneria Ambientale e Idraulica, XXXVI ciclo

***Advancements in Photogrammetric and LiDAR Techniques: Innovations,
Applications, and Implications for Precision Mapping and 3D Modeling***

Tutor: Prof. Valerio Baiocchi
coTutor: Prof.ssa Francesca
Giannone
Dottoranda: Felicia Monti
Curriculum ambientale

Anno Accademico: 2023/2024

Pubblicazioni e partecipazioni a convegni

- Alessandri, L., Baiocchi, V., Monti, F., *Ancient landscape reconstruction using archive data from the Pontine Plain (Italy): the Caprolace lagoon case study,* MetroArchaeo 2021 (International Conference on Metrology for Archaeology and Cutural Heritage)

- Baiocchi, V., Lombardi, M., Monti, F., *The contribution of open-source gis software and open spatial data for the re-evaluation of landslide risk and hazard in view of climate change*, GEOGRAPHIA TECHNICA

- Baiocchi, V., Giannone, F., Monti, F*., Orthorectification of Prisma images*, AIT2021 Volume, Intervento presentato alla X AIT International Conference

- Blanco, D., Alessandri, L., Baiocchi, V., De Laurenzi, A., Monti, F., Nicolosi, i., Urbini, S., Vatore, F., *A new branch of the Anio Novus aqueduct (Rome, Italy) revealed by archaeology and geophysics*, ISPRS Annals of the Photogrammetry, Remote Sensing and Spatial Information Sciences; Gottingen Vol. VIII-M-1-2021, 2021: 49-56. DOI:10.5194/isprs-annals-VIII-M-1-2021-49-2021

Fonte: M. Manzo, G.P. Ricciardi, F. Casu, G. Ventura, G. Zeni, S. Borgstro, P. Berardino, C. Del Gaudio, R. Lanari, Surface deformation analysis in the Ischia Island (Italy) based on spaceborne radar interferometry, 2005

Fonte: Bollettino mensile agosto 2017 INGV

L'interferometria è la misurazione delle **variazioni della fase**, relative ad ogni pixel, del segnale RADAR tra due acquisizioni distinte relative alla stessa area. Tale tecnica consente di misurare (lungo la LOS del sensore) lo spostamento del suolo con accuratezza centimetrica.
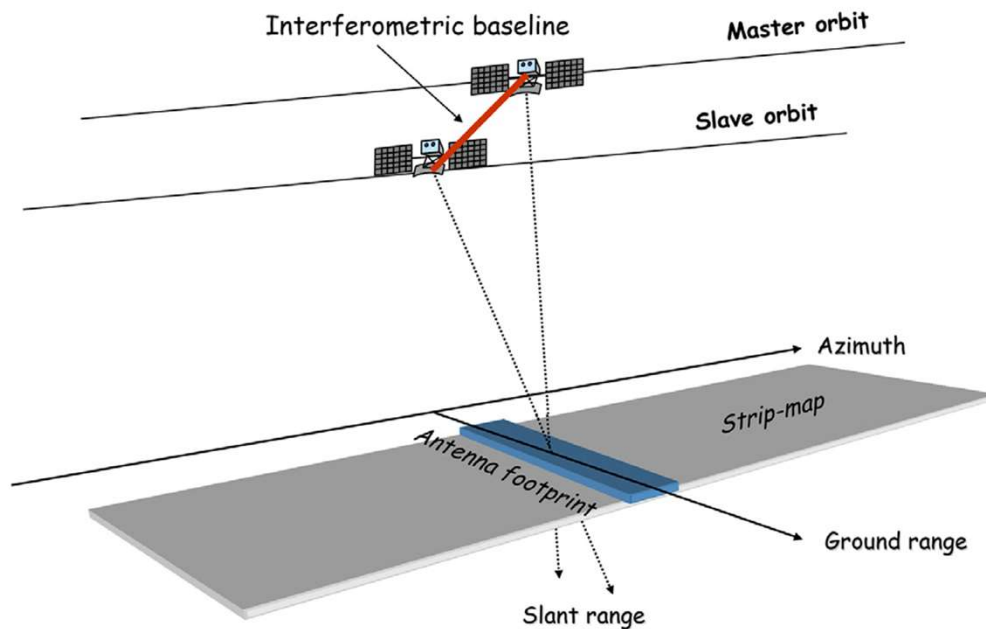
Le orbite devono essere nominalmente uguali, ma invitabilmente si ha:

- **Normal baseline Bn**: distanza relativa tra i satelliti, proiettata lungo la direzione ortogonale alla LOS

- Diverso angolo di acquisizione

Dunque, le due acquisizioni avranno una geometria radar leggermente diversa. Di conseguenza, per confrontare le due immagini è necessario ricampionarle su una stessa griglia comune.

L'interferometria è la misurazione delle **variazioni della fase**, relative ad ogni pixel, del segnale SAR tra due acquisizioni distinte relative alla stessa area.

Scopo: ricavare la fase interferometrica del punto P rispetto a un punto di riferimento O.

Master

S_k

θ

$|\overline{OP}|_n$

P

Δh

O r

x

Δr
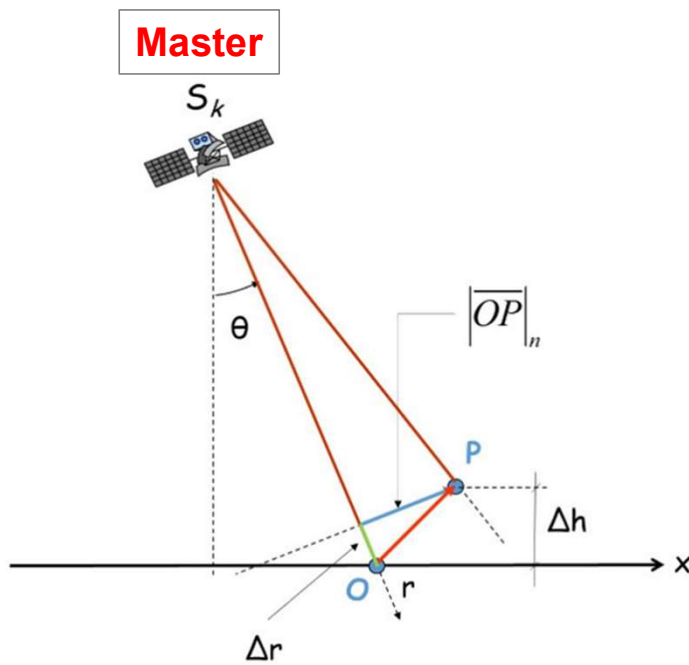
$$\Delta\varphi_{i,k} = \varphi_{i,k}(P) - \varphi_{i,k}(O) = \frac{4\pi}{\lambda}[R_{i,k}(P) - R_{i,k}(O)]$$

$$\begin{cases} R_{i,k}(P) = \overline{S_iP} - \overline{S_kP} \\ R_{i,k}(O) = \overline{S_iO} - \overline{S_kO} \end{cases}$$

$$\Delta\varphi_{i,k} = \frac{4\pi}{\lambda}\frac{B_n}{R_k}|\overline{OP}|_n$$

$$|\overline{OP}|_n = \frac{\Delta r}{tan\vartheta} + \frac{\Delta h}{sin\vartheta}$$

$$\Delta\varphi_{i,k} = \frac{4\pi}{\lambda}\frac{B_n}{R_k}\frac{\Delta r}{tan\vartheta} + \frac{4\pi}{\lambda}\frac{B_n}{R_k}\frac{\Delta h}{sin\vartheta}$$

$$\Delta\varphi_{i,k} = \Delta\varphi^{i,k^{FLAT}} + \Delta\varphi^{i,k^{TOPOG}}$$

Nella condizione ideale Bn=0
$$\Delta\varphi_{TOPOG}= 0$$
$$\Delta\varphi_{FLAT}= 0$$

$$\Delta\varphi_{mov}= \frac{4\pi}{\lambda}\Delta r$$

Sensore in banda C

λ=6 cm
$\Delta h_a \sim$ 1 cm

La variazione di fase comprende:

$$\Delta\varphi_{int}= \Delta\varphi_{flat} + \Delta\varphi_{topog} + \Delta\boldsymbol{\varphi_{mov}} + \Delta\varphi_{atmo}$$

$$\frac{4\pi}{\lambda}\frac{B_n\,r}{R\,tan\vartheta} \qquad \frac{4\pi}{\lambda}\frac{B_n\,\Delta h}{R\,sin\vartheta} \qquad \frac{4\pi}{\lambda}\Delta r$$

$$\Delta\varphi_{int}= \Delta\varphi_{mov} + \Delta\varphi_{atmo} + \Delta\varphi_{error}$$

- Incertezza delle orbite
- Decorrelazione

Fino ad oggi nessuna tecnologia è in grado di fornire una stima del ritardo atmosferico con **risoluzione spaziale** e una **sensibilità** simili a quelle dell'interferometria SAR.

Se il ritardo atmosferico non può essere stimato e rimosso con precisione, non è possibile recuperare in modo affidabile l'altezza del bersaglio.

Limiti dell'analisi InSAR:
- Decorrelazione del segnale
- Contributo atmosferico

2015   SENTINEL-1   2019

2019   COSMO SKY-MED   2023

21 agosto 2017

Sentinel-1A	16.08.2017 – 22.08.2017
COSMO SKY-MED	19.08.2017 – 23.08.2017

Disponibilità dei dati COSMO-SkyMed

- Descrizione del Progetto: Progetto Open Call Id 758 Titolo: *Monitoring of land in different zones of Italy using COSMO-SkyMed imagery*.

- 80 immagini di archivio

- 20 nuove acquisizioni

	Banda	Frequenza	Lunghezza d'onda
	P	0.25/0.5 GHz	100 cm
	L	1.0/2.0 GHz	30 cm
	S	2.0/4.0 GHz	10 cm
Sentinel 1	C	4.0/8.0 GHz	6 cm
COSMO Sky-Med	X	8.0/12.0 GHz	3 cm
	K	12/40 GHz	1 cm
	Q	40/50 GHz	0.5 cm

Single Interferogram processing

1. **Impostazione immagine Master/Slave**
2. **Coregistrazione delle immagini:**

immagini Sentinel con orbite precise possiamo eseguire la coregistrazione utilizzando solo le orbite.

È possibile caricare un dem per supportare la coregistrazione

3. **Analisi preliminare:**

Poiché abbiamo una serie di immagini, la prima cosa da fare è cliccare su **reflectivity map** and **amplitude stability index**, per creare:

Reflectivity map_CSK

- ○ **Reflectivity map**

- ○ **Amplitude stability index**

4. Georeferenziazione dei dati
5. Single Interferogram processing

- ○ **Flattening (Goldstein filter)**

- ○ **DEM Removal**

Interferogramma

- ● **Phase unwrapping**

Mappa di deformazione

0   0.25   0.50   0.75   1

	COSMO-SkyMed	Sentinel-1A
Ascending		
Descending		
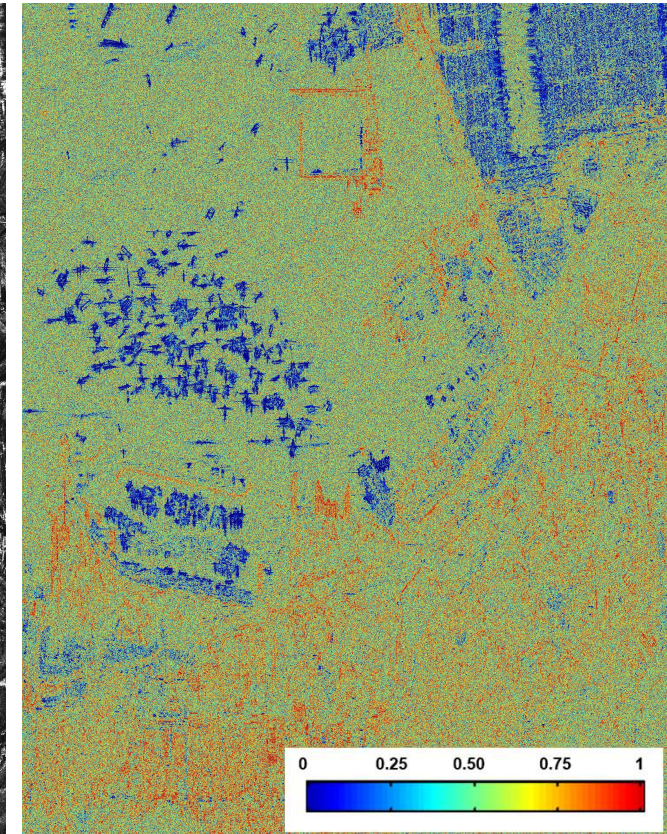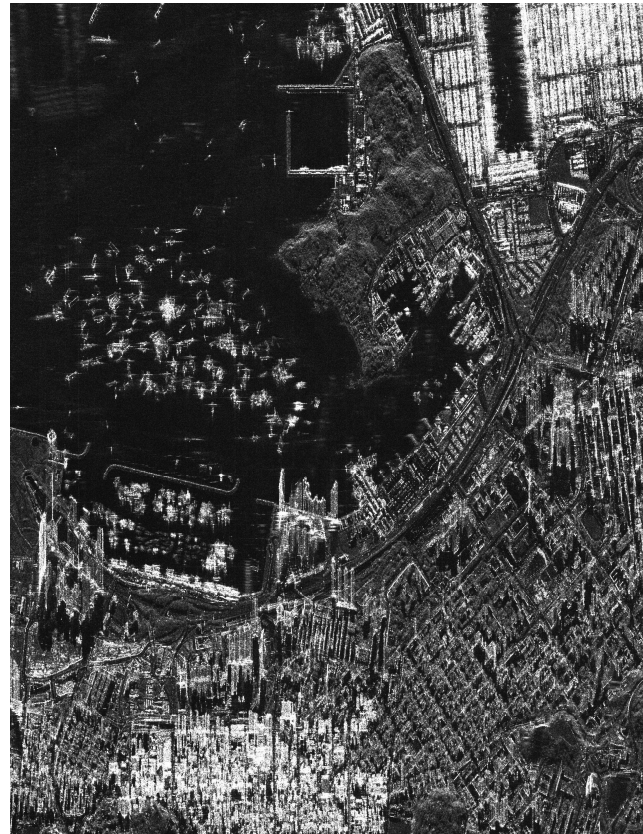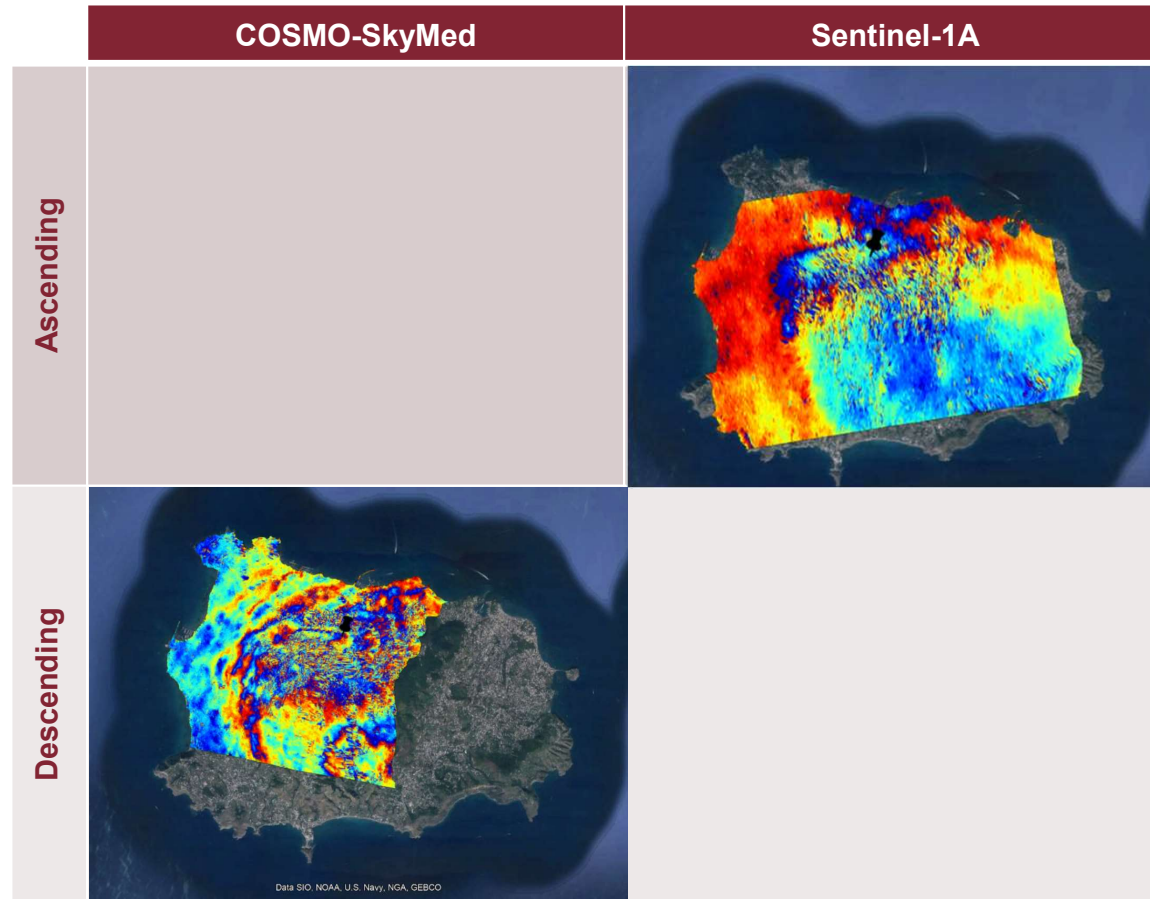
Sentinel 1
orbita ascendente

- 16.08.2017 – 22.08.2017
- Dimensione del pixel tra i 5 ed i 40 m in base alla modalità di acquisizione
- Opera in banda C con λ=5,54 cm
- Interferometria rileva spostamenti di $\frac{\lambda}{2} \approx 2,8\ cm$ per ciascuna frangia

*In corrispondenza della zona di Casamicciola si notano delle bande concentriche, ovvero delle **frange interferometriche**, indicatore principale che tra le due acquisizioni vi è stato un movimento sensibile.*
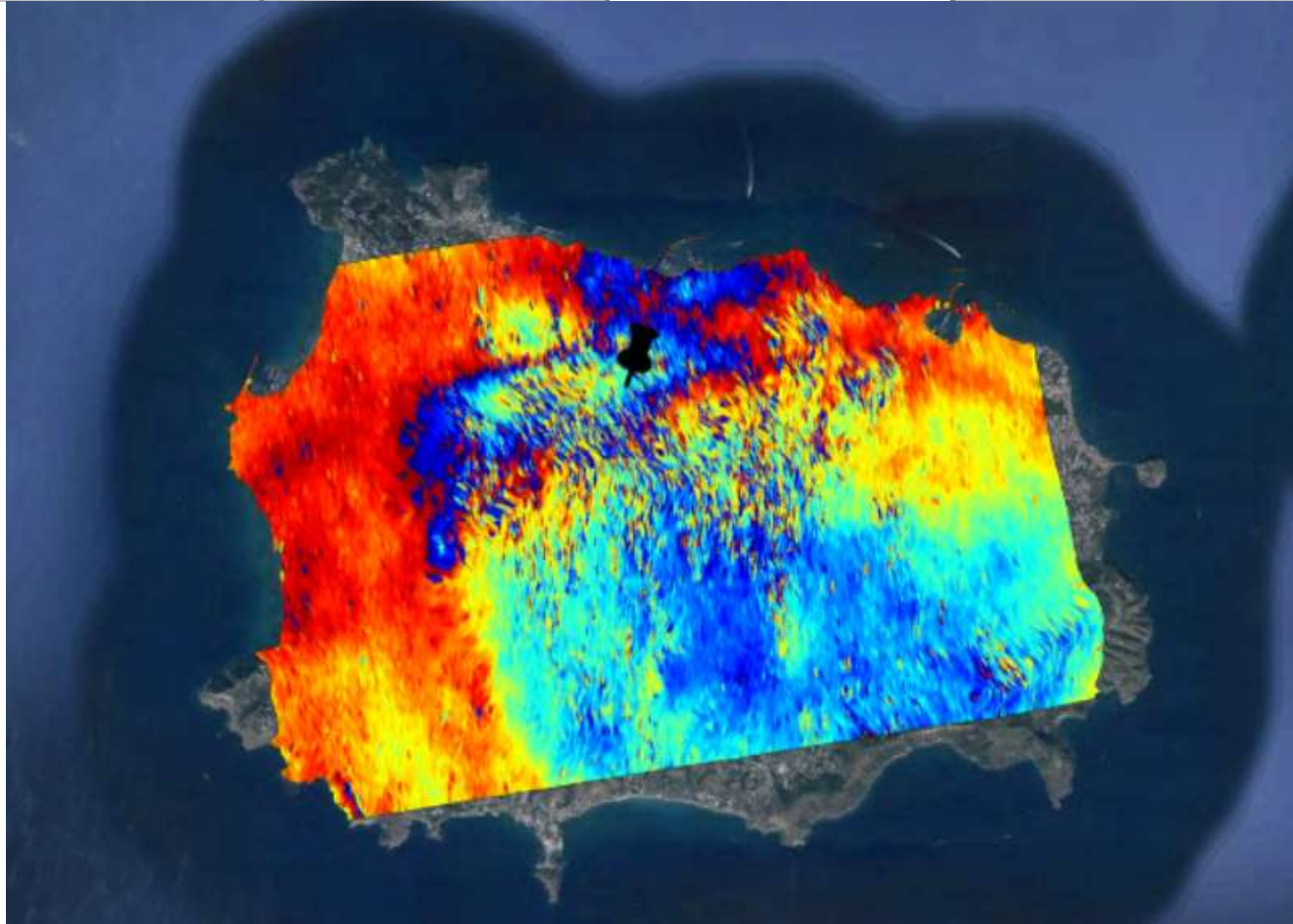
COSMO-SkyMed
orbita discendente

- 19.08.2017 – 23.08.2017
- Risoluzione 3x3 m
- Opera in banda X con λ=3 cm
- Interferometria rileva spostamenti di $\frac{\lambda}{2} \approx 1,5\ cm$ per ciascuna frangia

Si individuano circa due frange interferometriche, coerentemente con la sensibilità del sensore. L'interferogramma appare molto più disturbato dall'influenza dell'atmosfera.
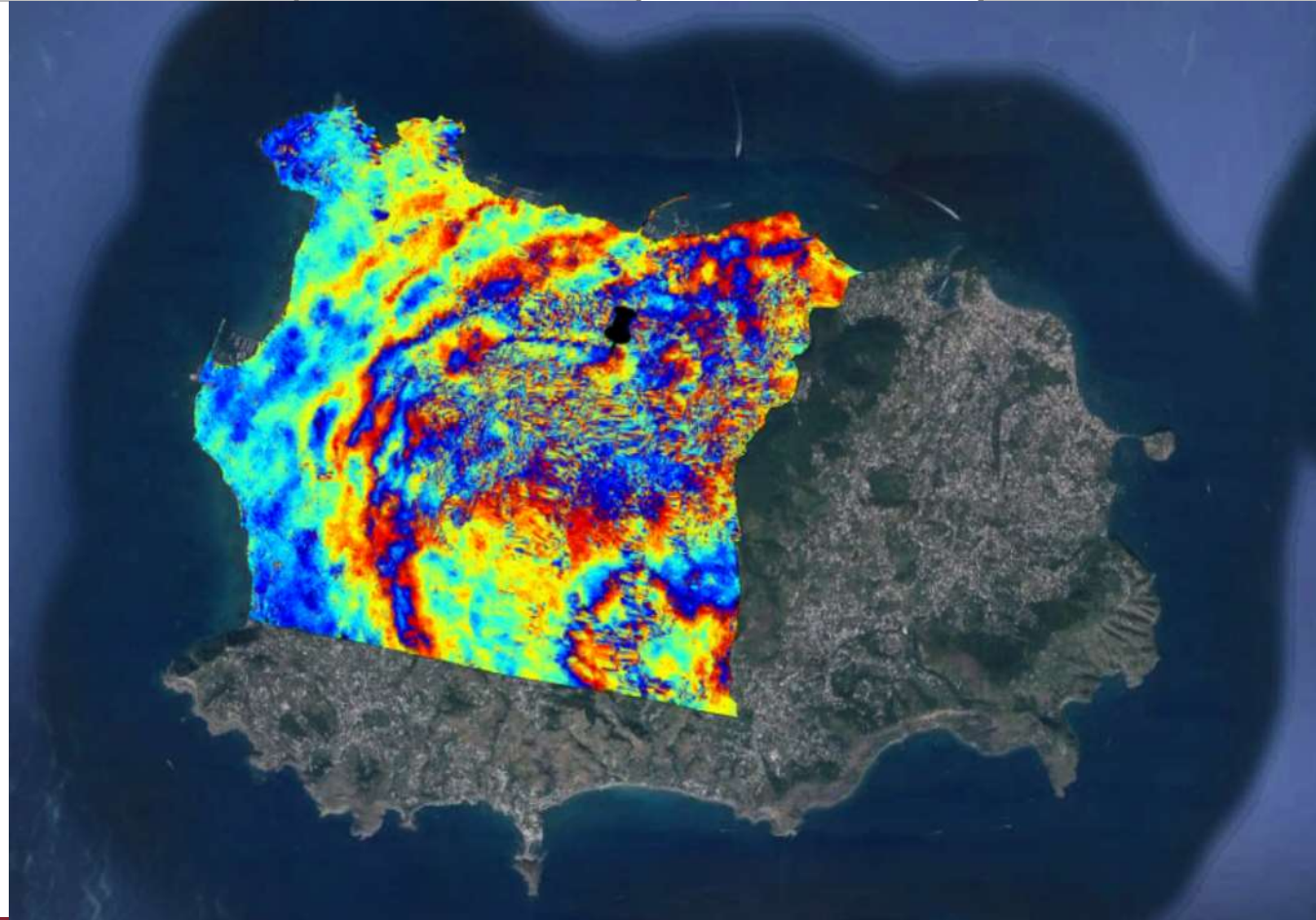
La **Map Coherence** consente di stimare la qualità dell'interferograma. La coerenza assume valore da 0 (la fase interferometrica è solo rumore) a 1 (completa assenza di rumore).
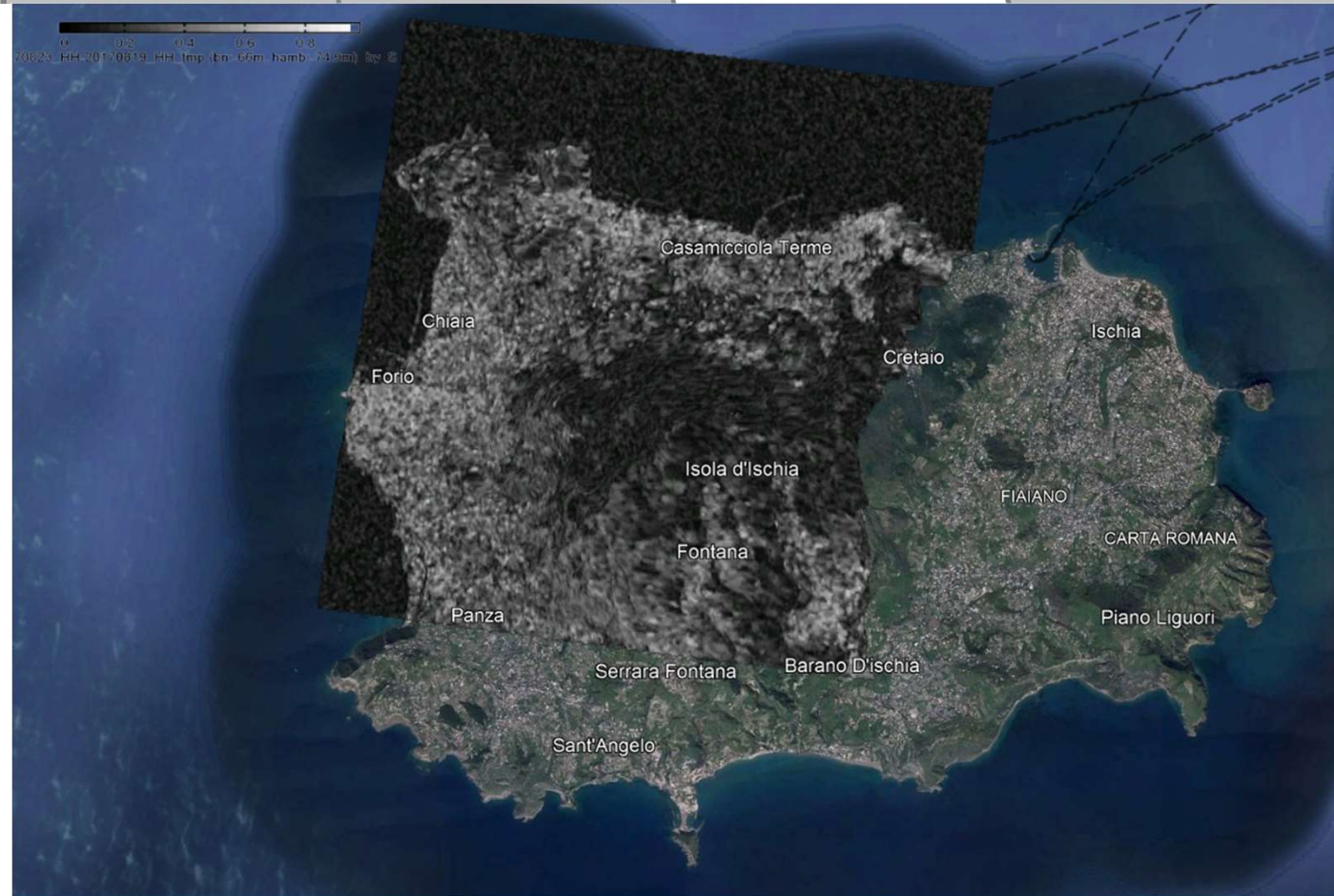
Cosmo-SkyMed
Mappa della velocità media al suolo (lungo la LOS)

L'area centro-nord dell'isola è stata quella interessata dalle deformazioni superficiali maggiori con un abbassamento del suolo fino a 3.6-4 cm come evidenziato dal dato SAR.

Fonte: Rapporto di sintesi preliminare sul Terremoto dell'isola d'Ischia (Casamicciola) M4.0 del 21 agosto 2017 - INGV

Displ. [mm]
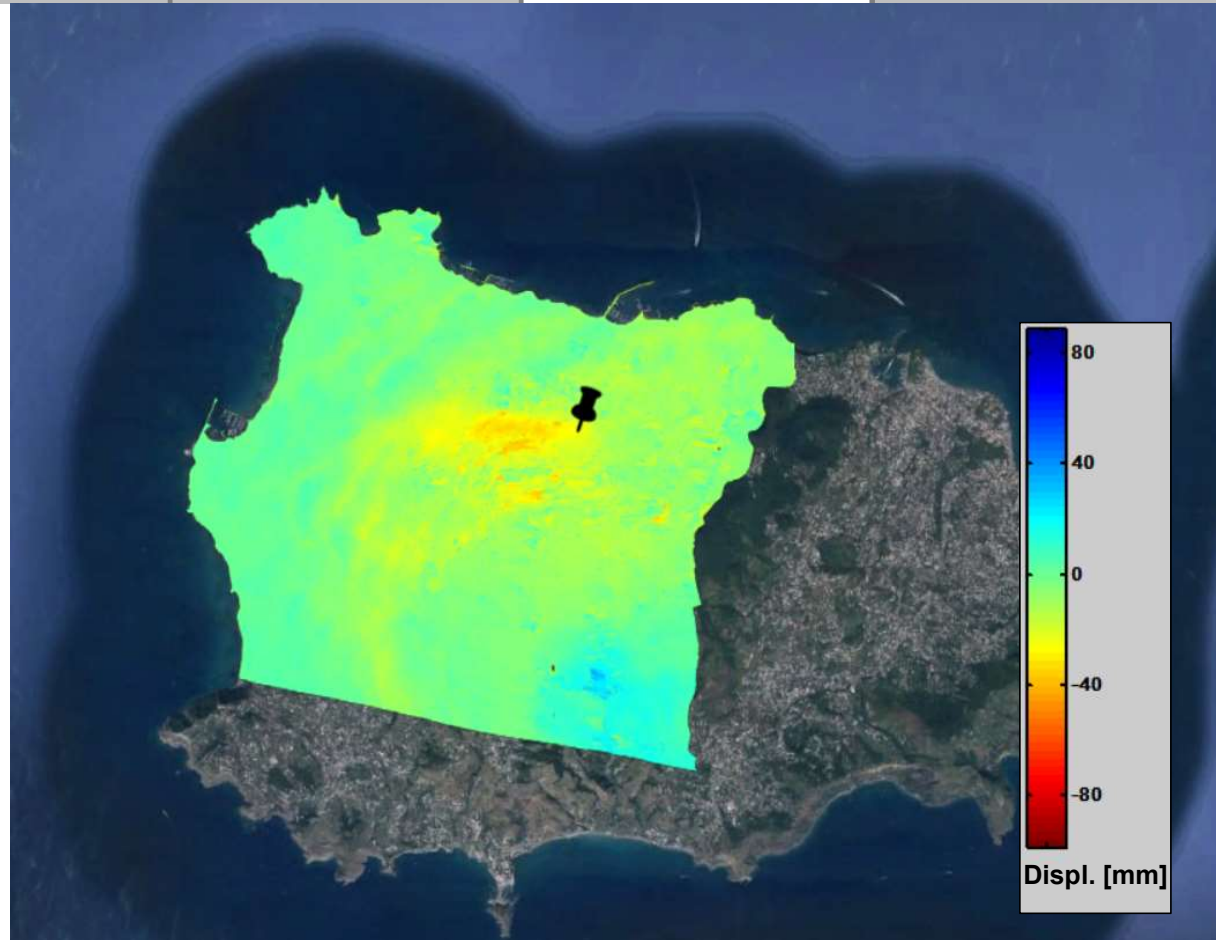
❑ **Villa Romana di Caposele** (Formia, LT)
❑ Tecniche geomatiche di rilievo confrontate:
▪ GEOSLAM Zeb Horizon
▪ TLS Faro
▪ DJI Matrice 300/RTK
▪ DJI Phantom 4
❑ Software: Cloud Compare 2.11.3 64 bit
Obiettivo: Sviluppare e calibrare tecniche geomatiche più o meno innovative per individuare le procedure più adatte a rilevare strutture grandi e complesse in tempi brevi, mantenendo precisioni almeno dell'ordine di qualche centimetro.

Il confronto ha mostrato deviazioni molto limitate, la cui validazione statistica è in corso, dimostrando che la tecnica SLAM può essere vantaggiosamente utilizzata in complessi archeologici così vasti dove la completezza della complessi archeologici è più importante dell'accuratezza millimetrica.
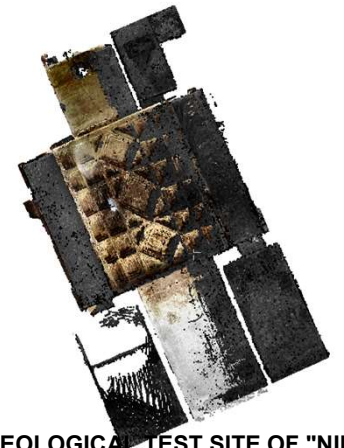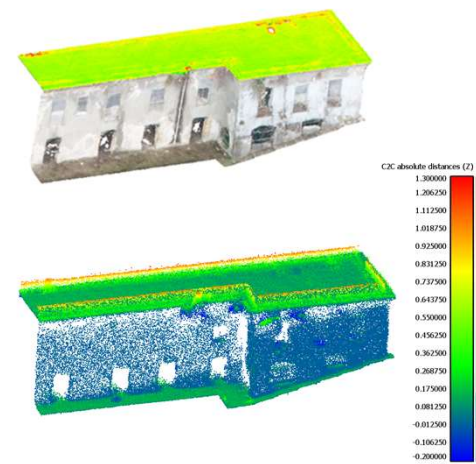
C2C absolute distances (Z)

EFFICIENT THREE-DIMENSIONAL SURVEY TECHNIQUES AND THEIR COMPARISON IN OPEN SOFTWARE IN THE ARCHAEOLOGICAL TEST SITE OF "NINFEO MAGGIORE" AND "NINFEO MINORE" OF FORMIA (LATINA, ITALY), L. Alessandri, V. Baiocchi, G. Melandri, F. Monti, A. Canu, L. Ruzzi, G. Servodio
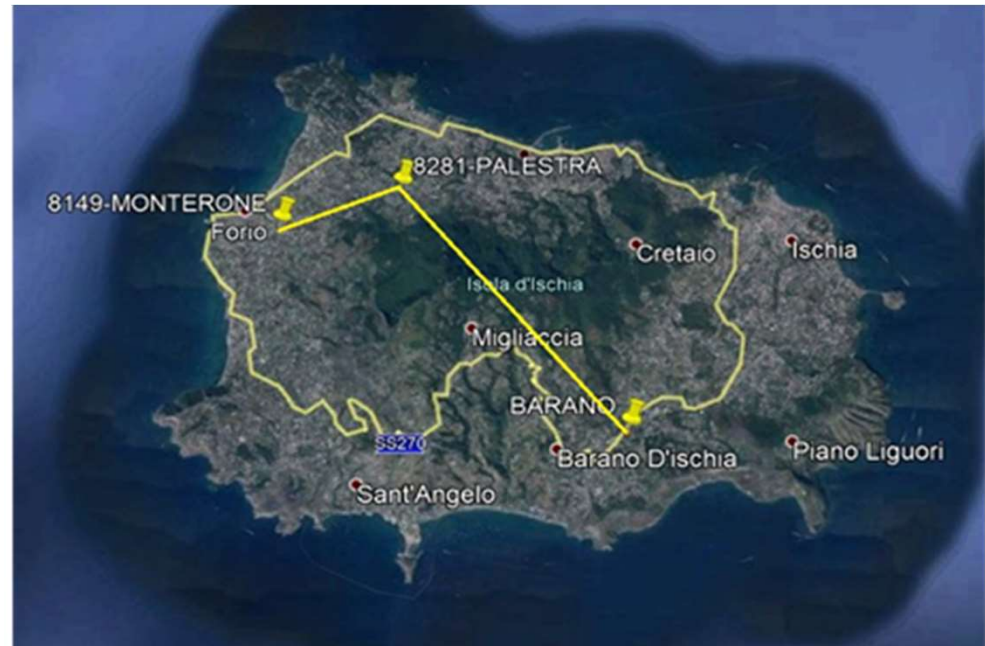
Nuvola di punti laser matrice 300
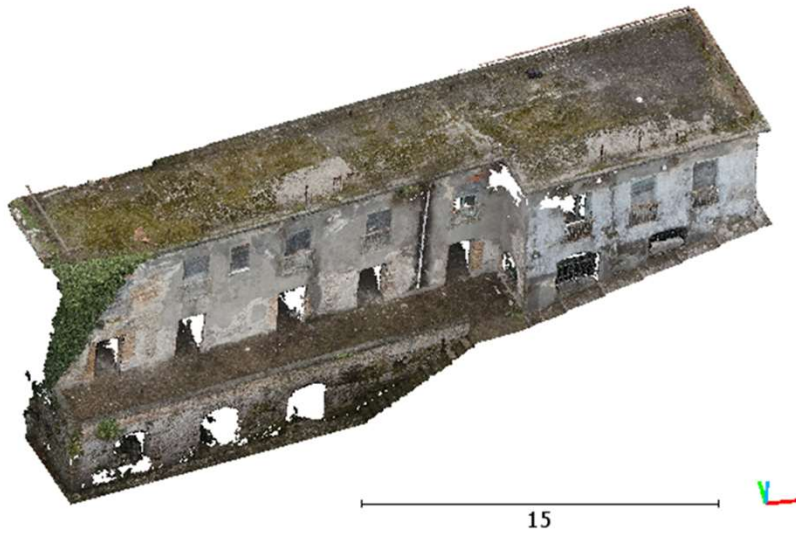
Nuvola di punti ottica matrice 300

Nuvola di punti ottica phantom 4

Ricevitori «South Galaxy» differenziali «low cost»
+
Ricevitore geodetico classico di controllo
+
Rete di stazioni permanenti INGV- OV e regione Campania

Bibliografia

- C.S. Fraser, T. Yamakawa, Insights into the affine model for high-resolution satellite sensor orientation, 2003
- Clive S. Fraser and Harry B. Hanley, Bias-compensated RPCs for Sensor Orientation of High-resolution Satellite Imagery, 2005
- Clive S. Fraser and Harry B. Hanley, Bias Compensation in Rational Functions for Ikonos Satellite Imagery, 2003
- Zhen Xiong and Yun Zhang, A Generic Method for RPC Refinement Using Ground Control Information
- C.S. Fraser, G. Dial b, J. Grodecki, Sensor orientation via RPCs, 2006

- Loizzo R., Ananasso C., Guarini R., Lopinto E., Candela L., Pisani A.R., THE PRISMA HYPERSPECTRAL MISSION, 2016
- ASI-AGI partners, Analisi Sistemi Iperspettrali per le Applicazioni Geofisiche Integrate, 2015
- Progetto OPTIMA, 2014

- Perissin D., Geometric Processing: Active Sensor Modeling and Calibration (SAR)
- Perissin D., Interferometric SAR MultiTemporal processing (techniques and applications)
- M. Manzo, G.P. Ricciardi, F. Casu, G. Ventura, G. Zeni, S. Borgstro, P. Berardino, C. Del Gaudio, R. Lanari, Surface deformation analysis in the Ischia Island (Italy) based on spaceborne radar interferometry, 2005

- Kraus K., Fotogrammetria, Volume 1: Teoria e applicazioni
- Mayer C., Gomes Pereira L. M., Kersten T. P., A Comprehensive Workflow to Process UAV Images for the Efficient Production of Accurate Geo-information, 2018
- La Rocca A., Lingua A. M., Grigillio D., Un'applicazione della fotogrammetria al monitoraggio di una frana in roccia; il caso studio di Belca, Slovenia
- USGS, Unmanned Aircraft Systems Data Post-Processing, Structure-from-Motion Photogrammetry